

**SPIN POLARIZABILITY OF A PROTON USING POLARIZED  
PHOTON BEAM AND POLARIZED BUTANOL TARGET AT MAINZ  
MICROTRON**

A Thesis

Submitted to the Faculty of Graduate Studies and Research  
in Partial Fulfillment of the Requirements

For the Degree of  
DOCTOR OF PHILOSOPHY

in

Physics

University of Regina

by

**Dilli Raj Paudyal**

**Regina, Saskatchewan, Canada**

**September, 2017**

**UNIVERSITY OF REGINA**  
**FACULTY OF GRADUATE STUDIES AND RESEARCH**  
**SUPERVISORY AND EXAMINING COMMITTEE**

Dilli Raj Paudyal, candidate for the degree of Doctor of Philosophy in Physics, has presented a thesis titled, ***Spin Polarizability of a Proton Using Polarized Photon Beam and Polarized Butanol Target at Mainz Microtron***, in an oral examination held on August 28, 2017. The following committee members have found the thesis acceptable in form and content, and that the candidate demonstrated satisfactory knowledge of the subject material.

External Examiner:           \*Dr. Douglas Higinbotham,  
Thomas Jefferson National Accelerator Facility

Supervisor:                    Dr. Garth Huber, Department of Physics

Committee Member:         Dr. Zisis Papandreou, Department of Physics

Committee Member:         Dr. Mauricio Barbi, Department of Physics

Committee Member:         Dr. Brian Sterenberg, Department of Chemistry

Committee Member:         Dr. David Hornidge, Adjunct

Chair of Defense:            Dr. Thomas Bredohl, Faculty of Graduate Studies & Research

\*participated via SKYPE

## ABSTRACT

Within this work, the data analysis and experimental results on the measurement of the double polarization observable (or beam-target asymmetry),  $\sum_{2z}$ , for real Compton scattering off the proton is presented. The  $\sum_{2z}$  values are measured via a circularly polarized photon beam incident upon a longitudinally polarized butanol target in the resonance region,  $E_\gamma = 250 - 310$  MeV. This experiment was performed at the MAMI-A2 tagged photon facility in Mainz, Germany, during two experimental beamtimes in 2014 and 2015.

This work also involves the extraction of proton spin polarizabilities, which are fundamental structure constants, similar to its charge and mass. These constants provide a measure of the global resistance of the nucleon's spin axis against displacement in an external electric or magnetic field, which makes them an excellent tool to study the structure of the nucleon. While the spin-independent, or scalar, electric ( $\alpha_{E1}$ ) and magnetic ( $\beta_{M1}$ ) polarizabilities of the nucleon have been measured, little effort has been made to extract the spin-dependent polarizabilities. These four leading order spin dependent polarizabilities,  $\gamma_{E1E1}$ ,  $\gamma_{M1M1}$ ,  $\gamma_{M1E2}$  and  $\gamma_{E1M2}$ , describe the spin response of a proton to electric and magnetic dipole and quadrupole interactions. This requires the precise measurement of the single and double polarization observables which are sensitive to these polarizabilities.

Through this analysis, the spin polarizabilities have been extracted by performing a global analysis with the aid of two QCD-based models. The extracted four spin polarizabilities are:  $\gamma_{M1M1} = 3.25 \pm 0.40$ ,  $\gamma_{E1E1} = -4.24 \pm 0.39$ ,  $\gamma_{E1M2} = 0.76 \pm 0.83$  and  $\gamma_{M1E2} = 1.24 \pm 0.39$ , in units of  $10^{-4} \text{ fm}^4$ . The uncertainties in  $\gamma_{E1E1}$ ,  $\gamma_{M1M1}$ ,  $\gamma_{E1M2}$  were improved by a factor of two to four, but  $\gamma_{M1E2}$  remained unchanged. These extracted spin polarizabilities are also in good agreement with dispersion, Heavy Baryon chiral perturbation and K-matrix theory predictions.

## ACKNOWLEDGEMENTS

I would not have been able to complete this dissertation without the support, guidance and inspirations of many people throughout the last five years. Firstly, I am grateful to my excellent supervisor Garth Huber for his intellectual guidance, continuous support of my Ph.D study and related projects, expert suggestions, and empathetic encouragement. His support and friendship are greatly appreciated, without his guidance, support and trust, none of this would have been possible. I would like to thank him for being not only an excellent mentor but also a close friend throughout my graduate career. I greatly appreciate the contributions of Dave Hornidge for all the support and insightful comments, and committee members Zisis Papandreou, Mauricio Barbi and Brian Stenberg for their suggestions and constructive criticisms. Nader Mobed deserves thanks for excellent lectures and also chairing PhD committee meetings every year. Many thanks to George Lolos for wonderful lectures.

I must thank Phil Martel for his help with all sorts of experimental questions and discussions on the data analysis every week during the group meetings. I would like to thank Compton group, specially Cristina Collicott, Vahe Sokhoyan, Evie Downie, Rory Miskimen, Aliasghar Rajabi, Zafar Ahmed and J.R.M. Anand. I would also like to thank Andreas Thomas, James Linturi, Patrick Adlarson, Mornacchi Edoardo, Federico Cividini and the entire A2 Collaboration as well as MAMI staff and frozen spin target group for their support and effort, which made this work a success. I would like to extend my thanks to Barbara Pasquini and Vladimir Pascalutsa for allowing us to use dispersion and heavy baryon chiral perturbation code, and University of Basel group for letting us to use calibration software. I want to thank the undergraduate students at Mount Allison University and The George Washington University who contributed during the run period of  $\sum_{2z}$  experiment.

Special thanks to Wenliang Li for unconstrained friendship and technical help,

specially for the stimulating discussions, for the sleepless nights we were working together during the first two years. You are one of the most selfless people I know and I look forward to our friendship, both personal and professional, after graduation. Of course, thanks go to all of my colleagues in the department of physics, Samip Basnet, Ryan Ambrose, Rory Evans, Ahmed Foda and Tegan Beattie.

Furthermore, this work would not have been possible without the support of my family. My parents, Tej Narayan and Tara Paudel, are the constant source of encouragement who valued education above all else and worked hard their entire life. To my wife Anju for the constant support and peaceful companionship, and to my son Prayush and Pragon for the parental pride. Thanks go to my brothers Khim Lal and Maniram Paudyal, and to my sisters Parwati and Ganga Paudyal. I would like to extend my sincere thanks to Anju's family as well.

Finally, I would like to acknowledge the Faculty of Graduate Studies and Research, Department of Physics, CINP and NSERC for all the funding support, and scholarships and awards. My special thanks are extended to Cheryl Risling and all other staffs.

# DEDICATION

**Dedicated to my family!**

# Contents

<b>Abstract</b>	<b>i</b>
<b>Acknowledgements</b>	<b>ii</b>
<b>Dedication</b>	<b>iv</b>
<b>Table of Contents</b>	<b>v</b>
<b>List of Tables</b>	<b>xi</b>
<b>List of Figures</b>	<b>xii</b>
<b>1 Introduction</b>	<b>1</b>
<b>2 Literature Review</b>	<b>8</b>
2.1 Formalism for Nuclear Compton Scattering . . . . .	8
2.1.1 Born Terms . . . . .	9
2.1.2 Non-Born Terms and Nucleon Polarizabilities . . . . .	10
2.1.2.1 Scalar Polarizabilities and Sum Rules . . . . .	11
2.1.2.2 Baldin Sum Rule . . . . .	13
2.1.2.3 Gerasimov-Drell-Hearn $\gamma_0$ Sum Rule . . . . .	13
2.1.2.4 Spin Polarizabilities . . . . .	14
2.1.2.5 Forward spin polarizability . . . . .	16
2.1.2.6 Backward spin polarizability . . . . .	18

2.1.3	Theoretical Model Predictions . . . . .	19
2.1.3.1	Mandelstam Plane and Invariant Amplitudes . . . . .	20
2.1.3.2	Low Energy Expansion . . . . .	25
2.1.3.3	HDPV: Fixed- $t$ Dispersion Relation Approach . . . . .	26
2.1.3.4	B $\chi$ PT: Baryon Chiral Perturbation Theory Approach . . . . .	28
2.2	Compton asymmetries for polarized beam and target . . . . .	29
2.2.1	Beam Target Asymmetry - $\sum_{2z}$ . . . . .	31
2.2.2	Beam Target Asymmetry - $\sum_{2x}$ . . . . .	32
2.2.3	Beam Asymmetry - $\sum_3$ . . . . .	34
<b>3</b>	<b>Experimental Procedure</b>	<b>37</b>
3.1	Experimental Detector Setup . . . . .	37
3.1.1	MAMI Electron Accelerator . . . . .	38
3.1.1.1	Polarized Electron Beam . . . . .	38
3.1.1.2	Mott polarimeter . . . . .	40
3.1.1.3	MAMI Floor Plan . . . . .	40
3.1.1.4	Race Track Microtron . . . . .	42
3.1.2	Tagged Photon Beam Facility . . . . .	44
3.1.2.1	Bremsstrahlung Photon Production and Tagging . . . . .	44
3.1.2.2	Polarized Photon Beam . . . . .	48
3.1.2.3	Photon Beam Collimation . . . . .	49
3.1.3	Photon Detectors . . . . .	50
3.1.3.1	Crystal Ball . . . . .	50
3.1.3.2	Particle Identification Detector . . . . .	51
3.1.3.3	Multi Wire Proportional Chamber . . . . .	53
3.1.3.4	Two Armed Photon Spectrometer . . . . .	55
3.1.3.5	TAPS Veto . . . . .	58

3.2	Principle of Frozen Spin Butanol Target . . . . .	59
3.2.1	Brute Force Polarization . . . . .	59
3.2.2	Dynamic Nuclear Polarization . . . . .	61
3.2.2.1	Mainz Frozen Spin Target . . . . .	62
3.2.2.2	NMR System and Polarization Measurement . . . . .	65
3.2.3	Carbon Target . . . . .	65
3.3	A2 Data Acquisition and Trigger System . . . . .	67
3.3.1	Data Acquisition Software:AcquDAQ . . . . .	70
3.3.2	CB Esum Trigger System . . . . .	70
3.3.3	Multiplicity Trigger . . . . .	71
3.3.4	Tagger Trigger . . . . .	71
3.3.5	Readout . . . . .	71
3.3.5.1	Tagger Readout . . . . .	72
3.3.5.2	CB, PID and MWPC Readout . . . . .	72
3.3.5.3	TAPS and Veto Readout . . . . .	73
3.3.5.4	Scalers . . . . .	74
<b>4</b>	<b>Analysis Software and Detector Calibration</b>	<b>75</b>
4.1	Analysis Software . . . . .	76
4.1.1	AcquRoot . . . . .	76
4.1.2	CaLib . . . . .	76
4.1.3	GoAT . . . . .	77
4.1.4	A2Geant . . . . .	78
4.2	Detector Cluster Algorithm . . . . .	78
4.3	Calibration of the detectors . . . . .	80
4.3.1	Calibration Run-Sets . . . . .	81
4.3.2	Time Calibration . . . . .	81

4.3.3	Energy Calibration . . . . .	82
4.3.4	CB Time Calibration . . . . .	83
4.3.5	CB Time-walk Correction Calibration . . . . .	84
4.3.6	CB Energy Calibration . . . . .	85
4.3.7	TAPS Time Calibration . . . . .	87
4.3.8	TAPS Long-Gate Energy Calibration . . . . .	87
4.3.9	TAPS Short-Gate Energy Calibration . . . . .	88
4.3.10	Tagger Time Calibration . . . . .	90
4.3.11	Target Position . . . . .	90
4.3.12	PID Azimuthal Angle Calibration . . . . .	91
4.3.13	PID Time Calibration . . . . .	92
4.3.14	PID Energy Calibration . . . . .	93
4.3.15	TAPS Veto Time Calibration . . . . .	94
4.3.16	TAPS Veto Energy Calibration . . . . .	94
<b>5</b>	<b>Data Analysis I : <math>\pi^0</math> Asymmetry</b>	<b>96</b>
5.1	Event Selection and Particle Reconstruction . . . . .	96
5.1.1	Tagger Random Background Subtraction . . . . .	96
5.1.2	$\pi^0$ Event Selection . . . . .	98
5.1.2.1	$\pi^0$ Coplanarity Angle . . . . .	100
5.1.2.2	Reconstruction of $\pi^0$ invariant mass . . . . .	101
5.1.2.3	Missing Mass . . . . .	102
5.2	Carbon Scaling Factor . . . . .	103
5.2.1	Base Scaling Factor . . . . .	104
5.2.2	Extra and Corrected Scaling Factors . . . . .	106
5.3	Charged Particle Detection . . . . .	109
5.3.1	Rootino Detection Efficiency . . . . .	110

5.3.2	Rootino Detection Efficiency Fitting Function . . . . .	113
5.4	$\pi^0$ Photo-production Asymmetry . . . . .	116
<b>6</b>	<b>Data Analysis II : Compton <math>\sum_{2z}</math> Asymmetry</b>	<b>119</b>
6.1	Identification of Final State Interaction . . . . .	119
6.1.1	Event Selection . . . . .	120
6.1.1.1	Compton Coplanarity Angle . . . . .	122
6.1.1.2	Opening Angle . . . . .	124
6.1.1.3	Missing Mass for Compton Scattering Events . . . . .	125
6.1.1.4	Upper Limit On The Missing Mass . . . . .	128
6.1.2	2014, 2015 Compton $\sum_{2z}$ Asymmetry Results . . . . .	131
6.2	Error Analysis . . . . .	133
6.2.1	Target and Photon Beam Polarization . . . . .	134
6.2.2	Carbon Scaling Factor . . . . .	135
6.2.3	Missing Mass Cuts . . . . .	135
6.2.4	Statistical Errors . . . . .	136
6.2.5	Summation of Errors . . . . .	136
6.3	Combined $\sum_{2z}$ Asymmetry Results . . . . .	137
6.3.1	Comparison to HDPV Model . . . . .	138
<b>7</b>	<b>Results and Discussion</b>	<b>142</b>
7.1	Data Fitting With HDPV Model . . . . .	143
7.2	Data Fitting With B $\chi$ PT Model . . . . .	146
7.3	Fitting and $\chi^2$ minimization . . . . .	147
7.3.1	Construct $\chi^2$ . . . . .	148
7.3.2	Verification of the Fitting Procedure . . . . .	151
7.3.2.1	Error Calculations . . . . .	151

7.3.2.2	Linearity	152
7.3.2.3	Starting Value of Polarizabilities	156
7.4	Study of Model Dependence	156
7.5	Comparison With Theory Models	157
7.6	Outlook	161
<b>A</b>	<b>Experimental Trigger</b>	<b>163</b>
<b>B</b>	<b>Carbon Scaling</b>	<b>165</b>
B.0.1	Extra Scaling Factor	165
B.0.2	Corrected Scaling Factor	167
B.0.3	Detection Efficiency Fitting Parameters	169
<b>C</b>	<b><math>\sum_{2z}</math> Above <math>\gamma p \rightarrow \pi^0 \pi^0 p</math> threshold</b>	<b>170</b>
C.0.4	Systematic Errors at $E_\gamma = 285 - 305$ MeV	171
	<b>List of Abbreviations</b>	<b>182</b>

# List of Tables

2.1	Behavior of electric and magnetic field . . . . .	14
3.1	Main parameters of the MAMI accelerator . . . . .	44
6.1	Missing mass cuts for three energy and five angular bins. . . . .	131
6.2	Compton $\sum_{2z}$ asymmetry results (2014 and 2015 beamtimes) . . . . .	133
6.3	Systematic error studies at $E_\gamma = 265 - 285$ MeV . . . . .	137
6.4	Final Compton $\sum_{2z}$ asymmetry results . . . . .	138
7.1	Spin polarizability results based on HDPV model fit . . . . .	145
7.2	Comparison of spin polarizabilities . . . . .	145
7.3	Spin polarizabilities based on B $\chi$ PT model fit . . . . .	146
7.4	Model predictions of spin polarizabilities . . . . .	161
B.1	Carbon base scaling factors for parallel data set (2014 beam time). . . . .	165
B.2	Carbon base scaling factors for parallel data set (2015 beam time). . . . .	166
B.3	Corrected carbon scaling factors for anti-parallel data set (2014 beam time). . . . .	167
B.4	Corrected carbon scaling factors for anti-parallel data set (2015 beam time). . . . .	168
B.5	Logistic function fitting parameters for parallel data set . . . . .	169
C.1	Systematic error studies at $E_\gamma = 285 - 305$ MeV . . . . .	171

# List of Figures

1.1	The Standard Model of particle physics . . . . .	3
1.2	The Standard Model of particle physics . . . . .	5
2.1	Nuclear Compton Scattering below $\pi$ -production threshold . . .	15
2.2	The GDH experiments . . . . .	17
2.3	Experimental differential cross sections for Compton scattering	18
2.4	Some typical intermediate states . . . . .	22
2.5	Singularities in the $s$ and $t$ planes . . . . .	23
2.6	The Mandelstam plane for Compton scattering . . . . .	25
2.7	Compton scattering with a longitudinally polarized target and a circularly polarized photon beam . . . . .	32
2.8	Compton $\Sigma_{2x}$ results at $E_\gamma = 273 - 303$ MeV . . . . .	33
2.9	$\Sigma_3$ for $E_\gamma = 297 \pm 10.1$ MeV . . . . .	35
3.1	MAMI Mott polarimeter . . . . .	39
3.2	Electron Beam Polarization . . . . .	41
3.3	MAMI floor plan and four experimental halls . . . . .	42
3.4	A schematic view of a RTM . . . . .	43
3.5	The Glasgow photon tagger spectrometer . . . . .	46
3.6	The bremsstrahlung distribution . . . . .	47
3.7	Moeller radiator . . . . .	49
3.8	A schematic picture of the detector setup . . . . .	50

3.9	Geometry of the Crystal Ball detector . . . . .	52
3.10	PID detector . . . . .	53
3.11	MWPC schematic diagram . . . . .	54
3.12	BaF <sub>2</sub> crystal with and without connected to a PMT . . . . .	56
3.13	BaF <sub>2</sub> and 72 PbWO <sub>4</sub> stacked in TAPS setup . . . . .	57
3.14	TAPS Veto plastic scintillator . . . . .	58
3.15	Brute Force Polarization . . . . .	60
3.16	MAMI frozen spin target . . . . .	63
3.17	Energy levels of the coupled electron-nucleon system . . . . .	64
3.18	Target Polarization . . . . .	66
3.19	A2 main experimental trigger . . . . .	69
4.1	Cluster algorithm . . . . .	80
4.2	Calibration Run-set . . . . .	82
4.3	Crystal Ball time calibration . . . . .	84
4.4	Schematic CB Time-Walk . . . . .	85
4.5	Crystal Ball time-walk correction . . . . .	86
4.6	$\pi^0$ invariant mass . . . . .	86
4.7	TAPS time calibration . . . . .	87
4.8	TAPS Long Gate Energy Calibration . . . . .	88
4.9	TAPS Short Gate Energy Calibration . . . . .	89
4.10	Tagger time calibration . . . . .	90
4.11	Target position calibration . . . . .	91
4.12	The Crystal Ball $\phi$ angle correlation . . . . .	92
4.13	PID time calibration . . . . .	93
4.14	PID energy calibration . . . . .	94
4.15	Veto time calibration . . . . .	95

4.16	Veto energy calibration . . . . .	95
5.1	Difference between the tagger and $\pi^0$ time . . . . .	97
5.2	Flow chart for $\pi^0$ meson selection . . . . .	99
5.3	Invariant mass for reconstructed $\pi^0$ . . . . .	101
5.4	Missing mass for reconstructed $\pi^0$ . . . . .	103
5.5	Tagger scaler distribution and scaling factor . . . . .	105
5.6	Ratio of missing mass spectrum for butanol and carbon targets	107
5.7	Corrected carbon scaling factor . . . . .	107
5.8	Missing mass distribution for $\pi^0$ Photo-production . . . . .	108
5.9	Carbon subtraction with corrected scale factor . . . . .	108
5.10	Rootino detection efficiency using photo-production events . . .	114
5.11	Rootino detection efficiency using photo-production events . . .	115
5.12	$\pi^0 \sum_{2z}$ Asymmetry on 2014 and 2015 beamtime . . . . .	117
6.1	Fiducial cuts applied . . . . .	121
6.2	A schematic diagram of the Compton scattering reaction . . .	123
6.3	Opening angle . . . . .	125
6.4	Missing mass distribution for two energy bins . . . . .	127
6.5	Asymmetry as a function of upper missing mass cut . . . . .	129
6.6	Compton $\sum_{2z}$ asymmetry results . . . . .	132
6.7	Final $\sum_{2z}$ asymmetry results . . . . .	140
7.1	$\chi^2/\text{DOF}$ as a function of $\gamma_{E1E1}$ and $\gamma_{M1M1}$ . . . . .	153
7.2	$\chi^2/\text{DOF}$ as a function of $\gamma_{E1M2}$ and $\gamma_{M1E2}$ . . . . .	154
7.3	$\chi^2/\text{DOF}$ as a function of $\alpha_{E1}$ and $\beta_{M1}$ . . . . .	155
7.4	$\sum_3$ for different values of $\gamma_{E1E1}$ . . . . .	156
7.5	$\sum_{2x}$ for different values of $\gamma_{E1E1}$ . . . . .	157

7.6	HDPV fits . . . . .	158
7.7	B $\chi$ PT fits . . . . .	159
7.8	Fitting results from HDPV and B $\chi$ PT models . . . . .	160
A.1	Subcomponents of an experimental trigger . . . . .	163
A.2	Experimental trigger components . . . . .	164
C.1	$\sum_{2z}$ asymmetry results at $E_\gamma = 310 - 330$ MeV . . . . .	170

# Chapter 1

## Introduction

The scientific quest to understand what matter is made of is one of the oldest human undertakings. There was very little progress until the beginning of the 20<sup>th</sup> century when J. J. Thompson discovered that cathode rays consist of fundamental particles: the electrons. During the early 20<sup>th</sup> century, there was an unprecedented development in both theoretical and experimental nuclear physics. In 1911, Ernest Rutherford performed an experiment using helium nuclei on a gold foil and discovered the experimental evidence of a positively charged core, the ‘nucleus’, and proposed the famous Rutherford’s model of the atoms [1]. Two years later, Neils Bohr proposed several improvements over Rutherford’s model [2]. He postulated that the electrons orbit the nucleus of an atom in discrete radii defined by their angular momenta which explained the emission lines in atomic spectra.

While theorists have long been capable of dreaming up possible explanations for various phenomena, it has only been within the past half-century that experimentalists have had the tools necessary to put some of those theories to test. The development in accelerator technology which started in the 1930s soon allowed intense, focused beams of particles to be used in fixed-target and, later, collider experiments,

opening the door for new experimental challenges. In the mid-1930s, just a few years after the first observation of the neutron by James Chadwick in 1932 [3], Yukawa [4] suggested that the attractive force between the nucleons was mediated via the exchange of massive virtual particles called mesons. In 1947, the existence of such particles was confirmed experimentally, stimulating work in the field of hadronic structure. Subsequently, Murray Gell-Mann [5] and George Zweig [6] each independently proposed the Quark Model to describe the classification scheme for hadrons in 1964, in which new elementary particles called quarks were introduced. According to this model, the quarks together with their antiparticles combine to form hadrons. Hadrons may be classified as baryons or mesons depending on the number of quarks/anti-quarks that are combined. A baryon, such as a proton or neutron consists of three valence quarks, while a meson such as the  $\pi$  meson consists of a quark and an anti-quark.

The framework of the quantum mechanics is based on the significant achievements like the wave-particle duality by Louis de Broglie in 1923 [7], the uncertainty principle by Werner Heisenberg in 1925 [8] and the wave equation by Erwin Schrodinger in 1926 [9]. Now, the Standard Model of particle physics first formulated in the mid 1970s has been established as an enormous success in classifying all the subatomic particles known as well as in explaining and predicting several nuclear and particle physics phenomena.

The Standard Model [11] of particle physics consists of three generations of quarks and leptons and a family of force carriers as shown in Fig. 1.1. In addition to the original proposed table, it includes a new scalar particle, the Higgs-boson, whose observation at CERN was announced in 2012. The first generation of matter is the visible building blocks of the universe which includes both quarks and leptons as spin-1/2 fermions. Force carriers that mediate the fundamental interactions (strong,

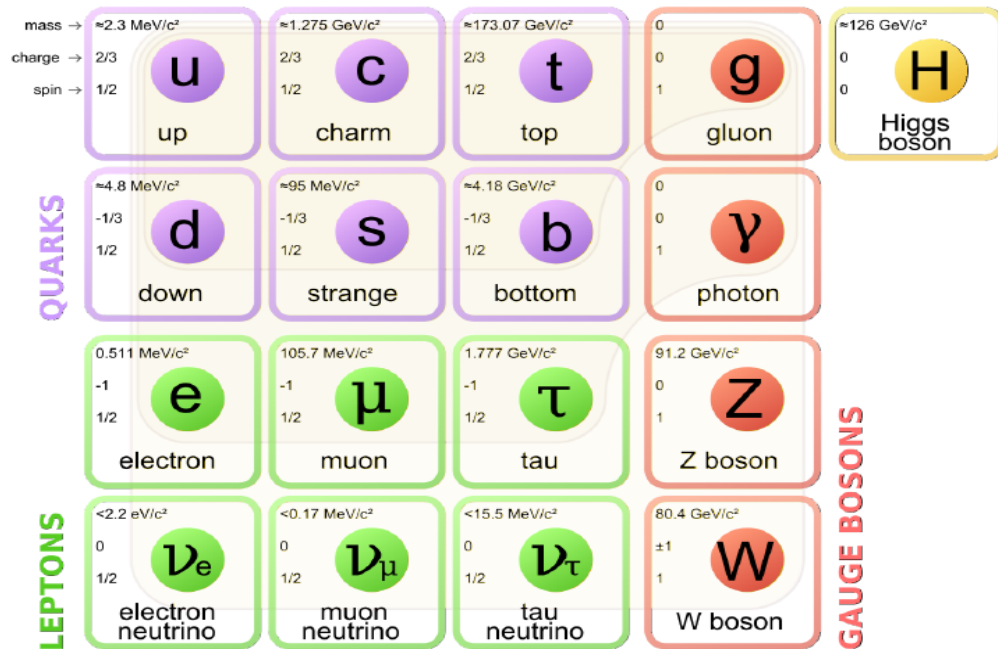


Figure 1.1: The Standard Model of particle physics showing three generations of matter, gauge bosons and the Higgs boson [10].

electromagnetic and weak) are spin-1 gauge bosons. However, there exist four known fundamental forces: gravity, the electromagnetic force, the weak force, and the strong force; gravity still remains excluded from the Standard Model. The Standard Model is based on the gauge groups  $SU(3) \otimes SU(2) \otimes U(1)$ .  $U(1)$  denotes the symmetry group of the electromagnetic interaction where the fermions act as singlets and interact by exchanging one boson.  $SU(2)$  is for the weak interaction where the left handed fermions act as pairs mediated by three bosons, and  $SU(3)$  for the strong interaction where the fermions act as triplets mediated by eight bosons.

After the discovery of quarks as the fundamental building blocks of hadrons, the theory of Quantum Chromodynamics (QCD) was developed [4]. QCD is a quantum field theory describing the strong interaction; that is, the interaction between quarks mediated by a massless particles called gluons. The concept of a massless force

mediator is very similar to the mediator in Quantum Electrodynamics (QED), in which photons act as a force mediator between charged particles.

In QCD, the quark-quark potential depends on the distance between the quarks and the interaction energy. The strength of the interaction between quarks and gluons is parametrized via the strong coupling constant,  $\alpha_s$ . In QCD, this coupling constant is not in fact a constant but varies with the energy of the system as shown in Fig. 1.2. At very large energy scale ( $\geq 1$  GeV) corresponding to distances much smaller than the typical hadron size ( $\ll 1$  fm), the coupling between the quarks and gluons and the coupling of gluons to themselves become very small such that the quarks inside a proton are nearly free, not subject to any force. This feature of QCD is known as *asymptotic freedom*. In this energy regime, the  $\alpha_s$  is much smaller than one, meaning that it is possible to use perturbation theory [12] to describe precisely the interactions because the perturbative expansion converges and is therefore solvable.

However, at lower interaction energy scale ( $\leq 1$  GeV) and larger distance such as those associated with the quarks inside the nucleon, the strength of  $\alpha_s$  becomes very large. As the quarks move further apart, the binding between them increases, eventually leading to a new quark-anti-quark pair being formed, and no matter how much energy is injected into a nucleon, and it is therefore almost impossible to isolate either a quark or a gluon. This feature of QCD is known as *colour confinement*. In this energy regime, it is not possible to use perturbation theory to describe reliably the interactions because the perturbative expansion diverges and is therefore not solvable. For this reason, the calculation of structure observables of the hadrons like size, shape and polarizability is not possible. Therefore, other non-perturbative methods like phenomenological models, or lattice based QCD calculations have been used to describe the strong interaction in the low energy regime [14]. However, phenomenological models have been successful and established as a bridge between the

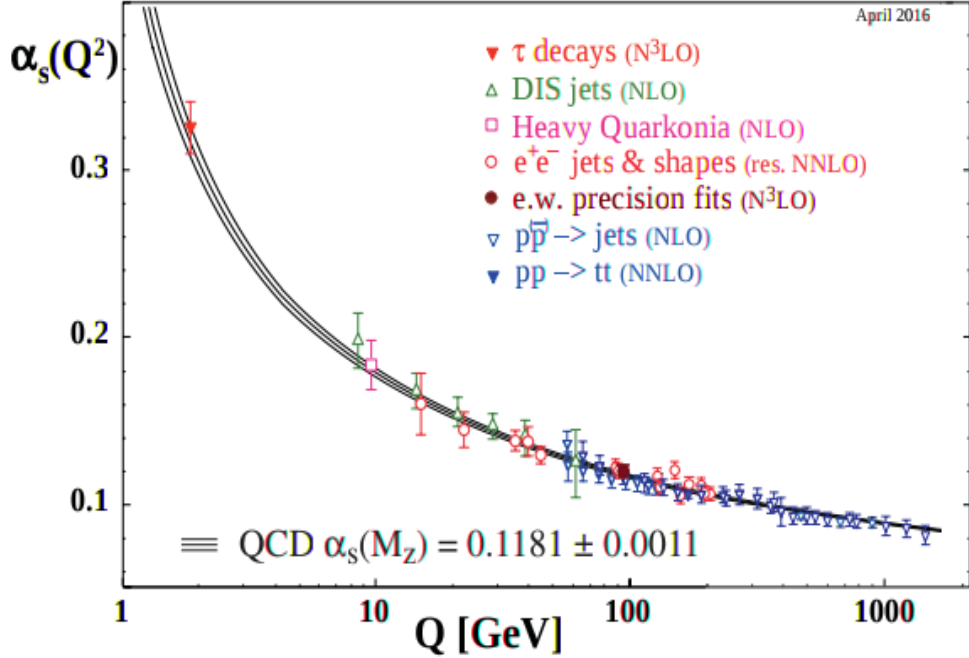


Figure 1.2: The strong coupling constant as a function of the momentum transfer  $Q$  (GeV). The respective degree of QCD perturbation theory used in the extraction of  $\alpha_s$  through diagrammatic expansion is indicated in brackets (NLO: next-to-leading order; NNLO: next-to-next-to leading order; res. NNLO: NNLO matched with resummed next-to-leading logs; N<sup>3</sup>LO: next-to-NNLO). Figure taken from [13].

mathematical models and experimental particle physics. Lattice QCD calculations are much more challenging due to the need of very large computing resources to bear on lattices of moderate size and the efficiency of algorithms. The most popular models for calculations involving few nucleon systems in the low-energy regime of QCD are Dispersion Relation (DR) and Chiral Effective Field Theory ( $\chi$ EFT). In  $\chi$ EFT, the symmetries of QCD are utilized such that the number of possible interactions is restricted, so that the quark and gluon fields of QCD may be replaced by hadronic degrees of freedom and the QCD Lagrangian density may be replaced by an effective Lagrangian density. The details of this theory are beyond the scope of this thesis. The reader is referred to [15] for further information.

A proton is a composite hadronic system which consists of three valence quarks,

plus virtual sea quarks and gluons. This dissertation focuses on the structure observables of a composite system called the polarizabilities. These are fundamental properties, similar to its charge and mass, and are benchmarks for our understanding of the symmetries and strength of the constituent interactions with each other within the proton.

At a classical level, polarizabilities reflect how much freedom charged constituents have to rearrange under the application of external electromagnetic fields, while at the quantum level, they indicate how easily the electromagnetic interactions induce transitions to low-lying excited states of nucleons. The physical content of the nucleon polarizabilities can be visualized best by effective multipole interactions for the coupling of the electric and magnetic fields of a photon with the internal structure of the nucleon. They are experimentally accessible by elastically scattering real photons off of the nucleon  $\gamma + N \rightarrow \gamma + N$  in what is known as nuclear Compton scattering reaction. In the low-energy limit, when the wavelength of scattered photon is large compared to the hadron size, the Compton scattering amplitude can be expanded in terms of the incoming photon energy. The polarizabilities are dominated by the lowest nucleonic states, namely by  $\pi N$  and  $\Delta(1232)$  resonance dynamics, while sensitivity to higher excitations is suppressed. This means that Compton scattering at low energies (below the  $\Delta$ ) resonance,  $\leq 300$  MeV, is dominated by long-distance properties of the nucleon. In particular, we note that the particles detected in the experiments are photons, protons and pions. Therefore, it is not worthwhile to perform Compton scattering at these energies in terms of quark masses, such as in lattice QCD or models of nucleon structure. Instead, we can perform experiments at low energy in terms of pions and nucleons degree of freedom and such measurements can be tested against the constraints extracted from the data using a theoretical approach that includes the low-energy dynamics.

Within this work, a brief overview of development and understanding of nuclear physics theory and experiment, literature review of various nucleon polarizabilities are presented in chapter 1 and 2. The experimental setup of the Crystal Ball experiment and calibration of individual detector elements are discussed in chapters 3 and 4. In chapter 5 and 6, the data analysis and experimental results on the measurement of the beam-target asymmetry, the  $\sum_{2z}$ , for both  $\pi^0$  photoproduction and Compton scattering channel are presented. The final results on the extraction of proton spin polarizabilities from this work, and a global analysis including previous measurement of the  $\sum_{2x}$  and  $\sum_3$  asymmetry with the aid of two QCD-based models are summarized in chapter 7.

# Chapter 2

## Literature Review

This chapter outlines our current understanding of the structure of the nucleon. Of particular interest is the study of the internal structure observables for the proton called polarizabilities, which are not as well understood as other static nucleon properties such as charge, mass or magnetic moment. Sec. 2.1 and Sec. 2.2 describe nuclear Compton scattering of off a proton and our understanding of single and double polarization observables.

### 2.1 Formalism for Nuclear Compton Scattering

Compton scattering, discovered by Arthur Holly Compton who was awarded the Nobel Prize in 1927 [16] “for his discovery of the effect named after him”, generally refers to the elastic scattering of a photon by a charged particle, usually an electron. This process was first described using a quantum mechanical treatment of electromagnetic radiation and relativistic kinematics of the electron. Compton’s experiment thus provided a unified demonstration of two of the great advances in physics in the early 20<sup>th</sup> century: relativity and the particle-like nature of light. However, the scattering process involved in this thesis is coherent elastic scattering of photons off

the nucleus, hence nuclear Compton scattering. In nuclear Compton scattering, the external electromagnetic field of the photon attempts to deform the nucleon. In low-energy nuclear physics, this process has been established as a well developed tool to probe the internal structure observables of the nucleon.

### 2.1.1 Born Terms

The elastic scattering of a photon from a bound nuclei can be described as resulting from the interaction of the nucleus with an electromagnetic field. The complete field consists of the electric field  $\vec{E}$  and magnetic field  $\vec{H}$ . The interaction between the nucleus and the field is mediated by the four-potential  $(\phi, \vec{A})$ , where  $\phi$  is the scalar potential and  $\vec{A}$  is the external vector potential of the photon. The most common way to investigate this electromagnetic interaction is by performing a Compton scattering of photons from nucleons. The interaction Hamiltonian can be expanded to different orders of incoming photon energy ( $\omega$ ). This order can be determined by the number of power of the photon energy. For example, electric field and magnetic field are order one, because they are time and spatial derivatives of the vector potential field respectively, while the vector potential field is defined to be order zero.

The most general field-theoretical Lagrangian for the nucleon field  $N$  with spin  $\frac{\sigma}{2}$ , where  $\sigma$  is the nucleon's Pauli spin matrices, and two photons (incident and scattered) of fixed and non-zero energy can be written in terms of external and internal degrees of freedom of nucleons as,

$$\mathcal{L} = \mathcal{L}_B + \mathcal{L}_{nB}, \quad (2.1)$$

where the Born terms ( $\mathcal{L}_B$ ) correspond to the external degrees of freedom and the non-Born term ( $\mathcal{L}_{nB}$ ) correspond to the internal dynamics of a nucleon. The Born

term can be written in terms of the Hamiltonian only up to first order as [17],

$$\mathcal{L}_B = N^\dagger [H_{eff}^{(0)} + H_{eff}^{(1)}] N, \quad (2.2)$$

where  $H_{eff}^{(0)}$  is the energy independent leading order Born term which corresponds to the Thompson scattering amplitude of a point-like charged particle of mass  $m$  and charge  $e$  given by

$$H_{eff}^{(0)} = \frac{(\vec{p} - e\vec{A})^2}{2M} + e\phi, \quad (2.3)$$

where  $e$  is the nucleon's electric charge,  $M$  is the nucleon's mass and  $\vec{p}$  is the momentum. At incident energies far below the  $\pi$ -production threshold ( $\sim 140$  MeV), photon scattering from the proton can be explained by the proton's static properties like its mass and charge. With increasing photon energies, an additional Born term arises due to the magnetic moment. This term, which is in the first-order effective Hamiltonian  $H_{eff}^{(1)}$  of Eq. 2.2, has the form,

$$H_{eff}^{(1)} = -\frac{e(1+\kappa)}{2M} \vec{\sigma} \cdot \vec{H} - \frac{e(1+2\kappa)}{8M^2} \vec{\sigma} \cdot [\vec{E} \times \vec{p} - \vec{p} \times \vec{E}], \quad (2.4)$$

where  $\kappa$  is the anomalous magnetic moment of the proton.

### 2.1.2 Non-Born Terms and Nucleon Polarizabilities

The fundamental properties of the nucleon such as charge, mass and anomalous magnetic moment are well known at low energies. The leading order properties that are sensitive to the internal quark dynamics of the nucleon are as-yet experimentally poorly understood. The internal dynamics and binding forces introduce more structure observables of a nucleon, because as soon as the internal excitation of the nucleon enters, many multipoles are induced that interact with an electromagnetic

field of frequency  $\nu$ . Each multipole oscillates with that same frequency and thus emits radiation with a characteristic angular distribution. The proportionality constant between each photon field and the corresponding induced multipole moment is called a polarizability. These are energy-dependent functions which parameterise the stiffness of the internal degree of freedom with particular quantum numbers against deformations of a given electric or magnetic multipolarity and energy. The polarizabilities are therefore called fundamental properties just as charge radius and magnetic moment which characterize the nucleon and can be understood as a response of an object that has sub structure to an applied electric or magnetic field.

### 2.1.2.1 Scalar Polarizabilities and Sum Rules

For increased energies that are still below the  $\pi$ -production threshold, the incident photons couple electromagnetically and undergo transitions of definite multiplicities and hence many multipoles are induced which describe the interaction between a nucleon field  $N$  with spin  $\frac{\sigma}{2}$  and two photons of fixed and non-zero energy. The non-Born terms of the Lagrangian is

$$\mathcal{L}_{nB} = 2\pi N^\dagger [H_{eff}^{(2)} + H_{eff}^{(3)} + H_{eff}^{(4)} + \dots] N. \quad (2.5)$$

The second order terms in the scattering amplitude of Eq. 2.5 introduce scalar or spin-independent polarizabilities as

$$H_{eff}^{(2)} = -4\pi \left[ \frac{1}{2} \alpha_{E1} \vec{E}^2 + \frac{1}{2} \beta_{M1} \vec{H}^2 \right], \quad (2.6)$$

where  $\alpha_{E1}$  and  $\beta_{M1}$  are the electric and magnetic scalar polarizabilities. These scalar dipole polarizabilities describe the response of internal structure of the nucleon to an applied  $\vec{E}$  and  $\vec{H}$ . They can be visualized by considering the nucleon as a composite

object that consists of a quark core surrounded by a virtual charged pion cloud. In presence of an electric field, induced current separates the positive pions from negative pions, stretching the nucleon along the direction of the electric field and hence it acquires an electric dipole moment. This induced electric dipole moment is proportional to the electric field, i.e.  $\vec{p}_e = 4\pi\alpha_{E1}\vec{E}$ , where  $\alpha_{E1}$  is often known as “electric stretchability” constant, because it is a measure of the pion charge cloud deformation within the electric field.

Similarly, in presence of a magnetic field, induced current in the pion cloud aligns the overall magnetic dipole moment along the direction of the magnetic field. This is because the quark core exhibits only a paramagnetic moment, whereas the pion charge cloud exhibits both a paramagnetic as well as a diamagnetic moment, but the paramagnetic moment dominates the diamagnetic moment and hence results in an overall dipole moment along the direction of the magnetic field. This magnetic dipole moment is proportional to the magnetic field, i.e.  $\vec{m} = 4\pi\beta_{M1}\vec{B}$ , where  $\beta_{M1}$  is also known as “magnetic align-ability” constant because it is a measure of the overall magnetic moment with the magnetic field.

These scalar dipole polarizabilities have been extracted via differential cross section results from low energy Compton scattering experiments. These experiments were performed at the MAInz MIcrotron (MAMI) tagged photon facility for incident photon energies of 55 – 165 MeV using the old TAPS setup, which covered the polar angular range of 59 – 155° [18]. In addition, there exist results from three previous experiments: Federspiel, *et al.*, for incident photon energy 32–72 MeV at 60 and 135° [19], MacGibbon, *et al.*, for incident photon energy 70 – 100 MeV at 90 and 135° [20] and Zieger, *et al.*, for incident photon energy 98–132 MeV at 180° [21] were combined to perform a global analysis [18]. Their global analysis also utilized a constraint given by the Baldin sum rule [22], which will be discussed in more detail in Sec. 2.1.2.2.

The Particle Data Group (PDG 2016) [13] values for these polarizabilities, including the global fit values by Olmos de Le'on, *et al.*, are

$$\alpha_{E1} = [11.2 \pm 0.3 (stat) \mp 0.4 (syst) \pm 0.3 (model)] \times 10^{-4} \text{ fm}^3, \quad (2.7)$$

$$\beta_{M1} = [2.5 \pm 0.4 (stat) \pm 0.4 (syst) \pm 0.4 (model)] \times 10^{-4} \text{ fm}^3. \quad (2.8)$$

### 2.1.2.2 Baldin Sum Rule

The Baldin sum rule, derived by A.M. Baldin in 1960 [22], establishes a relation between the low-energy nucleon structure quantities, the electric and magnetic scalar polarizabilities, and the nucleon excitation spectrum, such that these polarizabilities can be extracted from the measurement of the cross sections of real Compton scattering. This sum rule [23] is derived via the Kramers-Kronig relation [24] from the low-energy theorems and expansion of the forward-scattering amplitude in the photon energy as

$$\alpha_{E1} + \beta_{M1} = \frac{1}{2\pi^2} \int_{\omega_{th}}^{\infty} \frac{\sigma_{tot}(\omega)}{\omega^2} d\omega, \quad (2.9)$$

where  $\sigma_{tot}(\omega)$  is the total photo absorption cross section and  $\omega_{th}$  is the threshold energy required to produce a lightest meson (pion in this case).

### 2.1.2.3 Gerasimov-Drell-Hearn $\gamma_0$ Sum Rule

The Gerasimov-Drell-Hearn (GDH) sum rule [23, 25] relates the static properties of a nucleon, like anomalous magnetic moment  $\kappa$  and mass  $M$ , to its dynamic observable, like the total absorption cross sections of circularly polarized real photons on longitudinally polarized nucleons in the two relative spin configurations, parallel (3/2) and

antiparallel (1/2) as,

$$\frac{\alpha_e \kappa^2}{2M^2} = \frac{1}{4\pi^2} \int_{\omega_{th}}^{\infty} \frac{\sigma_{3/2}(\omega) - \sigma_{1/2}(\omega)}{\omega} d\omega, \quad (2.10)$$

where  $\alpha_e = 1/137.04$  is the fine structure constant,  $\sigma_{3/2}$  is the total photo-absorption cross section when the helicity of the beam and the polarization of the target are parallel and  $\sigma_{1/2}$  is when the helicity of the beam and the polarization of the target are antiparallel. In a similar way, the sum rule relates the forward spin polarizability,  $\gamma_0$ , to the total photoabsorption cross section as

$$\gamma_0 = -\frac{1}{4\pi^2} \int_{\omega_{th}}^{\infty} \frac{\sigma_{3/2}(\omega) - \sigma_{1/2}(\omega)}{\omega^3} d\omega. \quad (2.11)$$

#### 2.1.2.4 Spin Polarizabilities

The expansion of the effective Hamiltonian to the third order of photon energy can be explained based on the fact that it must respect basic symmetries of charge conjugation (C), parity (P) and time reversal (T) as shown in Table 2.1.

Quantity	C	P	T
$\vec{E}$	-	-	+
$\vec{H}$	-	+	-
$\vec{\sigma}$	+	+	-
$\partial_i$	+	-	+
$\partial_t$	+	+	-

Table 2.1: Behavior of electric field, magnetic field, nucleon spin, spatial derivative and time derivative under charge conjugation, C, parity, P, and time reversal, T [26].

To construct the third order Hamiltonian without breaking C, P and T, only four scalars  $\vec{\sigma} \cdot (\vec{E} \times \dot{\vec{E}})$ ,  $\vec{\sigma} \cdot (\vec{H} \times \dot{\vec{H}})$ ,  $E_{ij}\sigma_i H_j$  and  $H_{ij}\sigma_i E_j$  can be used. The terms  $\dot{\vec{E}}$ ,  $\dot{\vec{H}}$ ,  $E_{ij}$  and  $H_{ij}$  are the partial derivatives with respect to time and space defined as  $\dot{\vec{E}} = \partial_t \vec{E}$ ,  $\dot{\vec{H}} = \partial_t \vec{H}$ ,  $E_{ij} = \frac{1}{2}(\partial_i E_j + \partial_j E_i)$  and  $H_{ij} = \frac{1}{2}(\partial_i H_j + \partial_j H_i)$ , respectively.

These terms are straightforward extensions to the effective Lagrangian of zero-energy scattering, where the photons couple electrically or magnetically ( $X, Y = E, M$ ) and undergo transitions  $Xl \rightarrow Yl'$  of definite multiplicities  $l$  and  $l' = l \pm 1, 0$ . The interactions are unique up to field redefinitions using the equations of motion. Dipole couplings are proportional to the electric and magnetic field directly, or to their time derivatives. Quadrupole interactions couple to the irreducible second-rank tensors  $E_{ij}$  and  $H_{ij}$  [27]. Thus, with these scalars, the third order term in the scattering amplitude of Eq. 2.5 can be parametrized as the following equation,

$$H_{eff}^{(3)} = -4\pi \left[ \frac{1}{2} \gamma_{E1E1} \vec{\sigma} \cdot (\vec{E} \times \dot{\vec{E}}) + \frac{1}{2} \gamma_{M1M1} \vec{\sigma} \cdot (\vec{H} \times \dot{\vec{H}}) - \gamma_{M1E2} E_{ij} \sigma_i H_j + \gamma_{E1M2} H_{ij} \sigma_i E_j \right], \quad (2.12)$$

where  $\gamma_{E1E1}$ ,  $\gamma_{M1M1}$ ,  $\gamma_{M1E2}$  and  $\gamma_{E1M2}$  are the four spin polarizabilities of the proton.

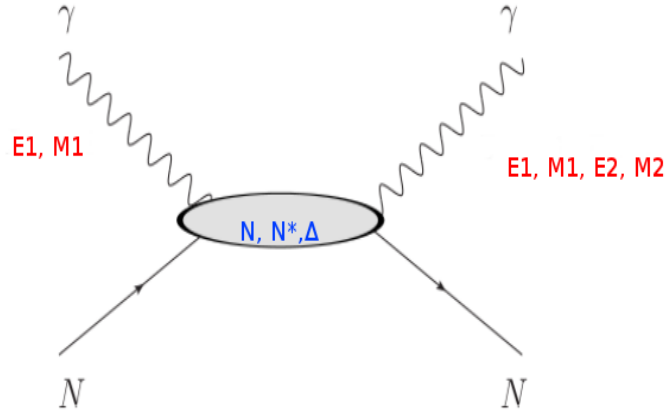


Figure 2.1: Nuclear Compton Scattering below  $\pi$ -production threshold, where  $El$  and  $Ml$  refer to the multiplicities of the incident and scattered photon, and  $N$ ,  $N^*$  and  $\Delta$  refer to the intermediate or excited state of the nucleon.

These four leading-order spin polarizabilities are low-energy manifestations of the

spin structure of the nucleon, which parameterize the response of the nucleon spin to an applied electric or magnetic field. The physics behind these spin polarizabilities involve the excitation of the spin- $\frac{1}{2}$  nucleon target to some intermediate state ( $\Delta$  or  $N^*$ ) via an electric or magnetic ( $E1$  or  $M1$ ) dipole transition and a successive de-excitation back into a spin- $\frac{1}{2}$  nucleon final state via an electric or magnetic dipole ( $E1$  or  $M1$ ) or quadrupole ( $E2$  or  $M2$ ) transition as in Fig. 2.1. Thus, the nomenclature of these four terms is related to the multipole fields associated with the electromagnetic radiation. For example,  $\gamma_{E1M2}$  represents the spin polarizability of a proton when it is excited to one of its possible intermediate states,  $\frac{3}{2}$  state (the excitation of a  $\Delta$ ) by absorbing dipole radiation  $E1$  and de-excited back to the  $\frac{1}{2}$  state by emitting quadrupole radiation  $M2$ . The two spin polarizabilities  $\gamma_{E1E1}$  and  $\gamma_{M1M1}$  correspond to dipole-dipole transitions, analogous to the classical Faraday effect related to birefringence inside the nucleon [28]. They describe how an incoming photon causes a dipole deformation in the nucleon spin, which in turn leads to dipole radiation. The two mixed-spin polarizabilities,  $\gamma_{E1M2}$  and  $\gamma_{M1E2}$ , represent scattering, where the angular momenta of the incident and outgoing photons differ by one unit [28].

### 2.1.2.5 Forward spin polarizability

Although the two scalar polarizabilities have been measured for the proton, very few experiments have attempted to extract these Spin Polarizabilities (SPs). Several experiments have provided constraints on linear combinations of SPs. One of the combinations that has been measured so far is the forward spin polarizability,  $\gamma_0$ , which comes from a set of two experiments of the GDH Collaboration [29] and is defined as

$$\gamma_0 = -\gamma_{E1E1} - \gamma_{E1M2} - \gamma_{M1M1} - \gamma_{M1E2}. \quad (2.13)$$

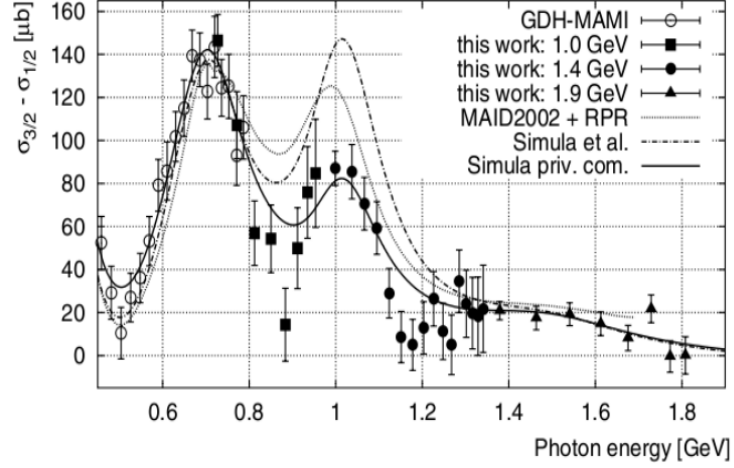


Figure 2.2: The GDH experiments: Measurement of the GDH sum rule and the forward spin polarizability making use of the difference between parallel and anti-parallel photo-absorption cross sections for circularly polarized photons scattering from a longitudinally polarized target [29].

The forward spin polarizability sum rule was evaluated from data taken at the tagged photon facilities at MAMI and the electron stretcher ring ELSA. A frozen spin target, similar to the one used in this dissertation’s experiment, provided the polarized nucleon. The MAMI data set [30] covered a range of incident photon energies,  $\omega$ , from 200 MeV to 800 MeV while the ELSA data set [31] covered energies from 700 MeV to 1800 MeV. DAPHNE at MAMI and the ‘GDH-Detector’ at ELSA [31] along with the forward detectors were used with nearly  $4\pi$  steradian (sr) coverage. The combined results of the photoabsorption cross sections difference are shown in Fig. 2.2 [29]. The GDH Collaboration determined the forward spin polarizability  $\gamma_0$  to be,

$$\gamma_0 = (-1.00 \pm 0.08_{stat} \mp 0.10_{sys}) \times 10^{-4} \text{ fm}^4. \quad (2.14)$$

### 2.1.2.6 Backward spin polarizability

The second linear combination that has been measured so far is the backward spin polarizability,  $\gamma_\pi$ , which comes from a back-angle Compton scattering experiment at MAMI and is defined as

$$\gamma_\pi = -\gamma_{E1E1} - \gamma_{E1M2} + \gamma_{M1M1} + \gamma_{M1E2}. \quad (2.15)$$

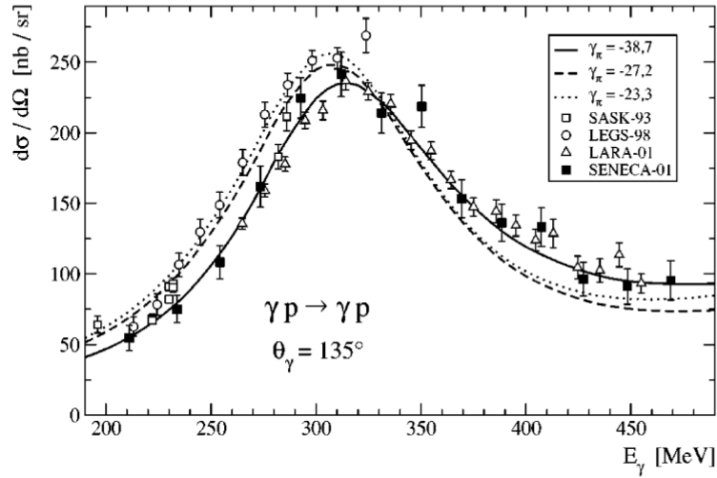


Figure 2.3: Experimental differential cross sections for Compton scattering measured using the LARge Acceptance arrangement (LARA) and segmented recoil counter SENECA at MAMI compared with data from experiments at Saskatoon and LEGS. Backward spin polarizability  $-38.7$ ,  $-27.2$  and  $-23.3$  in standard spin polarizability units of  $10^{-4} \text{ fm}^4$  determined using a dispersive fitting to back-angle Compton scattering data [32].

The back-angle Compton scattering experiment at MAMI [32] used a single large NaI detector at  $136^\circ$ , along with the forward wall Göttingen SENECA detector [30]. These data sets covered a range of incident photon energies,  $\omega$ , from 200 MeV to 470 MeV. The differential cross sections at scattering angle of  $\theta_\gamma^{c.m.} = 135^\circ$  were measured. A dispersion relation analysis was applied to the MAMI data set, along with the other data sets from Saskatoon [33], LEGS [34, 35] and LARA [36, 37]. The

LEGS data set disagrees with all other previous measurements (see Fig. 2.3). Due to this disagreement,  $\gamma_\pi$  was determined only fitting to MAMI, LARA and Saskatoon data sets as

$$\gamma_\pi = (-38.7 \pm 1.8) \times 10^{-4} \text{ fm}^4. \quad (2.16)$$

The large backward spin polarizability is dominated by a  $\pi^0$  pole term, the  $t$ -channel emission of a virtual  $\pi^0$  (Sec. 2.1.3.1). This contribution of large  $\pi^0$  pole term was evaluated by Schumacher [38] and found to be  $\gamma_\pi^{\pi^0\text{-pole}} = -46.7 \times 10^{-4} \text{ fm}^4$ . This term was subtracted from backward spin polarizability to find only the dispersive contribution (Sec. 2.2.1),

$$\gamma_\pi^{disp} = (8.0 \pm 1.8) \times 10^{-4} \text{ fm}^4. \quad (2.17)$$

### 2.1.3 Theoretical Model Predictions

Compton scattering on the proton at low and intermediate energies has thus far been studied mainly with unpolarized photons to produce unpolarized differential cross sections both in the region below pion threshold and in the  $\Delta(1232)$  region. With the advent of new experimental tools such as highly polarized photon beams and polarized targets, the experimental studies of the internal structure parameters of the nucleon have been improved significantly in the last few years.

Although in principle the individual SPs can be determined from analysis of experimental data, in practice this is not feasible. It is therefore required to make an experimental determination by indirect means, i.e., one can use theoretical models (e.g., the subtracted fixed- $t$  dispersion relation model, which will be discussed in detail in Sec. 2.2.1) to provide a complete low-energy analysis of the Compton amplitude and then to extract the SPs. There are various theoretical models for studying the nucleon polarizabilities. However, one of the key reasons that attract the attention

of experimental physicists is that none of the models agree on the results. Instead they predict a wide range of SP values. Due to this disagreement, an extraction of the SP from data would provide a useful tool in helping to validate (or invalidate) one, or some, of these models and would also provide a common ground for people working in theory and experiments. In this section, some of the theoretical models and underlying physics behind them for studying SPs will be discussed.

### 2.1.3.1 Mandelstam Plane and Invariant Amplitudes

In a Real Compton Scattering (RCS), the incident real photon interacts electromagnetically with a proton and scatters at some angle. The scattered photon emerges in general through a two-step mechanism involving the whole internal dynamics of the target nucleus through virtual excitations in the intermediate state. The conservation of momentum and energy in nucleon Compton scattering

$$\gamma(k, \lambda) + N(p) \rightarrow \gamma(k', \lambda') + N(p'), \quad (2.18)$$

is given by

$$k + p \rightarrow k' + p', \quad (2.19)$$

$$kc + m_p c^2 \rightarrow k'c + E_{p'}, \quad (2.20)$$

where  $k$  and  $k'$  are the four-momenta and  $\lambda$  and  $\lambda'$  are the helicities of the incoming and outgoing photons,  $p$  and  $p'$  are the four-momenta of initial and final state protons and  $E_{p'}$  is the total energy of the recoil proton respectively. We can solve Equations 2.19 and 2.20 to obtain the energy of the recoil proton as,

$$E_{p'} = \frac{k^2 c (1 - \cos \theta)}{m_p c + k(1 - \cos \theta)} + m_p c^2. \quad (2.21)$$

We can define a set of Lorentz invariant Mandelstam variables [39] in centre of mass frame as,

$$s = (k + p)^2 = (k' + p')^2, \quad (2.22)$$

$$t = (k - k')^2 = (p' - p)^2, \quad (2.23)$$

$$u = (k - p')^2 = (k' - p)^2. \quad (2.24)$$

It is also possible to define the nucleon mass  $M$  and scattering angle  $\theta$  in terms of these Mandelstam variables as,

$$s + u + t = 2M^2, \quad (2.25)$$

$$\sin^2 \frac{\theta}{2} = -st(s - M^2)^{-2}. \quad (2.26)$$

The typical electromagnetic interactions contributing to RCS are shown in Fig. 2.4. Figs. 2.4a and 2.4b represent the  $s$ - and  $u$ -channel Compton scattering process where the nucleon is taken as a structureless Dirac particle representing the Born contribution only from the nucleon pole term. Typical resonance excitation in the  $s$ -channel and its crossed version are shown in Fig. 2.4c and Fig. 2.4d, and typical mesonic contributions with photon scattering off an intermediate pion, the pion pole diagram and a correlated two pion exchange such as the “ $\sigma$  meson” are shown in Figs. 2.4e-2.4g respectively. Except for the diagrams 2.4a, 2.4b, and 2.4f, all other and higher diagrams in Fig. 2.4 have no pole structure, but correspond to excited states in  $s$ -,  $u$ - or  $t$ -channel processes.

The amplitude  $T_{fi}$  for the Compton scattering process is related to the  $S$ -matrix of the reaction as,  $\langle f|S - 1|i\rangle = i(2\pi)^4 \delta^4(k + p - k' - p')T_{fi}$ , and it can be expressed

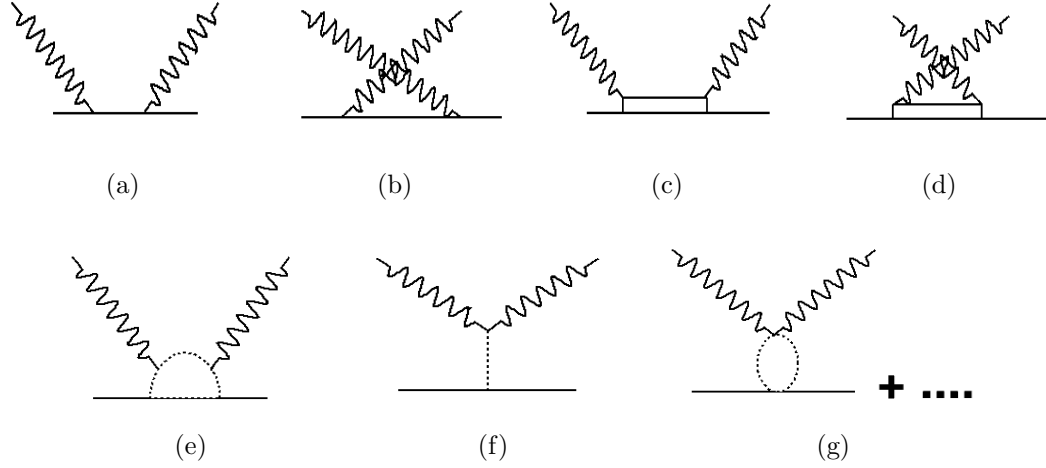


Figure 2.4: Some typical intermediate states contributing to Compton scattering off the nucleon.

in terms of six invariant amplitudes  $T_i$ ,  $i = 1, \dots, 6$  as [39, 40]

$$\begin{aligned}
 T_{fi} = \bar{u}'(p')e'^{*}\mu \left\{ -\frac{P'_\mu P'_\nu}{P'^2}(T_1 + (\gamma \cdot K)T_2) - \frac{N_\mu N_\nu}{N^2}(T_3 + (\gamma \cdot K)T_4) \right. \\
 \left. + i\frac{P'_\mu N_\nu - P'_\nu N_\mu}{P'^2 K^2}\gamma_5 T_5 + i\frac{P'_\mu N_\nu + P'_\nu N_\mu}{P'^2 K^2}\gamma_5(\gamma \cdot K)T_6 \right\} e^\nu u(p),
 \end{aligned} \quad (2.27)$$

where  $P'$ ,  $K$ ,  $Q$  and  $N$  are orthogonal four-vectors defined as  $P'_\mu = P_\mu - K_\mu \frac{P \cdot K}{K^2}$  with  $P = \frac{1}{2}(p + p')$ ,  $K = \frac{1}{2}(k + k')$ ,  $Q = \frac{1}{2}(p - p') = \frac{1}{2}(k' - k)$  and  $N_\mu = \epsilon_{\mu\alpha\beta\gamma} P'^\alpha Q^\beta K^\gamma$  with antisymmetric tensor  $\epsilon_{\mu\alpha\beta\gamma}$  fixed by the condition  $\epsilon_{0123} = 1$ . Also,  $u$  and  $u'$  are the bispinors of the nucleons defined as  $u\bar{u} = 2M$  with  $M$  as a nucleon mass,  $e$  and  $e'$  are the photon polarization vectors, and  $\gamma_5 = -i\gamma_0\gamma_1\gamma_2\gamma_3 = \begin{pmatrix} 0 & 1 \\ 1 & 0 \end{pmatrix}$  is the product of Dirac matrices, respectively.

These six invariant amplitudes,  $T_i$ , are functions of the two variables  $\nu = \frac{(s-u)}{4M}$  and  $t$ . However, these functions  $T_i(\nu, t)$  have no kinematical singularities, they are subject to kinematical constraints that arise from the fact that these terms  $P'^2$ ,  $N^2$  and  $P'^2 K^2$  in the denominator of the (Eq. 2.27) vanish at certain values of  $\nu$  and  $t$ . We can introduce linear combinations of the amplitudes  $T_i(\nu, t)$  to remove the

kinematic constraint. Therefore, we define the amplitudes  $A_i(\nu, t)$ ,  $i = 1, \dots, 6$  as linear combinations of  $T_i$  as [41]

$$\begin{aligned}
 A_1 &= \frac{1}{t} [T_1 + T_3 + \nu(T_2 + T_4)], & A_2 &= \frac{1}{t} [2T_5 + \nu(T_2 + T_4)], \\
 A_3 &= \frac{1}{\eta} \left[ T_1 - T_3 - \frac{t}{4\nu}(T_2 - T_4) \right], & A_4 &= \frac{1}{\eta} \left[ 2MT_6 - \frac{t}{4\nu}(T_2 - T_4) \right], \\
 A_5 &= \frac{1}{4\nu} [T_2 + T_4], & A_6 &= \frac{1}{4\nu} [T_2 - T_4],
 \end{aligned} \tag{2.28}$$

with

$$\eta = \frac{M^4 - su}{M^2} = 4\nu^2 + t - \frac{t}{4M^2}. \tag{2.29}$$

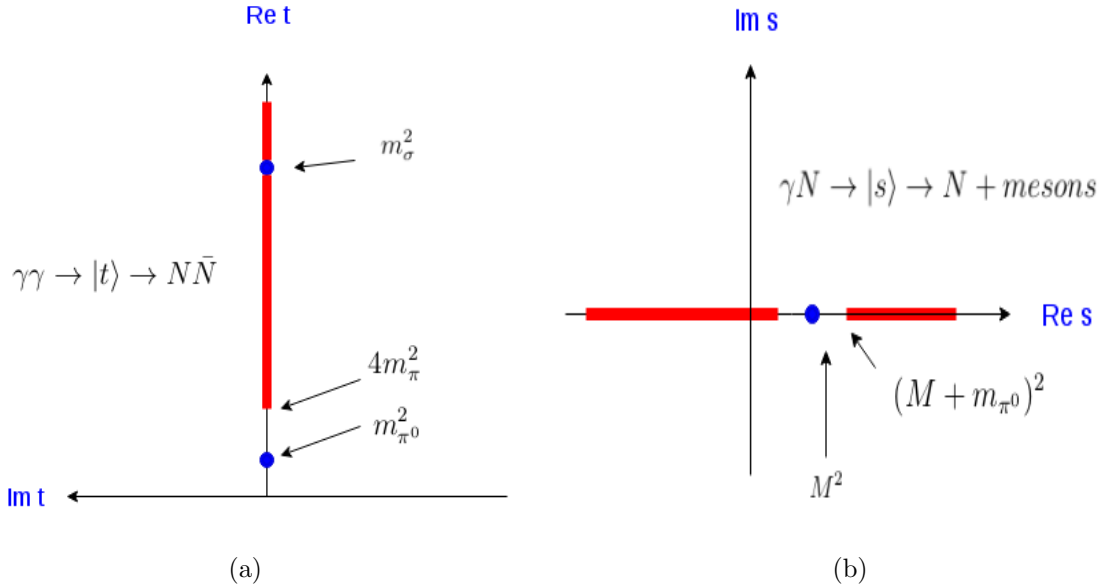


Figure 2.5: Singularities in the  $s$  and  $t$  planes. (a) shows the  $t$ -channel which includes a pole at  $t = m_{\pi^0}^2$  and a cut starting at  $t_{thr} = 4m_{\pi^0}^2$ . At  $t = m_\sigma^2$ , there is also a pole-like phase substructure defining a “mass”. (b) shows the  $s$ -plane which represents the nucleon pole at  $s = M^2$  and a right hand cut corresponding to the  $s$ -channel and a left-hand cut corresponding to the  $u$ -channel [38].

The amplitudes,  $A_i(\nu, t)$ , are even functions of  $\nu$  and have no kinematic singularities or kinematic constraints. But there are physical singularities which are the basis for constructing the amplitudes. Fig. 2.5a shows the main singularities in the Compton  $t$ -plane, which are poles on the positive real  $t$ -axis corresponding to the pseudoscalar mesons  $\pi^0$ ,  $\eta$  and  $\eta'$ , and a cut starting  $t = 4m_\pi^2$ . This cut consists of a  $\pi\pi$  channel with a  $\pi\pi$  phase substructure that may be interpreted in terms of the  $\sigma$  particle. The  $t$ -channel singularities of interest in connection with Compton scattering are positioned at  $t = m_{\pi^0}^2$  and at  $4M^2 \geq t \geq 4m_\pi^2$ , i.e. outside the physical region of the  $t$ -channel for the reaction  $\gamma\gamma \rightarrow NN$ . For the  $t$ -channel, this means that the two photon fusion process  $\gamma\gamma \rightarrow \pi\pi$  leading to the  $|\pi\pi\rangle$  intermediate state or some other resonant or nonresonant intermediate state  $|t\rangle$  takes place as a real (on-shell) process whereas the subsequent process  $\pi\pi \rightarrow N\bar{N}$  takes place virtually, i.e. below threshold for  $N\bar{N}$  pair production. This corresponds to low-energy Compton scattering processes proceeding through  $|\pi^0\rangle$ ,  $|\pi\pi\rangle$ , etc.,  $t$ -channel exchanges in the intermediate state with no excitation of the constituent-quark meson structure of the nucleon.

Whereas in the  $s$ -plane, as shown in Fig. 2.5b, the main singularities are on the real axis, a pole at  $s = u = M^2$  and two cuts, representing the  $s$ - and  $t$ -channels. The pole at  $s = u = M^2$  represents the Born term, i.e. Thomson scattering without excitation of internal degrees of freedom of the nucleon. The boundary of the  $s$ -channel physical region is defined through the threshold  $s_0 = (M + m_\pi)^2$  for the photo-absorption process.

The complex  $s$ - and  $t$ -planes can be merged into one plane called the Mandelstam plane by replacing  $s$  by  $\nu$  as in Fig. 2.6. The horizontally hatched region of the Mandelstam plane in Fig. 2.6 represents the  $s$ ,  $t$  and  $u$  channel physical region where Compton scattering is possible. In the Mandelstam plane, the physical regions are

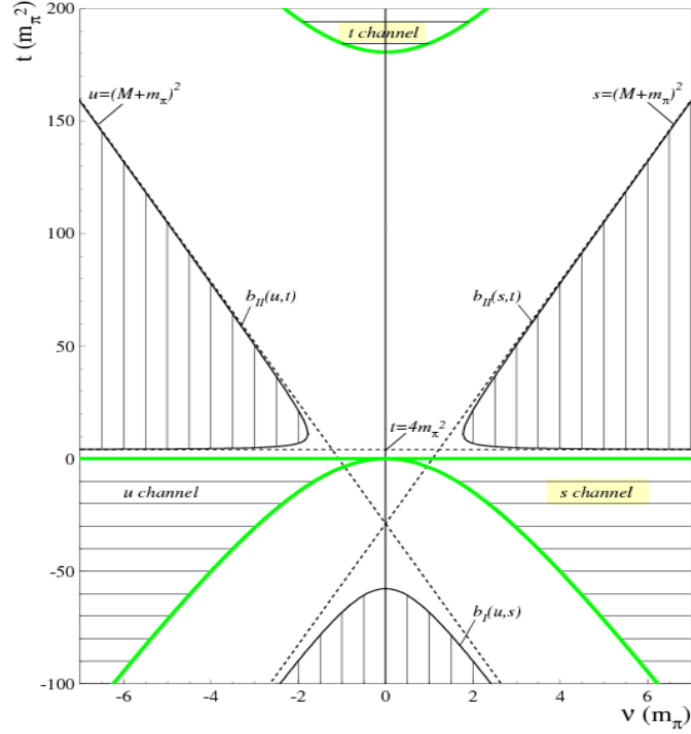


Figure 2.6: The Mandelstam plane for Compton scattering [38]. The physical regions are horizontally hatched and the spectral regions are vertically hatched.

given by the interval between  $\theta = 0$  and  $\theta = \pi$  of the physical scattering angle. The boundary  $\theta = 0$  is equivalent with  $t = 0$ . The vertically hatched area of Mandelstam plane represents the nonvanishing double spectral functions, where two of the three variables  $s$ ,  $t$  and  $u$  take on the values that correspond with a physical intermediate state.

### 2.1.3.2 Low Energy Expansion

The Compton scattering amplitudes,  $A_i(\nu, t)$ , can be expanded to different orders in  $w$  to better understand the scattering dependencies. The expansion up to the order  $w^2$  is called the Low Energy eXpansion (LEX). This expansion includes both the Born and non-Born contributions to the scattering process. The Born term describes the Compton scattering process off a point-like particle, i.e. typical Thomson scattering

without excitation of the internal degrees of freedom of the nucleon and the non-Born term including fundamental structure observables like electric and magnetic scalar polarizabilities. At photon energies above 20 MeV but still far below the  $\pi$ -production threshold, the differential cross section is given by the LEX [42, 43] in terms of electric and magnetic structure observables as,

$$\left(\frac{d\sigma}{d\omega}\right) = \left(\frac{d\sigma}{d\omega}\right)_B - \omega\omega' \left(\frac{\omega'}{\omega}\right)^2 \frac{e^2}{M} \left[ \frac{\alpha + \beta}{2}(1+z)^2 + \frac{\alpha - \beta}{2}(1-z)^2 \right] + \mathcal{O}(\omega^4), \quad (2.30)$$

where  $\left(\frac{d\sigma}{d\omega}\right)_B$  is the Born contribution of differential cross section,  $z = \cos\theta$  is the photon scattering angle and  $\omega'$  is the energy of the scattered photon, given by,

$$\omega' = \omega + \frac{t}{2M} = \omega \left[ 1 + \frac{\omega}{M}(1-z) \right]^{-1}. \quad (2.31)$$

### 2.1.3.3 HDPV: Fixed- $t$ Dispersion Relation Approach

The spin polarizabilities of the proton are extracted (Sec. 7.1) using the once-subtracted fixed- $t$  dispersion relation approach of Holstein, Drechsel, Pasquini and Vanderhaeghen (HDPV). This is important because as  $\omega$  increases ( $\omega^2$  and above), degrees of freedom related to the internal structure and spin of the nucleus will enter the scattering amplitudes and hence the LEX cannot be applied. DRs, which are partially constrained by experimental data, can provide a more powerful approach to study the Compton scattering amplitudes in these higher energy regions (e.g.  $\Delta$ -resonance region). Within the framework of DRs, it is possible to fix either  $\theta$  or Mandelstam variable  $t$ . The DRs at fixed value of  $\theta$  are called fixed-angle DRs, which cannot be applied at all angles with equally good precision but are best applied at backward angles. Due to this reason, DRs are extended to include larger angles at a fixed value of Mandelstam variable  $t$  and are known as fixed- $t$  DRs. The singularities in

the two planes (discussed in Sec. 2.1.3.1) are taken into account by imaginary parts of the amplitudes  $Im_s A_i(\nu', t)$  for the  $s$ -plane, and  $Im_t A_i(\nu', t)$  for the  $t$ -plane. The fixed- $t$  DRs relate the real parts of the scattering amplitudes to their imaginary parts through dispersion relations at a fixed value of Mandelstam variable  $t$  as [44, 45]

$$Re A_i(\nu, t) = A_i^B(\nu, t) + \frac{2}{\pi} \mathcal{P} \int_{\nu_{thr}}^{\infty} \frac{Im_s A_i(\nu', t)}{\nu'^2 - \nu^2} d\nu', \quad (2.32)$$

where  $\mathcal{P}$  denotes the Cauchy principal value,  $Im_s A_i$  are discontinuities across the  $s$ -channel cuts of the Compton scattering process evaluated using empirical photo-production data and  $\nu_{thr} = m_\pi + \frac{2m_\pi^2 + t}{4M}$  is the pion photoproduction threshold. Due to the asymptotic behaviour of  $A_i$  as  $\nu$  goes to  $\infty$ , the integral term of the dispersion relation in Eq. 2.32 does not converge for scattering amplitudes  $A_1$  and  $A_2$ . To ensure that all terms converge, dispersion relations are calculated at fixed- $t$ , subtracting the case at  $\nu=0$ . In this case, the subtracted dispersion relations are given by [45],

$$Re A_i(\nu, t) = A_i^B(\nu, t) + [A_i(0, t) - A_i^B(0, t)] + \frac{2}{\pi} \nu^2 \mathcal{P} \int_{\nu_{thr}}^{\infty} \frac{Im_s A_i(\nu', t)}{\nu'(\nu'^2 - \nu^2)} d\nu'. \quad (2.33)$$

In addition to the subtraction constant at  $\nu=0$ , we can also set  $t=0$  and define a set of low energy constants as

$$a_i = A_i(0, 0) - A_i^B(0, 0). \quad (2.34)$$

These low energy constants are directly related to the scalar and spin polarizabilities by

$$\begin{aligned}
\alpha_{E1} &= -\frac{1}{4\pi}(a_1 + a_3 + a_6), & \beta_{M1} &= \frac{1}{4\pi}(a_1 - a_3 - a_6), \\
\gamma_{E1E1} &= \frac{1}{8\pi M}(a_2 - a_4 + 2a_5 + a_6), & \gamma_{E1M2} &= \frac{1}{8\pi M}(a_2 - a_4 - a_6), \\
\gamma_{M1M1} &= -\frac{1}{8\pi M}(a_2 + a_4 + 2a_5 - a_6), & \gamma_{M1E2} &= -\frac{1}{8\pi M}(a_2 + a_4 + a_6), \\
\gamma_0 &= \frac{1}{2\pi M}a_4, & \gamma_\pi &= -\frac{1}{2\pi M}(a_2 + a_5).
\end{aligned} \tag{2.35}$$

Similarly the sum of scalar dipole polarizabilities is given by,

$$\alpha_{E1} + \beta_{M1} = -\frac{1}{2\pi}(a_3 + a_6), \quad \alpha_{E1} - \beta_{M1} = -\frac{1}{2\pi}a_1. \tag{2.36}$$

#### 2.1.3.4 B $\chi$ PT: Baryon Chiral Perturbation Theory Approach

In addition to HDPV, a Baryon Chiral Perturbation Theory (B $\chi$ PT) approach of Lensky and Pascalutsa [46] that involves a systematic low-energy expansion around the chiral limit is also used in this work to extract the spin polarizabilities. This approach is based on the nucleon Compton scattering in the framework of B $\chi$ PT with pion, nucleon and  $\Delta(1232)$  degrees of freedom, up to and including the Next-to-Next-to-Leading Order (NNLO).

The chiral expansion for the Compton amplitude begins at the order of  $\mathcal{O}(p^2)$ , representing the Born contribution only from the nucleon pole term as in Figs. 2.4a and its crossed counterpart in Figs. 2.4b. Therefore,  $\mathcal{O}(p^2)$  is known as leading order (LO). Because the baryons are much heavier than the pions, low energy structure constants do not enter until the next order in the B $\chi$ PT Lagrangian. The Next-to-Leading Order (NLO) that appear only in the order of  $\mathcal{O}(p^3)$  is shown in Fig. 2.4c and Fig. 2.4f. In addition, at order of  $\mathcal{O}(p^3)$ , there are contributions from a number of loop graphs (Fig. 2.4e and Fig. 2.4g). The physics behind these NLO loop diagram

is that the photon couples only minimally, i.e., to the electric charge of the pion and nucleon. This means there will be no isovector term,  $\gamma\pi NN$ , when the pion couples to the nucleon via pseudoscalar coupling, therefore the number of one-loop graphs can be reduced. This way the resulting expressions for amplitudes become simpler.

Furthermore, in the NNLO, the photons couple minimally to  $\Delta$ -isobar propagator, therefore other diagrams containing more than one  $\Delta$  should be suppressed by extra powers of  $p/\Delta$ . At energies below the pion-production threshold, the NLO effects are very small at backward angles but are significant at forward angles. However, in the NNLO  $\Delta$ -isobar contributions, the situation is quite the opposite. The NNLO calculations are needed to describe the nucleon spin polarizabilities because they appear only in the third order in the Compton scattering Hamiltonian. The  $B\chi$ PT model is one of the  $\chi$ PT models expected to be sufficiently reliable for the nucleon spin polarizability studies. The details of this model are beyond the scope of this thesis and hence the reader is referred to [46, 47] for further detail.

## 2.2 Compton asymmetries for polarized beam and target

The photon polarization properties can be described in terms of the Stokes parameters  $\xi_i$  ( $i = 1, 2, 3$ ). We consider a reference frame with the  $z$ -axis along the direction of the incoming photon ( $\hat{q}$ ), the  $x$ -axis in the scattering plane and in the half plane of the outgoing photon, and the  $y$ -axis perpendicular to the scattering plane along the direction ( $\hat{q} \times \hat{q}'$ ). The Stokes parameter  $\xi_i$  in terms of photon-polarization density matrix is defined as [17],

$$\langle e_\alpha e_\beta^* \rangle = \frac{1}{2}(1 + \vec{\sigma} \cdot \vec{\xi})_{\alpha\beta} = \frac{1}{2} \begin{pmatrix} 1 + \xi_3 & \xi_1 - i\xi_2 \\ \xi_1 + i\xi_2 & 1 - \xi_3 \end{pmatrix}, \quad (2.37)$$

where  $e_\mu$  is the photon polarization vector chosen in the radiation gauge,  $\vec{e} \cdot \vec{q} = 0$ , and  $\alpha, \beta = 1, 2$  denote either of the two orthogonal directions  $x$  and  $y$ . The total degree of photon polarization is given by  $\xi = \sqrt{\xi_1^2 + \xi_2^2 + \xi_3^2} \leq 1$ . While this definition of  $\xi_i$  is frame dependent, we can define Lorentz invariant quantities  $\xi_2$  and  $\xi_l = \sqrt{\xi_1^2 + \xi_3^2}$  which describe the degree of circular and linear polarization of a photon. Furthermore,  $\xi_2 = \pm 1$  corresponds to the right and left helicity states. In the case of linear polarization, the azimuthal angle  $\phi$  between the electric field and the scattering plane is defined by  $\cos 2\phi = \xi_3/\xi_l$  and  $\sin 2\phi = \xi_1/\xi_l$ . Thus,  $\xi_3 = \pm 1$  corresponds to linearly polarized photons polarized parallel ( $\phi = 0$ ) and perpendicular ( $\phi = \frac{\pi}{2}$ ) to the scattering plane, and  $\xi_1 = \pm 1$  corresponds to linearly polarized photons polarized with an angle  $\phi = \pm \frac{\pi}{4}$ , respectively.

The spin polarizabilities of the proton can be extracted by measuring various single and double polarization observables using both polarized beam and target. These polarization observables are known as asymmetries and quantify the change in the cross section due to specific polarization orientation. These observables are traditionally represented by  $\sum$  and defined as follows;

- $\sum_j$  with subscripts  $j = (x, y, z)$ , indicate the single polarization asymmetry where the photon beam is unpolarized but the nucleon is polarized. For example,  $\sum_y$  is a single polarization asymmetry where a photon beam is unpolarized and the nucleon is polarized along the  $\pm y$  axis.
- $\sum_i$  with subscripts  $i = (1, 2, 3)$ , indicates the single polarization asymmetry where the photon beam is polarized but the nucleon is unpolarized. For example,  $\sum_3$  is a single polarization asymmetry where a photon beam is polarized

in a direction given by Stokes parameter  $\xi_3 = \pm 1$ , meaning that the photons are linearly polarized in a direction parallel ( $\phi = 0$ ) or perpendicular ( $\phi = \frac{\pi}{2}$ ) to the scattering plane and the nucleon is unpolarized.

- $\sum_{ij}$  with subscripts  $i = (1, 2, 3)$  and  $j = (x, y, z)$ , indicate the double polarization asymmetry where both the photon beam and the nucleon is polarized. For example,  $\sum_{2z}$  is a double polarization asymmetry where a photon beam is polarized in a direction given by Stokes parameter  $\xi_2 = \pm 1$ , meaning that the photons are circularly polarized with left and right helicity states and the nucleon is polarized along the  $\pm z$  axis.

### 2.2.1 Beam Target Asymmetry - $\sum_{2z}$

In a series of Compton scattering experiments approved at MAMI [48],  $\sum_{2z}$  experiment is one of the experiment to measure double polarization observable and extract all four spin polarizabilities by performing a global analysis. The beam-target asymmetry  $\sum_{2z}$  is a double polarization asymmetry which is measured using a circularly polarized photon beam (direction given by Stokes parameter  $\xi_2 = \pm 1$ ) on a longitudinally polarized target (polarization along the  $\pm z$  axis).

The helicity of the beam is flipped once per second so it is straightforward to show beam-target asymmetry in terms of the polarized cross sections as

$$\sum_{2z} = \frac{\sigma_{+z}^R - \sigma_{+z}^L}{\sigma_{+z}^R + \sigma_{+z}^L} = \frac{\sigma_{-z}^R - \sigma_{-z}^L}{\sigma_{-z}^R + \sigma_{-z}^L}, \quad (2.38)$$

where  $\sigma_{\pm z}^R$  and  $\sigma_{\pm z}^L$  represent the cross sections for a positive and negative longitudinally polarized target with a right and left helicity state of the beam, respectively. These four Compton scattering cross sections can be visualized from four possible configurations as in Fig. 2.7. Due to parity, as can be seen from Fig. 2.7 that  $\sigma_{+z}^R = \sigma_{-z}^L$

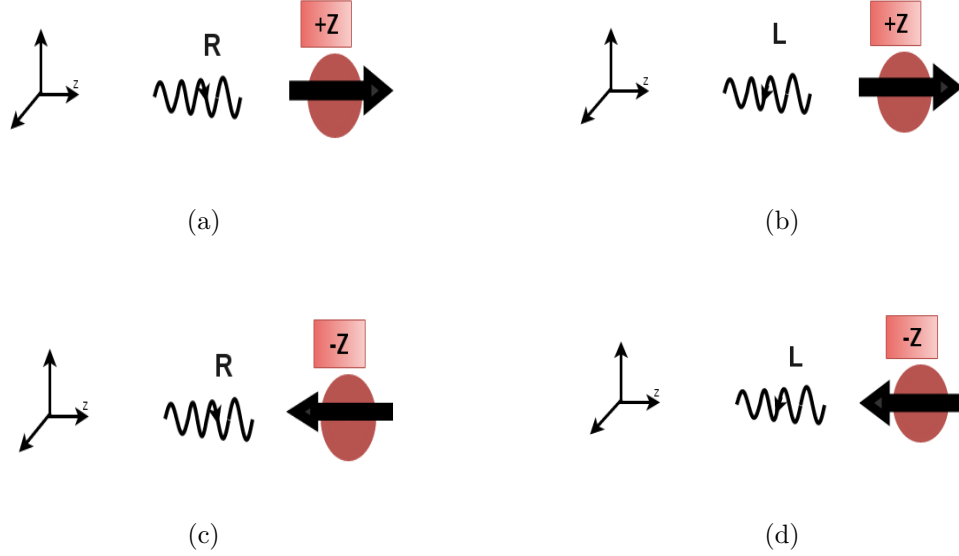


Figure 2.7: Different orientations for Compton scattering with a circularly polarized photon beam on a longitudinally polarized target. (a), (b) show the right and left helicity state of the beam with target polarization in  $+z$  direction ( $\sigma_{+z}^R, \sigma_{+z}^L$ ). (c) and (d) show the right and left helicity state of the beam with target polarization in  $-z$  direction ( $\sigma_{-z}^R, \sigma_{-z}^L$ ).

and  $\sigma_{+z}^L = \sigma_{-z}^R$  and applying this  $\sum_{2z}$  can be written as

$$\sum_{2z} = \frac{\sigma_{-z}^L - \sigma_{+z}^L}{\sigma_{-z}^L + \sigma_{+z}^L} = \frac{\sigma_{-z}^R - \sigma_{+z}^R}{\sigma_{-z}^R + \sigma_{+z}^R}. \quad (2.39)$$

### 2.2.2 Beam Target Asymmetry - $\sum_{2x}$

The beam-target asymmetry  $\sum_{2x}$  is defined as a double polarization asymmetry which is measured using a circularly polarized photon beam (direction given by Stokes parameter  $\xi_2 = \pm 1$ ) on a transversely polarized target (polarization along the  $\pm x$  axis). In terms of polarized cross sections including the right and left helicity states of the beam,  $\sum_{2x}$  can be written as

$$\sum_{2x} = \frac{\sigma_{+x}^R - \sigma_{+x}^L}{\sigma_{+x}^R + \sigma_{+x}^L} = \frac{\sigma_{-x}^R - \sigma_{-x}^L}{\sigma_{-x}^R + \sigma_{-x}^L}, \quad (2.40)$$

where  $\sigma_{\pm x}^R$  and  $\sigma_{\pm x}^L$  represent the cross sections for a positive and negative transversely polarized target with a right and left helicity state of the beam, respectively.

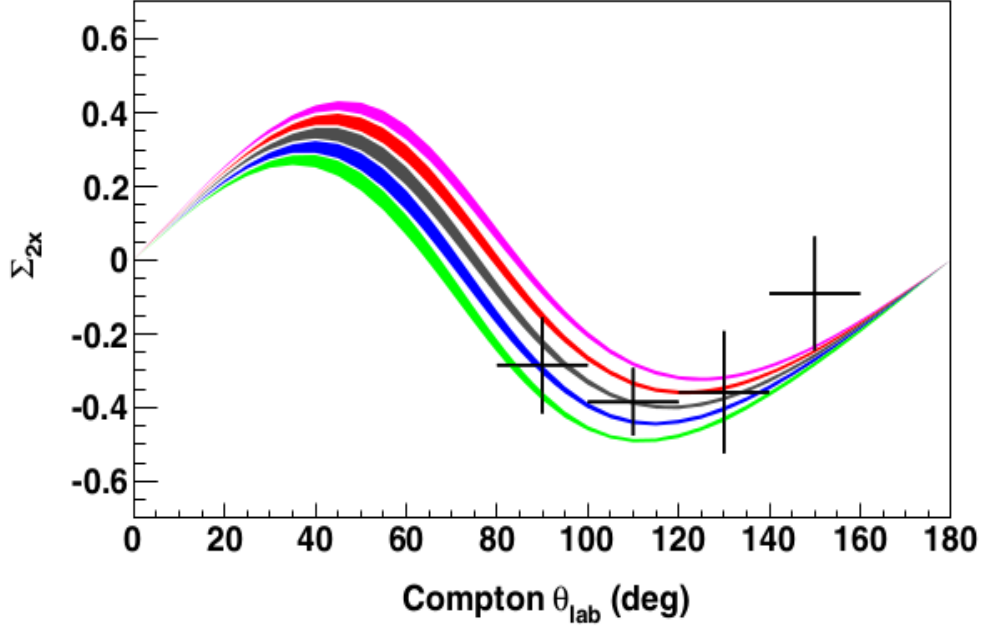


Figure 2.8: Beam target asymmetry  $\Sigma_{2x}$  results at  $E_\gamma = 273 - 303$  MeV. The curves are from a dispersion theory calculation [28] with  $\alpha$ ,  $\beta$ ,  $\gamma_0$ , and  $\gamma_\pi$  held fixed at their experimental values, and  $\gamma_{M1M1}$  fixed at  $2.9 \times 10^{-4} \text{ fm}^4$ . From bottom to top, the green, blue, brown, red, and magenta bands are for  $\gamma_{E1E1}$  equal to 6.3, 5.3, 4.3, 3.3, and 2.3, in standard units of  $10^{-4} \text{ fm}^4$ , respectively. The width of each band represents the propagated errors from  $\alpha$ ,  $\beta$ ,  $\gamma_0$ , and  $\gamma_\pi$  combined in quadrature [49].

The data for  $\Sigma_{2x}$  experiment were collected in September 2010 and February 2011 with both the positive and negative target polarization configuration and the data analysis was completed by P. Martel [50]. The spin polarizabilities of the proton were extracted using the once-subtracted fixed- $t$  dispersion approach of HDPV [28]. Fig. 2.8 shows the  $\Sigma_{2x}$  results for incident photon energies in the range  $E_\gamma = 273 - 303$  MeV along with the dispersion relation calculations for values of  $\gamma_{E1E1}$  ranging from  $-6.3$  to  $2.3 \times 10^{-4} \text{ fm}^4$ , but with  $\gamma_{M1M1}$  fixed at the HDPV value of  $2.9 \times 10^{-4} \text{ fm}^4$  [28, 44]. Data were fit using HDPV calculations allowing  $\gamma_0$ ,  $\gamma_\pi$ ,  $\alpha_{E1} + \beta_{M1}$  and  $\alpha_{E1} - \beta_{M1}$  to vary by their experimental errors. The curves clearly demonstrate the

sensitivity of the asymmetries to  $\gamma_{E1E1}$  showing a preferred solution as

$$\gamma_{E1E1} = (-4.3 \pm 1.5) \times 10^{-4} \text{ fm}^4, \quad (2.41)$$

where the uncertainty includes the fitting error of the model to the data.

The most recent analysis by Martel, *et al.*, extracted the four leading order terms of the proton's spin polarizabilities, combining the published results from single-polarization asymmetry [18] with linearly polarized photons  $\sum_3$  from the LEGS collaboration [34] and Martel, *et al.*,  $\sum_{2x}$  results from the MAMI [49]. Only asymmetry points obtained by the LEGS collaboration below double-pion photoproduction threshold for the incident energies from  $E_\gamma = 213 - 333$  MeV and angular range of  $\theta_{\gamma'} = 70 - 130^\circ$  were considered. As before, data were fit using the HDPV calculations allowing  $\gamma_0$ ,  $\gamma_\pi$ ,  $\alpha_{E1} + \beta_{M1}$ ,  $\alpha_{E1} - \beta_{M1}$  and  $\gamma_{M1M1}$  (no longer fixed in this case) to vary by their experimental errors. The extraction of four spin polarizabilities, combining the LEGS data set and Martel, *et al.*,  $\sum_{2x}$  results are [49],

$$\begin{aligned} \gamma_{E1E1} &= (-3.5 \pm 1.2) \times 10^{-4} \text{ fm}^4, \\ \gamma_{M1E1} &= (3.16 \pm 0.85) \times 10^{-4} \text{ fm}^4, \\ \gamma_{E1M2} &= (-0.7 \pm 1.2) \times 10^{-4} \text{ fm}^4, \\ \gamma_{M1E2} &= (1.99 \pm 0.29) \times 10^{-4} \text{ fm}^4. \end{aligned} \quad (2.42)$$

These results include the fitting error of the model to the data .

### 2.2.3 Beam Asymmetry - $\sum_3$

The beam asymmetry  $\sum_3$  is defined as a single polarization asymmetry, which is measured using a linearly polarized photon beam (direction given by Stokes parameter  $\xi_3 = \pm 1$ , i.e. polarized in a direction parallel ( $\phi = 0$ ) or perpendicular ( $\phi = \frac{\pi}{2}$ ) to

the scattering plane) on an unpolarized target. In terms of cross sections for an unpolarized target including a linearly polarized beam parallel and perpendicular to the scattering plane,  $\Sigma_3$  can be written as

$$\Sigma_3 = \frac{\sigma^{\parallel} - \sigma^{\perp}}{\sigma^{\parallel} + \sigma^{\perp}}, \quad (2.43)$$

where  $\sigma^{\parallel}$  and  $\sigma^{\perp}$  represent the cross sections for an unpolarized target with a linearly polarized beam parallel and perpendicular to the scattering plane, respectively.

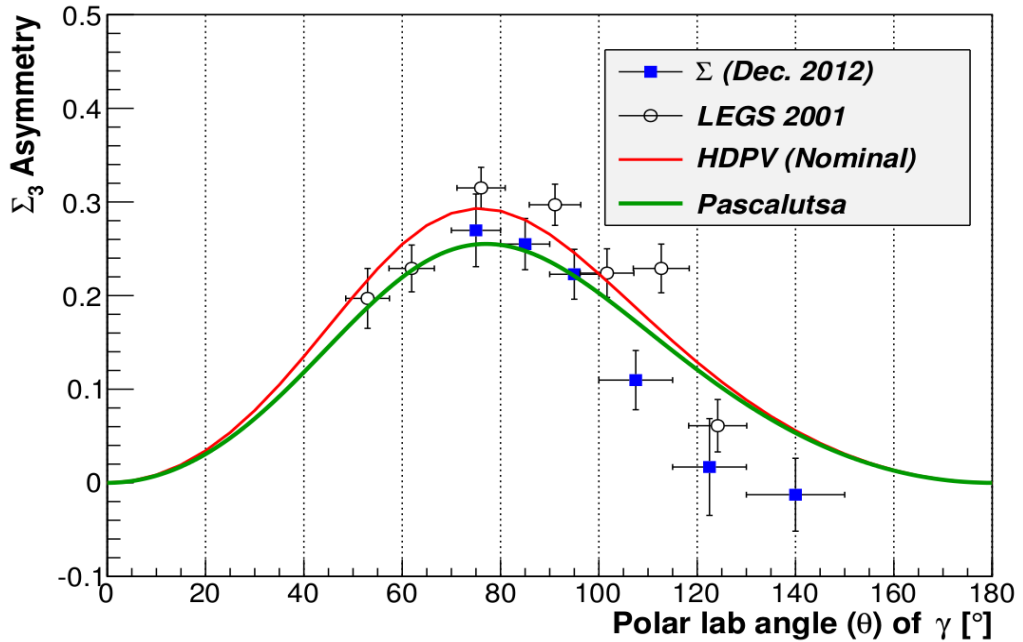


Figure 2.9: Beam asymmetry  $\Sigma_3$  at  $E_\gamma = 297 \pm 10.1$  MeV [51]. The curves are from LEGS data [34], HDPV calculations [17, 28], and Lensky and Pascalutsa [46]. Only statistical errors are shown.

The  $\Sigma_3$  data were collected in December 2012 with unpolarized liquid hydrogen target and the data analysis was completed by Collicott, *et al* [51]. Fig. 2.9 shows  $\Sigma_3$  results for incident photon energies in the range  $E_\gamma = 273 \pm 10.1$  MeV compared with results from the LEGS collaboration. These results were also compared with HDPV [44], and B $\chi$ P) [46] calculation. The fitting routine varies  $\gamma_0$ ,  $\gamma_\pi$ ,  $\alpha_{E1} + \beta_{M1}$

and  $\alpha_{E1} - \beta_{M1}$  by their experimental errors. The extracted  $\gamma_{M1M1}$  using results from Collicott, *et al.*,  $\sum_3$  experiment

$$\gamma_{M1M1} = (3.16 \pm 0.85) \times 10^{-4} \text{ fm}^4. \quad (2.44)$$

The same fitting routine used by Martel, *et al.* [49], extracted the four leading order terms of the proton's spin polarizabilities, combining Collicott  $\sum_3$  and Martel  $\sum_{2x}$  results from MAMI. Only asymmetry points obtained by Collicott, *et al.*, below double-pion photoproduction threshold for the incident energies of  $E_\gamma = 297.0 \pm 10.1$  MeV and angular range of  $\theta_{\gamma'} = 75 - 140^\circ$  were considered. Similar to the Martel, *et al.*, analysis, data were fit using the fixed- $t$  dispersion relation code of Pasquini, *et al.* [44], using the constraint from  $\gamma_0$ ,  $\gamma_\pi$ ,  $\alpha_{E1} + \beta_{M1}$ ,  $\alpha_{E1} - \beta_{M1}$  and  $\gamma_{M1M1}$ . The extraction of four spin polarizabilities, combining the data set from Collicott, *et al.*,  $\sum_3$  results and Martel, *et al.*,  $\sum_{2x}$  results, are

$$\begin{aligned} \gamma_{E1E1} &= (-5.0 \pm 1.5) \times 10^{-4} \text{ fm}^4, \\ \gamma_{M1E1} &= (3.13 \pm 0.88) \times 10^{-4} \text{ fm}^4, \\ \gamma_{E1M2} &= (1.7 \pm 1.7) \times 10^{-4} \text{ fm}^4, \\ \gamma_{M1E2} &= (1.26 \pm 0.43) \times 10^{-4} \text{ fm}^4. \end{aligned} \quad (2.45)$$

# Chapter 3

## Experimental Procedure

### 3.1 Experimental Detector Setup

In this Section, the experimental setup of the Crystal Ball (CB) at MAMI, located on the campus of the Johannes Gutenberg University of Mainz, is described. The experiment was carried out at the tagged photon beam facility in the A2 experimental hall. The first set of data for this thesis work was collected during two experimental run periods, one with the carbon target from April 9 to April 17, 2014 and the other one with the butanol target from May 2 to May 18, 2014. Also, the second set of data was taken during two experimental run periods, first with butanol target from June 23, 2015 to July 11, 2015 and the second one with carbon target from July 11, 2015 to July 16, 2015. The MAMI electron accelerator provided a high quality electron beam with an energy of 450 MeV. This electron beam was used to produce an energy-tagged bremsstrahlung photon beam with the Glasgow-Mainz photon tagging spectrometer. The photon beam was then directed to the frozen spin butanol target, located at the center of the CB calorimeter, inducing the nuclear reactions of interest for the analysis. The detector system consists of a plastic scintillation Particle Identification Detector

(PID), two layers of Multi-Wire Proportional Chambers (MWPCs), central detector CB, and a forward detector, the Two Arms Photon Spectrometer (TAPS). The CB provided the energy and angular information of the particles emitted into over 94% of the solid angle around the target. The PID, a cylinder of 24 plastic scintillator strips, was used to identify charged particles detected in the CB. The MWPCs were used to obtain accurate information about the track of a charged particle from the target. The TAPS system, including the plastic scintillator veto in front of every detector, provided the identification of the particles in the forward region. The experimental detector components are described in more detail in the following section.

### **3.1.1 MAMI Electron Accelerator**

#### **3.1.1.1 Polarized Electron Beam**

MAMI is an electron accelerator facility that can provide unpolarized as well as polarized electron beams with energies up to 1.59 GeV [52]. It consists of four cascaded microtrons, an injector linac, a thermal source for unpolarised electrons and a laser-driven source for electrons with about 80% spin polarization. For an unpolarized electron beam, the cathode of a simple 100 keV thermionic electron gun is heated to high temperature and these heated electrons tend to break free of their atoms and dwell near the surface of the cathode. The beam time structure is a continuous wave sequence of electron pulses with 2.45 GHz repetition rate. This time structure is indistinguishable (electron bunches have 0.4 ns spacing) for almost all particle detection systems since their signal bandwidth is much smaller than the pulse repetition rate. Continuous wave machines are essential for coincidence experiments to reduce the background from accidental coincidences.

In addition to an unpolarized electron beam, MAMI can provide longitudinally polarized electron beam by irradiating a circularly polarized laser light with a wave-

length of  $\lambda = 780$  nm on a strained semiconductor crystal, GaAsP [53]. A  $180^\circ$  flip of polarization, i.e. from spin up to spin down, and vice versa, is provided by reversing the helicity of the laser light with a Pockels cell at a rate of approximately 1 Hz, thereby reducing the systematic uncertainty that would result from a fixed beam polarization [54]. This polarization technique involves: the source of electron beam, beam transport system, the spin rotator and the polarimeter for the degree of electron polarization measurement. After extraction of the longitudinally polarized electrons from the source, the polarization vector can be rotated by a Wien filter into the transverse direction, which is required for a Mott asymmetry measurement. The beam is accelerated in three radio frequency sections, providing acceleration up to 3.97 MeV at the end of the third section [55]. A schematic view of the Mott polarimeter along with the injector part of MAMI is shown in Fig. 3.1a. The beam energy can be changed by varying the phase using a phase ( $\phi$ ) in the wave-guide between klystron and the third accelerating section as shown in Fig. 3.1a.

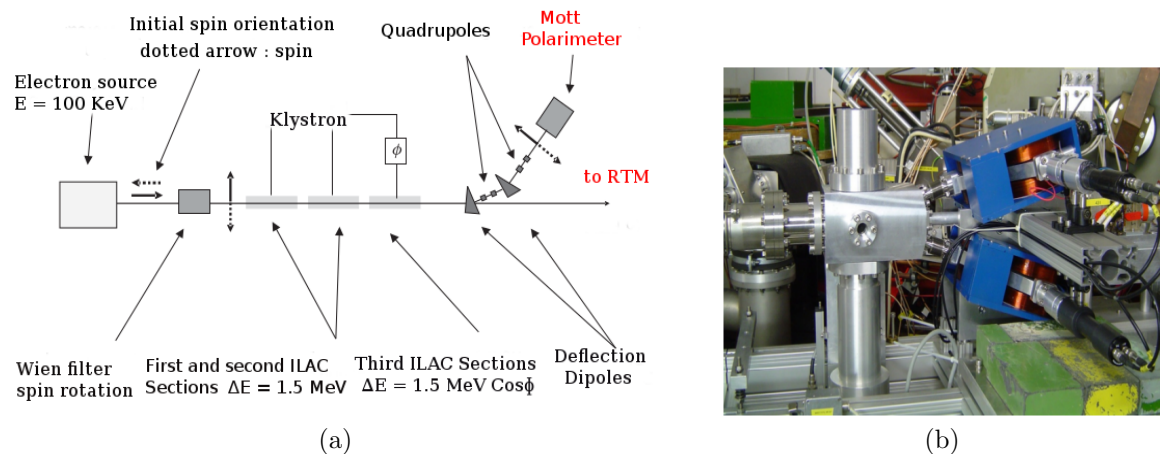


Figure 3.1: (a) Schematic layout of Mott polarimeter at the 3.97 MeV injector of the MAMI Race Track Microtron cascade [56]. (b) MAMI Mott polarimeter, where electron beam enters from the left, and scattered electrons are bent by dipole magnet into the detectors [57].

### 3.1.1.2 Mott polarimeter

Since the experiments at MAMI require run times of several weeks, it is important to monitor the long term drifts of the beam polarization. For this purpose, a standard Mott polarimeter (Fig. 3.1b) at the 3.97 MeV injector of the MAMI accelerator cascade is used [57]. For a polarization measurement, the polarized beam is first delivered into the polarimeter with the help of two  $15^\circ$  bending dipole magnets. The beam is focused onto the Mott target (gold nuclei,  $Z = 79$ ) in the polarimeter by a second quadrupole doublet, as in Fig. 3.1a [56]. The process is based on Mott scattering. In a Mott scattering, for example, a charged particle traveling in the  $\hat{z}$  direction with polarization in the  $\pm\hat{x}$  direction will have an asymmetry in the  $\pm\hat{y}$  direction. In our case, the polarization vector is in the horizontal plane and the scattering plane is chosen to be vertical. Thus, two identical detection systems are used to detect electrons that are scattered upward or downward with respect to the horizontal plane. The elastic count rate is measured once per second, and after each measurement the beam polarization is reversed. Since two detectors are used and the polarization is reversed in every one second, an asymmetry can be calculated from the two subsequent measurements. These asymmetry measurements are done after every tagging efficiency run within the MAMI accelerator on a daily basis. The average value of electron beam polarization for the first round of 2014 butanol beam-time was  $(86.78 \pm 0.03)\%$ , as in Fig. 3.2.

### 3.1.1.3 MAMI Floor Plan

The floor plan of the MAMI accelerator is shown in Fig. 3.3. In 2014 – 2015, the MAMI facility consisted of four experimental halls, A1 hall for electron scattering experiments, A2 hall for tagged photon experiments, A4 hall for parity violation experiments and X1 hall for X-ray experiments. MAMI-A1 officially came into operation

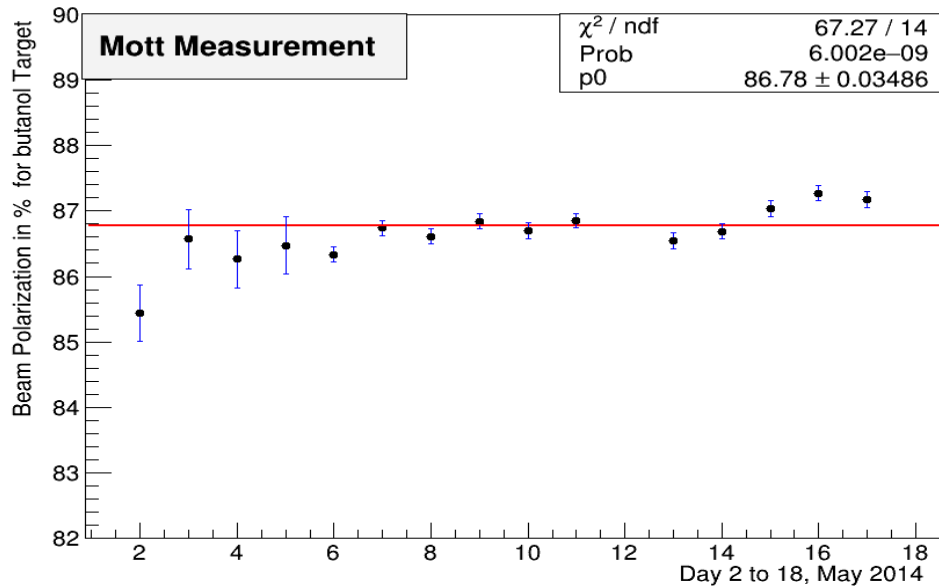


Figure 3.2: Electron Beam Polarization for the first round of 2014 butanol beam-time.

in 1979 using the first Race Track Microtron [52], RTM1 (discussed in Sec. 3.1.1.4), and a Van-de-Graff injector, delivering an electron beam of 14 MeV. The MAMI accelerator facility has been upgraded several times in the past 38 years. The major upgrades in the facility were addition of RTM2 (MAMI-A2) in 1983, which increased electron energy up to 183 MeV and addition of RTM3 (MAMI-B) in 1990 which increased electron energy up to 855 MeV [58]. The current MAMI-C configuration, which consists of cascades of three RTMs (RTM1, RTM2 and RTM3) and a Harmonic Double Sided Microtron (HDSM), was set into operation in December 2006 producing a continuous high quality electron beam of maximum energy 1.59 GeV. For energies beyond 855 MeV, it was unrealistic to double the size of the dipole magnet compared to the magnet used in RTM3 of MAMI-C and hence the HDSM, that has a similar concept to the RTM were added. It uses four bending magnets which bend electrons by 90° along with the two LINAC sections. For the  $\sum_{2z}$  Asymmetry experiment, the HDSM stage of the MAMI was not used.

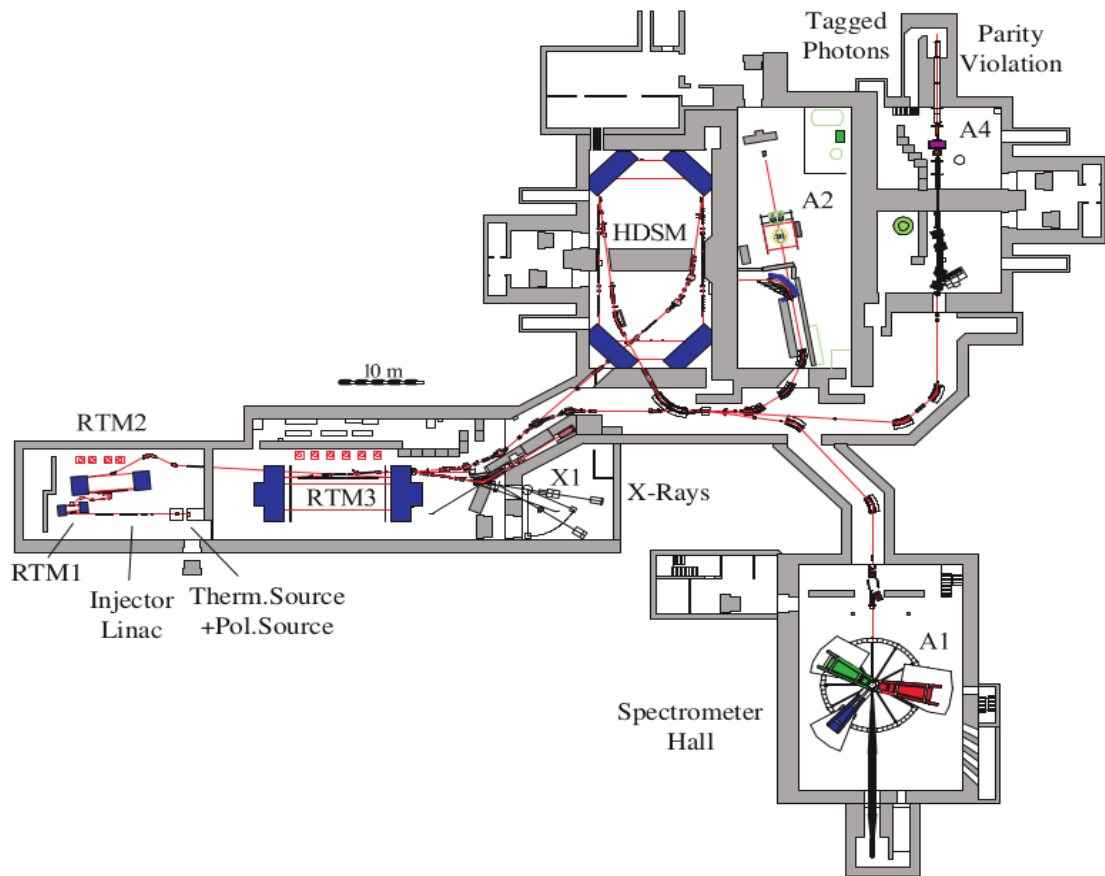


Figure 3.3: An overview of the MAMI floor plan and four experimental halls. The  $\Sigma_{2z}$  asymmetry experiment for this dissertation work was carried out in hall A2 [59].

This experiment was performed in A2 hall, and during the experimental run period the electrons were accelerated through the series of three RTMs. The longitudinally polarized electrons, with polarization up to 85%, were produced by using a polarized laser light on a semi-conductor crystal as discussed in Sec. 3.1.1.1. These electrons were preaccelerated to 511 keV and injected to the injector linear accelerator, in which they are brought to an energy of 3.97 MeV.

### 3.1.1.4 Race Track Microtron

A RTM is an accelerator which recirculates electron beam through the same LINAC several times. It consists of a linear accelerator with Radio Frequency (RF) cavities

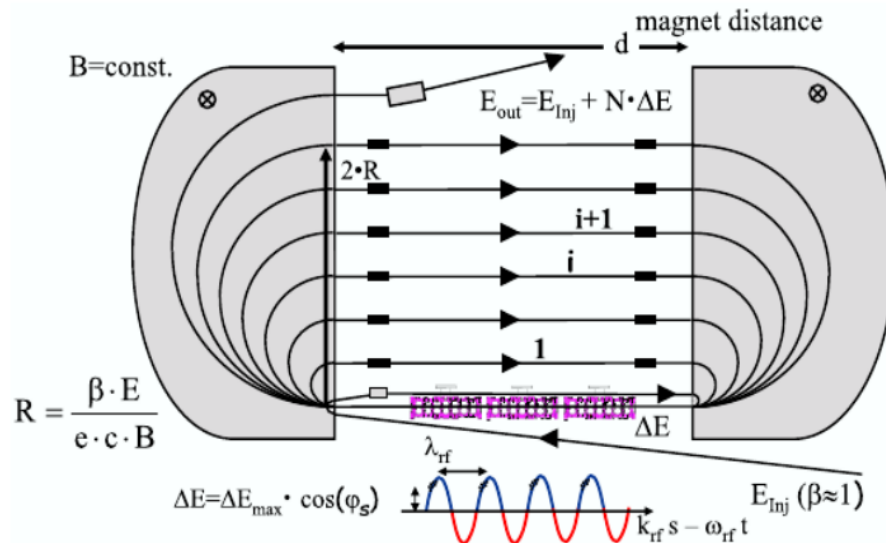


Figure 3.4: A schematic view of a RTM with two large dipole magnets on either side and focusing magnets in between them [52].

of 2.45 GHz placed between two dipole magnets with uniform fields, which deflect the electrons by 180 degrees at both sides of the apparatus, as illustrated in Fig. 3.4. Electrons are injected into the LINAC and are accelerated by a series of standing wave cavities powered by radio-frequency klystrons. As the energy of the electron is step-wise increased, the radius of curvature of the path through the bending magnets increases as well. The increase in energy of an electron through the LINAC per cycle is  $\Delta E = ecB/2\pi\nu_{rf}$ , where  $e$  is the electron charge,  $B$  is the magnetic field,  $c$  is the speed of light and  $\nu_{rf} = c/\lambda_{rf}$  is the klystron frequency [52]. As a result, each re-circulation orbit becomes larger and higher energies can be reached with relatively modest accelerating gradients ( $\approx 1$  MeV/m). As the accelerating gradient is small, the RTM can run in a continuous wave mode, allowing a 100% duty factor beam. The design also ensures excellent intrinsic energy resolutions, as electrons with too-large beam energy have a slightly larger orbit radius and arrive at the LINAC out of phase with the RF accelerating field and thus undergo smaller accelerations until this phase difference vanishes. To ensure that the beam bunches see the same phase of the

alternating voltage in the accelerating section, the difference in time between each successive re-circulation loop has to be an exact integer multiple of the period of the RF supply to this accelerating section. After the electron beam has been accelerated to a certain energy, a small ‘kicker’ magnet ejects it out of the RTM pathway into the beam handling system.

RTM1 accelerates electrons up to 15.3 MeV in 18 re-circulations. These electrons are first fed into RTM2, passing through the LINAC 52 times with an extraction energy of 185.9 MeV, and then into RTM3 recirculating 90 times with an extraction energy of 883.1 MeV. It is possible to select the energy of the beam by extracting the electrons from the intermediate re-circulation trajectory in the RTM3. The output energy of RTM is  $E_{out} = E_{inj} + N \cdot \Delta E$ , where  $E_{inj}$  is the LINAC injected energy with  $\beta \approx 1$  (speed of a particle relative to the speed of light) for relativistic electrons,  $N$  is the number of cycles of the electron beam and  $\Delta E$  is the additional increase in energy per cycle. The RTM parameters are summarized in Table 3.1.

Stages	Injector	RTM 1	RTM 2	RTM 3
Injection Energy (MeV)	511	3.97	15.3	185.9
Extraction Energy (MeV)	3.97	15.3	185.9	883.1
Magnetic Field (T)	-	0.106	0.572	1.323
Weight of Magnets (t)	-	4.2	90.3	911.6
Number of turns	-	18	51	90
LINAC length (m)	4.93	0.80	3.55	8.87
$\Delta E$ per cycle (MeV)	-	0.62	3.35	7.75

Table 3.1: Main parameters of the MAMI accelerator stages [51].

### 3.1.2 Tagged Photon Beam Facility

#### 3.1.2.1 Bremsstrahlung Photon Production and Tagging

The photon beam in the A2 experimental hall is derived from the production of bremsstrahlung (braking radiation) photons during the passage of the MAMI electron

beam through a Moeller radiator (alloy of cobalt and iron), as in Fig. 3.7a. These bremsstrahlung photons are produced when an electron of mass  $m_e$  is deflected by a much heavier nucleus in the radiator. In the bremsstrahlung process, the electrons are decelerated by the electromagnetic field of the radiator's nuclei and the emitted photons produce a continuous energy spectrum that falls off with increasing photon energy up to that of the incident electron energy. This process will happen for a small fraction (about 0.1%) of the electrons incident on the Moeller radiator depending on thickness, and results in a decrease in the electron kinetic energy, so that a recoiling post-bremsstrahlung electron has a kinetic energy  $E'$ . The incident electron energy  $E_e$  is well known and we can use conservation of energy to obtain the energy of the bremsstrahlung photon  $E_\gamma$  as [54]

$$E_\gamma = E_e - E'. \quad (3.1)$$

The spectrum of bremsstrahlung photons from a Moeller radiator is continuous in the range  $0 \leq E_\gamma \leq E_e$ .

The knowledge of  $E_e$  in Equation 3.1 enables the determination of the bremsstrahlung photon energy by measuring  $E'$ . The path of an electron can be bent by using a large dipole magnet and the system is referred to as the Glasgow tagged photon spectrometer or tagger. This is a magnetic electron spectrometer consisting of a large dipole magnet and a Focal Plane Detector (FPD) array and determines the bremsstrahlung energy via the tagging technique [60]. Apart from measuring photon energies, the tagger measures the total flux of scattered electrons, which can be used to determine the number of photons impinging on the target from detection efficiency measurements. For all absolute observables, such as total or differential cross sections, the total number of photons is crucial. Fig. 3.5 shows the tagging process using a tagger system.

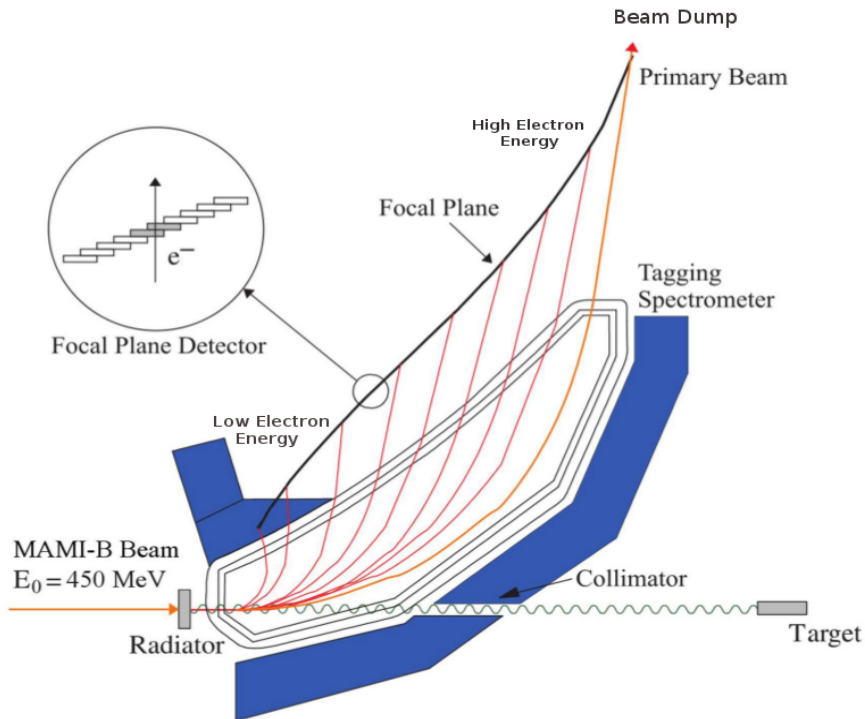


Figure 3.5: The Glasgow photon tagger spectrometer, where an electron beam enters from the lower left and strikes the radiator. The bremsstrahlung photon passes to the right through a collimator, while the electrons will see their trajectory deflected to the FPD with a curvature radius proportional to their energy [51].

The physics behind this technique is very simple, because the photons are electrically neutral, while electrons are not, so a magnetic field may be used to deflect the post-bremsstrahlung electron without disrupting the path of the photon. To accomplish this, the tagger dipole creates a magnetic field in the vertical direction in the lab perpendicular to the electron beam direction after the radiator. The Lorentz force  $\vec{F}$  exerted on an electron with charge  $e$  and velocity  $\vec{v}$  when it passes through a magnetic field with a magnetic flux density  $\vec{B}$  is given by

$$\vec{F} = -e(\vec{v} \times \vec{B}). \quad (3.2)$$

The magnetic field thus deflects the post-bremsstrahlung electrons from their orig-

inal path, and the electrons that do not radiate passing through the radiator are bent into the Faraday cup of the beam dump. The radius of curvature of a charged particle within the magnetic field depends on the momentum of the electron when it reaches the tagger. For a given field strength  $B$ , and a known radius of curvature  $R$  of the particle, the momentum is obtained using the relation  $p = eR \cdot B$ . A low-energy electron (which corresponds to a high-energy bremsstrahlung photon) will be deflected the most, while an electron that has passed through the radiator without interacting will be deflected the least.

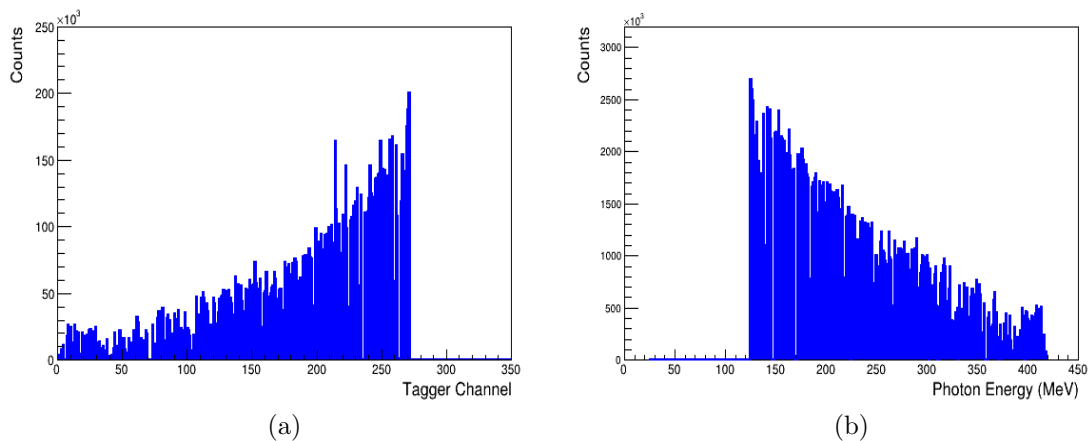


Figure 3.6: (a) Tagger channel hit distribution. (b) The bremsstrahlung distribution of photon energies for an incident electron beam energy of 450 MeV.

The tagger focal plane consists of 353 overlapping plastic scintillators, each 80 mm long, 2 mm thick and variable widths ranging from 9 to 32 mm, and coupled to an individual PMTs. The scintillator strips are partially overlapped and electronically paired, so that an electron hit requires coincident signals in two adjacent detectors, reducing accidental events. This leads then to 352 logical detectors. The scintillators are read out individually by Hamamatsu R1635 photomultiplier tubes that are shielded from the tagger magnetic field by steel plates. A high beam intensity can lead to a saturation of the tagger elements at the extreme high electron energies (low

photon energies), due to the  $1/E_\gamma$  distribution of the bremsstrahlung process. Additionally, the photomultipliers can get damaged by high currents. The high electron energy channels that correspond to low photon energies were turned off to reduce the trigger rate during both the 2014 and 2015 beamtimes. This then reduced the DAQ deadtime, so a higher electron beam current could be used to maximize the photon flux in the region of interest,  $E_\gamma = 200 - 425$  MeV. Only 270 tagger channels during the 2014 beamtime, and 180 tagger channel during the 2015 beamtime, were used. Figs. 3.6a-3.6b show the distribution of the tagger channel hits and the corresponding bremsstrahlung distribution of photon energies for an incident electron beam energy of 450 MeV.

### 3.1.2.2 Polarized Photon Beam

If the electron beam is longitudinally polarized, the electrons partially transfer their polarization to the photons and the radiated photons will be circularly polarized. The degree of circular polarization of the photon beam, obtained by the helicity transfer of spin polarized electrons, is given in terms of photon energy and the incoming electron energy [50],

$$P_\gamma = P_e \frac{4E_\gamma E_e - E_\gamma^2}{4E_e^2 - 4E_\gamma E_e + 3E_\gamma^2}, \quad (3.3)$$

where  $E_\gamma$  is the energy of the photon, and  $E_e$  and  $P_e$  are the energy and polarization of the electron beam, respectively. The degree of circular polarization of the photons increases as the photon energy increases, as shown in Fig. 3.7b, and for the highest values of photon beam energy the degree of photon polarization is approximately equal to the electron's polarization ( $P_\gamma \approx P_e$ ). For the  $\sum_{2z}$  butanol beam-time, three different photon energy ranges (265 – 285, 285 – 305 and 310 – 330 MeV), have been chosen and the corresponding average values of degree of photon polarization are 68.12, 72.10 and 76.24%, respectively.

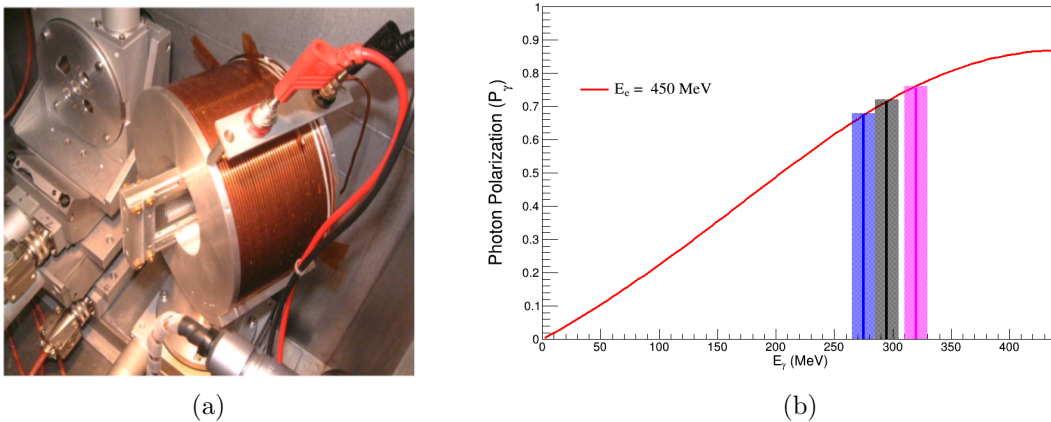


Figure 3.7: (a) Moeller radiator inside the A2 Goniometer [61] with relative angle between the Moeller foil and the direction of electron beam  $25 \pm 0.1^\circ$ . (b) The degree of photon polarization as a function of the photon energy for a 450 MeV electron beam. The average value of photon polarization in the range  $E_\gamma = 265 - 285$  MeV (blue line),  $E_\gamma = 285 - 305$  MeV (black line) and  $E_\gamma = 310 - 330$  MeV (magenta line).

### 3.1.2.3 Photon Beam Collimation

In order to obtain a well defined beam spot within the target diameter, the photon beam is collimated before leaving the tagger magnet. This is important, because the bremsstrahlung photons are emitted in a cone centered about the direction of the incident electron beam with an opening angle  $\theta$ . This opening angle depends on the Lorentz factor  $\gamma = E_e/m_e c^2$ , and is given by

$$\theta \approx \frac{1}{\gamma} = \frac{m_e c^2}{E_e}, \quad (3.4)$$

where  $E_e$  is the electron beam energy,  $m_e$  is the electron mass and  $c$  is the speed of light. The photon beam was collimated using a lead collimator (20 mm long and 2 mm diameter) located 2.5 m downstream of the radiator. This led to a beam spot size of  $\sim 1.3$  cm diameter in the target.

### 3.1.3 Photon Detectors

The detector setup for the experiment includes a central detector system, CB calorimeter combined with PID for particle identification and MWPC for charged particle tracking, and TAPS in the forward wall. The schematic diagram of this setup is shown in Fig. 3.8, and is described in the following sections.

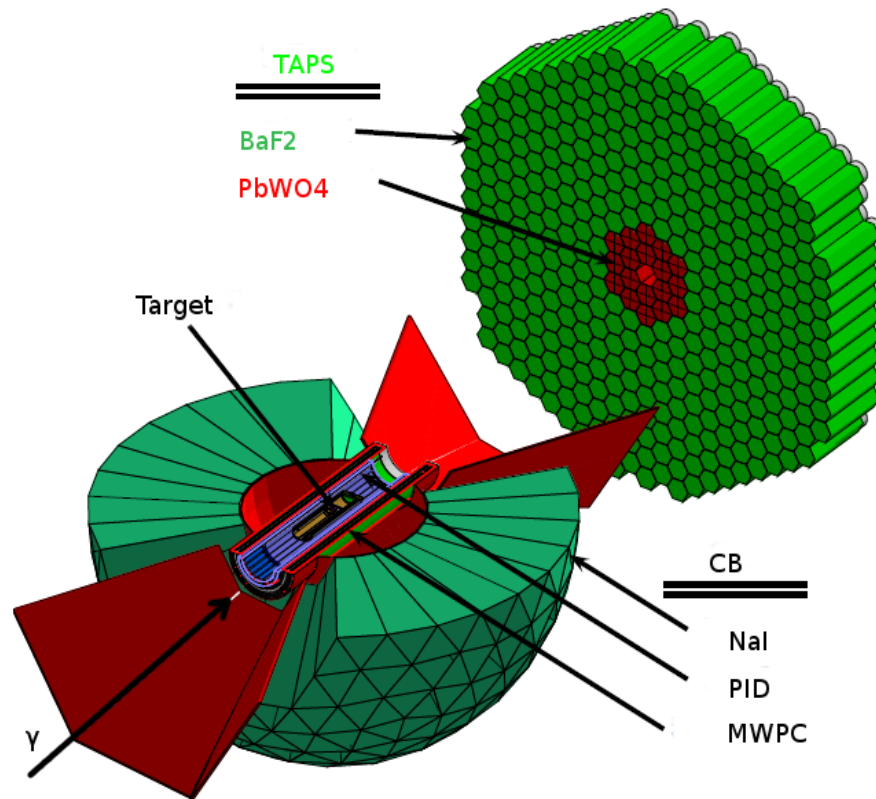


Figure 3.8: A schematic picture of the detector setup in the A2 hall [62].

#### 3.1.3.1 Crystal Ball

The CB detector was initially designed for colliding experiments jointly by SLAC and Brookhaven national laboratory in 1970's. It ran from 1974 until 1982 @ SLAC and the very first measurement of  $J/\psi$  and its excited states [63, 64] were the great achievements during the SLAC era of the CB. It was then moved to Deutsches Eleck-

tronen Synchrotron (DESY) in Hamburg between 1982 – 1987 and contributed to the study of bottom quarks. It was put in a storage at SLAC for a period of eight years and later used to study strange and non-strange baryon resonances at Brookhaven National Laboratory from 1995 to 2002 before moving into its current location in the A2 hall of MAMI.

The Crystal Ball calorimeter is a sphere consisting of 672 optically insulated NaI(Tl) crystals with truncated triangular pyramid shape. The crystals are arranged in two hemispheres that cover about 94% of  $4\pi$  and a polar angular range of  $21^\circ$  to  $159^\circ$ . It provides an energy resolution of 3 – 4% within the region of interest, a polar angular resolution of  $3^\circ$ , and an azimuthal resolution equal to the polar resolution divided by  $\sin \theta$  [64]. Each hemisphere has inner and outer radii of 25.3 cm and 66.0 cm, respectively [65]. It also has a spherical cavity in the center with radius of 25.3 cm. The target and inner detectors, the PID and the MWPC are located in that cavity. Since the CB was designed for a colliding beam experiment, it has two cone-shaped tunnels which serve as the entrance and exit of the photon beam.

The geometry of NaI crystal is unique, with a 40.6 cm long truncated triangular pyramid. The triangular sides at the top of the pyramid are 5.1 cm wide and at the bottom of the pyramid are 12.7 cm wide [67]. A group of nine crystals is stacked to form a minor triangle, a group of four minor triangles forms a major triangle, and a group of twenty major triangles forms an icosahedron as in the left-hand side of Fig. 3.9. Each crystal is optically coupled to a SRCL50B01 photomultiplier tube with glass windows as shown in the right-hand side of Fig. 3.9.

### 3.1.3.2 Particle Identification Detector

In order to distinguish between neutral and charged particles detected by the Crystal Ball, the system is equipped with a set of inner detectors between the target cell and

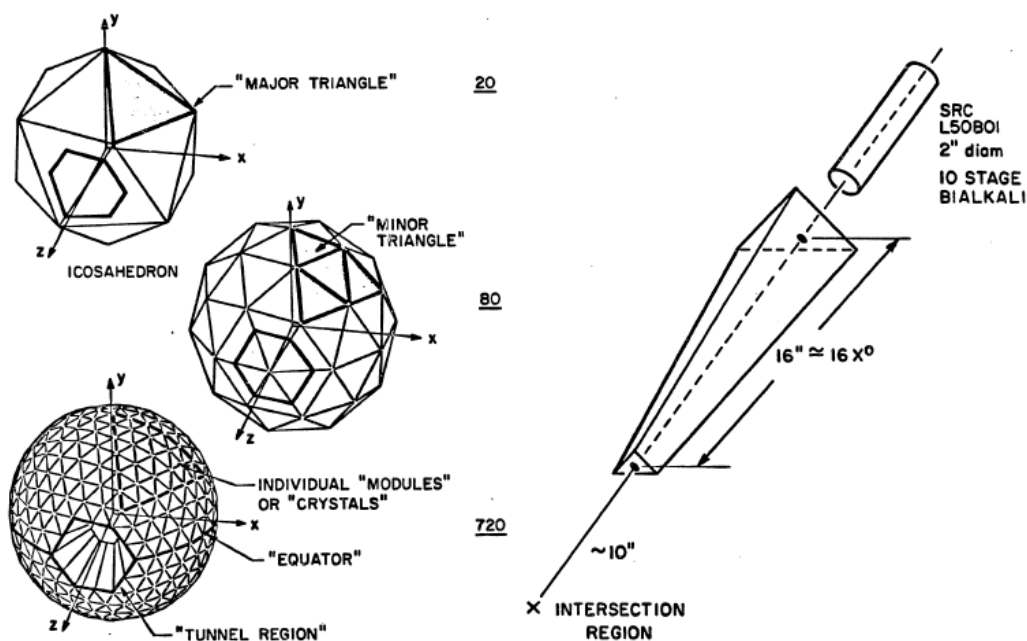


Figure 3.9: Geometry of the Crystal Ball detector and the NaI crystals. The left pannel shows the icosahedron shaped detector with 20 major and 80 minor triangles and the right-hand pannel show the crystal geometry [66].

CB. The first inner detector surrounding the target is the PID, which consists of a 10 cm diameter cylindrical barrel of 24 EJ-204 plastic scintillators. Each element is 500 mm long, 15.3 mm wide and 4 mm thick [50, 68]. The cross section of each element is a right angled trapezoid to minimize the gaps between each other when formed into the barrel. They are also individually wrapped in aluminum foil to ensure optical isolation and the entire detector is covered in a black Tedlar to provide light proofing. Scintillation light induced in each scintillator travels through a light guide and is read out by separate Hamamatsu H3164-10 photomultipliers connected to one end of PID as shown in Fig. 3.10a. The PID barrel covers from  $15^\circ < \theta < 159^\circ$ .

The PID is a part of the inner detectors of the CB system which provides identification of particle species. By matching a hit in the PID with a corresponding hit in the CB, it is possible to use the  $\Delta E/E$  technique to identify the charged particle

species. In this technique, a coincident deposited energy in the PID versus the cluster energy in CB is used for the separation of charged pions, electrons and protons. As for the lighter particles, like electrons and pions, the energy deposition is roughly 1 – 2 MeV. However, heavier particles like the proton deposit energy inversely proportional to their total energy, with slower protons depositing a higher fractions of their total energy. A two-dimensional histogram of the energy loss,  $\Delta E$ , measured in the PID, and the energy,  $E$ , measured in the CB, results in two distinct bands associated with different particle species is shown in Fig. 3.10b.

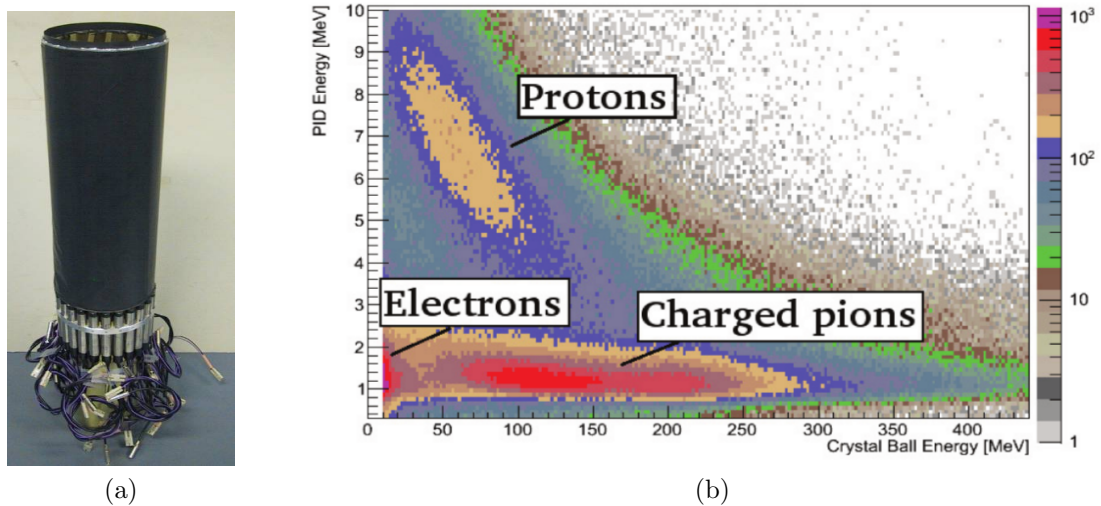


Figure 3.10: (a) Cylindrical barrel of 24 EJ-204 plastic scintillators forming a PID detector. (b) An example plot of differential energy loss  $\Delta E$  in the PID as a function of the energy,  $E$  measured in CB which results in distinct bands associated with the different charged particles [51, 68].

### 3.1.3.3 Multi Wire Proportional Chamber

The second inner detector surrounding the target is the two coaxial cylindrical MWPC, which each consists of three layers: internal strips, wires and external strips. The inner and outer layers act as cathodes for the proportional counter, and a set of thin, equally spaced, anode wires are sandwiched between them as shown in Fig. 3.11a.

The cathodes are made from 1-mm-thick cylindrical conductors covered by 25  $\mu\text{m}$  Kapton foil and 0.1- $\mu\text{m}$ -thick aluminum coating on the external surfaces of the chamber walls. Both interior surfaces are laminated with 4-mm-wide aluminum strips of 0.1  $\mu\text{m}$  thickness with a 0.5 mm gap between adjacent strips [69]. The inner wire chamber has 232 wires, 69 inner strips and 77 outer strips. The outer wire chamber has 296 wires, 89 inner strips, and 99 outer strips. The cathode strips cross each other twice along the length of the chamber, which is necessary to establish which anode wires have fired to identify the correct intersection point.

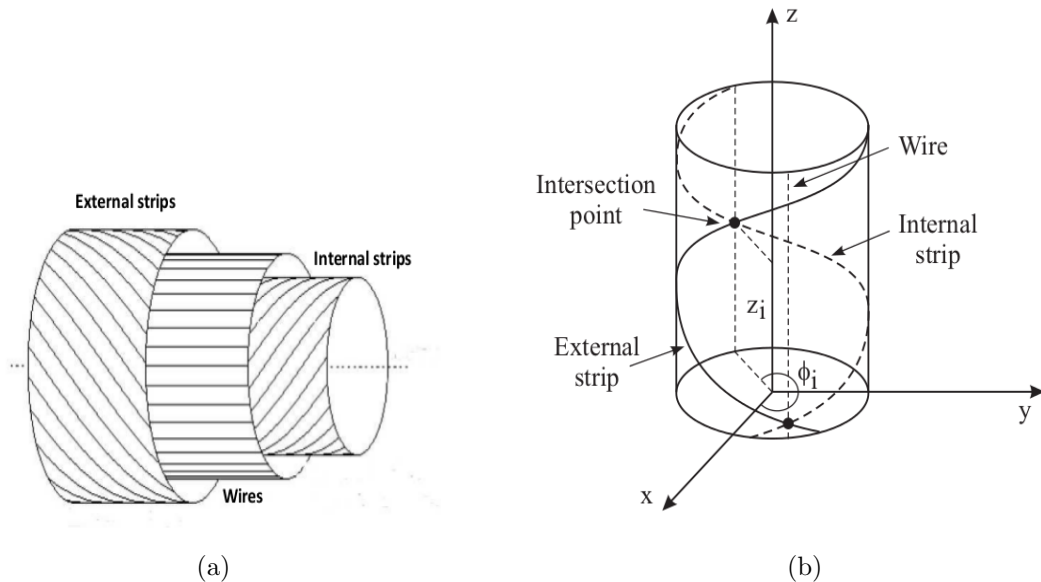


Figure 3.11: (a) MWPC schematic diagram showing the position of anode and cathodes and, (b) Reconstruction of the charged particle trajectory in MWPCs [70].

The MWPCs are filled with a mixture of 65.5% argon, 28% ethane, 0.5% freon ( $CF_4$ ) and 6% alcohol [70, 71]. When a charged particle passes through a chamber, it ionizes the gas mixture. The resulting electrons migrate towards the anode wire due to the potential difference between the cathodes and the anodes. This creates an avalanche of electron-ion pairs through secondary ionization, which are collected in one or more of the wires, inducing positive ions on both cathodes and accelerated

to the internal and external strips. Reconstruction of the tracks of charged particles which hit the CB uses the coordinates of the charged particles interaction with two coaxial cylindrical MWPCs cathode strip readouts. By knowing the center of the charge distribution induced on the cathode strips, the azimuthal angle  $\phi$  and the longitudinal coordinate  $z$  of the impact points are evaluated. The impact reconstruction of a charged particle trajectory in the MWPCs is shown in Fig. 3.11b. Once  $\phi$  and  $z$  are known for each chamber, a straight line can be fitted through these coordinates and the polar angle  $\theta$  and the azimuthal angle  $\phi$  of the track are obtained. The vertex reconstruction for two or more charged tracks is done by finding the intersection point of the trajectories. In the case of only one trajectory, the vertex position is defined as the closest point to the  $z$  axis. These wire chambers have a coverage of  $360^\circ$  in azimuthal angle  $\phi$  with  $3^\circ$  resolution, and  $21 - 159^\circ$  in polar angle  $\theta$  with  $3^\circ$  resolution because of the opening at the front and rear of the cylinders, giving a coverage of 94% of  $4\pi$  steradians.

#### 3.1.3.4 Two Armed Photon Spectrometer

Due to the lack of acceptance at the forward angle of the CB, the TAPS was assembled into a single forward wall and installed to detect photons and charged particles that escape from the CB exit hole. The TAPS forward wall is very important because this is a fixed target experiment and the reaction products are Lorentz boosted forward. It is placed downstream of the CB and the distance from the target center to TAPS detector center is about 1.8 m. The detector consists of an array of 366 BaF<sub>2</sub> crystals along with the 72 PbWO<sub>4</sub> crystals in the two innermost rings, as shown in Fig. 3.12a-3.12b. The crystals are arranged in a hexagon-like structure with eleven rings and six logical sectors. To ensure that the BaF<sub>2</sub> crystals are light tight, each crystal is optically isolated by wrapping them in eight layers of 38  $\mu\text{m}$  thick reflecting Teflon

foil and one layer of 15  $\mu\text{m}$  aluminum foil. Individual  $\text{BaF}_2$  elements are read out by Hamamatsu R2059-01 photomultiplier tubes connected to the cylindrical ends of the crystals. The distance of the TAPS detector downstream of the target cell from the target center is  $\sim 150$  cm.

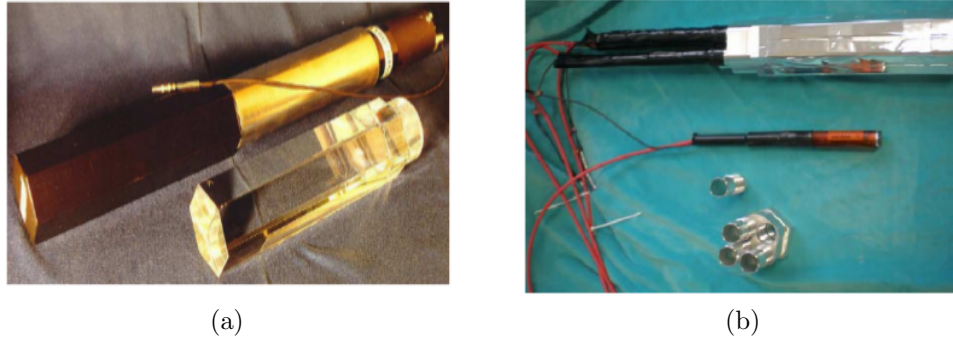


Figure 3.12: (a)  $\text{BaF}_2$  crystal and  $\text{BaF}_2$  crystal connected to a PMT. (b) A complete module of four  $\text{PbWO}_4$  [68].

The  $\text{BaF}_2$  crystals have a hexagonal shape with a 5.9 cm front-face diameter, 22.5 cm length and 2.5 cm long cylindrical end cap with a diameter of 5.4 cm. The overall 25 cm  $\text{BaF}_2$  detector material is 12 radiation lengths in thickness and allows stopping of photons up to 380 MeV and charged pions up to 185 MeV [72]. The  $\text{BaF}_2$  crystal has two special material properties which are considered very good for the construction of scintillation detectors. First,  $\text{BaF}_2$  has a fast rise time of the scintillation pulse, and because of this feature the intrinsic time resolution (about 200 ps) of a single crystal is very good. This feature enables the accurate particle identification using the time-of-flight information of the particle. Second,  $\text{BaF}_2$  produces scintillation light with two components, a fast component and a slow component, corresponding to the decay times of  $\approx 0.9$  ns and  $\approx 650$  ns [73]. These features are essential to separate slower hadrons like protons and neutrons from the faster particles like photons, electrons and pions. The fast light component provides a very good time resolution needed for time of flight measurements (up to  $t \approx 170$  ps for a single

detector), whereas the slow light component provides a very good energy resolution because of the high light yield. Due to the different mechanisms of energy deposition of photons and, e.g., hadrons, these two light components lead to different signal shapes for the corresponding particles. The relative contribution of the fast component to the total light output is higher in the case of photons than for, e.g., protons or neutrons. This can be used for particle identification by integrating the signal over a short and a long time interval and comparing the two resulting calibrated energies.

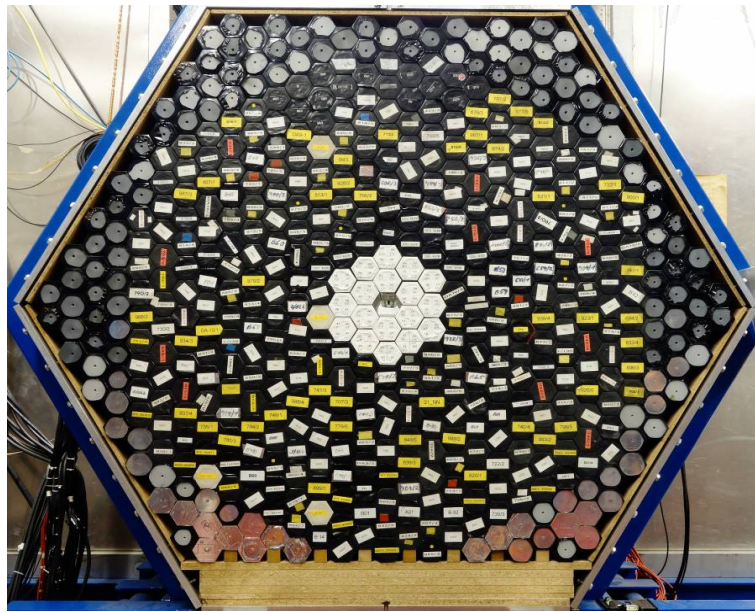


Figure 3.13: Head-on view of 366  $\text{BaF}_2$  and 72  $\text{PbWO}_4$  stacked in TAPS setup.

The  $\text{PbWO}_4$  crystals were installed in the two innermost rings of TAPS in 2009, as in Fig. 3.13. This was important to better handle the high intensity particle flux and to improve the angular resolution at small forward angles. This is achieved by the short signal decay time of around  $\approx 10$  ns [74]. In addition, the higher density of  $\text{PbWO}_4$  compared to  $\text{BaF}_2$  allowed the installation of smaller crystals. The small trapezoidal shape of every crystal allows a combination of four  $\text{PbWO}_4$  crystals to integrate into the TAPS geometry of one  $\text{BaF}_2$  crystal. Each crystal is 20 cm in length, which corresponds to 22.5 radiation lengths and has a 6 ns delay time [61].

They are individually wrapped in 70  $\mu\text{m}$  reflector foil VME 2000 with an additional layer of 20  $\mu\text{m}$  aluminum foil to insure that the light stays within the crystal, and are coupled to photonis XP-1911 photomultiplier tubes.

### 3.1.3.5 TAPS Veto

The front face of every  $\text{BaF}_2$  crystal, and group of four  $\text{PbWO}_4$  crystals are covered with a layer of thin plastic scintillators, as shown in Fig. 3.14b. Their function is similar to the PID, to provide  $\Delta E/E$  information, since the PID has the same forward polar acceptance as the Crystal Ball, and cannot be used with the TAPS detector. The individual plastic scintillators are assembled in a hexagonal frame that are made from 5 mm thick EJ-204 with a groove machined on one side for the WaveLength Shifting fibers (WLS-fibers). These are composed of the same plastic material, as the PID scintillators. They are connected via BCF-92 WLS-fiber to multi-anode Hamamatsu H6568 photomultiplier tubes with 16 channels, which allows for a direct correlation between a hit in a veto crystal and a hit in a  $\text{BaF}_2/\text{PbWO}_4$  crystal. Fig. 3.14a shows the WLS-fiber embedded in the groove of the veto module.

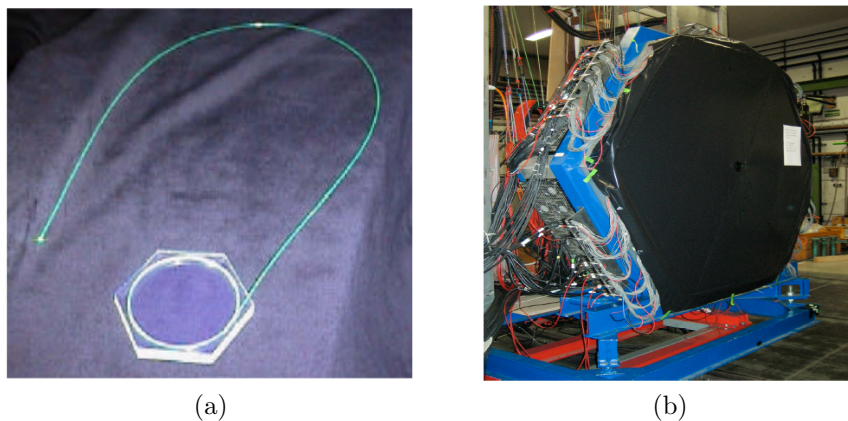


Figure 3.14: (a) Veto plastic scintillator with the WLS-fiber embedded in a groove. (b) A black foil which serves as a light isolation for the veto wall [61, 68].

## 3.2 Principle of Frozen Spin Butanol Target

To obtain a highly polarized source of protons, our experiment utilizes the process of Dynamic Nuclear Polarization (DNP) [75, 76]. Understanding the frozen spin target polarization and finding the absolute value of polarization is crucial for asymmetry experiments, so the theoretical background of the target polarization and the experimental results are described in the following section.

### 3.2.1 Brute Force Polarization

The nucleon is a spin- $\frac{1}{2}$  fermion with two possible orientations commonly named as spin: up ( $+\frac{1}{2}$ ) and down ( $-\frac{1}{2}$ ). In an unpolarized material, the spins of the nucleons are distributed randomly, while in a polarized material there is a preferred direction in the spin orientation. The nucleon polarization is defined in terms of the expectation value of finding their spins oriented in a certain direction. If we consider a particle of spin,  $S$ , and magnetic moment,  $\mu$ , placed in a high magnetic field,  $B$ , and cooled to low temperature,  $T$ , polarization occurs via the Zeeman interaction. At thermal equilibrium, the populations of the Zeeman levels or magnetic sub-levels obey the Boltzmann distribution as

$$N_1 = N_2 \cdot \exp\left(\frac{-\Delta E}{\kappa T}\right), \quad (3.5)$$

where  $\kappa$  is the Boltzmann constant, and  $\Delta E = E_1 - E_2 = \mu B$  is the energy difference between the two Zeeman levels corresponding to the population number  $N_{1,2}$  [77]. The degree of polarization of spin- $\frac{1}{2}$  protons or electrons can be written as

$$P = \frac{N_+ - N_-}{N_+ + N_-} = \tanh\left(\frac{\mu B}{2\kappa T}\right). \quad (3.6)$$

where  $N_+$  denotes the number of spins aligned with the external magnetic field while  $N_-$  denotes the number of spins not aligned with the field. A positive polarization means that there are more spins aligned with the field, as is obvious from the Equation 3.6. The reverse is true for a negative polarization.

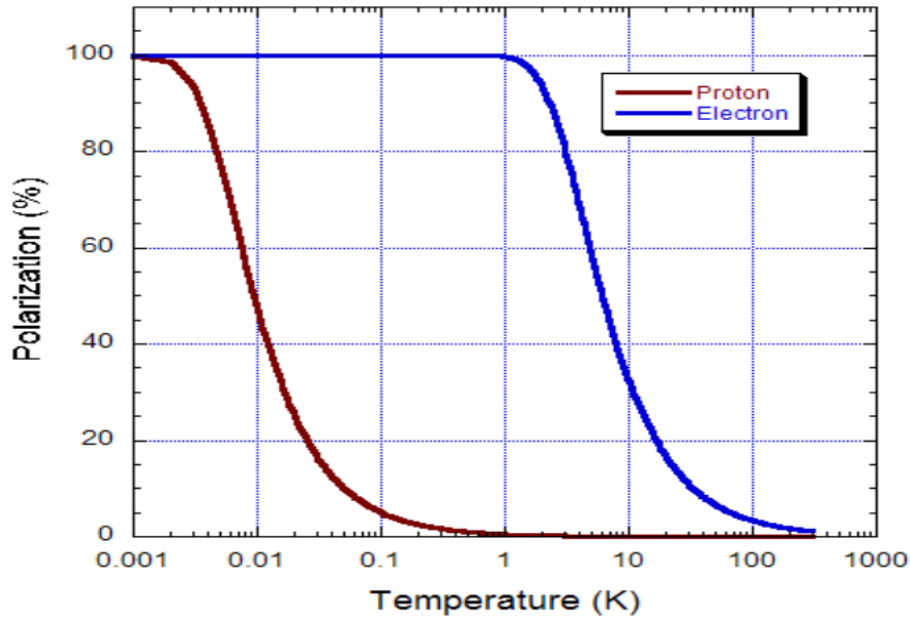


Figure 3.15: Brute Force Polarization as a function of temperature for electrons and protons [78].

This method of polarizing a target via the Zeeman interaction is called Brute Force Polarization (BFP). Because the electrons have smaller magnetic moment than the proton, the energy gap  $\Delta E$  is smaller and the degree of polarization for electrons is much higher than for protons. From Equation 3.5, it follows that in a magnetic field of 2.5 T and a temperature of 1 K, electrons can be polarized up to 93%, as in Fig. 3.15, while protons reach a value of only 0.25%. In the presence of a magnetic field of 10 T at a temperature 25 mK, only 47% proton polarization can be achieved after a long time. Achieving reasonable proton polarization using this method is very difficult and expensive since a high magnetic field and very low temperatures are necessary. In addition, it takes several weeks to obtain the final nuclear polarization

under thermal equilibrium condition due to the weak spin-lattice interaction [77].

### 3.2.2 Dynamic Nuclear Polarization

To overcome the challenges of BFP, many polarized target experiments exploit the process of DNP. The fundamental principle behind the DNP process is to consider the electron-nucleon system and transfer the polarization from the electron to the nucleon using optical pumping, i.e. by microwaves with appropriate frequency. In this process, first of all, a hydrogenous compound is doped with a small concentration of free radicals, i.e. unsaturated electron spins. In a large magnetic field and at low temperatures, these electrons are polarized, since their occupation of the two different magnetic substates follow the Boltzman distribution.

A high magnetic field can be achieved with commercial superconducting magnets and low temperatures are reached by means of a  $^3\text{He}/^4\text{He}$  dilution cryostat. The free electron spin couples to neighboring protons to form atomic systems. Irradiating the sample with microwaves of appropriate frequency induces transitions where both the electron and the proton flip their spins. This leads to a preferred orientation of the nuclear spin, i.e. nuclear polarization. The average lifetime of nuclei in the higher state is called the relaxation time and it depends on the ratio of magnetic moment to its angular momentum (gyromagnetic ratio) and the mobility of the lattice. The relaxation time of the electrons in the higher energy state is short due to the interaction of the electrons with the lattice. The electrons therefore flip back and are available for further spin flip transitions with other protons. The relaxation time of the nuclei, on the other hand, is long due to larger gyromagnetic ratio and mobility of the lattice. This allows the nuclei to accumulate preferentially in a state selected by the frequency of the microwaves, thus leading to a high polarization of the sample in a reasonable time frame.

An ideal proton target material would be molecular hydrogen; however, at low temperatures the transition from the ortho to the para state makes it almost impossible to polarize. Therefore, other materials like butanol have been used for this purpose. Butanol is superior to other materials because it has very high degree of polarization, short polarization build up time, high dilution factor (ratio of the number of polarizable free nucleons to the total number of nucleons), long relaxation time and simple preparation plus handling.

### 3.2.2.1 Mainz Frozen Spin Target

At MAMI, the Frozen Spin Target (FST) system consists of a beads of frozen butanol ( $C_4H_9OH$ ) surrounded by a  $^3He/^4He$  dilution refrigerator, microwaves and Nuclear Magnetic Resonance (NMR) system, polarizing magnet, internal holding magnet, pumping and circulation system and control systems, as shown in Fig. 3.16d. The beads of TEMPO-doped butanol ( $C_4H_9OH$ ) target material [79] are shown in Fig. 3.16a. These are spherical in shape with 2 mm diameter, and are enclosed in the target container (2 cm in length, 2 cm in diameter). The Mainz frozen spin target dilution refrigerator operates by pumping helium at a temperature of 25 mK. In addition, these beads do not fill up the entire volume of the target cavity, and hence a  $60.7 \pm 2\%$  [68] filling factor has been applied in the data analysis.

The complete polarization procedure has two important modes, called polarizing mode and the Frozen Spin mode. First, in the so-called polarizing mode the target is cooled down to about 200 mK and an external magnetic field of 2.5 Tesla is applied. The continuous operation of high cooling power  $^3He/^4He$  dilution refrigerator, developed in collaboration with the polarized target group of the Joint Institute for Nuclear Research (JINR) Dubna, provides the low temperature. The superconducting magnet, which can produce a magnetic field up to 5 Tesla, provides an external

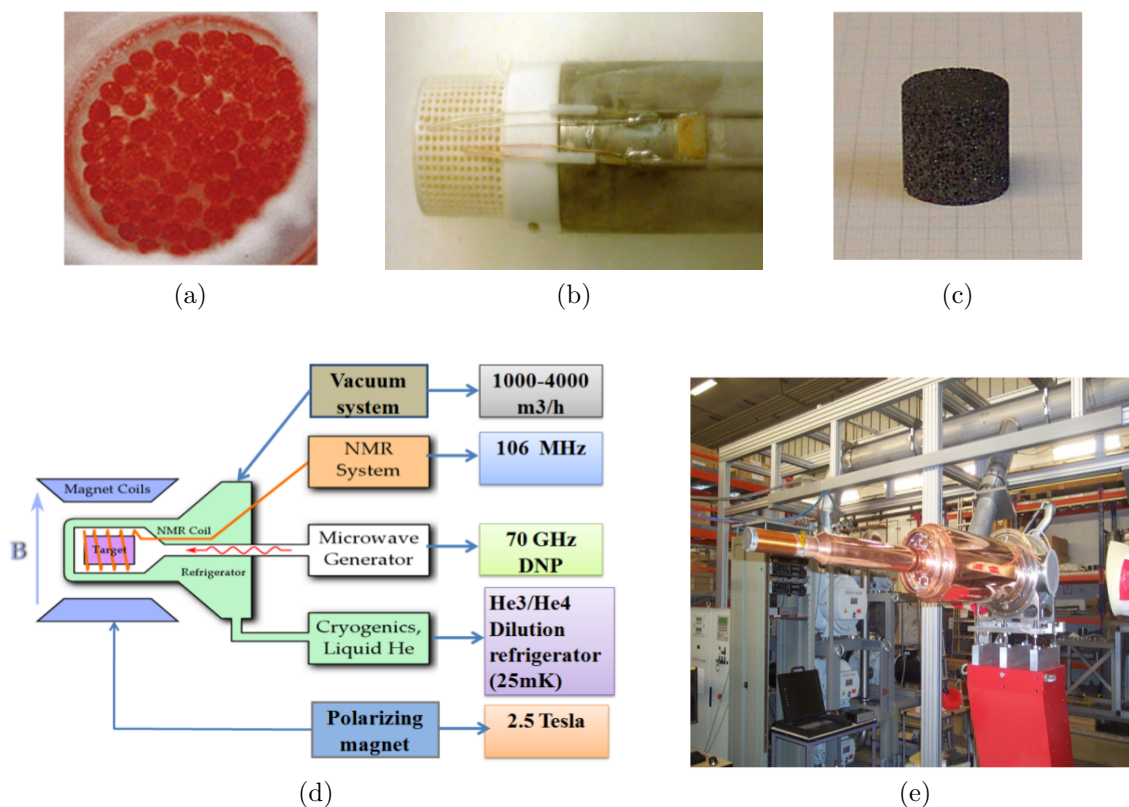


Figure 3.16: (a) Tempo doped butanol target material, (b) Target cell attached to the target insert, (c) Carbon foam target material, (d) Schematic diagram showing main components of a frozen spin target and (e) MAMI frozen spin target [50, 68].

magnetic field. At this point, microwave power is fed into the target in order to increase the degree of polarization via the DNP method. When the microwaves with a frequency of  $\nu = \nu_e - \nu_p$  (Fig. 3.17) are pumped into the target, where  $\nu_e$  and  $\nu_p$  are the Larmor frequencies of electrons and protons respectively, spin flips between the electrons and protons will transfer the polarization to the protons over time. The Larmor frequency of a proton and an electron at 2.5 Tesla are  $\nu_p = \frac{\mu_p B}{\pi \hbar} = 106$  MHz and  $\nu_e = \frac{\mu_e B}{\pi \hbar} = 70$  GHz, respectively [80].

Once the maximum degree of polarization is reached, the microwaves are switched off and the temperature is reduced to 25 mK by going into frozen spin mode (dilution refrigeration mode). At this moment, the degree of polarization is measured several

times and the average value of initial degree of polarization,  $P_i$ , is calculated. The external magnet is then removed and the superconducting internal holding magnet (Fig. 3.16d) inside the cryostat of the target provides 0.4 Tesla to maintain the target polarization in the frozen-spin mode. In this mode, the cryostat is very stable and data taking can begin. Once the polarization drops below 50%, the target needs to be repolarized. The polarization of the target can also be reversed by simply adjusting the frequency to  $\nu = \nu_e + \nu_p$ , as in Fig. 3.17, thereby populating the other level in the hyperfine splitting without changing the holding field.

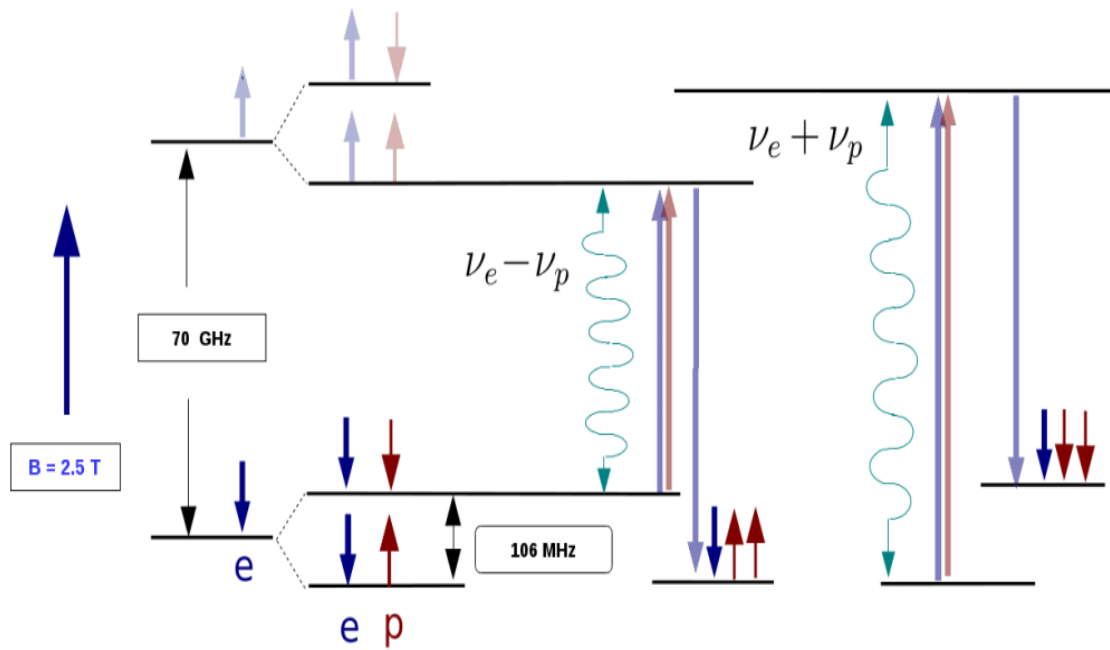


Figure 3.17: A schematic diagram of the energy levels of the coupled electron-nucleon system showing the spin flip transition when exposed to microwaves with a frequency,  $\nu = \nu_e \pm \nu_p$ . Irradiating the electrons with microwave frequency,  $\nu_e - \nu_p$ , result in positive polarization (central panel) and microwave frequency,  $\nu_e + \nu_p$ , result in negative polarization (right panel).

### 3.2.2.2 NMR System and Polarization Measurement

The degree of polarization of the target material is measured via the NMR technique. The resonance frequency for the NMR circuit is adjusted to the Larmor frequency of the particle of interest and the probability of the transition (Fig. 3.17) is measured to determine the degree of polarization. The degree of polarization is proportional to the area under the NMR signal. Target polarization measurements are not possible during data taking because the polarizing magnet and the Crystal Ball detector cannot surround the target at the same time. In addition, the magnetic field strength and homogeneity of the internal holding coil are not sufficient for a polarization measurement. Therefore, the target polarization measurements are completed at the start and end of the data taking period for separate target polarization orientations. The average value of polarization at the start and end of the positive and negative target polarization orientation,  $P_i$  and  $P_f$  are listed in Fig. 3.18. The relaxation time,  $\Delta t = t_f - t_0$ , for the target polarization can be calculated using  $P_f = P_i e^{-\frac{\Delta t}{\tau}}$ , where  $P_f$  is the polarization after a period of time  $t_f$  and  $P_i$  is the polarization at the start of data taking at time  $t_0$ . The uncertainty in the degree of target polarization is basically the result of error in  $P_i$  and  $P_f$ , and it was determined to be  $\approx 2.5\%$  for the 2014 beamtime [68].

### 3.2.3 Carbon Target

The frozen spin butanol target contains carbon and oxygen in the butanol plus liquid helium as a cryogen, and they contribute a major source of background in the experiment. In addition to the competing background from pion photoproduction off of the proton, this target allows for both coherent and incoherent Compton scattering and pion photoproduction off of these additional nuclei. Therefore, a separate data run was taken with a carbon target (Fig. 3.16c) by inserting it into the same cryostat

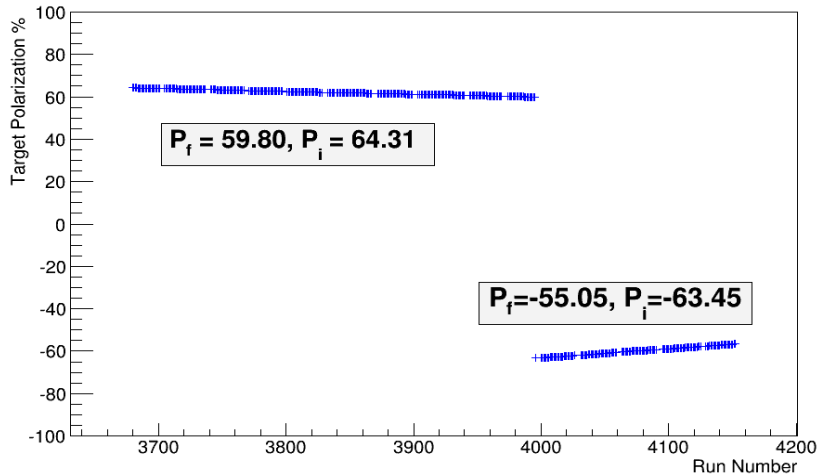


Figure 3.18: A sample plot of positive and negative target polarization for 2014 beamtime.

to account for the background subtraction. It is very important to insert the carbon target into the same target cell (Fig. 3.16b) because the subtraction removes any contribution from the windows, and/or shells of the cryostat material. This carbon target is very special because the density and length of the material is chosen in such a way that its total number of nucleons is approximately the same as the total number of non-hydrogen nucleons ( $^{12}\text{C}$  and  $^{16}\text{O}$ ) in the butanol target plus the  $^3\text{He}/^4\text{He}$  cryogen. For example, butanol ( $\text{C}_4\text{H}_9\text{OH}$ ) has four carbon atoms with 48 nucleons, one oxygen atom with 16 nucleons and 10 hydrogen atoms with 10 nucleons. The number density of non-hydrogen or heavy nucleons in the butanol target, including the contribution from 1 helium atom with 4 nucleons is

$$n_{total} = n_{bu} + n_{He} = \frac{L_{bu} \times \rho_{bu} \times N_{bu}}{M_{bu}} + \frac{L_{He} \times \rho_{He} \times N_{He}}{M_{He}}, \quad (3.7)$$

where,  $L_{bu}$  and  $L_{He}$  is the effective length of the butanol target and the helium in the refrigeration bath. The effective length of a butanol target is defined as,  $L_{bu} = L_T \times F_f$ , where,  $L_T = 2$  cm, is a length of the target cell, and  $F_f = 60.7 \pm 2\%$ ,

is a butanol filling factor. Also the effective length of helium is defined as,  $L_{He} = (L_T \times (1 - F_f)) + 0.2$  cm, (with an extra 0.2 cm to account for the additional helium in the cryostat downstream of the target cell) [50]. The total area number density of the frozen spin target is then

$$n_{total} = \frac{1.2cm \times 0.94 \frac{g}{cm^3} \times 64}{74.1 \frac{g}{mol}} + \frac{1.0cm \times 0.14 \frac{g}{cm^3} \times 4}{4.0 \frac{g}{mol}} = 1.11 \text{ mol cm}^{-2}. \quad (3.8)$$

By using the density of the carbon foam as measured at MAMI,  $\rho = 0.53$  gm cm<sup>-3</sup>, and setting the number density of the carbon equal to the number density of butanol as obtained in Equation 3.8, we can find the desired length of the carbon target as,

$$L_C = \frac{n_C \times M_C}{N_C \times \rho_C} = \frac{1.11 \frac{mol}{cm^2} \times 12.01 \frac{g}{mol}}{0.53 \frac{g}{cm^3} \times 12} = 2.10 \text{ cm}, \quad (3.9)$$

This shows that the choice of 2 cm target length of carbon target material is reasonable to match the total number of nucleons but not sufficient. To address this 5% discrepancy as well as other factors related to the nuclear physics of C vs O, He nuclei, an extra scaling factor can be determined to directly subtract carbon target from the butanol target runs (Sec. 6.2.2).

### 3.3 A2 Data Acquisition and Trigger System

The analog signals that are produced in the PhotoMultiplier Tubes (PMTs) of all detector systems are converted to useful information by digitizing the output signal with the help of electronics. The digitization procedure involves the transformation of time into a digital form via Time to Digital Converter (TDC), and amplitude of the various signals via Analog to Digital Converter (ADC), and a discriminated input to

a logic circuit which triggers the event readout. The Data AcQuisition (DAQ) system collects information from the sub-systems like the tagger, CB, TAPS and stores them to digital files. The DAQ system is always occupied when it is busy writing an event, and during this time it cannot record another event (dead time). In order to reduce the burden of the DAQ with unwanted events produced at very low thresholds, and to keep the dead time of the detector system at a reasonable level, a multi-level trigger system has been implemented. In general, the trigger system reduces the recording of unwanted events to a minimum and acts as an online filter to decide whether an event is accepted or rejected.

The A2 DAQ and trigger systems were upgraded in 2013 to allow for higher data throughput. The upgrade included a complete integration of the TAPS forward angle calorimeter into the general DAQ scheme. The main A2 experimental trigger system, which consists of TAPS master, CB multiplicity and Moeller trigger, is shown in Fig. 3.19. The CB experimental trigger and its sub-components are shown in Appendix A. The A2 master consists of input section, Trigger Level Sections (TLS) L1 and TLS L2, and end section. The first level signal (e.g., CB Esum) enters the system at point “A”, as in Fig. A.1 and the second level signal (e.g., Multiplicity: M0 and Coplanarity: CB, PID, TAPS, Veto) enters somewhat later at point “B”. At point “C”, the decision will be made on which experiment will trigger the signal. The reader is referred to [82] for detailed information. During the 2014 beamtime, CB Esum was used as a first level trigger (L1 trigger), accepting events with any multiplicity in second level (L2 trigger). While, during the 2015 beamtime in addition to CB Esum, TAPS pulser was used as a first level trigger.



### 3.3.1 Data Acquisition Software:AcquDAQ

AcquDAQ is a C++ based data acquisition software, developed by John Anand [83] using the software libraries available in the CERN ROOT and used within the Mainz A2 collaboration. The DAQ system provides slow-control and event-by-event readout of the photon tagger, the CB electromagnetic calorimeter, central MWPC tracker, plastic-scintillator PID systems and the TAPS forward-angle calorimeter. A variety of front-end controllers are supported, reading data from VMEbus (Versa Module Europa bus) , FASTBUS and Computer-Aided Measurement And Control (CAMAC) systems. AcquDAQ also provides an interface to configure and control the Mainz programmable trigger system, which uses Field Programmable Gate Array (FPGA) hardware.

### 3.3.2 CB Esum Trigger System

The CB Esum trigger is based on the the total energy deposited in the Crystal Ball elements. It is formed by summing up all analog signals from the photomultiplier tubes coupled to each NaI crystal. The summed analog signal is split into two parts and passed through the first discriminator with a low threshold and the second discriminator with a high threshold. The low threshold forms a first level trigger condition which initiates a CB trigger signal and inhibits the system from accepting more signals. The high threshold forms the final Esum experimental trigger. If the energy sum signal passes both thresholds, the information from all CB ADCs and TDCs are read out and stored, after which the system is un-inhibited. If the energy sum signal passes the low threshold but not the high threshold, a “fast clear” signal is passed to all CB ADCs and TDCs. This resets the hardware and un-inhibits the system. For the 2014 beamtime, the trigger was set for  $E_{\text{sum}} > 40$  MeV, thereby rejecting any event that did not deposit at least 40 MeV into the NaI and for 2015 beamtime,

the trigger was set for  $E_{\text{sum}} > 90$  MeV, thereby rejecting any event that did not deposit at least 90 MeV into the NaI. An overview of the experimental trigger and its components is given in Appendix A with further details provided in [84, 85, 86].

### 3.3.3 Multiplicity Trigger

The multiplicity trigger contains information on the total number of detected particles in the CB and TAPS sectors and feeds it to the TLS L2 stage (Fig. A.1). It was done by summing individual NaI signals into groups of sixteen and individual BaF<sub>2</sub> signals into group of six, and requiring that one or more such groups pass a threshold of around 40 MeV in CB and 15 MeV in TAPS. For this experiment, during both the 2014 and 2015 beamtime, it was decided to run with the simple Esum trigger accepting events with any multiplicity.

### 3.3.4 Tagger Trigger

The analog signal from each PMT of the tagger FPD is fed into the main rack of the tagger electronics featuring an amplifier/discriminator and a coincidence unit, which produces an AND signal between neighbouring scintillators. The logic OR of all 352 channels is supplied to the main experimental trigger logic unit. Unlike in the old setup (before October 2013), the separate trigger system has been removed and the tagger trigger is now implemented in the central experimental trigger.

### 3.3.5 Readout

When the required L2 trigger conditions are met, ADC and TDC information from all the detector elements are read out by AcqDAQ. The readout for various detectors systems will be discussed in the following section.

### 3.3.5.1 Tagger Readout

The tagger readout is based entirely on whether individual focal plane scintillator elements are hit or not. When scintillation occurs in a focal plane element and the signal is above a preset discriminator threshold for that particular channel, the logic pulse output from the discriminator is delayed and then fed to multi-hit CATCH (Compass, Accumulation, Transfer and Control Hardware) TDCs, which were originally designed for use in the COMPASS experiment to record the timing for that event. Unlike standard TDCs which have a start or stop signal, CATCH TDCs have a free running continuous clock which oscillates at a frequency of 10 GHz with a 117 ps/channel conversion rate [84]. All of the CATCH TDCs have their oscillators synchronized through a Trigger Control System (TCS) module, designed at CERN. This allows an entire batch of these modules to have one reference TDC that the trigger is read into, providing a reference count of the oscillator. When an event passes the experimental trigger conditions, the oscillator value of the reference TDC is recorded. If any of the other TDCs record a hit, the relevant oscillator value is stored. To obtain the timing information for each hit, the reference TDC value is then subtracted from the oscillator value, and converted to a time using the 117 ps/channel conversion rate. The CATCH TDCs are able to record the oscillator values of several hits, with a timing resolution between two pulses of 20 ns, before the event is read out. The ability to handle multiple hits therefore reduces the dead-time of the system. Additionally, the split signal coming from the tagger PMTs is also sent to a FASTBUS scaler unit, which then counts the total number of tagged electrons.

### 3.3.5.2 CB, PID and MWPC Readout

The NaI, PID, and MWPC use CATCH TDCs to digitize the timing signal. In the CB, 16 adjacent NaI crystals form a logical group and their signals are handled

groupwise. In a first step, the signals from the PMTs are led to a splitter, which produces two parts of the signals. While the PID is read out into traditional ADCs, the NaI and MWPC detectors are read into Sampling ADCs (SADCs). These SADCs sample the inputs at a rate of 40 MHz and maintain a buffer of these samples for 2  $\mu$ s period [82, 84]. Here, the time intervals corresponding to the three different regions of each sample: a section before a pulse, the majority of the pulse itself, and a section of the pulse tail were integrated. The combination of the first two provides automatic pedestal suppression, by removing the baseline from the peak and requiring the remaining signal to be above threshold. Since the pedestal is subtracted online event-by-event, a calibration of the pedestal position is not necessary in the afterward offline calibration for the CB ADCs.

The second of the split signals is sent to a Leading-Edge Discriminator (LED) and the signals are checked against the two thresholds. If the signal passes the lower threshold, the corresponding time information is converted by a CATCH TDC. The high threshold discriminator information is used to check the particle multiplicity in a later step. The signals from the 24 PID elements are also split and one part is delayed and then integrated by ADCs, whereas the second part is sent to a discriminator and then to CATCH TDCs for the time digitization.

### 3.3.5.3 TAPS and Veto Readout

The TAPS trigger system was upgraded to use the VME Universal Logic Modules (VUPROM) in a manner similar to the main experimental trigger. VUPROM control classes in AcquDAQ have been extended to account for the TAPS trigger. TAPS ADC/TDC modules are configured and readout by AcquDAQ. The analog signal from the BaF<sub>2</sub> crystals is sent to two discriminators, a lower Constant Fraction Discriminator (CFD) and a higher threshold Leading Edge Discriminator (LED). The signals

which are above the CFD threshold of 3 MeV (just above the noise level) and LED threshold of 30 MeV provide a signature of a hit in the crystal. It gives the the start signal for energy integration in both long and short gate ADCs to take into account the two scintillation light components of the BaF<sub>2</sub> crystals, and for the time measurement in the TDC. Two LEDs, LED1 and LED2 per channel can be used for trigger purposes. If the signal is above the LED threshold, it is sent to the main trigger system and can contribute to the multiplicity trigger. On a positive trigger decision, the digitized energy and time informations are sent to the storage computers.

#### **3.3.5.4 Scalers**

As discussed in Sec. 3.1.2.1, the analog signal from the FPD PMTs is fed to the tagger electronics via a discriminator and a coincidence unit. If the signal passes the discriminators, a logical pulse is sent to TDC which records the timing of the multiple hits per event. In addition, the signals are sent to the FASTBUS scalers which count the total number of hits in the FPD elements and are read out once in every 1000 events. During the experiment, the photon flux is derived from these tagger electron scalers. These scalers are in principle free-running, but are gated with an inhibit signal from the tagger DAQ busy signals. This means the system remains inhibited until either a fast clear signal is delivered or the trigger passes the experimental trigger threshold and the event is read out. The inhibit-gated scaler counts are not automatically corrected for the live time of the tagger DAQ system because the dead time effects in the DAQ systems are canceled as the tagger scalers are disabled while the system is busy.

## Chapter 4

# Analysis Software and Detector Calibration

In this chapter, the various data analysis software packages: AcquRoot [83], Calib [66], GoAT [51] and A2Geant [87], along with the different stages involved in extraction of events of specific reaction channel and calibration of individual detector elements are described. The raw signals from the detectors are converted into real physical units, i.e. time in nanoseconds, energy in MeV, and azimuthal ( $\phi$ ) and polar ( $\theta$ ) angles in radians via calibration. These calibrated values, in combination with a clustering-pattern recognition algorithm, were used in the analysis package AcquRoot to decode raw Time-to-Digital Converter (TDC) and Analog-to-Digital Converter (ADC) information into particle tracks, and a user-specific physics reconstruction code GoAT to perform particle identification and data sorting.

## 4.1 Analysis Software

### 4.1.1 AcquRoot

AcquRoot is an object oriented data analysis framework written in the C++ programming language using the software libraries available in the ROOT toolkit. It comprises two parts: AcquDAQ for data acquisition, and AcquRoot for online and offline data analysis. AcquRoot processes the raw ADC and TDC data produced by AcquDAQ for each detector system, converting it into meaningful kinematic information of the detected particles. It also contains a hierarchy of classes that first decode the ADC and TDC information of the CB-TAPS detector system and then provides energy and timing information associated with an element of the detector system. A user-specific physics reconstruction code is then used to perform analyses relating to specific reaction channels, such as the event selection techniques described in the following section.

### 4.1.2 CaLib

The offline calibration of all detector elements is done using the CaLib software designed by the University of Basel group, which uses the AcquRoot physics class called TA2MyCaLib to analyze actual data files with a rough set of calibration parameters. The root files produced by this physics class are examined in CaLib with a Graphical User Interface (GUI) macro resulting in new calibration parameters like gains, thresholds, etc. and written to the SQL database in Mainz. This SQL database was accessed from Regina via Virtual Private Network (VPN) during the data analysis. The calibration information is stored in the setup files, which are loaded by AcquRoot on start-up. The data can be either divided into various sets, depending on the time frame and experimental conditions, to calibrate independently or merge and calibrate

together to obtain the best result. For some detectors, calibration parameters are determined from the analysis of a combination of several detector elements at once. Because of this, in some cases only a single pass through the data is required, but in others, the process is iterated several times producing new calibration parameters to re-analyze the data each time. As the calibrations for many detectors depend on each other, it has to be completed in a specific order. The calibration task was distributed between the author and a colleague Ali Rajabi from the University of Massachusetts. The calibrations performed specifically by the author on the 2014 carbon beamtime and on both the 2015 butanol and carbon beamtimes are given in more detail in Sec. 4.3.

### 4.1.3 GoAT

The GoAT (Generation of Analysis Trees) software designed by C. Collicott is a C++ based analysis framework that uses a AcqRoot physics class called TA2GoAT to produce ROOT trees with all detector information. The TA2GoAT physics class is linked to the CaLib database via a SQL access class, which makes it possible to access and include calibration information from the CaLib database to the output ROOT trees. GoAT actually collects particle track information from Crystal Ball and TAPS, and stores the energy, time and angular information of the particle. Additionally, it also stores the trigger, detector hits, and photon polarization information. The output ROOT trees from AcqRoot, containing full event-by-event information, is fed as an input and run in GoAT, which then provides the method for particle identification and data sorting. Within GoAT, once the particle tracks are identified, they can be combined to reconstruct mesons. Finally, after the sorting of the required reaction channel, data analysis was completed using a user physics class called MYPHYSICS written by the author, which was incorporated in GoAT.

#### 4.1.4 A2Geant

The Monte Carlo event generator named ‘EventGen’, written by P. Martel [50], based on theoretical Compton and  $\pi^0$  cross sections was used to generate a large number of pseudo-events which serve as an input for A2Geant. EventGen simply generates pseudo events based on theoretical cross sections, for example, it utilizes the dispersion code of Pasquini et al. [17, 45] to generate Compton scattering cross sections. EventGen does not take into account interactions between the particles and the experimental setup resulting in energy loss and/or multiple scattering in the Frozen Spin Target cryostat, as well as the electromagnetic showers and energy smearing in the detectors themselves. To study these effects, A2Geant software was developed by colleagues from the University of Edinburgh, which is written in C++ using the CERN Geant4 simulation library [88] where all features of the detector setup and target are modeled in a virtual detector setup. The A2Geant program tracks the reaction products through the virtual detector setup, where they interact with the detector materials. The energy deposition in the detector components is registered and stored in binary files, which are then analyzed with AcqRoot. These files were analyzed using the exact same physics class used for analyzing experimental data to test the reconstruction efficiency.

## 4.2 Detector Cluster Algorithm

When a particle hits the detector, it produces an electromagnetic shower. Depending on the particle and its energy, the shower then induces a signal, not just in one crystal, but in a group of adjacent crystals. In order to reconstruct the energy and direction of the detected particle, the detector signals originating from the same shower have to be found and grouped into a so-called cluster. Clusters were identified as photons in

the Crystal Ball detector with the aid of the PID and similarly in TAPS with the aid of the TAPS Veto. In addition to the conventional  $\Delta E/E$  (energy deposition in the PID/CB) separation, the azimuthal angle of the Crystal Ball cluster was compared with the  $\phi$ -angle of a hit in a PID element. If the difference between the angles of the cluster and the PID hit was less than about  $15^\circ$ , the cluster was identified as a charged particle based on detector resolution. All other clusters were taken to be photons. This angular limit was determined by taking into account the number of PID elements and the reaction vertex distribution due to the finite beam spot size on the target.

Clusters in either CB or TAPS are formed by an iterative algorithm called the clustering algorithm. The cluster search process starts by finding the list of detector hits that passed the LED cluster threshold (2 MeV) in CB and the CFD cluster threshold (3 MeV) in TAPS, and sorted then according to their energy. The element with maximum energy was marked as the center of a cluster and its TDC information was taken as the corresponding particle time. Afterwards, hits within the surrounding crystals were marked as neighbours. If their energies were above the threshold, the corresponding elements were added to the cluster and removed from the list of hits. This was very important to avoid the contribution of one crystal in more than one cluster. This process continued until all hits in the crystals were assigned to a cluster. The topology of a NaI crystal in a cluster of the Crystal Ball has 12 defined neighbours (Fig. 4.1a), and BaF<sub>2</sub> crystal in a cluster of the TAPS has six defined neighbours (Fig. 4.1b).

The total energy of the cluster is determined by summing the energies of the central element and the energy of all neighbouring elements, and the position of the

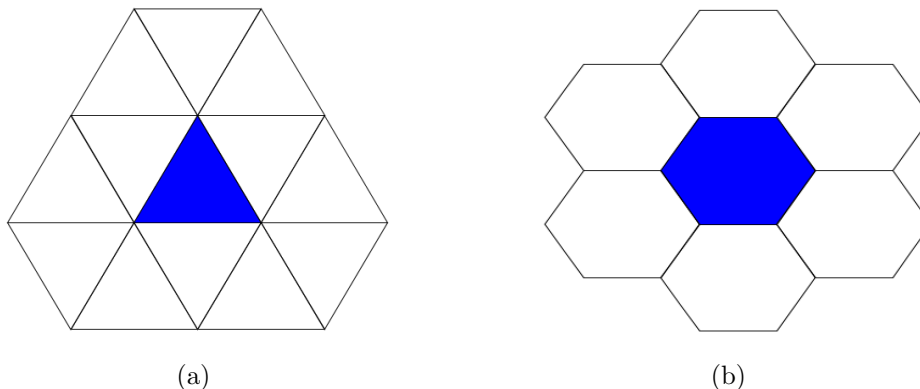


Figure 4.1: (a) 12 NaI nearest neighbors of an element for clustering algorithm. (b) six BaF<sub>2</sub> nearest neighbors of an element for clustering algorithm.

cluster is obtained via a  $\sqrt{E}$  weighted average of the crystal positions as shown here:

$$E_{tot} = \sum_i E_i \quad \text{and} \quad \vec{r}_{tot} = \frac{\sum_i \vec{r}_i \sqrt{E_i}}{\sum_i \sqrt{E_i}}. \quad (4.1)$$

Once a cluster has been determined, a cluster energy threshold is applied such that any clusters that fall below a minimum energy deposition are discarded. For both the Crystal Ball and TAPS, a 15-MeV cluster threshold has been applied.

### 4.3 Calibration of the detectors

In order to perform a data analysis, the detector systems and their components must be calibrated to output useful and meaningful physics information from the raw data taken at the experimental facility. While the analog signal from each photomultiplier tube coupled to each detector element is fed into an ADC and a TDC, the aim of the calibration process is to digitize ADCs and TDCs in terms of energy and time. The physical positions of detectors do not change unless a detector is found to be defective (there were no issues during either the 2014 or 2015 beamtimes). However,

some changes are made on purpose to improve the experimental conditions, and change in temperature in the experimental hall can sometimes not be avoided and might influence the detectors. The calibration procedure has to take into account all instabilities of the most important quantities like the neutral pion peak position in the invariant mass of the two detected photons.

### 4.3.1 Calibration Run-Sets

The time dependence of calibrations need to be checked for each data run to investigate the stability of data. The time of hit for all detector elements is summed together and a Gaussian function is fit to establish the overall peak position for a given run number. The variation in reconstructed peak time position for each detector, CB, PID, TAPS is minimal (less than 0.1 ns), and therefore only one data set was created for time calibration during both the 2014 and 2015 beamtimes. A sample CB time with respect to run number from the 2015 butanol beamtime is shown in Fig. 4.2a. However, the variation in invariant mass peak position for the CB was significant. Therefore, distinct run sets for positively and negatively polarized butanol as well as carbon target beamtime are made for both 2014 and 2015 beamtime (a sample  $\pi^0$  invariant mass peak position with respect to run number is shown in Fig. 4.2b) and the calibration for each is completed separately.

### 4.3.2 Time Calibration

The main principle of the time calibration is that the time difference between either of the two decay photons from  $\pi^0$  photoproduction or a photon and a proton for the Compton scattering should be zero. This time information for every detector hit can be measured by using TDCs. The different detectors used in this experiment have different time measurement procedures based on where the start and stop signals

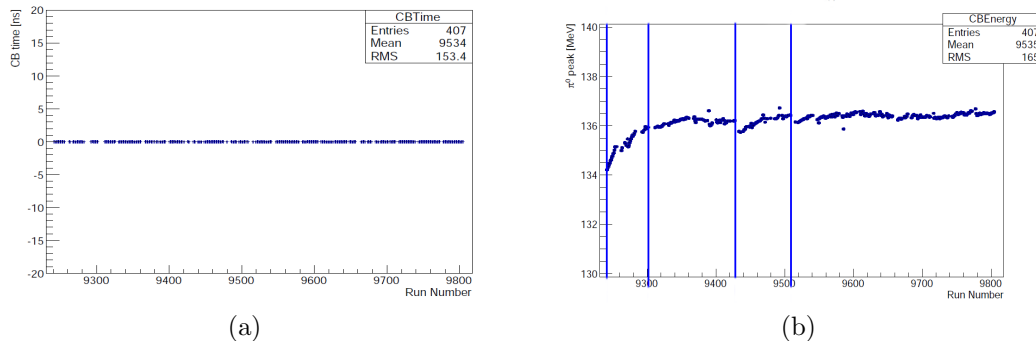


Figure 4.2: (a) A sample run-set of CB time with respect to run number from the 2015 butanol beamtime. (b) A sample  $\pi^0$  invariant mass peak position with respect to run number from the 2015 butanol beamtime.

come from. For CB, Tagger and PID detectors, TDCs are started by the trigger and are stopped by the signal coming from individual detectors, i.e.  $t = t_{trigger} - t_{detector}$ , whereas for TAPS and Veto detectors, the reverse is true, i.e.  $t = t_{detector} - t_{trigger}$ . When these start and stop signals are provided, TDCs map the time spread to a discrete channel value. The relation between the physical time ( $t$ ), conversion gain ( $g$  ns/channel), channel number ( $c$ ) and channel offset  $o$  is given by  $t = g(c - o)$  [89]. Therefore, the primary goal of the time calibration is to find the values  $g$  and  $o$  for a given set of runs. Since the TDCs have an intrinsic conversion gain, only the offsets are determined on an element by element basis. To determine these offsets, the timing spectrum of each detector element is fitted with a Gaussian and from the resulting mean values, the new individual offsets are calculated using the relation  $o_{new} = o_{old} \frac{Mean}{Gain}$  [50],

### 4.3.3 Energy Calibration

The energy calibration has two stages. First, we match the PMT gains to low energy photons via the potentiometer of the PMT voltage. Second, apply an iteration method reconstructing  $\pi^0$  from two measured photons. This section summarizes the iterative

method that involves reconstruction of invariant mass of the two photons from  $\pi^0 \rightarrow \gamma\gamma$  decay. As the mass of the  $\pi^0$  is well known, its decay into two photons provides a very good technique to calibrate the detector energy. The energy information for every detector hit can be obtained by using ADC channels. In principle, the ADC measures the amount of charge in a given PMT pulse by integrating the electronic signals from the photo-multipliers, and returning a digital channel number,  $c$ . The amount of charge is almost directly proportional to the deposited energy,  $E_{dep}$ , of the measured particle. The relation between the deposited energy,  $E_{dep}$ , in MeV, conversion gain,  $g$  in MeV/channel, channel number,  $c$ , and pedestal position (zero energy),  $p$ , is given by  $E_{dep} = g(c - p)$  [66].

Thus, the goal of the energy calibration is to find correct values for these constants  $g$  and  $p$ . The pedestal,  $p$ , corresponds to the channel that has zero energy value and was set properly before the experiment so the only task is to adjust the conversion gains. To determine these gains,  $g$ , the invariant mass,  $M_{\gamma\gamma}$ , of the  $\pi^0$  meson is reconstructed from the decay into two photons and a Gaussian function is fitted. The mean value of the  $\pi^0$  peak position in the invariant mass spectrum is used to determine the new gain factor out of old gain using the relation  $g_{new} = g_{old} \frac{m_{\pi^0}^2}{mean^2}$  [50]. This process is iterated several times until the invariant mass is aligned at the mass of neutral pion for all of the crystals.

#### 4.3.4 CB Time Calibration

The conversion gain  $g$  of the TDCs used in the NaI detectors have a fixed value of 117 ps/channel [50]. Therefore, only the offset  $o$  has to be determined. We need to identify the cluster pair in the NaI detectors of the CB and then, for each identified pair, the NaI element is plotted versus the difference in the cluster time between the two hits in the central element of each cluster, as in Fig. 4.3a. A projection of the

individual NaI time is shown in Fig. 4.3b. After 15 iterations, the time difference between crystal pairs is aligned to zero.

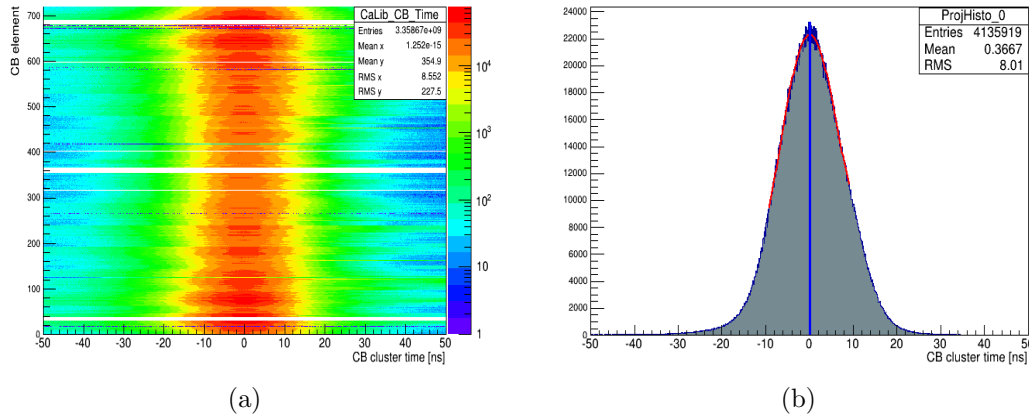


Figure 4.3: (a) The spectrum of the time difference between two neutral hits identified as a cluster pair for all 672 CB elements. (b) The projection for a single element.

### 4.3.5 CB Time-walk Correction Calibration

The TDCs that are used with the CB are started by the trigger. Due to the variation of pulse size in the crystals, the time of the event which causes the triggering, depends on the energy of the particle that is triggered. The energy of the particle is converted via an ADC, and the time taken for the ADC signal to pass the experimental threshold depends on the signal amplitude. NaI crystals have typical characteristic features of relatively slow rise times of signals, and thus a strong energy dependence of the time measurement. Thus, hits with higher energies have a steeper rise in the electronic signal and consequently a smaller time difference  $\Delta T$  between the rise of the signal to the crossing of the threshold and this effect is called “time-walk effect”. A schematic of this effect is shown in Fig. 4.4. A correction has to be applied to account for this time difference between the signals reaching the discriminator level.

The main principle to establish the time-walk correction is to plot the time versus the energy for every detector element and the slices of the two dimensional spectra

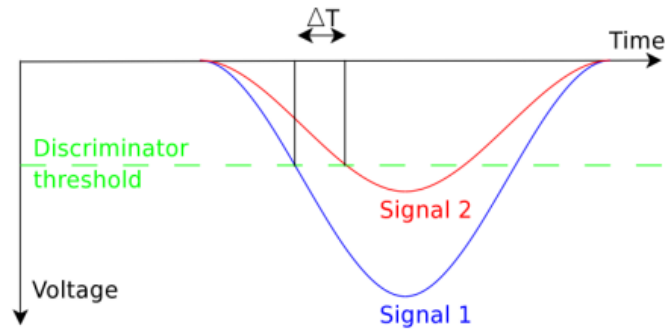


Figure 4.4: Schematic CB Time Walk. Two signals with the same peak value but reaching the discriminator level at different times.

are then fitted with a Gaussian. So, we first identify two cluster events in the NaI detectors and the time difference between the NaI detector time and Tagger detector time is calculated. In order to have a cleaner signal, only  $\pi^0$  events are selected and additional cuts on the invariant mass and missing mass of the  $\pi^0$  have been applied. For those cluster events that pass these invariant mass and timing conditions, the energy and the time difference are filled into a histogram, as in Fig. 4.5a, and then fitted with a Gaussian function. The peak positions for different energies are plotted as blue dots and the resulting behavior can then be again fitted by using the function from  $t(E_{dep}) = a + \frac{b}{(E_{dep}+c)^d}$ , as in Fig. 4.5b. These parameters  $a$ ,  $b$ ,  $c$  and  $d$  are individually determined for all detector elements [90].

### 4.3.6 CB Energy Calibration

The CB energy calibration aligns the  $2\gamma$  invariant mass peak at the mass of  $\pi^0$  meson. We identify the cluster pair in the NaI detectors and then, for each identified pair, the invariant mass of the two photon candidates from  $\pi^0$  photo-production in the CB is plotted against the central element of each of the cluster, as in Fig. 4.6a. A projection of the individual NaI energies is shown in Fig. 4.6b. After several iterations, the reconstructed invariant mass peak position for three sets of positively polarized

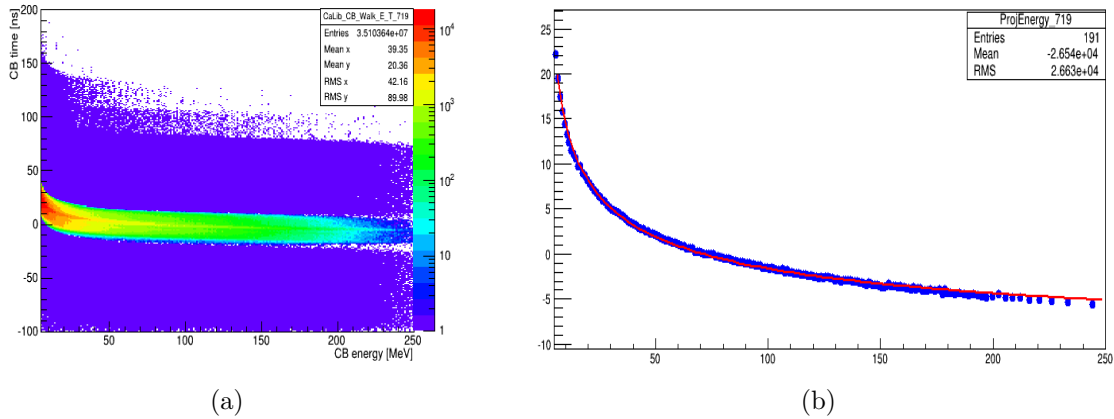


Figure 4.5: (a) CB time depending on deposited energy showing the time-walk effect. (b) The peak position for different energy slices plotted as a blue dots and the behaviors is fitted with the function defined above.

target and one set of negatively polarized target data sets are aligned at the  $\pi^0$  mass.

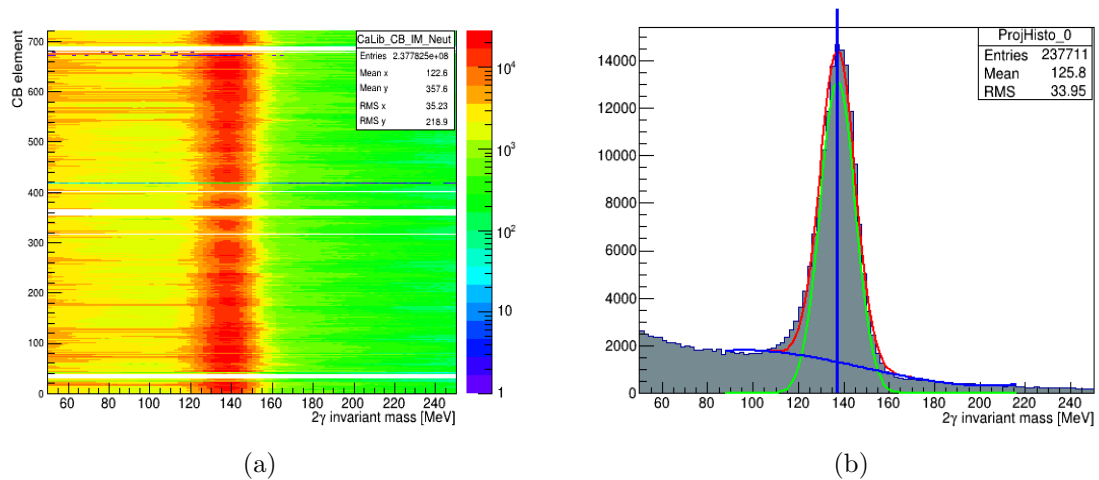


Figure 4.6: (a) The invariant mass spectrum for two neutral hits identified as a cluster pair for all 672 CB elements. (b) The projection for a single element.

### 4.3.7 TAPS Time Calibration

The conversion gain  $g$  of the TDCs used in BaF<sub>2</sub> detectors have a fixed value of 50 ps/channel [50]. Therefore, only the offset  $o$  has to be determined. The TDC offsets are determined in an identical way to the CB where we identify the cluster pair in the BaF<sub>2</sub> detectors of the TAPS and then, for each identified pair of BaF<sub>2</sub> element, the time difference is plotted between the two hits in central element of each cluster as in Fig. 4.7a. A projection of the individual TAPS time is shown in Fig. 4.7b.

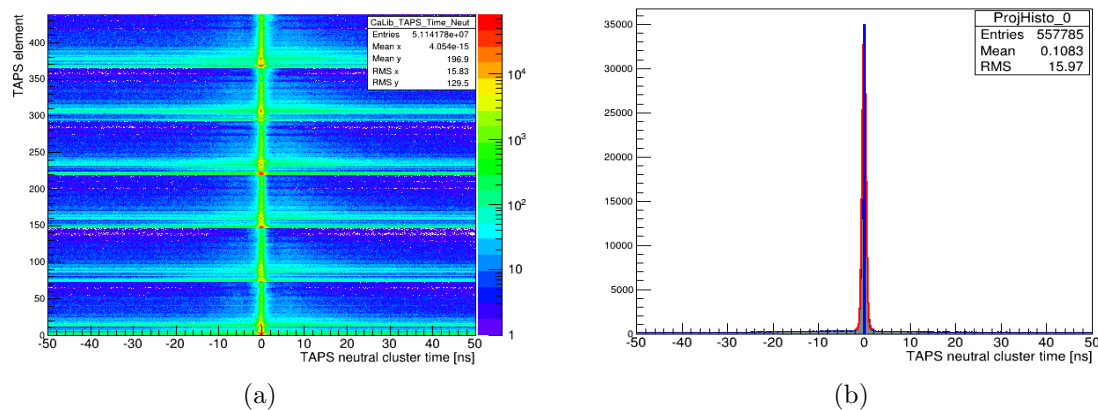


Figure 4.7: (a) The spectrum of the time difference between two neutral hits identified as a cluster pair for all 366 TAPS elements. (b) The projection for a single element.

### 4.3.8 TAPS Long-Gate Energy Calibration

The BaF<sub>2</sub> analog signal has two different ADCs, one with a long and the other with a short integration gate and hence are called Long Gate (LG), and Short Gate (SG). The LG integrates the entire analog signal similar to NaI ADCs and gives the correct gains for all the TAPS crystals. For LG Energy calibration, events with two neutral clusters in the BaF<sub>2</sub> are selected and the neutrality of the cluster is determined by examining the hits in the veto detectors in front of them. For each identified neutral cluster, the BaF<sub>2</sub> hit versus the invariant mass is plotted for the central element. The

histogram of invariant mass peak position for all BaF<sub>2</sub> elements is shown in Fig. 4.8a and an example fit to a single element is shown in Fig. 4.8b.

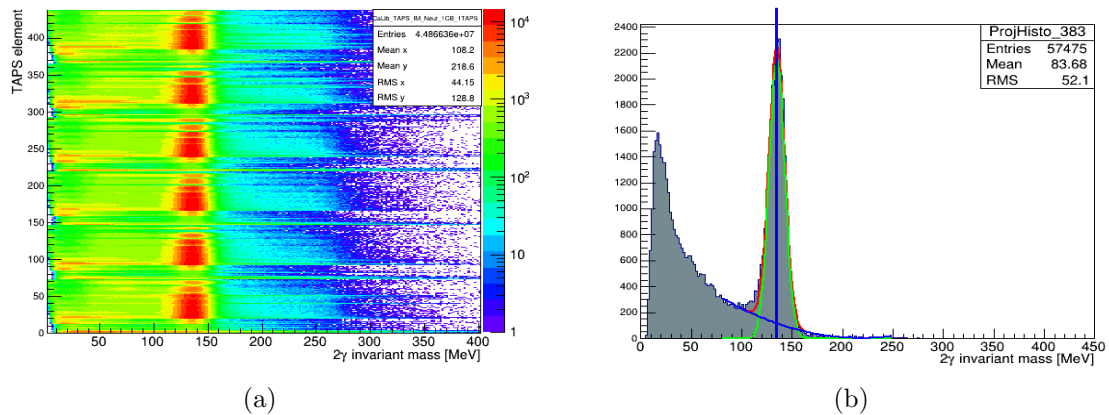


Figure 4.8: (a) The invariant mass spectrum for one neutral hit in NaI and one for all 366 TAPS elements. (b) The projection for a single element.

### 4.3.9 TAPS Short-Gate Energy Calibration

A typical characteristic feature of a BaF<sub>2</sub> crystal is that it has two scintillation light components. In order to account for these two scintillation components, we perform a separate SG energy calibration. The main principle of the SG energy is the discrimination of nucleons and photons in the TAPS detector. Since nucleons and photons deposit their energies through different mechanisms, the portions of the two scintillation light components vary. Furthermore, the timing response of the BaF<sub>2</sub> crystals is significantly different for photons and nucleons. The SG energy calibration uses Pulse Shape Analysis (PSA) techniques, where only a part from nucleon and most from photon analog signal will be integrated to account for the two scintillation light components. The PSA angle and radius can then be calculated from the two components  $\phi_{PSA} = \tan^{-1} \frac{E_{SG}}{E_{LG}}$  and  $r_{PSA} = \sqrt{E_{SG}^2 + E_{LG}^2}$  [90].

The PSA radius vs PSA angle plot has characteristic band-like structures and thus allows the discrimination of the photons and nucleons, as in Fig. 4.9a. Nucleons are

located below  $\phi_{PSA}=45$  degrees, while the photons are distributed around 45 degrees for all radii. For the photon, whose response in BaF<sub>2</sub> is relatively fast, the energy from the SG ADC will be very close to the energy from the LG ADC, therefore the PSA angle should be 45 degrees. The SG energy calibration aims to shift the photons to  $\phi_{PSA} = 45^\circ$ .

For the calibration process, we identify the central elements of the cluster in BaF<sub>2</sub> and, for each cluster detected, a pulse shape analysis is reconstructed for a narrow and wide integration window, producing a PSA radius and PSA angle as in Fig. 4.9a. The two different PSA radius intervals have been chosen, one at high and the other at the low radii. For both intervals, the projections onto the  $\phi_{PSA}$  axis were fitted with a Gaussian and based on the two mean PSA-radii and the two PSA-angles, new gains are calculated using the condition  $E_{short} = E_{long}$ . An example PSA fit for a single BaF<sub>2</sub> element with wide integration window is shown in Fig. 4.9b. For PSA angle and PSA radius, there are two equations and two unknown variables so we expect one analytic solution, but due to systematic errors in the fitting procedure, several iterations had to be performed until convergence was reached.

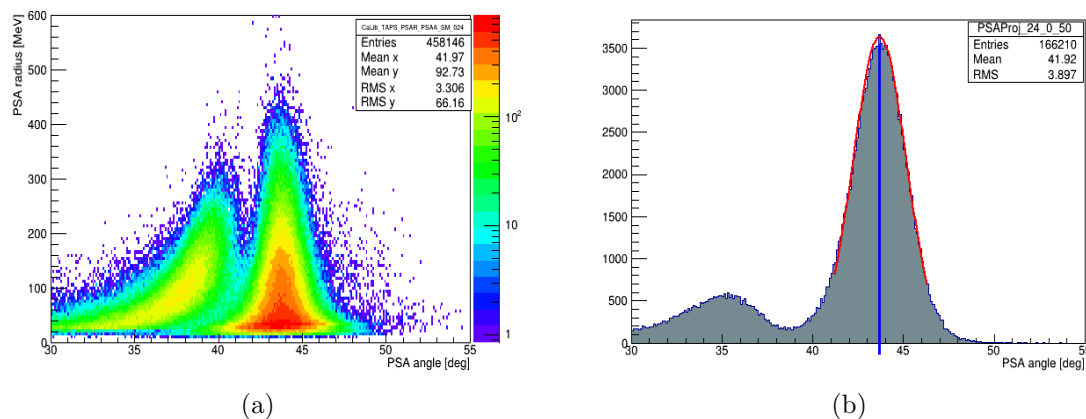


Figure 4.9: (a) TAPS PSA radius vs angle. Nucleons are located in below 45 degrees, while photons are distributed around 45 degrees for all radii. (b) Sample fit to the PSA angle for channel 306 with wide integration window.

### 4.3.10 Tagger Time Calibration

The conversion gain  $g$  of the TDCs used in the Tagger detectors also have a fixed value of 117 ps/channel [50], so only the TDC offsets are determined in the same way as for the NaI detectors of the CB. For all combinations of neutral particles in TAPS and hits in the Tagger, the time differences between the Tagger and the TAPS elements were plotted for all the activated Tagger elements, as in Fig. 4.10a. The coincidence time peak was fitted with a Gaussian in order to determine the peak positions and new offsets were calculated. A projection of the individual Tagger time is shown in Fig. 4.10b. The upper sections of focal plane detectors (above Tagger channel 220 during the 2014 beamtime and above Tagger channel 180 during the 2015 beamtimes) which corresponds to lowest photon energies, were turned off to allow higher DAQ livetime at high rates.

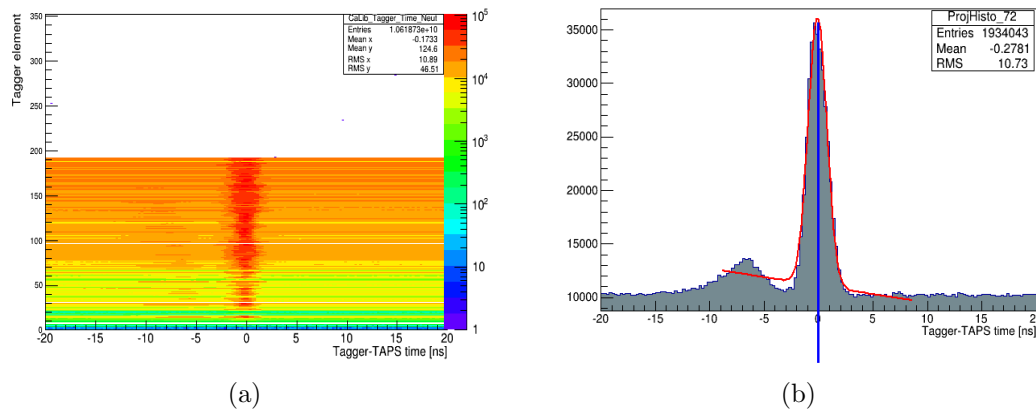


Figure 4.10: (a) The spectrum of the time difference between a hit in Tagger and a hit in TAPS for all the combinations of neutral particles. (b) The projection for a single element.

### 4.3.11 Target Position

The position of the target with respect to the NaI is calibrated by identifying each pair of neutral events that hit the detectors. For each pair of neutral events, the

invariant mass is calculated for various positions of the target center, as in Fig. 4.11a. The target position can be determined by adjusting those various positions of the target to minimize the width of invariant mass peak and the projections of this for each target position bin are fitted with a Gaussian, as in Fig. 4.11b. The sigma of the Gaussian fit has its minimum value at the actual center and these values are obtained separately for different data sets. The reconstructed target center values were used in the simulation.

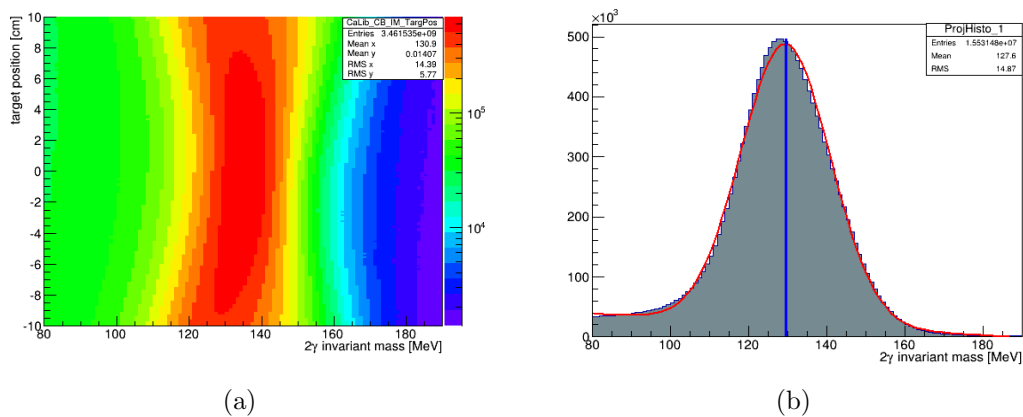


Figure 4.11: (a) The spectrum of the all the hit positions in target, (b) The projection for a single element.

### 4.3.12 PID Azimuthal Angle Calibration

The PIDs are used for detection and identification of charged particles, so the proper alignment with respect to the hit in the NaI detector needs to be determined. Events which have one hit in CB and one hit in PID are selected and then the azimuthal angle of a NaI cluster hit as a function of the PID element is plotted as shown in Fig. 4.12a. The final azimuthal position of each PID element is then extracted by fitting a Gaussian to the projection for each element, as in Fig. 4.12b, and then fitting a line to the centroids of each Gaussian as a function of PID element across all 24

channels. A linear fit is performed plotting the  $\phi$  angles versus the PID element and from the fitting function the corresponding azimuthal angles of all PID elements can be extracted.

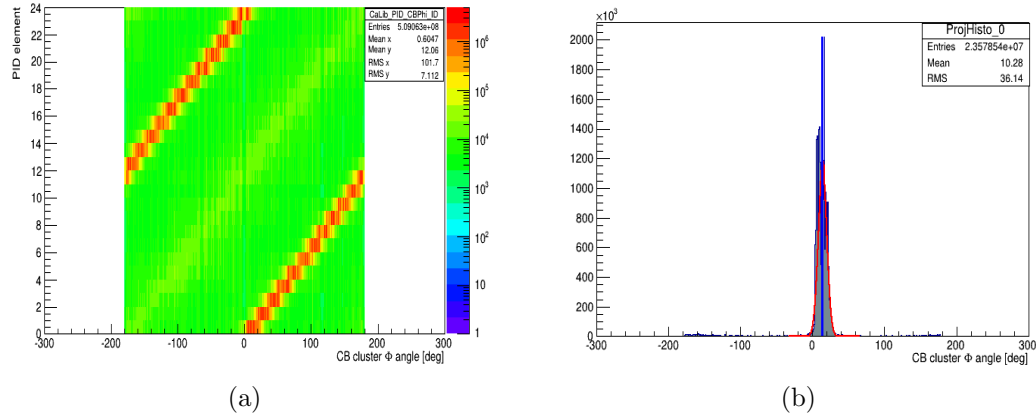


Figure 4.12: (a) The spectrum for one hit in CB and one hit in PID aligned at different angles for all 24 PID elements. (b) The projection for a single element.

### 4.3.13 PID Time Calibration

The conversion gain  $g$  of the TDCs used in PID detectors also have a fixed value of 117 ps/channel [50], so only the TDC offsets are determined in the same way as for the NaI detectors of CB. The two different charged hits in PID are identified as a pair and then the time difference between them is plotted as a function of the PID elements, as in Fig. 4.13a. We fit the time peak for all 24 channels and calculate the new gain out of the old and also new peak position. A projection of the individual PID element times is shown in Fig. 4.13b. The reconstructed peak position varies by less than 0.1 ns over all 24 PID elements.

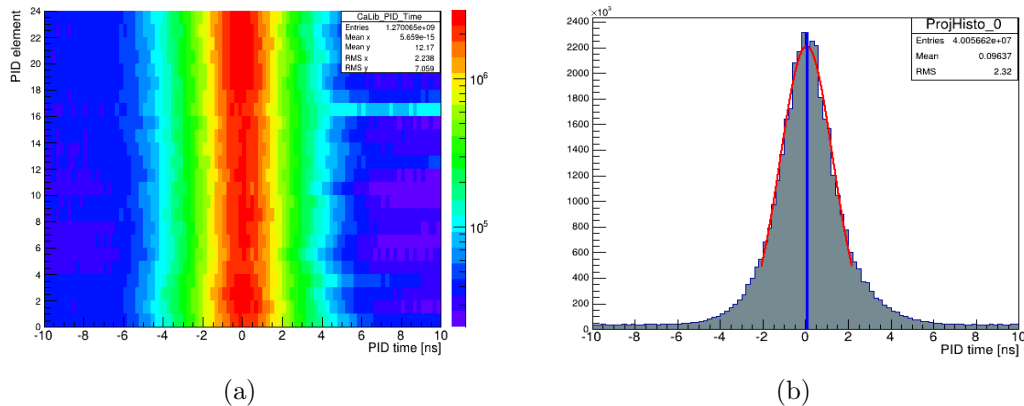


Figure 4.13: (a) shows the spectrum of the time difference between two charged hit identified as a pair in PID for all 24 PID elements, (a) shows the projection for a single element.

#### 4.3.14 PID Energy Calibration

The PID detectors are used to distinguish charged particles from neutral particles. Due to different masses and energies of charged particles, their different energy depositions will lead to distinct band structures. Since the PID elements are only 4 mm thick, charged particles will typically not deposit all of their energy, so the energy deposited in the PID can be compared to the energy deposited in NaI. The basic idea is to determine the correct pedestal and conversion gains for all 24 PID elements such that the deposited energy of a proton agrees with the simulated value. Thus, this procedure requires a simulation of energy deposition in both the PID and NaI for a range of proton energies, which allows for a comparison between simulation and real data. For the experimental data, the PID ADC channel is plotted as a function of NaI cluster energy, as in Fig. 4.14a. These histograms are projected onto the y-axis for different NaI cluster energies, as in Fig. 4.14b, and the proton peak positions were fitted both for simulated and experimental data. During the 2014 beamtime, PID ADCs were not working, but the problem was fixed during the 2015 beamtime. So that, the PID energy calibration was therefore performed only for the 2015 beamtime.

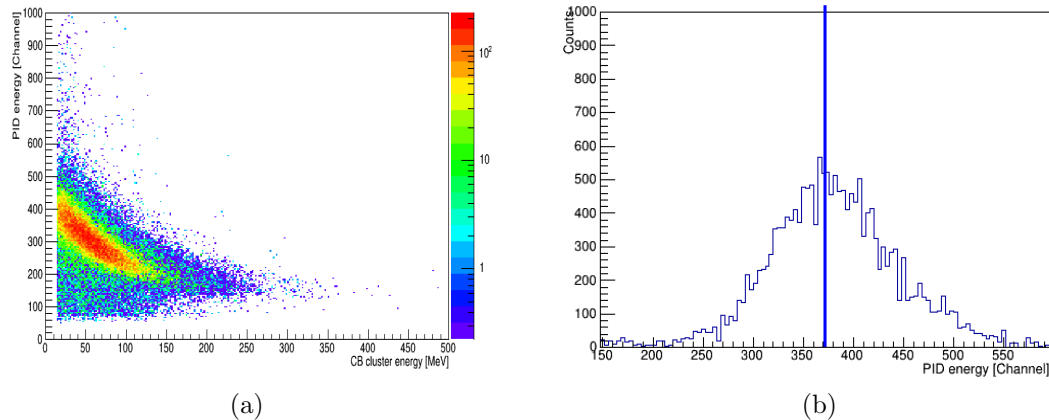


Figure 4.14: (a) PID energy vs NaI cluster energy. (b) Sample projection onto the y-axis for one slice of NaI cluster energy.

#### 4.3.15 TAPS Veto Time Calibration

The conversion gain  $g$  of the TDCs used in the Veto detectors also have a fixed value of 50 ps/channel [73], so only the TDC offsets are determined in the same way as for the PID. We identify the cluster pair in Veto detectors and then for each identified pair of veto element, the time difference is plotted between the two hits in the central element of each cluster, as in Fig. 4.15a. A projection of the individual Tagger time is shown in Fig. 4.15b.

#### 4.3.16 TAPS Veto Energy Calibration

The Veto detectors are used in the same way as the PID detectors to identify charged particles. Due to different masses and energies of charged particles, their different energy depositions will lead to distinct band structures. Every BaF<sub>2</sub> detector has a single Veto module mounted in front, a charged particle will fire the veto element and the corresponding BaF<sub>2</sub> elements. For each non-neutral cluster detected in TAPS, the

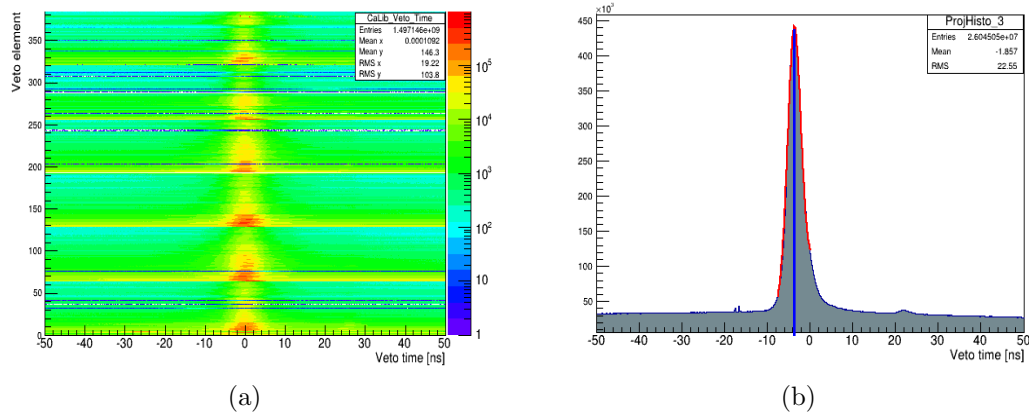


Figure 4.15: (a) The time difference between two neutral hits identified as a cluster pair in Veto for all 366 Veto elements. (b) Projection of a single element.

energy deposited in  $\text{BaF}_2$  is compared to the energy deposited in the veto detectors as in Fig. 4.16a. A fit is then performed on the veto energy to extract an energy for the proton peak as in Fig. 4.16b. This proton peak is then used to calculate a veto energy gain correction.

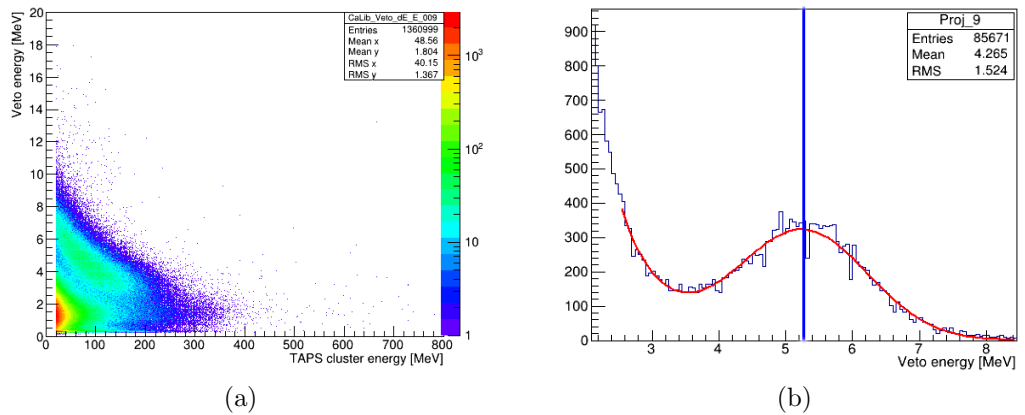


Figure 4.16: (a) Veto energy vs  $\text{BaF}_2$  energy. (b) Projection of a single element.

# Chapter 5

## Data Analysis I : $\pi^0$ Asymmetry

Exclusive  $\pi^0$  photo-production is not only a significant source of “physics background” to Compton scattering experiments, but also a useful reaction for systematic tests of experimental systems. Our experimental setup is such that we can reconstruct the  $\pi^0$  decay photons, requiring that the invariant mass of the two photon system is close to the  $\pi^0$  mass. A, a detailed study of  $\pi^0$  photo-production asymmetry is completed and presented in this section.

### 5.1 Event Selection and Particle Reconstruction

#### 5.1.1 Tagger Random Background Subtraction

During the experiment, some electron hits in the tagger that correspond to photons in CB/TAPS participate in a reaction with the target. This is due to the fact that some photons pass through without interacting, while many others are lost due to collimation of the beam. The event, in the tagger, which are in timing coincidence with the photons interacting with the target, are called “prompt” events while those without any timing coincidences are “random” events. These uncorrelated events,

which are normally referred to as background events, are numerous and hence need to be subtracted during the analysis.

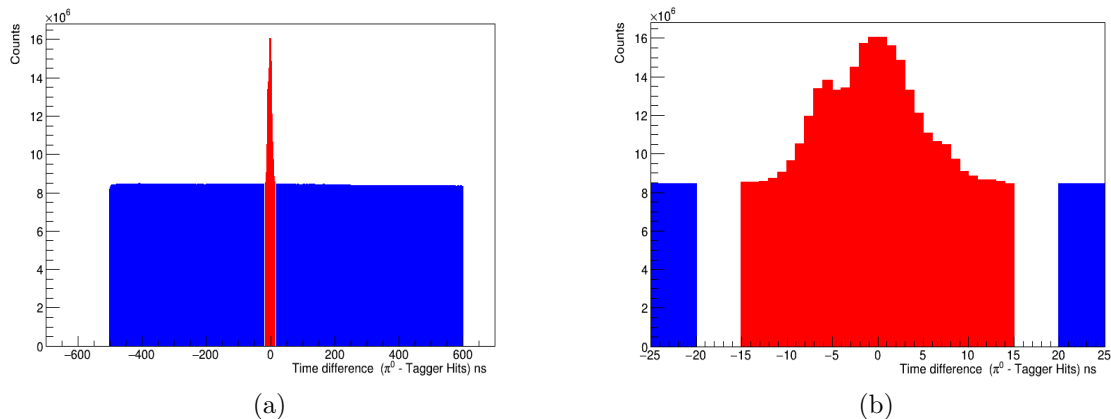


Figure 5.1: (a) Difference between the tagger and  $\pi^0$  time; the prompt and random windows are shown in red and blue respectively. (b) Zoomed in on the prompt peak.

Fig. 5.1a shows the prompt and random timing windows for event hits in the tagger, which are in timing coincidence with the reconstructed  $\pi^0$ . The prompt electrons have a peak around 0 ns for detector element hits corresponding to photons that interacted with the target and the random electrons on either side of the prompt peak are a flat background. The timing coincidence of 30 ns, as in Fig 5.1b, is used to identify prompt electrons denoted by  $p$ , and two large windows, 480 ns wide on the left of the prompt peak denoted  $r1$ , and 580 ns wide on the right of the prompt peak denoted  $r2$ , are used to identify the random/accidental contribution. The subtraction of random/accidental coincidences was performed by filling the same histograms with different weights for events from the prompt and the two random intervals as  $N_{true-events} = N_p - w_r N_r$ , where  $N_p$  and  $N_r$  is the number of events in prompt and random regions of Fig. 5.1a, and  $w_r$  is the prompt to random normalization factor of the time interval given by  $w_r = \frac{p}{r1+r2}$ . In fact, this subtraction of weighted events of the random window removes the random events under the prompt peak. The statisti-

cal error is calculated as the square root of the sum of the weights. This error can be improved when  $w_r$  is minimized by using large intervals for the random coincidences. Because coincidence time peaks of some tagger channels were slightly asymmetric, safe limits of  $\pm 4\sigma$  (gap between red and blue on either side of Fig 5.1b) were applied. The ratio of prompt peak to the random background is roughly 4.5:1 for the 2014 beamtime and 5:1 for the 2015 beamtime due to different beam current and trigger conditions.

### 5.1.2 $\pi^0$ Event Selection

AcquRoot has been used to store the full event-by-event information in a ROOT tree. These output trees from AcquRoot were then run in the GoAT analysis framework where particle and meson reconstruction was performed. This was achieved through different detector and particle reconstruction classes. A global configuration file was used to set up all the reconstruction and sorting choices of different decay channels. After sorting of the required reaction channel, analysis was completed using a user physics class written by the author, which was incorporated in GoAT. This section summarizes the fundamental steps applied for the identification and reconstruction of particles directly observed in the Crystal Ball and TAPS detector systems.

The flow chart shown in Fig. 5.2 summarizes the order of event selection and different data cuts applied to clean up the  $\pi^0$  photoproduction channel. The neutral pion is the lightest meson with a mass of  $(134.9766 \pm 0.0006)$  MeV/ $c^2$  and a lifetime of  $(8.52 \pm 0.18) \times 10^{-17}$  s [91]. Due to its very short lifetime, it is not possible to detect directly within the calorimeters. Therefore, its presence is inferred from the reconstruction of two decay photons that are combined to obtain its mass. Thus, for the reaction channel  $\gamma p \rightarrow \pi^0 p \rightarrow \gamma\gamma p$ , two neutral particles ( $\pi^0 \rightarrow \gamma\gamma$ ) with no recoil proton track in the final state were identified. While the PID TDCs were

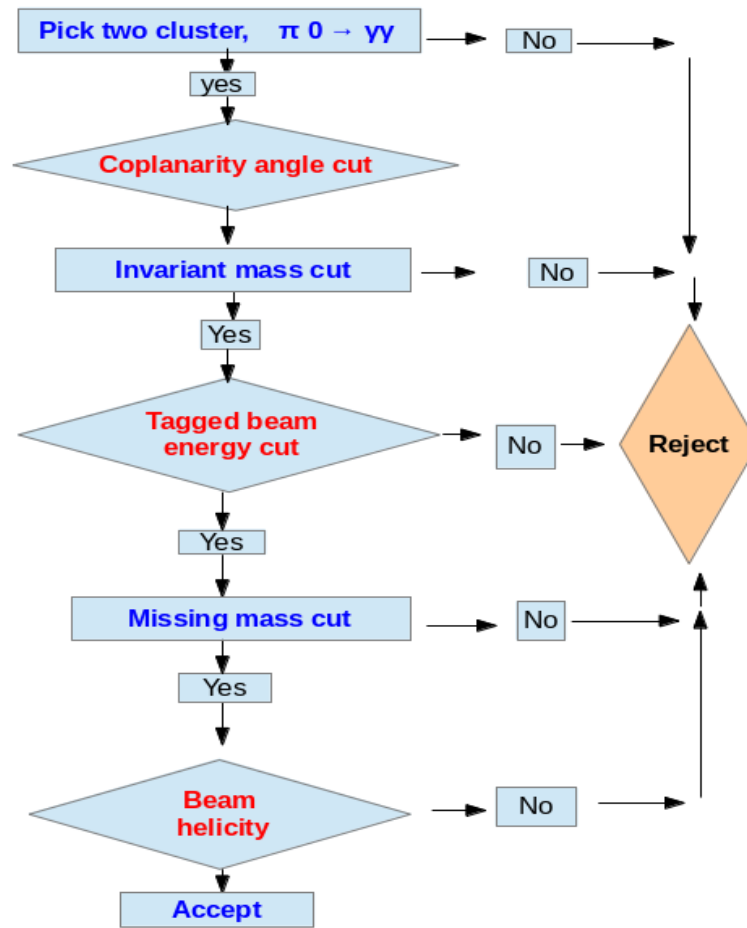


Figure 5.2: Flow chart for  $\pi^0$  meson selection.

working fine for the 2014 beamtime, the PID ADCs had some firmware issues , so the conventional  $\Delta E/E$  charged particle separation method was turned off for the entire 2014 data analysis. Instead, the MWPCs and the TAPS-Veto detectors were used for tracking and identification of any charged hits, as was done also in Ref. [51]. Because there were no issues with the PID ADC during 2015 beamtime, the data analysis was completed with and without the conventional  $\Delta E/E$  charged particle separation method. In order to make sure that the detected photons were consistent with the reconstruction of a  $\pi^0$ , a cut on the number of hits in the calorimeter (cluster multiplicity) was applied. A cut in cluster multiplicity reduces the event sample into

the most probable events for the reaction. This was done by requiring an event with a maximum of three clusters in the calorimeters. To eliminate false clusters due to split-off within the crystals and remove other competing processes (about 1%), events with more than three clusters in the calorimeters were rejected.

The events were classified as charged or neutral, based on whether the hit has a track in the MWPC and deposited some energy in the veto or not. For example, events with two neutral hits in the CB were selected, where the neutrality of the charged particle is determined if there is no correlation in the PID or MWPC. The various kinematic cuts, including  $\pi^0$  coplanarity cut, invariant mass cut, tagged photon energy cut and missing mass cut are presented in the following section.

#### 5.1.2.1 $\pi^0$ Coplanarity Angle

Even though the  $\pi^0$  photoproduction cross section is about hundred times larger than that of Compton scattering, background from other competing reactions has to be identified and suppressed with several analyses of the reaction kinematics. The azimuthal angle of the reconstructed neutral pion and a recoil proton can be used to check whether these particles are in the same reaction plane spanned by the incoming photon, or not. The  $\pi^0$  coplanarity angle is the difference in the azimuthal angle of the  $\pi^0$  and recoil proton. The coplanarity condition is  $\Delta\phi = |\phi_{\pi^0} - \phi_p| = 180^\circ$ . A Monte Carlo simulation, where  $\pi^0$  events were generated, passed through the A2 Geant4 simulation and then analyzed with the same A2 GoAT physics class, followed by the same users physics class as the data, was used to check the peak of the  $\Delta\phi$  distribution. Thus by comparing the experimental distribution to simulation, a fixed coplanarity cut of  $\Delta\phi = 180 \pm 15^\circ$  was applied on the reconstructed events.

### 5.1.2.2 Reconstruction of $\pi^0$ invariant mass

The energy and momentum information of two decay photons are used to define the invariant mass of the  $\pi^0$ ,

$$M_{\gamma\gamma} = \sqrt{E_{\gamma\gamma}^2 - \vec{p}_{\gamma\gamma}^2} = \sqrt{(E_{\gamma_1} + E_{\gamma_2})^2 - (\vec{p}_{\gamma_1} + \vec{p}_{\gamma_2})^2}, \quad (5.1)$$

where  $E_{\gamma_1}$ ,  $E_{\gamma_2}$ ,  $\vec{p}_{\gamma_1}$  and  $\vec{p}_{\gamma_2}$  are the energy and the momentum vectors of the two photons, respectively. This relation can further be simplified in terms of the opening angle  $\phi$  between the two photons,

$$M_{\gamma\gamma} = \sqrt{2E_{\gamma_1}E_{\gamma_2}(1 - \cos\phi)}, \quad (5.2)$$

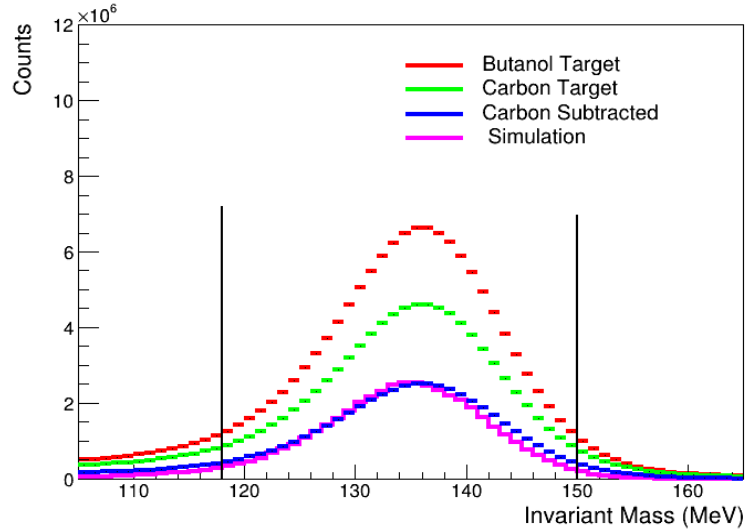


Figure 5.3: An example invariant mass distribution for reconstructed  $\pi^0$  photoproduction events at tagged photon energy, 285 – 305 MeV from the 2014 beamtime. The two black vertical lines show a cut applied on the weighted invariant mass. The error bars are shown but too small to be visible in this scale.

The  $\pi^0$  reconstruction is performed to identify particles belonging only to its decay. A photon pair resulting from a  $\pi^0$  decay should have an invariant mass of

134.98 MeV/c<sup>2</sup> within experimental resolution. In this analysis, a two particle invariant mass  $M_{ij}$  is computed for all possible  $i, j$  pairs. A weighted invariant mass is computed using a unique weighting factor, defined as  $W_{factor} = \frac{|M_{ij}-M_{\pi^0}|}{w_{\pi^0}}, i \neq j$ , where  $M_{ij}$  is the reconstructed invariant mass from  $\gamma_i$  and  $\gamma_j$ ,  $M_{\pi^0}$  is the exact mass of  $\pi^0$  ( $M_{\pi^0} = 134.98$  MeV) and  $w_{\pi^0}$  is the width of the invariant mass cut, as shown in Fig. 5.3. This width is important, because it ensures that the  $M_{ij}$  is within  $M_{\pi^0} \pm w_{\pi^0}$ .

For both the 2014 and 2015 beamtimes, an invariant mass width  $w_{\pi^0} = 20$  MeV/c<sup>2</sup> was applied. Also, the photon combinations with  $W_{factor} \leq 1$  were considered. The invariant mass spectrum agrees well with the Monte Carlo simulation, as shown in Fig. 5.3.

### 5.1.2.3 Missing Mass

The missing mass method is very useful to account for an undetected final state particle, because during the experiment not all the produced protons are fully detected in the calorimeters. This is due the fact that high energy protons go through the calorimeter crystals without fully depositing their energy, while some low energy protons do not reach the calorimeters due to energy loss in the target and PID . Therefore, the recoil particle can be reconstructed using a method called the missing particle method. In this method, we use four-vector information of the reconstructed  $\pi^0$ , the initial state (incoming photon and a proton at rest) and the detect a part of the final state (two decay photons from  $\pi^0$ ). The four-momentum conservation rules can then be applied to determine the missing particle. The missing mass in this case should be the mass of the proton as,

$$m_{miss} = \sqrt{(E_{\gamma_i} + m_p - E_{\pi^0})^2 - (\vec{p}_{\gamma_i} - \vec{p}_{\pi^0})^2}. \quad (5.3)$$

The missing mass spectrum is asymmetric, as shown in Fig. 5.4. This is because

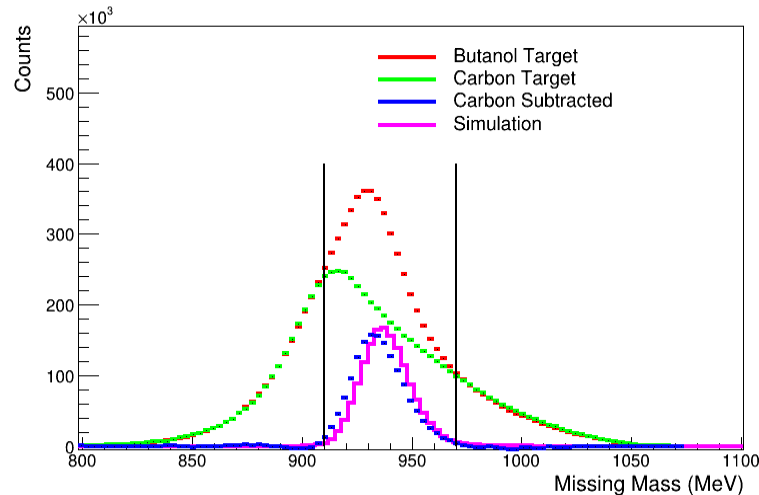


Figure 5.4: A sample missing mass distribution for reconstructed  $\pi^0$  for tagged photon energy at 285 – 305 MeV over all  $\pi^0$  angle. The two black vertical lines show a cut applied on the reconstructed missing mass. The error bars are shown but too small to be visible in this scale.

of the fact that the target is not a pure hydrogen target. The background is due to the photo-production process from the nucleons, such as carbon and oxygen in the butanol target, as well as the liquid He coolant. Thus, understanding and accurately subtracting of the background is very important to get a clean signal from only the free proton. It is observed from Fig. 5.4 that the reconstructed proton missing mass is in agreement with the Monte Carlo simulation, except on the tails of the peak. This remaining background on the left and right of the peak can be eliminated by applying cuts on the missing proton mass. The backgrounds for the three tagged photon energy ranges are different, so much tighter cuts in missing proton mass have been applied in cases where background contamination was significant.

## 5.2 Carbon Scaling Factor

The butanol target contains other non-hydrogen nuclei, like carbon and oxygen, which also participate in final state interactions, so their contributions need to be subtracted.

This was done by selecting a pure carbon target containing the same number of nucleons as the carbon and oxygen in the butanol [50]. In order to scale the carbon data set, a scaling factor was determined based on the the ratio of live-time corrected tagger scalers, and the ratio of butanol and carbon target yield.

### 5.2.1 Base Scaling Factor

The  $\sum_{2z}$  asymmetry experimental runs were broken into two main parallel and anti-parallel data sets (Sec. 2.2.1), as well as subsets for positive and negative butanol target polarization runs. Apart from the butanol target, separate dedicated data sets were taken with the carbon target. This was required to remove any contribution from the non-hydrogen elements in the butanol target. While the target is not a pure proton target, several other variables play an important role in subtracting out the carbon contribution to the missing mass spectra. Two variables playing an important role in subtracting out the carbon contribution to the missing mass spectra are the photon beam polarization and the carbon scaling factor. The scaling factor basically scales the separate experimental runs on a carbon target to each of the runs on the polarized butanol target.

In order to scale the carbon data set, the ratio of the overall butanol target integrated luminosity to the overall carbon target integrated luminosity was determined, termed the “base scaling factor”. This was done by adding live-time corrected individual tagger scaler histograms for the entire data set (one for positive and one for negative target polarization and one for the carbon background target) and dividing the butanol by the carbon data subset. The base scaling factor is different for different subsets, as well as for different regions of the tagger. The positively polarized butanol (blue) and carbon target total histograms (red color) are shown in Fig. 5.5a and the ratio between them for each tagger channel is shown in Fig. 5.5b. Similarly, the neg-

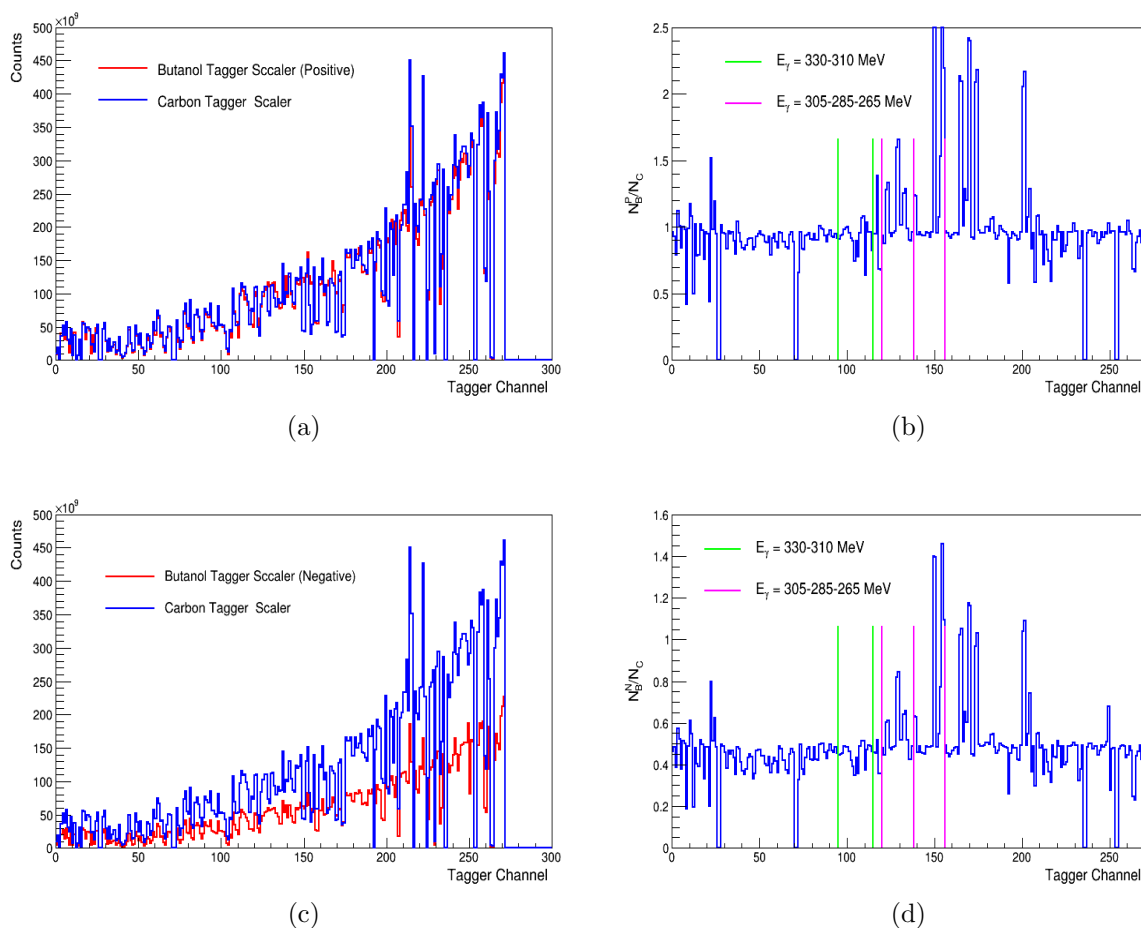


Figure 5.5: (a) Tagger scaler distribution for positively polarized butanol target and carbon target runs. (b) Ratio of positive to carbon tagger scalers. (c) Tagger scaler distribution for negatively polarized butanol target and carbon target. (d) Ratio of negative to carbon tagger scalers. The fluctuations represent missing tagger channels not the statistical fluctuations.

actively polarized butanol (blue) and carbon target total histograms (red color) are shown in Fig. 5.5c and the ratio between them corresponding to each tagger channel is shown in Fig. 5.5d.

### 5.2.2 Extra and Corrected Scaling Factors

The base carbon scaling factor obtained from a ratio of tagger scalers is insufficient to account for the nuclear  $\pi^0$  photo-production background due to additional nuclear effects and hence the missing mass ratio method was used to find the extra correction needed to properly scale the carbon runs [68]. The missing mass and invariant mass distributions from neutral pion photo-production simulations were used to examine the energy and angular dependence of the scaling factor. These simulations suggested that  $\pi^0$  photo-production is the most dominant background for the Compton scattering process, that varies significantly across both energy and angle. For this reason, each of the data sets are further subdivided into three separate energy bins:  $E_\gamma = 265 - 285$  MeV,  $285 - 305$  MeV and  $310 - 330$  MeV and five different angular bins:  $\theta = 80 - 95^\circ$ ,  $95 - 110^\circ$ ,  $110 - 125^\circ$ ,  $125 - 140^\circ$  and  $140 - 150^\circ$ , respectively. Hence, the carbon scaling results outlined in this section are also presented for three different energy ranges, two of them below, and one of them just above the  $\gamma p \rightarrow \pi^0 \pi^0 p$  threshold ( $308.85$  MeV/ $c^2$ ). The same analysis code was used for both butanol and carbon targets, meaning that the code passed through the same loops, applied the same event selection criteria and kinematic cuts as in the  $\pi^0$  data analysis section.

Initially, the missing mass spectra for carbon target were scaled by the base scaling factor and then the missing mass spectra obtained with the butanol target for the three energy and five angular bins (separately for parallel and anti-parallel configurations) were divided by the missing mass spectra obtained with the carbon target for the  $\pi^0$  photo-production channel. A combination of a Gaussian and a constant was fitted to the resulting spectra, as shown in Fig. 5.6a and Fig. 5.6b. The Gaussian described the peak position, while the magnitude of the constant describes the baseline. The fitting parameter of the constant is named as an ‘extra scaling factor’, which

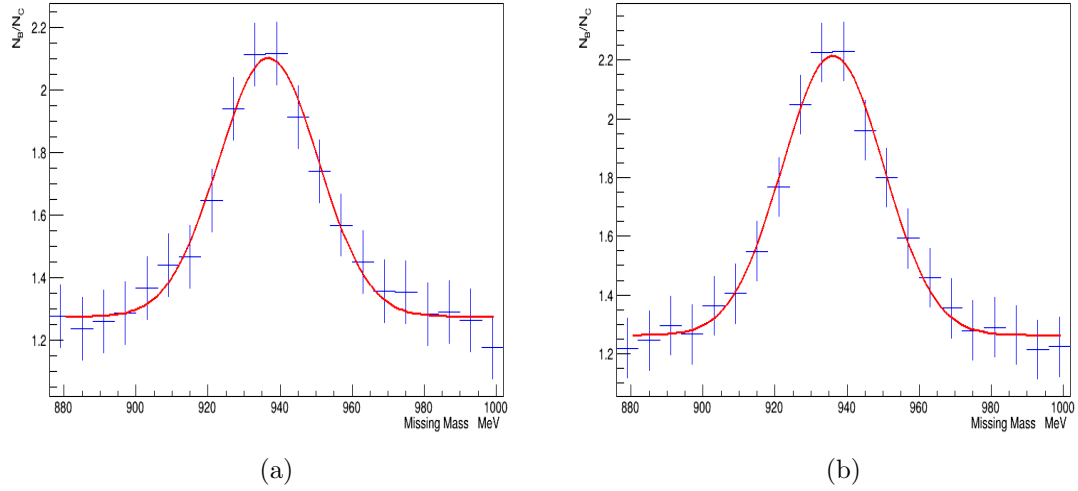


Figure 5.6: An example spectrum of the ratio of missing proton mass for butanol and carbon targets in the energy range  $E_\gamma = 285 - 305$  MeV at photon angles  $\theta = 125 - 140^\circ$  for (a) the parallel data set and (b) the anti-parallel data set. The red line is the combined fit of a Gaussian plus a constant term. The fit parameter of the constant defines the extra scaling factor.

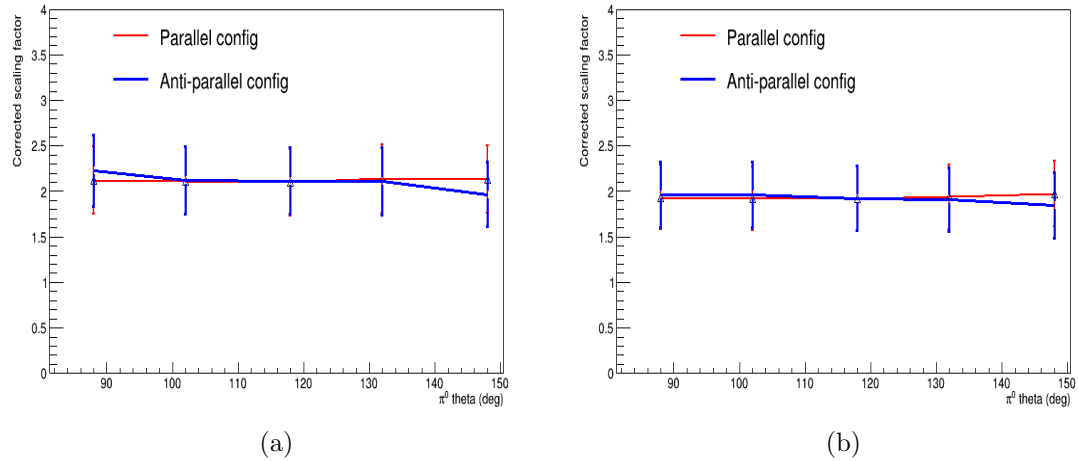


Figure 5.7: Corrected carbon scaling factor in the energy range (a)  $E_\gamma = 265 - 285$  MeV and (b)  $E_\gamma = 285 - 305$  MeV.

is a function of  $\pi^0$  angle for those three energy bins. The summary of these extra carbon scaling factors is shown in Appendix B.1. These corrected scaling factors were obtained by multiplying the extra scaling factor for all three energy and five angular

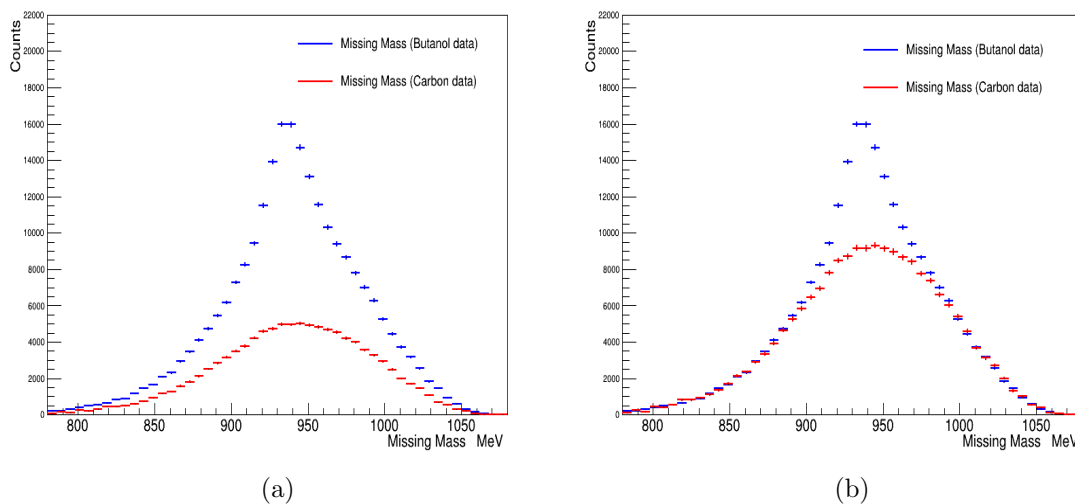


Figure 5.8: Missing mass distribution in the energy range  $E_\gamma = 285 - 305$  MeV at  $\theta_{\pi^0} = 125 - 140^\circ$  for the parallel configuration. (a) carbon is scaled by a base scaling factor and (b) is scaled by a corrected scaling factor.

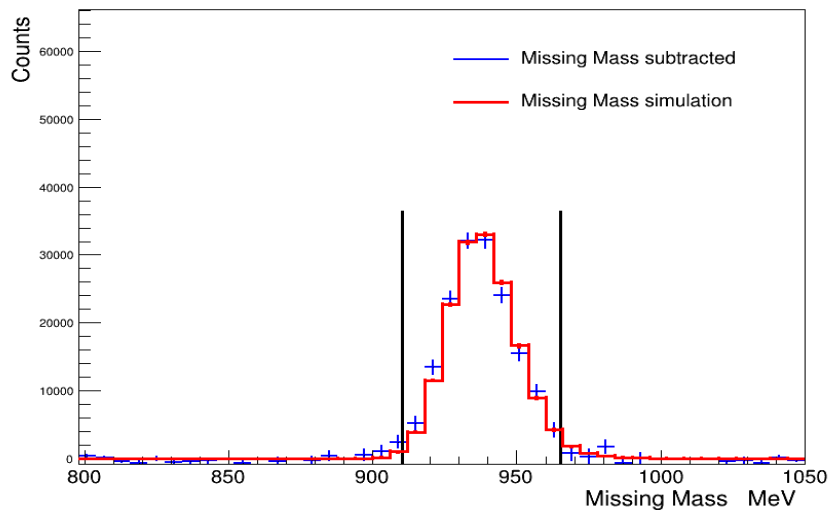


Figure 5.9: An example distribution of missing mass for reconstructed  $\pi^0$  at tagged photon energy  $E_\gamma = 285 - 305$  MeV,  $\theta_{\pi^0} = 125 - 140^\circ$  compared with the simulation at the same energy and  $\theta_{\pi^0}$  angle. The two black vertical lines indicate the missing mass cut applied on the reconstructed events.

bins by the base scaling factor. Fig. 5.7a and Fig. 5.7b show the corrected scaling factor as function of  $\pi^0$  angle at  $E_\gamma = 265 - 285$  MeV and  $E_\gamma = 285 - 305$  MeV. The

summary table of the corrected carbon scaling factors for both the 2014 and 2015 beamtime is presented in Appendix B.3.

The carbon missing mass distributions were scaled with these corrected scaling factor. These scaled carbon missing mass distributions were subtracted from the butanol missing mass distributions. Fig. 5.8a and Fig. 5.8b show the carbon-subtracted missing mass distributions using the base and the corrected scaling factors. From Fig. 5.8a, it is clear that the base scaling factor (discussed in Sec. 5.2.1) is not sufficient to describe the background in the missing mass spectrum. This indicates the importance of the missing mass ratio method and corrected scaling factor determination to ideally match the background. The missing mass distribution after scaling a carbon target with the corrected scaling factor is shown in Fig. 5.8b. In this case, the background in the missing mass spectrum is well-described by the scaled carbon missing mass. However, the carbon target missing mass spectra were scaled by the corrected scaling factor at all five  $\pi^0$  angles and the missing mass subtraction was completed for both the parallel and anti-parallel configurations. A sample missing mass distributions for  $E_\gamma = 285 - 305$  MeV at  $\theta_{\pi^0} = 125 - 140^\circ$  for the parallel configuration is shown in Fig. 5.9. As can be seen that the subtracted missing mass after scaling carbon by the corrected scaling factor is in good agreement with the simulation.

### 5.3 Charged Particle Detection

The detection of the recoil nucleons is necessary for the reliable isolation of the exclusive Compton final state from other competing reactions. Although the detection efficiency term in the double polarization observable measurement formula cancels out, it is important to understand the dominant source of background for Compton

scattering. This large background introduces a significant challenge when studying Compton scattering. In addition, a correct normalization has to be performed and many different factors play a role into the final results. Since our detector system is not perfect, particles, and hence events, are lost and have to be corrected by their detection efficiencies.

For a better understanding of the various effects, it is important to reduce the complexity of the data analysis. This was done by selecting neutral pion photo-production data and the ratio method that requires the detection of both the charged and neutral particles in the final state. The 2014 and 2015 beamtimes for  $\pi^0$  photo production events were analyzed separately to obtain the proton (any charged particle which could be proton or positive pion, etc.) detection efficiency by requiring only the neutral pion events for the channel  $\gamma p \rightarrow \pi^0 p$  and recoil charged track in the final state, where  $\pi^0 \rightarrow \gamma\gamma$ .

In this section, the final yields for recoil charged particle detected within the specified opening angle are compared with the final yields for any recoil particle identified as a charged and missed recoil charged particle. The proton detection efficiency is measured for the whole tagged photon energy range in terms of proton kinetic energy at various angles. These efficiencies are then applied to better identify the  $\pi^0$  background and maximum upper missing mass cut for each energy and angular bin in the simulation.

### 5.3.1 Rootino Detection Efficiency

The nature of the detected particle is determined with a combination of information obtained by the Pulse Shape Analysis (PSA) of Vetos from the TAPS system and  $\Delta E/E$  charge particle separation of PID/CB from the CB system. A discrimination between photons, electrons, protons and neutrons is possible. All of the particles were

categorized as charged or neutral. A particle was marked as a charged particle based on the energy deposition in any of the charged particle detectors, PID, MWPC, or TAPS Veto. The charged track was labeled as a pseudo-particle, known as rootino, and stored as a charged particle. All other tracks, those without any energy deposition in the charged particle detectors, were marked as neutral and stored as photons. Due to the PID ADC issues as discussed in Sec. 5.1.2, the conventional  $\Delta E/E$  charge particle separation technique was not applied for rootino detection efficiency studies. Instead, the MWPC and the TAPS-Veto detectors were used for tracking and identification of any charged hit as was done in the  $\pi^0$  photo production asymmetry studies and also in Ref. [51]. To estimate the efficiency of the rootino detection process, we compared the number of events where the final state recoil particle was detected as charged, to the sum of the events where a recoil particle was detected as a charged particle and the events where recoil particle was completely missed.

The detectors that are used for particle detection have a different response to a charged particle, like a proton, as opposed to a photon, so the choice of the reaction  $\gamma p \rightarrow \pi^0 p$  for the recoil charged particle detection calculation was obvious because its analysis is important in understanding the dominant background of the Compton scattering process. Therefore, the A2 Geant simulation is key to investigate whether the recoil charged particle is actually detected or not and also to determine the energy loss by the particle traveling from the event center to a detector. When particles travel from the event vertex to a detector, they have to traverse through the target material, the  $^3\text{He}/^4\text{He}$  refrigeration bath, the cryostat shells, the transverse holding coil, air, and various detectors, as well as their structural shells. This causes the charged particle to undergo interactions with the various types of material losing energy along the way,

$$E_{loss}^{tot} = E_{loss}^{butanol} + E_{loss}^{He} + E_{loss}^{cryo} + E_{loss}^{coil} + E_{loss}^{air} + E_{loss}^{str}. \quad (5.4)$$

However, the requirement of a detected charged particle limits the energy and angle ranges that can be reconstructed. A minimum energy, which is known as a threshold energy, is required for the charged particle to exit the butanol target and be detected in the Crystal Ball or TAPS detectors. This requirement places a threshold on the proton kinetic energy of roughly 60 MeV.

The proton detection efficiencies were calculated as a function of kinetic energy and polar angle in the lab frame. These quantities were calculated from the  $\pi^0$  kinematics, independent of the fact that the nucleons were detected or not. Due to the gap between the Crystal Ball hemispheres, only specific polar ranges where the likelihood of detecting possible charged particle is maximal are included in this analysis.

The Rootino detection efficiencies can be defined as

$$\epsilon_r(E_\gamma, \theta) = \frac{N_C}{N_C + N_M}, \quad (5.5)$$

where  $N_C$  represents the number of counts where a possible recoil particle is detected, identified as any charged particle (protons, positive pions etc) and  $N_M$  represents the number of counts where a possible recoil particle goes undetected or missed by the detector.

However, because the proton typically suffers from significant energy losses, understanding the direction of the charged particle is important for this efficiency analysis. This is done by determining the angle between the missing momentum vector and the detected charged particle opening angle. Thus, the final state recoil particle that has been detected and identified as a charged particle should be within a cone of specified

opening angle. The opening angle cut, dictated by the simulation as discussed in Section 5.1, has been applied for the nucleon detection efficiency calculations. In terms of opening angle, the detection efficiency formula is,

$$\epsilon_r(E_\gamma, \theta) = \frac{N'_C(\theta_{OA})}{N_C + N_M}, \quad (5.6)$$

where  $N'_C(\theta_{OA})$  is the number of counts where a possible recoil particle is detected, identified as any charged particle which satisfies the  $10^\circ$  opening angle cut.

### 5.3.2 Rootino Detection Efficiency Fitting Function

The detection efficiency plots were fitted with a function called the “logistic function”, given by

$$f(x) = \frac{L}{1 + e^{-k(x-x_0)}}, \quad (5.7)$$

where  $x_0$  is the  $x$ -value of the half maximum (Threshold Energy) logistic curve (red curve in Fig 5.10 and Fig 5.11),  $e$  is the natural logarithm base,  $L$  is the curve’s maximum value (Maximum Detection Efficiency), and  $k$  is the steepness of the curve. The fitting parameters for ‘parallel’ and ‘anti-parallel’ data sets are presented in Tables B.5 and B.6, respectively. These fitting parameters were applied to the simulation to gain a better understanding of background and find the upper limit in the integration of the missing mass.

The detection efficiencies have been measured separately for the positively and negatively polarized data sets at different polar angles. The data set for positively polarized target with right helicity state of the beam and negatively polarized target with left helicity state of the beam have been named as the ‘parallel’ data-set, and for positively polarized target with left helicity state of the beam and negatively polarized target with right helicity state of the beam have been named as the ‘anti-parallel’ data-

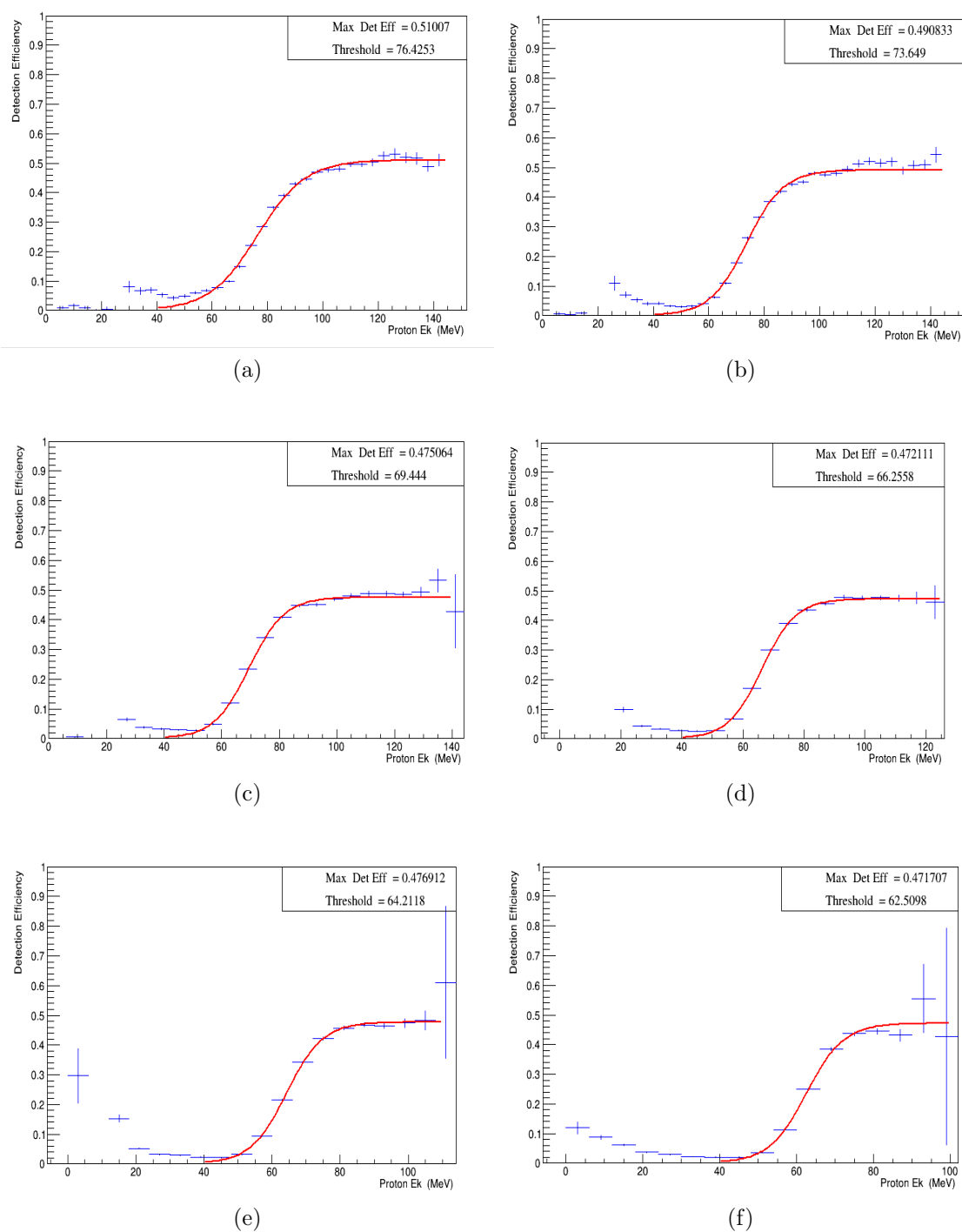


Figure 5.10: An example rootino detection efficiency using photo-production events for parallel data set from the 2014 beamtime. The efficiency distributions were fitted with a logistic function (red curve). The recoil particle detected at polar range of (a) 20 – 25°, (b) 25 – 30°, (c) 30 – 35°, (d) 35 – 40°, (e) 40 – 45°, and (f) 45 – 50°.

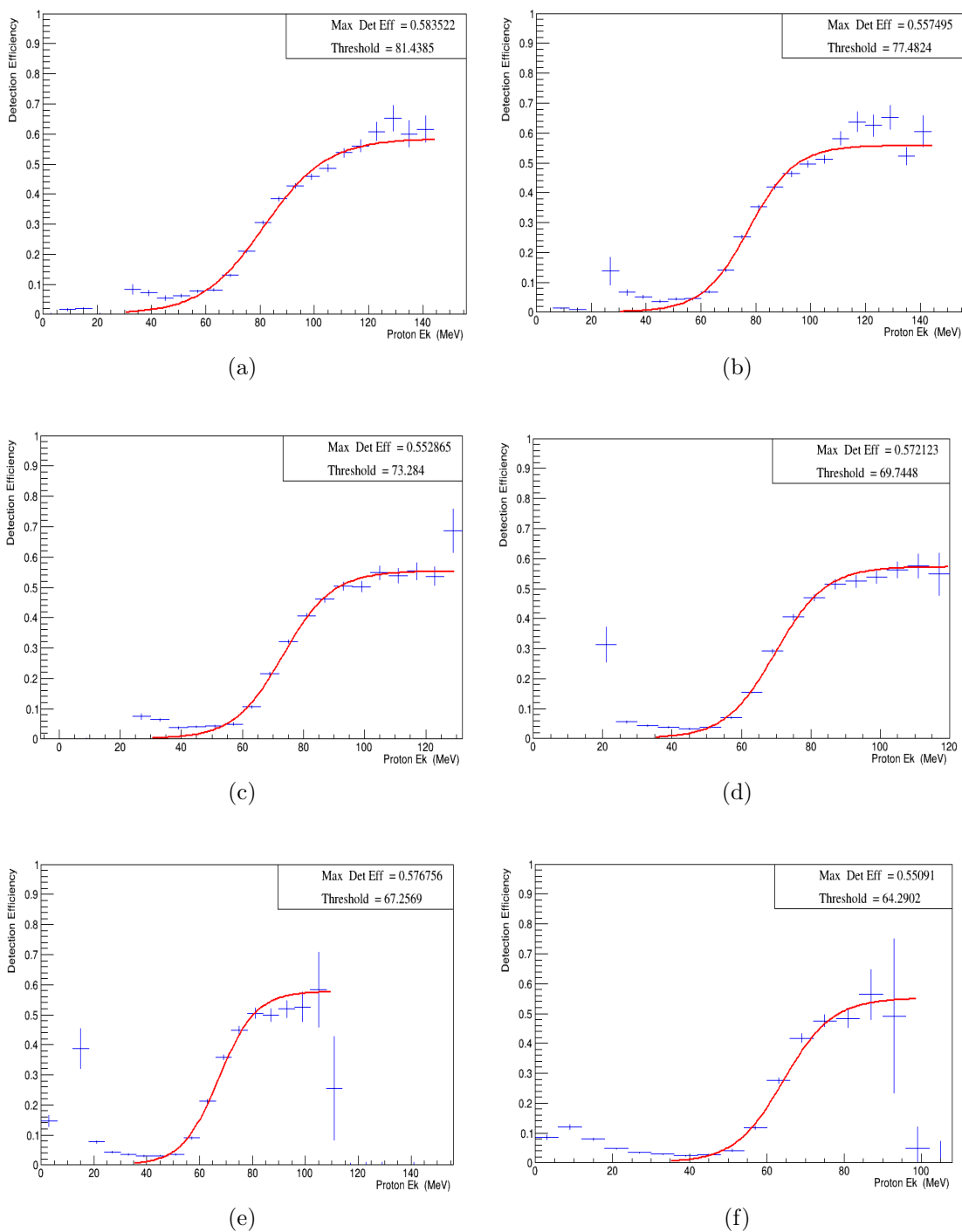


Figure 5.11: An example rootino detection efficiency using photo-production events for anti-parallel data set from the 2014 beamtime. The efficiency distributions were fitted with a logistic function (red curve). The recoil particle detected at polar range of (a) 20 – 25°, (b) 25 – 30°, (c) 30 – 35°, (d) 35 – 40°, (e) 40 – 45°, and (f) 45 – 50°.

set. The yields for carbon target data were scaled with the corrected scaling factor, as discussed in Section 5.2.2, and subtracted from the yield of the butanol target to get the detection efficiency results. These detection efficiencies were normalized with the correct target polarization values, as discussed in Section 2.2. The example detection efficiency plots, along with the maximum value of detection efficiency and threshold to detect a charged particle, at six different polar angles  $20 - 25^\circ$ ,  $25 - 30^\circ$ ,  $30 - 35^\circ$ ,  $35 - 40^\circ$ ,  $40 - 45^\circ$  and  $45 - 50^\circ$  for the both ‘parallel’ and ‘anti-parallel’ data sets from the 2014 beamtime are shown in Fig 5.10 and Fig 5.11, respectively. Other angular ranges are not included due to the kinematic ranges for the  $\pi^0$  photoproduction with a 450 MeV endpoint energy.

## 5.4 $\pi^0$ Photo-production Asymmetry

The  $\pi^0$  photo-production asymmetry is measured at two different tagged photon energy ranges,  $E_\gamma = 265 - 285$  MeV and  $E_\gamma = 285 - 305$  MeV by using the  $\sum_{2z}$  formula defined in Sec. 2.5a. For each  $\pi^0$  tagger hit pair which passes the event selection criteria outlined in Sec. 5.1, the  $\pi^0$  angle is filled separately for prompt and random events. The random subtraction is performed using the accidental factor discussed in Sec. 5.1.1. Beyond a prompt-random subtraction, fiducial cuts (discussed in Sec. 6.1.1), coplanarity cut (Sec. 5.1.2.1), tagged photon energy cut and invariant mass cut (Sec. 5.1.2.2), and missing mass cut (Sec. 5.1.2.3) have been applied.

The carbon target subtraction was performed using the corrected scaling factors discussed in Sec. 5.2.2. The  $\pi^0$  asymmetry results as a function of  $\pi^0$  angle from both the 2014 and 2015 beamtimes are shown in Fig. 5.12. These results are also compared with Scattering Analysis Interactive Database (SAID) model [92, 93]. This model is based on one-pion exchange process for elastic scattering of protons and neutrons, at

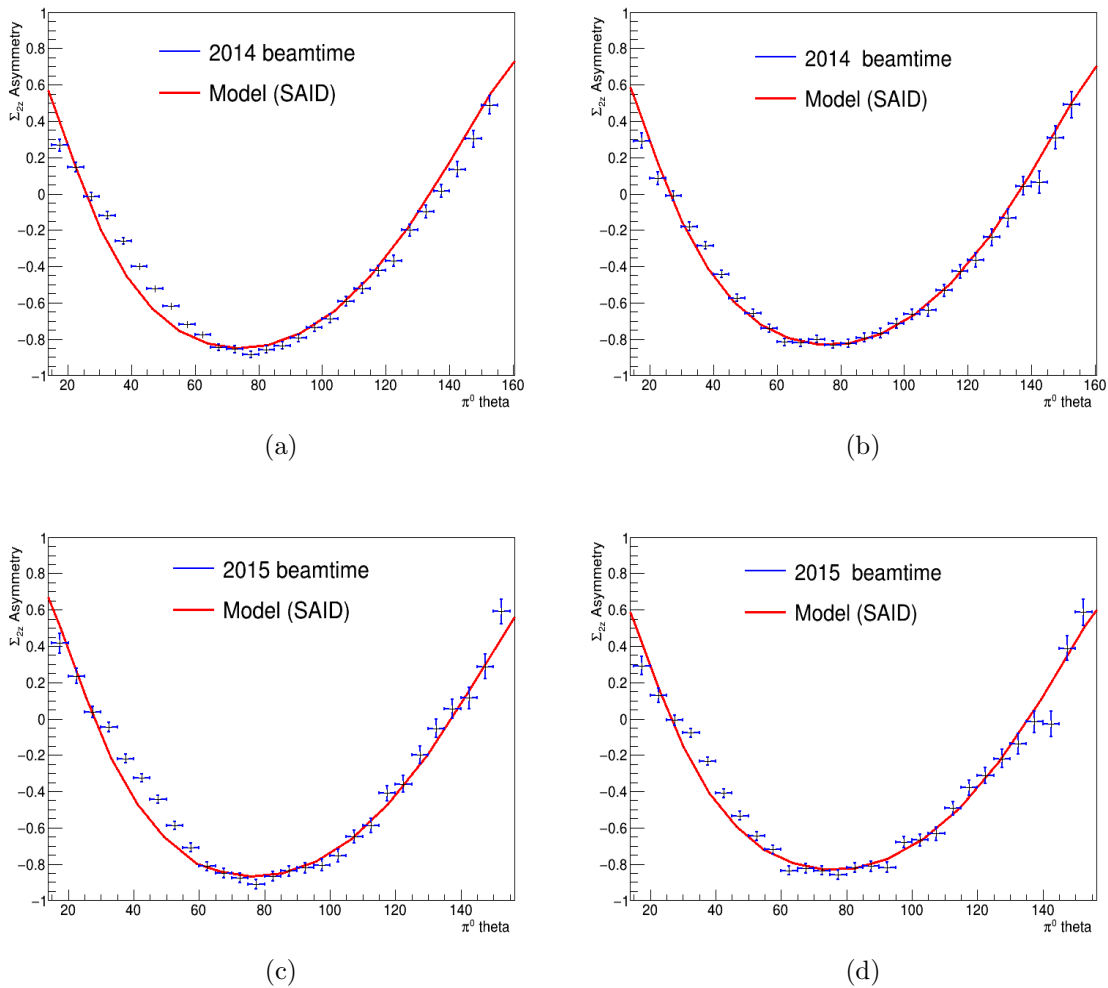


Figure 5.12:  $\Sigma_{2z}$  asymmetry for  $\pi^0$  photoproduction as a function of  $\pi^0$  angle in lab frame. Results are compared with SAID model [92]. (a), (c) show the  $\pi^0$  asymmetry at tagged photon energy, 265 – 285 MeV, from the 2014 and 2015 beamtime. (b), (d) show the  $\pi^0$  asymmetry at tagged photon energy, 285 – 305 MeV, from the 2014 and 2015 beamtime.

low to medium energies in terms of a partial-wave expansion. It is clearly seen that the  $\Sigma_{2z}$  asymmetry results for the  $\pi^0$  photoproduction events are in good agreement with the SAID model. The asymmetry results presented in this work cover the complete angular range of CB and TAPS ( $2 - 159^\circ$ ) and two tagged photon energy ranges,  $E_\gamma = 265 - 285$  and  $285 - 305$  MeV. For each data point, only statistical errors are

shown.

## Chapter 6

# Data Analysis II : Compton $\sum_{2z}$ Asymmetry

This chapter summarizes the detailed steps applied in the data analysis of the Compton scattering reaction,  $\gamma p \rightarrow \gamma p$ , in the  $\Delta(1232)$  resonance region. The experimental run conditions during the 2014 and 2015 beamtimes were slightly different, so the data were analyzed separately and results on the Compton  $\sum_{2z}$  asymmetry were later combined, based on a weighted average. The particle identification, event selection, kinematic cuts, Compton missing mass and its upper integration limit, and final results on the Compton  $\sum_{2z}$  asymmetry are presented in the following sections.

### 6.1 Identification of Final State Interaction

Compton scattering,  $\gamma p \rightarrow \gamma p$ , seems to have a simple final state, but it is very important to correctly identify the individual particles detected in the CB-TAPS detector system. As discussed in Sec. 3.1.3.1, the CB-TAPS system provides various techniques for charged and neutral particle identification. The most conventional  $dE/E$  charged particle separation method, discussed in Sec. 3.1.3.2, can be used to

identify protons, electrons and charged pions for both the Crystal Ball and TAPS. Depending on the beam energy and physics reaction of interest, alternative methods, such as Time Of Flight (TOF) or PSA of the two scintillation light components of the BaF<sub>2</sub> crystals, as described in Sect. 4.3.9, can also be used for TAPS. Although the discrimination of the photons and neutrons in the TAPS is possible through TOF or PSA, the same technique cannot be applied for the CB, because the distance between the target center and the detectors is comparably small and the NaI crystals have relatively poor timing resolution. Electromagnetic showers from the photon hits spread over a large number of modules, resulting in a larger cluster size than the hits from neutrons. Therefore, a cut based on the cluster size of the particle track can be applied to separate photons from neutrons and misidentified protons.

Because of the PID ADC issues during the 2014 beamtime discussed in Sec. 5.1.2, a very simple approach based on the particle track as discussed in Sec. 5.3.1 was adopted in this data analysis. Although the conventional  $dE/E$  charged particle separation method was turned off for the 2014 beamtime, the data analysis of the 2015 beamtime was completed with, and without, the conventional  $dE/E$  charged particle separation method. The missing mass spectra from the 2015 beamtime were compared with and without the conventional  $dE/E$  method applied and the difference was found to be negligible.

### 6.1.1 Event Selection

A Compton scattering event is identified in the analysis by selecting final states where a single neutral particle and a single charged track, both with deposited energies above 15 MeV (cluster threshold), are detected in the CB and TAPS detectors. The coincidence between the time of the neutral particle, and the time of a hit in the tagger, allows for tagging of the initial state photon. In order to remove randomly

coincident events from the selection, the random background was sampled in two timing windows and subtracted from the signal after normalization according to the width of the selected time intervals, as discussed in Sec. 5.1.1.

Although, in principle the combined CB and TAPS covers the angular range of 2-159°, there are regions near the two cone-shaped CB tunnels (which serve as the entrance and exit of the photon beam) that are not efficient. These regions are (i) the forward hole in the TAPS detector, 0-6°, (ii) the region between TAPS and the CB, 18 – 25°, and (iii) the backward hole in the CB, 150 – 180°, as shown in Fig. 6.1. Respective fiducial cuts have been applied.

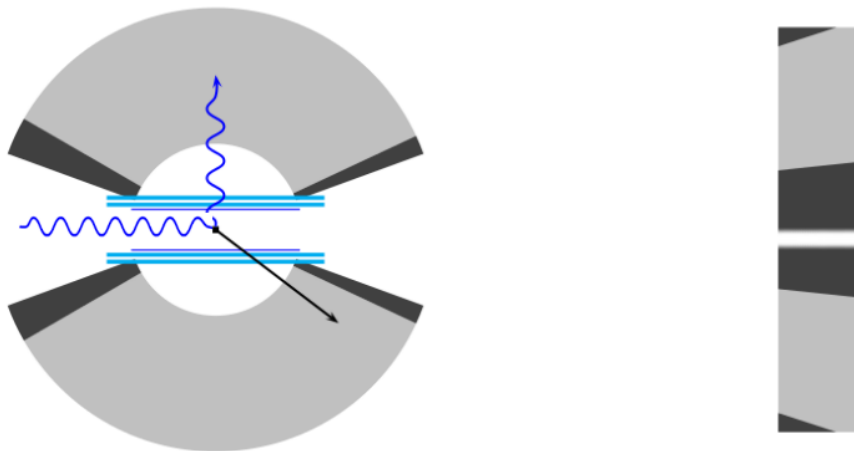


Figure 6.1: Cross section of detectors showing fiducial cuts. A possible region for the CB detector setup where a  $\pi^0$  decay photon can escape.

The missing mass and invariant mass distributions from the neutral pion photoproduction simulations discussed previously in Sec. 5.1.2.3 were used to examine the energy and angular dependence. These simulations suggested that  $\pi^0$  photoproduction varies significantly across both energy and angle. For this reason, the data analysis was divided into two parts: one just below, and one just above the  $\gamma p \rightarrow \pi^0 \pi^0 p$  threshold (of 308.85 MeV/ $c^2$ ). The analysis below threshold was further

divided into two energy bins:  $E_\gamma = 265 - 285$  MeV, which corresponds to tagger channels 156 – 138, and  $E_\gamma = 285 - 305$  MeV, which corresponds to tagger channels 138-120. These were further divided into five Compton scattered photon angular bins:  $80 - 95^\circ$ ,  $95 - 110^\circ$ ,  $110 - 125^\circ$ ,  $125 - 140^\circ$  and  $140 - 150^\circ$ .

The upper and lower limits in energy and angle are based on both experimental and physics limitations. One of the physics limitations is that in order for the proton to have enough momentum to reach the detectors, the photon must be scattered or emitted at large angle. This can be demonstrated by using the energy and momentum conservation relations for Compton scattering defined in Equation 2.21. For example, for an incident a photon energy of 300 MeV at  $\theta = 90^\circ$ ,  $(1 - \cos\theta) = 1$ , the kinetic energy of the proton can be obtained as  $T' = E_{p'} - mc^2 = 73$  MeV. As the Compton angle  $\theta$  of the scattered photon decreases,  $E_{p'}$  continues to decrease until it only has the energy of its rest mass, and so  $T'$  decreases to zero. Since we require a proton in our final state, and a kinetic energy of roughly 70 MeV is required (Sec. 5.3.1) to reach the CB + TAPS detector due to energy loss in the target and inner detector elements, only the Compton scattering events with a scattered photon angle between  $80 - 150^\circ$  are considered for the data analysis.

#### 6.1.1.1 Compton Coplanarity Angle

After the hit identification and event selections, background from competing reactions can be suppressed with several analyses of the reaction kinematics. The angular information of the scattered photon and a charged particle detected in the final state is a very important kinematic constraint for the Compton scattering data analysis. The kinematic diagram for the reaction channel,  $\gamma p \rightarrow \gamma p$ , is shown in Fig. 6.2a. We assume that the incoming photon is traveling along the  $z$  direction and interacts with a proton at rest and scatters at an angle  $\theta$ . The azimuthal angles of the scattered

photon and a recoil proton can be used to check whether these particles are in the same reaction plane spanned by the incoming photon, or not. The difference in the azimuthal angles of a scattered photon and a recoil proton is called the Compton coplanarity angle, and the coplanarity condition is given by

$$\Delta\phi = |\phi_\gamma - \phi_p| = 180^\circ. \quad (6.1)$$

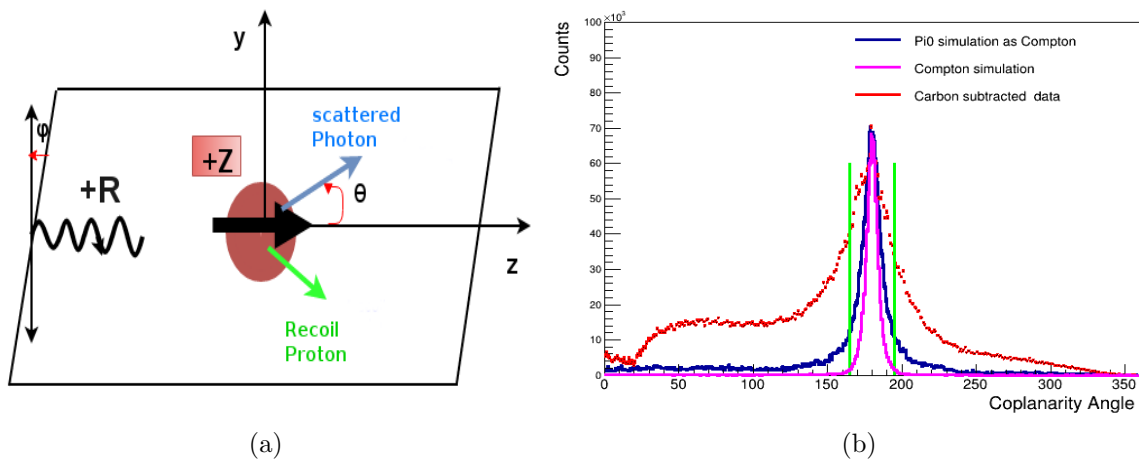


Figure 6.2: (a) A schematic diagram of a Compton scattered photon and a recoil proton in the same plane. (b) Coplanarity distribution for simulated Compton scattering events compared with the data. The simulated spectrum for Compton scattering events is shown in magenta, simulated  $\pi^0$  events which were analyzed as if they were a Compton photon is shown in blue, and the carbon-subtracted data are shown in red.

A sample coplanarity spectrum for the butanol target data is shown in Fig. 6.2b. For events with recoil protons, one of the largest background comes from  $\pi^0$  photoproduction. In addition to Monte Carlo simulation of Compton events,  $\pi^0$  events were also simulated, passed through the A2 Geant4 simulation and then analyzed with the same A2 GoAT physics class as the data. These simulation results for the  $\Delta\phi$  distribution show a nice peak around  $180^\circ$ . A cut on the fixed coplanarity angle,  $\Delta\phi = 180 \pm 15^\circ$ , as indicated by the two green vertical lines, was applied on the

reconstructed events.

### 6.1.1.2 Opening Angle

Charged particles suffer a significant amount of energy loss when they travel from the event center to a detector, as discussed previously. Specifically, the requirement of detection of a recoil charged particle eliminates all of the coherent nuclear background, since the target atoms are too heavy to escape the target. Assuming that the reaction was Compton scattering from a proton, and using standard two-body kinematics for each accepted charged particle, a check requiring that it traveled in a direction similar to the expected one as in Fig. 6.3a is made. This is done by determining the angle between the detected and missing particles, referred to as the proton opening angle. Thus, the opening angle is defined as the angle between detected proton, and where the proton was expected based on Compton kinematic reconstruction of the photon

$$\cos(\Omega_{OA}) = \frac{\vec{p}_{miss} \cdot \vec{p}_{recoil}}{|\vec{p}_{miss}| \times |\vec{p}_{recoil}|}. \quad (6.2)$$

Fig. 6.3b shows the comparison between the opening angle spectra for a carbon-subtracted butanol target data (coplanarity cut applied) and the MC simulation for Compton scattering. The Compton events were simulated using the Event Generator (EventGen) and passed through the Geant4 and the exact same config files in several steps as in Sec. 6.1.1.1. The simulated opening angle results show a sharp peak around  $5^\circ$ , which is in good agreement with the data. The large background, as seen in Fig. 6.3b, is believed to be mainly due to the dominant quasifree  $\pi^0$  photoproduction process from the bound nucleons such as carbon and oxygen in the butanol target. Therefore, much  $\pi^0$  background can be eliminated by applying a cut on the opening angle and hence a  $10^\circ$  opening angle cut as indicated by blue vertical line has been applied in the data analysis.

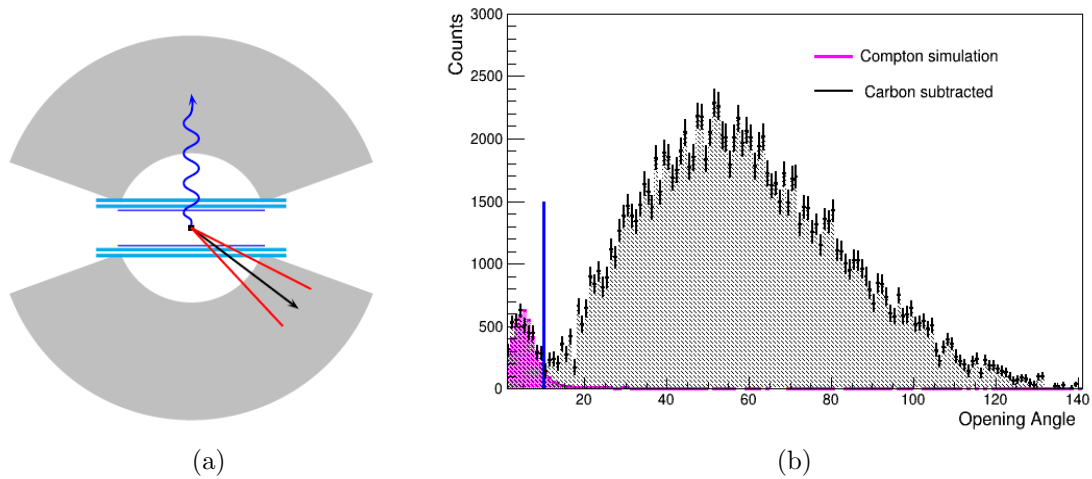


Figure 6.3: (a) Opening angle requiring that the proton is detected within a cone around its expected angle and (b) Opening angle for simulated Compton scattering compared with data. A cut on the opening angle is indicated by the blue vertical line.

### 6.1.1.3 Missing Mass for Compton Scattering Events

For the Compton scattering process,  $\gamma p \rightarrow \gamma p$ , an incoming photon and a rest proton are in the initial state and a scattered photon and a recoil proton is detected in the final state. The four-momentum conservation rule can be defined as,

$$(E_{\gamma_i}, \vec{p}_{\gamma_i}) + (E_{pin}, \vec{p}_{pin}) = (E_{miss}, \vec{p}_{miss}) + (E_{\gamma_f}, \vec{p}_{\gamma_f}), \quad (6.3)$$

where  $(E_{\gamma_i}, \vec{p}_{\gamma_i})$  and  $(E_{\gamma_f}, \vec{p}_{\gamma_f})$  are the four vectors of the incident and scattered photon, and  $(E_{pin}, \vec{p}_{pin})$  is the four vector of initial proton. This rule can be used to determine the undetected final state particle (or a missing particle) as

$$m_{miss} = \sqrt{(E_{miss})^2 - (\vec{p}_{miss})^2}. \quad (6.4)$$

The missing mass in this case should be the mass of the proton (938.27 MeV/c<sup>2</sup>).

This relation can be further simplified to

$$m_{miss} = \sqrt{(E_{\gamma_i} + m_p - E_{\gamma_f})^2 - (\vec{p}_{\gamma_i} - \vec{p}_{\gamma_f})^2}. \quad (6.5)$$

Fig. 7.8 shows an example missing mass distribution for events with a single photon and a charged track. Fiducial cuts (Sec. 6.1.1), coplanarity and opening angle cuts (Sec. 6.1.1.1), and tagged photon energy cut (Sec. 6.1.1.2) have been applied. Because the background varies significantly across both energy and angle, it is important to examine the energy and angular dependence. Therefore, the two tagged photon energy bins, below  $\gamma p \rightarrow \pi^0 \pi^0 p$  threshold were divided into five Compton  $\theta$  bins, and were analyzed separately. Fig. 7.8 shows missing mass spectra for  $E_\gamma = 265 - 285$  and  $E_\gamma = 285 - 305$  MeV, both at Compton  $\theta = 125 - 140^\circ$  from the 2014 and 2015 beamtimes. These are final, carbon-subtracted missing mass spectra using the corrected scaling factor discussed in Sec. 5.2.2. The Compton simulation and experimental missing mass distributions show a good agreement in the region from 900 – 940 MeV/c<sup>2</sup>, but on the other hand the region above 940 MeV/c<sup>2</sup> has some inconsistency. To investigate this inconsistency, simulated  $\pi^0$  events were analyzed as if they were from the Compton reaction and are summed together with simulated Compton scattering events to create an expected distribution. From these spectra, it is clear that there is good agreement of the data with the expected distribution up to missing mass  $\approx 1000$  MeV/c<sup>2</sup>. In some cases, at forward angle  $\theta = 80 - 95^\circ$  where the recoil proton has the minimum energy to be detected, the Compton scattering peak and the background distribution could not replicate the experimental data.

It is observed from these spectra that  $\pi^0$  photoproduction is the major source of background, which has a larger impact above a missing mass of approximately

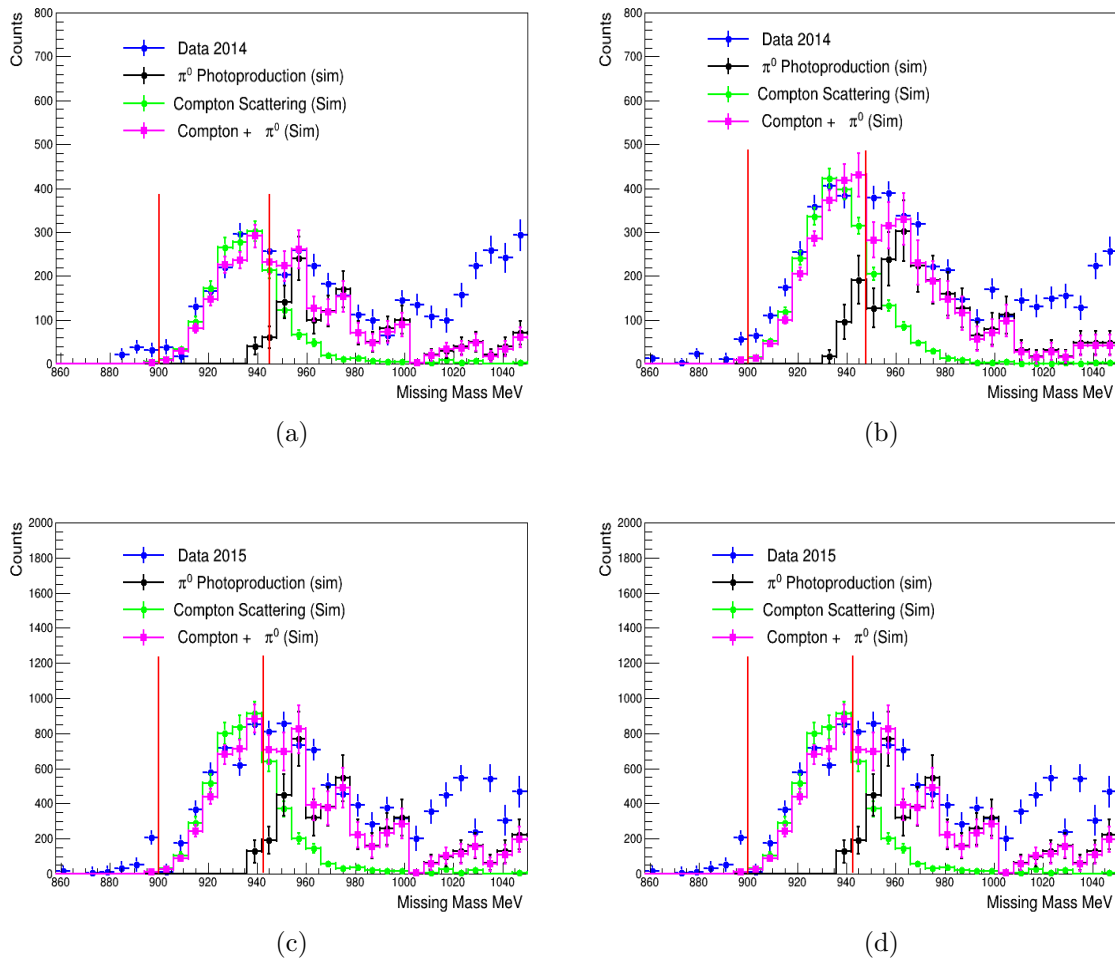


Figure 6.4: An example missing mass spectrum for two tagged photon energy bins. (a), (c) 2014 and 2015 beamtime results at  $E_\gamma = 265 - 285$  MeV. (b), (d) 2014 and 2015 beamtime results at  $E_\gamma = 285 - 305$  MeV. Experimental results for  $\theta = 125 - 140^\circ$ , are shown in blue, MC simulated results from Compton scattering and  $\pi^0$  photoproduction are shown in green and black, and the sum of two contributions to show an expected distribution is in magenta. Two red vertical lines represent the missing mass integration limit.

940 MeV/ $c^2$  and hence it is necessary to set a clear upper missing mass limit that coincides with the turn-on-point of  $\pi^0$  photoproduction. It is also clear from these simulations that there is very little or no  $\pi^0$  background below a missing mass of approximately 938 MeV/ $c^2$ . Although these simulations are helpful to find out the upper missing mass limit, a detailed asymmetry versus missing mass study, combined

with the simulation at different energy and angular bins, has been completed to determine ideal upper limit in missing mass and is presented in Sec. 6.1.1.4.

#### 6.1.1.4 Upper Limit On The Missing Mass

The correct missing mass integration limit is crucial to cleanly identify Compton scattering events and reject background processes. While the  $\pi^0$  photoproduction simulation is reliable in the majority of cases, further measures must be taken to reject any significant background contamination. Obviously, though missing mass spectra can be integrated up to the most conservative limit  $938 \text{ MeV}/c^2$  (proton mass), we want to have as many Compton events as possible to minimize statistical error and maximize the physics impact of results, so a minimum amount of  $\pi^0$  contamination is desired. A new, more rigorous approach was developed to determine the reliable upper missing mass limit. In this approach, for each energy and angular bin, the asymmetry was produced versus missing mass at a fixed integration limit  $900 - 930 \text{ MeV}/c^2$ . This asymmetry was then recalculated slowly moving the upper missing mass limit to higher values, keeping the lower limit fixed, in steps of  $2 \text{ MeV}/c^2$ , all the way to  $970 \text{ MeV}/c^2$ . For example, the first data point uses the missing mass integration limit  $900 - 930 \text{ MeV}/c^2$ , the second data point uses  $930 - 932 \text{ MeV}/c^2$ , and so on (Fig. 6.5). Thus, the integration limit is increased every time and the last data point is the result of missing mass integration limit of  $900 - 970 \text{ MeV}/c^2$ . As the upper missing mass limit is moved to higher values, the asymmetry calculation should converge upon the same value with reduced statistical errors. However, as the missing mass limit is moved in to a region with large amount of the background contribution, the asymmetry will begin to diverge.

A  $\pi^0$  photoproduction simulation discussed in Sec. 6.1.1.3 was used as a reference to check the variation in asymmetry in the data. The correct upper missing mass

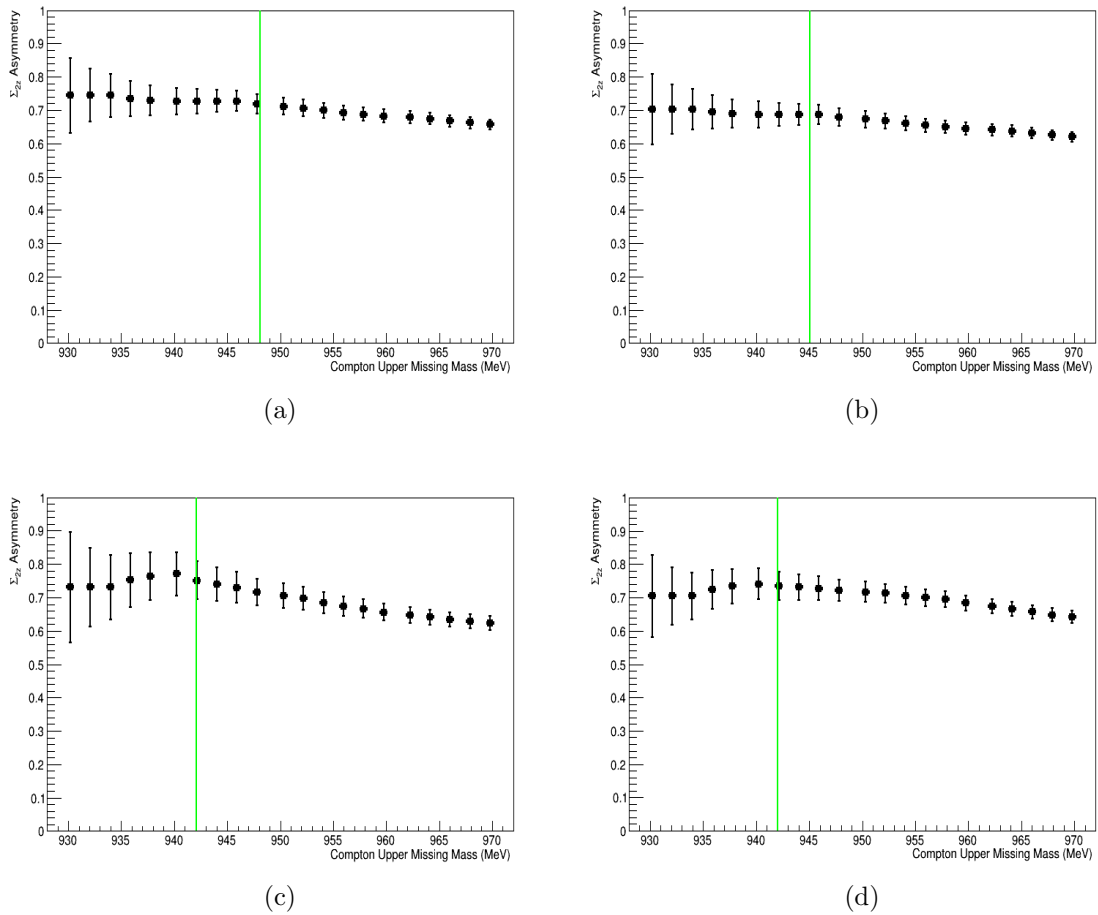


Figure 6.5: Asymmetry as a function of upper missing mass limit for the two energy bins at  $\theta = 125 - 140^\circ$ . The green vertical line shows the position of upper missing mass cut. (a), (c) 2014 and 2015 beamtime results at  $E_\gamma = 265 - 285$  MeV. (b), (d) 2014 and 2015 beamtime results at  $E_\gamma = 285 - 305$  MeV.

limits have been determined based on the following criteria:

- Compton  $\sum_{2z}$  asymmetry distribution is generated as a function of missing mass in the region  $900 - 970$  MeV/ $c^2$ .
- The lower limit on the missing mass is fixed to  $900$  MeV/ $c^2$  and asymmetry is allowed to vary by moving the missing mass limit to higher values up to  $970$  MeV/ $c^2$ .

- The upper limit on the upper missing mass is greater than or equal to the proton mass ( $938 \text{ MeV}/c^2$ ).
- The  $\pi^0$  photoproduction simulations, which were analyzed as if they were Compton events (spectrum shown with black points in Fig. 7.8), are used to determine a safe upper missing mass cut (typically  $938 - 942 \text{ MeV}/c^2$ ) and the resulting asymmetry for this region is taken as a reference value.
- The background contamination from  $\pi^0$  photoproduction ( $\pi^0$  contamination of 5%) is accepted in this analysis. This 5% is reasonable to address the discrepancy in the choice of 2 cm carbon target length (Sec. 3.2.3) and various other competing reaction from C, O and He nuclei.
- The asymmetry does not vary by more than 5% by moving to a higher missing mass limit compared to the reference listed above.

An additional adjustment of  $\pm 4 \text{ MeV}/c^2$  on the upper missing mass limit has been made for two angular bins,  $\theta = 80 - 95^\circ$  and  $\theta = 140 - 150^\circ$ . The adjustment to the first angular bin is made because, as discussed previously, only events reconstructed from the recoils that deposited enough energy ( $\approx 73 \text{ MeV}$  kinetic energy) in the Crystal Ball. The adjustment to the second angular bin is due to some of the inefficient or less efficient modules near the fiducial region.

Fig. 6.5 shows an example plot of asymmetry versus upper missing mass for the Compton angular range  $\theta = 125 - 140^\circ$ . A summary of the upper missing mass limits determined at a given energy and angular bin for both the 2014 and 2015 beamtimes is presented in Table 6.1.

Beamtime	Compton Angular Range	Missing Mass Upper Limit		
		$E_\gamma = 265 - 285$ MeV	$E_\gamma = 285 - 305$ MeV	$E_\gamma = 310 - 330$ MeV
2014	80 – 95°	952	950	949
	95 – 110°	947	949	946
	110 – 125°	948	949	948
	125 – 140°	945	948	945
	140 – 150°	949	946	950
2015	80 – 95°	945	946	948
	95 – 110°	942	945	944
	110 – 125°	941	942	944
	125 – 140°	942	942	941
	140 – 150°	940	940	941

Table 6.1: Missing mass cuts determined for three energy and five angular bins of Compton scattering. The upper missing mass limits are based on  $\pi^0$  photoproduction taken as a reference and detailed Compton  $\sum_{2z}$  asymmetry versus upper missing mass limit study.

### 6.1.2 2014, 2015 Compton $\sum_{2z}$ Asymmetry Results

Since the  $\sum_{2z}$  asymmetry is defined in terms of the difference in cross section between the right and left helicity states of the beam, as in Equation 2.38, due to relatively quick helicity flipping of the beam (approximately 1 Hz), the various factors needed to convert cross section into counts are identical. These factors include,

$$N(E, \theta) = \sigma(E, \theta)\Omega(\theta)\Phi(E)L\rho t\epsilon(E, \theta), \quad (6.6)$$

where  $\sigma(E, \theta)$  is the cross section,  $\Omega(\theta)$  is the solid angle,  $\Phi$  is the photon flux,  $L$  is the target length,  $\rho$  is the target density,  $t$  is the running time and  $\epsilon(E, \theta)$  is the efficiency, which is actually made up of tagging and detection efficiencies. These factors cancel out between the numerator and the denominator. Therefore, the  $\sum_{2z}$  asymmetry can be simplified as a ratio of the difference between the normalized yield for right and

left helicities of the beam to their sum,

$$\sum_{2z} = \frac{1}{P_{circ}^\gamma \cdot P_z^t} \left( \frac{(N_{+z}^R + N_{-z}^L) - (N_{+z}^L + N_{-z}^R)}{(N_{+z}^R + N_{-z}^L) + (N_{+z}^L + N_{-z}^R)} \right), \quad (6.7)$$

where  $P_{circ}^\gamma$  and  $P_z^t$  are the degree of the photon beam polarization and target polarization for polarized butanol target, respectively.

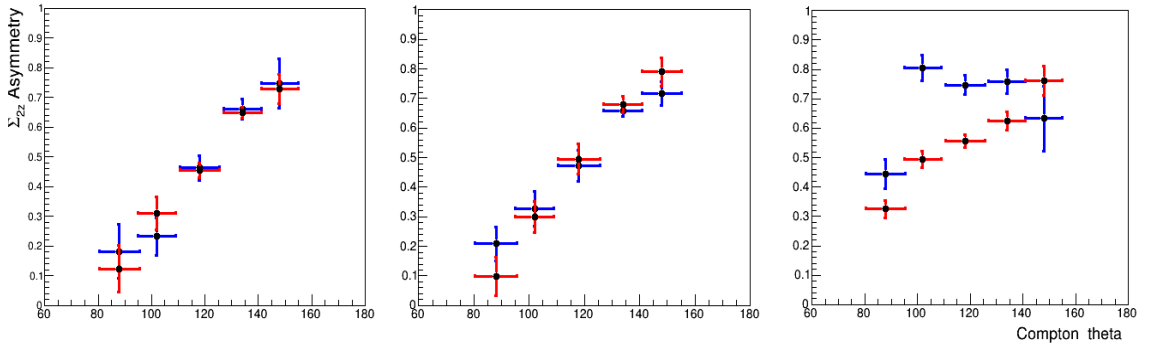


Figure 6.6: Compton  $\sum_{2z}$  asymmetry results from the 2014 and 2015 beamtimes for all three tagged energy bins. Blue points are from 2014 beamtime and red points are from 2015 beamtime. Only statistical errors are shown. The left, middle and right panel are for  $E_\gamma = 265 - 285$ ,  $285 - 305$  and  $310 - 330$  MeV, respectively.

After finding the optimal integration limit on the carbon-subtracted missing mass spectra, we integrate the missing mass for a given angular bin to find the Compton  $\sum_{2z}$  asymmetry. Fig. 6.6 shows the Compton  $\sum_{2z}$  asymmetry results including only the statistical error. These results for 2014 and 2015 beamtime are statistically consistent and hence can be combined to obtain final results. A summary of Compton  $\sum_{2z}$  asymmetry results, along with the statistical error, is shown in Table 6.2.

The  $\sum_{2z}$  asymmetry result can be altered by various experimental parameters. Some of the experimental parameters, such as the photon beam polarization and the carbon scaling factor used in subtracting out the carbon contribution to the missing mass spectra, and are energy dependent, while some other parameters, such

Beamtime	Compton Angle	Asymmetry, $\Sigma_{2z} \pm \delta\Sigma_{2z}(stat)$		
		$E_\gamma = 265 - 285$ MeV	$E_\gamma = 285 - 305$ MeV	$E_\gamma = 310 - 330$ MeV
2014	88°	0.1823 ± 0.0909	0.2083 ± 0.0577	0.4435 ± 0.0502
	102°	0.2322 ± 0.0629	0.3278 ± 0.0378	0.8054 ± 0.0246
	118°	0.4631 ± 0.0416	0.4723 ± 0.0316	0.7463 ± 0.323
	134°	0.6607 ± 0.0329	0.6591 ± 0.0203	0.7577 ± 0.408
	148°	0.7466 ± 0.0827	0.7178 ± 0.0397	0.6325 ± 0.1110
2015	88°	0.1231 ± 0.0782	0.0981 ± 0.0639	0.3255 ± 0.0390
	102°	0.3097 ± 0.0565	0.2997 ± 0.0514	0.4936 ± 0.0278
	118°	0.4544 ± 0.0237	0.4952 ± 0.0502	0.5570 ± 0.0213
	134°	0.6488 ± 0.0189	0.6797 ± 0.0273	0.6244 ± 0.0314
	148°	0.7279 ± 0.0506	0.7897 ± 0.0469	0.7611 ± 0.0502

Table 6.2: Compton  $\Sigma_{2z}$  asymmetry results from the 2014 and 2015 beamtimes for three energy and five Compton angular bins.

as the target polarization, are energy independent. The photon beam polarization, as discussed in Sec. 3.2.2.2, was used to normalize the  $\Sigma_{2z}$  asymmetry results. Because the target polarization is measured only at the beginning and the end of each data taking period with different target orientations, the degree of target polarization for each run was calculated using a linear interpolation, as discussed in Section 3.2.2.2.

The target polarization, is in principle, evaluated on a run-by-run basis, but the changes are very small for all the data files when evaluated on a day-by-day basis. Therefore, an average target polarization for a given day was determined and the data were normalized accordingly (day-by-day target polarization correction) for both the 2014 and 2015 beamtimes.

## 6.2 Error Analysis

The uncertainty in the measurement of the  $\Sigma_{2z}$  asymmetry consists of both systematic and statistical uncertainties. The systematic uncertainties define errors which are not determined by statistics, but are introduced by an uncertainty in the measurement

inherent in the system. The systematic errors in experimental observations are based on instrumental effects. The polarization observable has several inputs from measuring instruments: target polarization, beam polarization, normalization factor from the photon beam flux and carbon scaling factor. These systematic uncertainties and their systematic errors affect the polarization observable. The systematic uncertainties from beam polarization and target polarization between the 2014 and 2015 beamtimes are the same. The other systematic errors, including statistical and carbon scaling factor, are different between the two beamtimes and hence a detailed analysis has been completed. The systematic errors presented in this section are caused by global sources, i.e. they are common for all the analyses and had, therefore, only to be calculated once.

### 6.2.1 Target and Photon Beam Polarization

The dominating systematic error in the calculation of the  $\sum_{2z}$  asymmetry is the beam and target polarization. The physics behind how the electrons have to be spin polarized using a circularly polarized laser light at the electron source to produce circularly polarized photon beam is discussed in Sec. 3.1.1.1. As discussed in Sec. 3.1.1.1, the degree of the polarization of the electron beam is measured with a Mott polarimeter using the Mott scattering technique, where electrons are scattered from a thin gold foil within the MAMI accelerator. The uncertainty in the electron beam polarization for both the 2014 and 2015 beamtimes is  $\approx \pm 1\%$  (Table 6.3 and Table C.1). The uncertainty in the target polarization basically arises from the uncertainty in the measurement of the starting and ending polarization values, and this was evaluated to be  $\approx \pm 2\%$  (Table 6.3 and Table C.1).

### 6.2.2 Carbon Scaling Factor

Since the target contains nuclei other than hydrogen, these contributions are subtracted with the use of a pure carbon target containing the same number of nucleons as the carbon and oxygen in the butanol, and the liquid helium cryogen [50]. In order to scale the carbon data set, a scaling factor was determined by forming the ratio of butanol and carbon target missing mass, as explained in Sec. 5.2.2. To extract the systematic error, the carbon scaling factors were changed by  $\pm 10\%$  and the  $\sum_{2z}$  asymmetry was calculated to extract the relative difference (Table 6.3 and Table C.1). The  $\pm 10\%$  variation resulted an unidirectional shift in  $\sum_{2z}$  asymmetries, i.e. all the bins move in the same direction. The shift in asymmetry was evaluated to be  $\approx \pm 8 - 12\%$  depending on energy and the angular bin. This  $\pm 10\%$  is an appropriate choice based on the  $\pm 5\%$  discrepancy in the choice of carbon target and  $\pm 5\%$  background contamination from  $\pi^0$  photoproduction as discussed in Sec. 6.1.1.4.

### 6.2.3 Missing Mass Cuts

The  $\sum_{2z}$  asymmetry was evaluated by applying a cut on the missing proton mass distribution. The choice of the integration limits on the upper missing mass region caused a change in the Compton yield, with a narrow cut eliminating more background but also resulting in a loss of some useful events. A wider cut retains more events, but has a higher possibility of including more background. Therefore, the cuts on the reconstructed proton missing mass (Sec. 6.1.1.4) were used to extract the  $\sum_{2z}$  asymmetry. To extract the systematic error, the standard cut positions discussed in Sec. 6.1.1.4 were changed by  $\pm 5$  MeV/ $c^2$  and the  $\sum_{2z}$  asymmetry was calculated to extract the relative difference (Table 6.3 and Table C.1). The shift on the asymmetries was random, i.e. go up and down randomly from bin-to-bin and was evaluated to be  $\approx \pm 10\%$ .

### 6.2.4 Statistical Errors

To calculate the statistical error in the  $\sum_{2z}$  asymmetry, Equation 6.7 is simplified to

$$\sum_{2z} = \frac{1}{P_{circ}^\gamma \cdot P_z^t} \left( \frac{N_p - N_a}{N_p + N_a - s_f N_c} \right), \quad (6.8)$$

where  $N_p$ ,  $N_a$  and  $N_c$  are the yields for parallel, antiparallel and carbon data sets, and  $s_f$  is the corrected carbon scaling factor. The error propagation method from Ref. [94] has been used to calculate the statistical error in  $\sum_{2z}$  asymmetry as

$$\delta\Sigma_{2z}(stat) = \sqrt{\left(\frac{\partial\Sigma_{2z}}{\partial N_p}\right)^2 (\delta N_p)^2 + \left(\frac{\partial\Sigma_{2z}}{\partial N_a}\right)^2 (\delta N_a)^2 + \left(\frac{\partial\Sigma_{2z}}{\partial N_c}\right)^2 (\delta N_c)^2}. \quad (6.9)$$

The summary of statistical error is presented in Table 6.3 and Appendix C.

### 6.2.5 Summation of Errors

The summation of errors was handled by separating them into correlated and point-to-point (pt-to-pt) uncertainties. It is important to address the angular dependence of some of the parameters like the carbon scaling factors. The uncertainty of the experimental parameters: target polarization, beam polarization and carbon scaling factor are totally correlated for the measurement of the  $\sum_{2z}$  asymmetry, but this is not so for the uncertainty due to the missing mass integration limit. Thus, the systematic errors from the first three sources are added in quadrature as,

$$(\delta\Sigma_{2z})_{syst-scale} = \sqrt{(\delta\Sigma_{2z}(P_z^t))^2 + (\delta\Sigma_{2z}(P_{circ}^\gamma))^2 + (\delta\Sigma_{2z}(s_f))^2}. \quad (6.10)$$

These uncertainties are then plotted as a separate band, corresponding to every Compton angle (Sec. 6.3.1).

However, the error from the cuts on the reconstructed proton missing mass is

completely random and hence are summed up in quadrature with the statistical uncertainty) as,

$$(\delta\Sigma_{2z})_{pt-to-pt} = \sqrt{(\delta\Sigma_{2z}(stat))^2 + (\delta\Sigma_{2z}(syst - rand))^2}. \quad (6.11)$$

Beamtime	Compton Angle	Types of Error ( $\pm$ )						
		stat	syst-rand	pt-to-pt	syst-target	syst-beam	syst-carbon	syst-scale
2014	88°	0.0909	0.0182	0.0927	0.0036	0.0018	0.0109	0.0116
	102°	0.0629	0.0232	0.0670	0.0046	0.0023	0.0116	0.0126
	118°	0.0416	0.0231	0.0475	0.0093	0.0046	0.0185	0.0212
	134°	0.0329	0.0330	0.0465	0.0123	0.0066	0.0264	0.0299
	148°	0.0827	0.0448	0.0940	0.0149	0.0075	0.0373	0.0409
2015	88°	0.0782	0.0123	0.0792	0.0025	0.0012	0.0074	0.0079
	102°	0.0565	0.0309	0.0644	0.0062	0.0031	0.0155	0.0170
	118°	0.0237	0.0227	0.0328	0.0091	0.0045	0.0182	0.0208
	134°	0.0189	0.0324	0.0375	0.0123	0.0065	0.0260	0.0295
	148°	0.0506	0.0436	0.0668	0.0146	0.0073	0.0363	0.0398

Table 6.3: Summary of correlated as well as uncorrelated error analysis for the Compton  $\Sigma_{2z}$  asymmetry at  $E_\gamma = 265 - 285$  MeV.

Tables 6.3 shows the summary of error analysis at  $E_\gamma = 265 - 285$  MeV for both the 2014 and 2015 beamtimes. The summary of the other two energy bins is given in Appendix C.

### 6.3 Combined $\Sigma_{2z}$ Asymmetry Results

In Sec. 6.1.2, the  $\Sigma_{2z}$  asymmetry results for the Compton scattering process from the 2014 and 2015 beamtimes were presented. This section summarizes the final results on the  $\Sigma_{2z}$  asymmetry, obtained by combining the results from the two beamtimes based on the measurement of the weighted average. For two separate measurements

of a quantity  $Z$ , the weighted average is defined as [94],

$$Z_{wav} = \frac{\sum_i Z_i W_i}{\sum_i W_i}, \quad W_i = \frac{1}{\sigma_i^2}, \quad (6.12)$$

where, the sums are over two measurements,  $i = 1, 2$ , and the weight  $W_i$  of each measurement is reciprocal square of the corresponding uncertainty (pt-to-pt error in Table C.1). Because the weight factor,  $W_i$ , associated with each measurement involves the square of the corresponding uncertainty,  $\sigma_i$ , the measurement that is much less precise than the other contributes very much less to the final result. The uncertainty in  $Z_{wav}$  is calculated using the error propagation formula

$$\delta(Z_{av}) = \frac{1}{\sqrt{\sum_i W_i}}. \quad (6.13)$$

Beamtime	Compton Angle	Asymmetry, $\Sigma_{2z} \pm \delta\Sigma_{2z}(pt - to - pt)$		
		$E_\gamma = 265 - 285$ MeV	$E_\gamma = 285 - 305$ MeV	$E_\gamma = 310 - 330$ MeV
Combined	88°	0.1483 ± 0.0602	0.1564 ± 0.0446	0.3550 ± 0.0551
	102°	0.2725 ± 0.0464	0.3161 ± 0.0383	0.6684 ± 0.0484
	118°	0.4572 ± 0.0270	0.4798 ± 0.0322	0.6143 ± 0.0278
	134°	0.6535 ± 0.0292	0.6682 ± 0.0289	0.6739 ± 0.0249
	148°	0.7342 ± 0.0545	0.7491 ± 0.0439	0.7392 ± 0.0557

Table 6.4: Final Compton  $\Sigma_{2z}$  asymmetry results at three energy and five Compton angular bins. The errors represent the pt-to-pt error averaged between 2014 and 2015 beamtime for corresponding energy and angle.

### 6.3.1 Comparison to HDPV Model

To study the sensitivity of the  $\Sigma_{2z}$  asymmetry results on the proton spin polarizabilities, a fixed- $t$  dispersion relation approach, HDPV [28, 44, 45], was used to generate theoretical  $\Sigma_{2z}$  predictions. This code generates tables of polarized lab cross sections

at fixed lab energy for various values of scalar and spin polarizabilities in their standard units. These cross sections were used to generate a pseudo-data set of the  $\sum_{2z}$  asymmetry. Since the dispersion code used in this analysis to produce theoretical asymmetries is valid only below  $\gamma p \rightarrow \pi^0 \pi^0 p$  threshold, only the  $\sum_{2z}$  asymmetry results for the two combined sets at  $E_\gamma = 265 - 285$  MeV and  $E_\gamma = 285 - 305$  MeV are compared with the theoretical model.

The HDPV  $\sum_{2z}$  model allows one to choose the spin polarizability basis either in terms of  $\alpha_{E1} + \beta_{M1}$ ,  $\alpha_{E1} - \beta_{M1}$ ,  $\gamma_{E1E1}$ ,  $\gamma_{M1M1}$ ,  $\gamma_{E1M2}$ ,  $\gamma_{M1E2}$ , or in terms of  $\alpha_{E1} + \beta_{M1}$ ,  $\alpha_{E1} - \beta_{M1}$ ,  $\gamma_0$ ,  $\gamma_\pi$ ,  $\gamma_{M1M1}$ ,  $\gamma_{E1E1}$ . The second basis was chosen because  $\gamma_0$  and  $\gamma_\pi$  are a linear combination of the dipole ( $\gamma_{E1E1}$ ,  $\gamma_{M1M1}$ ) and quadrupole ( $\gamma_{E1M2}$ ,  $\gamma_{M1E2}$ ) terms and allowing them to vary essentially allows the quadrupole terms to vary as well. Thus, the theoretical  $\sum_{2z}$  model varies  $\alpha_{E1} + \beta_{M1}$ ,  $\alpha_{E1} - \beta_{M1}$ ,  $\gamma_0$  and  $\gamma_\pi$  constrained by the experimental error. The following nominal values were used in the dispersion code as an input to generate the theoretical  $\sum_{2z}$  model predictions:

$$\begin{aligned}
 \alpha_{E1} + \beta_{M1} &= (13.8 \pm 0.4) \times 10^{-4} \text{ fm}^4, \\
 \alpha_{E1} - \beta_{M1} &= (7.6 \pm 1.7) \times 10^{-4} \text{ fm}^4, \\
 \gamma_0 &= (-1.00 \pm 0.18) \times 10^{-4} \text{ fm}^4, \\
 \gamma_\pi &= (8 \pm 1.8) \times 10^{-4} \text{ fm}^4.
 \end{aligned} \tag{6.14}$$

Furthermore, to determine whether the  $\sum_{2z}$  asymmetry exhibits sensitivity to  $\gamma_{E1E1}$  or  $\gamma_{M1M1}$ , two different sensitivity bases were generated. In the first sensitivity basis,  $\gamma_{E1E1}$  was fixed at HDPV value of  $-4.3 \times 10^{-4} \text{ fm}^4$  and  $\gamma_{M1M1}$  was allowed to vary between 2.9 to 4.9 in standard unit. While in a second sensitivity basis,  $\gamma_{M1M1}$  was fixed at the HDPV value of  $2.9 \times 10^{-4} \text{ fm}^4$  and  $\gamma_{E1E1}$  was allowed to vary between  $-3.5$  to  $-5.5$  in standard unit. In addition, the range of polar angles from  $0$  to  $180^\circ$  in steps of  $10^\circ$  was selected.

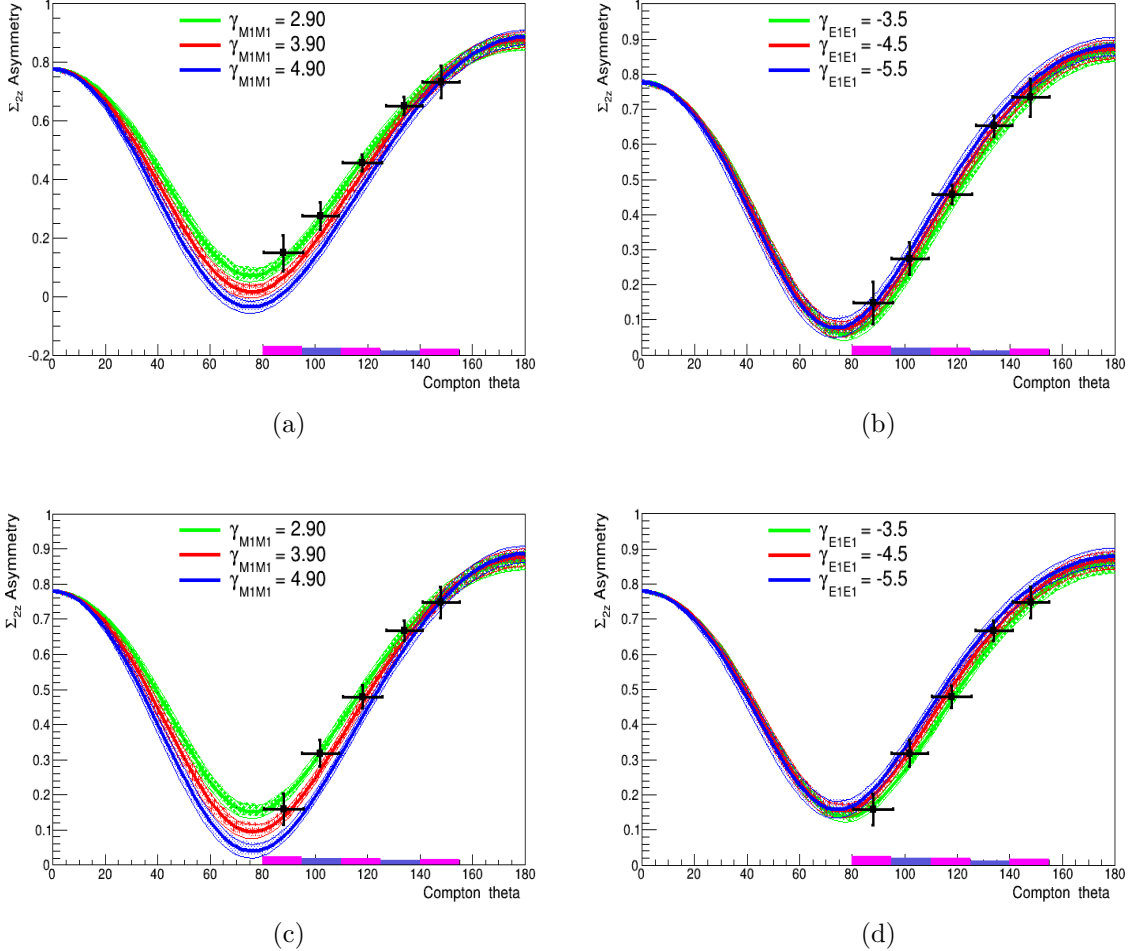


Figure 6.7: Compton  $\Sigma_{2z}$  asymmetry as a function of scattered photon angle. The top panel is for  $E_\gamma = 265 - 285$  MeV and the bottom panel is for  $E_\gamma = 285 - 305$  MeV. The curves are from the HDPV dispersion theory calculation of Pasquini, *et al.*, [28, 44, 45] making use of constraints on  $\gamma_0$ ,  $\gamma_\pi$ ,  $\alpha_{E1} + \beta_{M1}$  and  $\alpha_{E1} - \beta_{M1}$  allowed to vary within experimental error. The correlated systematic uncertainties are shown as a separate block corresponding to every Compton angle. (a), (c)  $\gamma_{E1E1}$  is fixed at  $-4.3$  and  $\gamma_{M1M1}$  allowed to vary. The green, red and blue bands are for  $\gamma_{M1M1}$  equal to 2.9, 3.9 and 4.9. The width of each band represents the propagated errors. (b), (d)  $\gamma_{M1M1}$  is fixed at 2.9 and  $\gamma_{E1E1}$  allowed to vary. The green, red and blue bands are for  $\gamma_{E1E1}$  equal to  $-3.5$ ,  $-4.5$  and  $-5.5$ . Polarizabilities are in the standard units of  $10^{-4} \text{ fm}^4$ .

The final Compton  $\sum_{2z}$  asymmetry results are plotted in Fig. 6.7 along with the dispersion theory curves for two energy ranges. Fig. 6.7a and Fig. 6.7c show final results for various values of  $\gamma_{M1M1}$  ranging from 2.9 to 4.9, while holding  $\gamma_{E1E1}$  fixed at  $-4.3$ . The various colour bands represent different values for  $\gamma_{M1M1}$ , while the spread of each band is a result of allowing  $\gamma_0$ ,  $\gamma_\pi$ ,  $\alpha_{E1} + \beta_{M1}$  and  $\alpha_{E1} - \beta_{M1}$ , to vary about their experimental errors. It is clear from these plots that the  $\sum_{2z}$  data exhibits a very strong sensitivity to  $\gamma_{M1M1}$ . The same data are plotted in Fig. 6.7b and Fig. 6.7d with curves generated by varying  $\gamma_{E1E1}$  in the range  $-3.5$  to  $-5.5$  in the standard units, while holding  $\gamma_{M1M1}$  fixed at 2.9. Unlike the previous case,  $\sum_{2z}$  exhibits a very weak sensitivity to  $\gamma_{E1E1}$ , allowing widely varying choices of this spin polarizability to adequately fit the data points.

The error bars shown are pt-to-pt statistical plus random systematic as discussed in Sec. 6.2.5. The systematic errors from the three different sources (Sec. 6.2): target polarization, beam polarization and carbon scaling factor from the 2014 and 2015 beamtimes are determined based on the weighted average and shown as a separate block for every Compton angle in Fig. 6.7.

Although the dispersion code used in this analysis to produce theoretical asymmetries is valid only below  $\gamma p \rightarrow \pi^0 \pi^0 p$  threshold, it is obviously still of interest to measure the  $\sum_{2z}$  asymmetry above  $\gamma p \rightarrow \pi^0 \pi^0 p$  threshold as this may stimulate further theoretical work to extend their models to this energy range. Therefore, the analysis above  $2\pi^0$  threshold has been completed for the energy range,  $E_\gamma = 310 - 330$  MeV, which corresponds to tagger channels, 115 - 95, for the same five Compton angular bins without theoretical curves. The results, for the energy range  $E_\gamma = 310 - 330$  MeV, are shown in Fig. C.1.

# Chapter 7

## Results and Discussion

In Chapters 5 and 6, the  $\sum_{2z}$  asymmetry results from the  $\pi^0$  photoproduction and Compton scattering channels were presented. Given the high cross section and relatively background-free signal, the  $\pi^0$  photoproduction channel proved not only to be an excellent reaction for asymmetry studies, but also an ideal reaction to perform systematic checks, as discussed in Sec. 6.2.

Having a well understood dominant  $\pi^0$  photoproduction background, the data analysis of the Compton scattering channel for the measurement of the  $\sum_{2z}$  asymmetry became more reliable and easier. The Compton  $\sum_{2z}$  asymmetry results were obtained from the 2014 and 2015 beamtimes separately and then combined to find the best estimate based on their weighted average. The goal of the Compton  $\sum_{2z}$  asymmetry experiment is two fold. The first one is focused on the study of model dependence within the  $\Delta$ -resonance region. Another goal of the experiment is to extract proton spin polarizabilities, which appear in the third-order effective Hamiltonian for Compton scattering and provide a measure of the spin-dependent global resistance of the nucleon's internal degrees of freedom against displacement in an external electric or magnetic field.

## 7.1 Data Fitting With HDPV Model

A global analysis of single- and double-polarized Compton scattering data in the  $\Delta(1232)$  region was performed to study the model dependence of proton's spin polarizabilities and extract them. This was done by fitting the asymmetry data using a HDPV code provided by Barbara Pasquini [17, 45], as discussed in Sec. 6.3.1. In addition to handling the experimental constraints, such as  $\alpha_{E1} + \beta_{M1}$ ,  $\alpha_{E1} - \beta_{M1}$ ,  $\gamma_0$ ,  $\gamma_{M1M1}$  and  $\gamma_{E1E1}$ , the fitting routine also provides the freedom to select or reject the experimental error in  $\gamma_\pi$  as a constraint.

As discussed in Sec. 2.1.2.6, the LEGS data set (with  $\gamma_\pi = -23.2 \times 10^{-4} \text{ fm}^4$ ) [34] is particularly interesting, since it shows a large discrepancy from all other data sets (the global result combining MAMI, LARA [36, 37] and Saskatoon [33] data set give  $\gamma_\pi = -38.7 \times 10^{-4} \text{ fm}^4$ ). Because our experimental measurements of  $\sum_{2x}$ ,  $\sum_3$  and  $\sum_{2z}$  are based on the asymmetries, not the cross sections, but the extraction of  $\gamma_\pi$  is based on the measurement of differential cross sections, it is important to cross check if the discrepancy exists only in the cross sections, and not in the asymmetries. Given that  $\gamma_0$  and  $\gamma_\pi$  have been measured experimentally, and that the uncertainty in  $\gamma_0$  is small, it is of interest to investigate the effect of including the  $\gamma_\pi$  data that show a larger discrepancy from all other model predictions. Therefore, the fitting was performed with and without the backward spin polarizability,  $\gamma_\pi$ , as a constraint for the Paudyal ( $\sum_{2z}$ ) data set. This fitting was also performed for the combined (Paudyal + Collicott ( $\sum_3$ ) + Martel ( $\sum_{2x}$ )) data set. The four extracted spin polarizabilities from the

Paudyal data set (this work) are as follows:

$$\begin{aligned}
 \gamma_{M1M1} &= 3.24 \pm 1.05 \times 10^{-4} \text{ fm}^4, \\
 \gamma_{E1E1} &= -4.06 \pm 1.46 \times 10^{-4} \text{ fm}^4, \\
 \gamma_{E1M2} &= 0.47 \pm 2.00 \times 10^{-4} \text{ fm}^4, \\
 \gamma_{M1E2} &= 1.36 \pm 1.43 \times 10^{-4} \text{ fm}^4,
 \end{aligned}
 \tag{7.1}$$

where the uncertainty reflects the fitting error of the model to the data described further in Sec. 7.3. Similarly, the extracted two backward and forward polarizabilities are:

$$\begin{aligned}
 \gamma_0 &= -1.01 \pm 0.18 \times 10^{-4} \text{ fm}^4, \\
 \gamma_\pi &= 8.18 \pm 1.61 \times 10^{-4} \text{ fm}^4.
 \end{aligned}
 \tag{7.2}$$

The extracted polarizabilities performing a global fit to only the Paudyal data set compared to the combined data set (Paudyal + Collicott + Martel) from three Compton asymmetry experiments,  $\sum_{2z}$ ,  $\sum_3$  and  $\sum_{2x}$ , are summarized in Table 7.1.

Martel, *et al.*, used the same fitting routine and extracted the four leading order terms of the proton's spin polarizabilities combining the  $\sum_3$  results from the LEGS collaboration and the  $\sum_{2x}$  results from his thesis experiment [50]. A recent analysis by Collicott, *et al.*, also extracted these four spin polarizabilities combining the  $\sum_{2x}$  asymmetry results from Martel, *et al.*, and the  $\sum_3$  asymmetry results from Collicott's thesis experiment [51].

Because both  $\sum_{2z}$  and  $\sum_3$  exhibit a strong sensitivity to  $\gamma_{M1M1}$ , it is important to compare the results within each experiment. It is clearly seen from Table 7.2 that the polarizabilities extracted using  $\sum_{2z}$  results from this work are in good agreement with the  $\sum_3$  results.

Polarizability	Data Sets			
	Paudyal		Paudyal + Collicott + Martel	
	With $\gamma_\pi$ con- straint	Without $\gamma_\pi$ constraint	With $\gamma_\pi$ con- straint	Without $\gamma_\pi$ constraint
$\alpha_{E1}$	$10.67 \pm 0.49$	$10.68 \pm 0.49$	$10.53 \pm 0.48$	$10.53 \pm 0.48$
$\beta_{M1}$	$3.13 \pm 0.49$	$3.11 \pm 0.49$	$3.24 \pm 0.48$	$3.24 \pm 0.48$
$\gamma_{E1E1}$	$-4.06 \pm 1.46$	$-2.86 \pm 2.25$	$-4.24 \pm 0.39$	$-4.24 \pm 0.39$
$\gamma_{M1M1}$	$3.24 \pm 1.05$	$2.58 \pm 2.02$	$3.25 \pm 0.40$	$3.24 \pm 0.57$
$\gamma_{E1M2}$	$0.47 \pm 2.00$	$-1.59 \pm 3.47$	$0.76 \pm 0.83$	$0.77 \pm 1.18$
$\gamma_{M1E2}$	$1.36 \pm 1.43$	$2.89 \pm 3.04$	$1.24 \pm 0.39$	$1.23 \pm 0.54$
$\alpha_{E1} + \beta_{M1}$	$13.80 \pm 0.40$	$13.79 \pm 0.40$	$13.77 \pm 0.40$	$13.77 \pm 0.40$
$\alpha_{E1} - \beta_{M1}$	$7.54 \pm 0.89$	$7.57 \pm 0.89$	$7.28 \pm 0.86$	$7.28 \pm 0.88$
$\gamma_0$	$-1.01 \pm 0.18$	$-1.01 \pm 0.18$	$-1.00 \pm 0.18$	$-1.00 \pm 0.18$
$\gamma_\pi$	$8.18 \pm 1.60$	-	$7.97 \pm 1.36$	-
$\chi^2/dof$	0.23	0.24	0.83	0.87

Table 7.1: Polarizabilities ( $10^{-4} \text{ fm}^4$ ) extracted using either the Paudyal (this work), or the Paudyal, Collicott and Martel data sets. The HDPV code by Pasquini *et al.* [17, 45] was used to fit and extract the spin polarizabilities. Fitting errors of the model to the data are shown. A  $\chi^2$  per degree of freedom for each fit is also included.

Polarizability	Data Sets		
	LEGS + Martel	Collicott + Martel	Paudyal + Collicott + Martel
$\gamma_{E1E1}$	$-3.5 \pm 1.2$	$-5.0 \pm 1.5$	$-4.24 \pm 0.39$
$\gamma_{M1M1}$	$3.16 \pm 0.85$	$3.13 \pm 0.88$	$3.25 \pm 0.40$
$\gamma_{E1M2}$	$-0.7 \pm 1.2$	$1.7 \pm 1.7$	$0.76 \pm 0.83$
$\gamma_{M1E2}$	$1.99 \pm 0.29$	$1.26 \pm 0.43$	$1.24 \pm 0.39$
$\gamma_0$	$-1.03 \pm 0.18$	$-1.00 \pm 0.18$	$-1.00 \pm 0.18$
$\gamma_\pi$	$9.3 \pm 1.6$	$7.8 \pm 1.8$	$7.98 \pm 1.36$
$\alpha_{E1} + \beta_{M1}$	$14.0 \pm 0.4$	$13.8 \pm 0.4$	$13.77 \pm 0.40$
$\alpha_{E1} - \beta_{M1}$	$7.4 \pm 0.9$	$6.6 \pm 1.7$	$7.29 \pm 0.86$
$\chi^2/dof$	1.05	1.25	0.83

Table 7.2: Polarizabilities (in  $10^{-4} \text{ fm}^4$ ) extracted using the LEGS + Martel, Collicott + Martel and Paudyal + Collicott + Martel data sets. The fitting and extraction of the spin polarizabilities was performed using the HDPV code by Pasquini, *et al.* [17, 45], for all three data sets. Fitting errors of the model to the data are shown. A  $\chi^2$  per degree of freedom for each fit is also included.

## 7.2 Data Fitting With $B\chi$ PT Model

The  $\sum_{2z}$  asymmetry data were also fit by using the  $B\chi$ PT calculation of Lensky and Pascalutsa [46]. The same experimental constraints and bases as in HDPV were applied for both the Paudyal data set and the combined (Paudyal + Collicott + Martel) data set. The extracted polarizabilities are summarized in Table 7.3.

Polarizability	Data Sets			
	Paudyal		Paudyal + Collicott + Martel	
	Without constraint	$\gamma_\pi$	With $\gamma_\pi$ con- straint	Without constraint
$\alpha_{E1}$	$10.76 \pm 0.49$		$10.27 \pm 0.48$	$10.39 \pm 0.48$
$\beta_{M1}$	$3.04 \pm 0.49$		$3.51 \pm 0.48$	$3.38 \pm 0.48$
$\gamma_{E1E1}$	$-4.59 \pm 3.15$		$-2.87 \pm 0.42$	$-3.20 \pm 0.53$
$\gamma_{M1M1}$	$-10.20 \pm 0.34$		$2.29 \pm 0.39$	$1.70 \pm 0.42$
$\gamma_{E1M2}$	$4.90 \pm 2.57$		$0.60 \pm 0.85$	$2.06 \pm 1.08$
$\gamma_{M1E2}$	$10.90 \pm 0.78$		$0.98 \pm 0.35$	$0.44 \pm 0.41$
$\alpha_{E1} + \beta_{M1}$	$13.80 \pm 0.40$		$13.78 \pm 0.40$	$13.77 \pm 0.40$
$\alpha_{E1} - \beta_{M1}$	$7.72 \pm 0.89$		$6.76 \pm 0.87$	$7.01 \pm 0.88$
$\gamma_0$	$-1.01 \pm 0.18$		$-0.99 \pm 0.18$	$-1.01 \pm 0.18$
$\gamma_\pi$	-		$5.54 \pm 1.25$	-
$\chi^2/dof$	0.38		1.30	1.20

Table 7.3: Polarizabilities (in  $10^{-4} \text{ fm}^4$ ) extracted using Paudyal and the combined (Paudyal + Collicott + Martel) data set. A  $B\chi$ PT [46] code was used to fit and extract the spin polarizabilities. Fitting errors of the model to the data are shown. A  $\chi^2$  per degree of freedom for each fit is also included.

The fitting was performed with and without the backward spin polarizability,  $\gamma_\pi$ , as a constraint for both the Paudyal and the Paudyal + Collicott + Martel data sets, as done in Sec. 7.1. When  $\gamma_\pi$  is included as a constraint in the  $B\chi$ PT code for the Paudyal data set, it returns some meaningless polarizability values, with an unacceptable  $\chi^2$  and blows up. This means that the Paudyal data set by itself does not have the required strength to fit the spin polarizabilities when using this model. However, fitting the combined data set returns some meaningful polarizability values, as shown in Table 7.3.

### 7.3 Fitting and $\chi^2$ minimization

The minimization technique in general uses an input parameters, the function to minimize and the parameters to adjust in order to minimize the function. The input parameters to this study were the desired polarizabilities, and the function passed to it was a  $\chi^2$  function. Therefore, in both the HDPV and B $\chi$ PT studies, the polarizabilities were fit using a  $\chi^2$  minimization technique. This was done by developing a formalism that introduced an analytical algebraic solution that reduced the problem to a matrix equation, and then by reversing the matrix equation, the fitted values for polarizabilities were obtained. The fitting routine employed in this study assumed a linear approximation for the dependence of the asymmetries (a similar relation exists for the cross section) on the polarizabilities as

$$A_i(\{P\}) = A_i(\{\bar{P}\}) + \sum_{j=1}^6 \frac{\partial A_i(\{\bar{P}\})}{\partial P_j} (P_j - \bar{P}_j), \quad (7.3)$$

where  $\{\bar{P}\}$  is the set of six polarizabilities used as starting points in calculating the first partial derivatives of the asymmetries and  $\{P\}$  is the set of polarizabilities at some new values. The following procedure was implemented to fit the polarizabilities:

- Select the set of six polarizabilities as the starting points, and for each of the data points, calculate a theoretical point (or constraint).
- Perturb the polarizability data one by one by some fixed step to calculate the new theoretical points.
- Determine the partial derivative by finding the difference in theory over difference in parameter.
- Solve for  $\chi^2$  minimum (Sec. 7.3.1) and determine the parameter values and errors.

- Repeat the process with current parameters until  $\chi^2$  converges to a desired limit.

### 7.3.1 Construct $\chi^2$

The  $\chi^2$  for a given observable, including the constraints that are simply linear combinations of the polarizabilities, is defined as

$$\chi^2 = \sum_{i=1}^{N_{obs}} \sum_{j=1}^{N_{pnt}} \left( \frac{A_{ij}^{exp}(E_\gamma, \theta) - A_i(E_\gamma, \theta, (\{P\}))}{\sigma_{A_{ij}(E_\gamma, \theta)}} \right)^2 + \text{constraints}, \quad (7.4)$$

where  $N_{obs}$  is the number of asymmetry observables,  $N_{pnt}$  is the number of polarizabilities,  $A_{ij}^{exp}(E_\gamma, \theta)$  is the energy and polar angle dependent experimental asymmetry,  $A_i(E_\gamma, \theta, (\{P\}))$  is the energy and polar angle dependent theoretical asymmetry (from HDPV and B $\chi$ PT ) as a function of six polarizabilities, and  $\sigma_{A_{ij}^{exp}(E_\gamma, \theta)}$  is the uncertainty in  $A_{ij}(E_\gamma, \theta)$  . The constraints in Equation 7.4 are given by

$$\begin{aligned} \text{constraints} = & \left( \frac{(\alpha + \beta)^{ex} - (\alpha + \beta)}{\sigma(\alpha + \beta)} \right)^2 + \left( \frac{\gamma_\pi^{ex} - \gamma_\pi}{\sigma\gamma_\pi} \right)^2 + \\ & \left( \frac{(\alpha - \beta)^{ex} - (\alpha - \beta)}{\sigma(\alpha - \beta)} \right)^2 + \left( \frac{\gamma_0^{ex} - \gamma_0}{\sigma\gamma_0} \right)^2 . \end{aligned} \quad (7.5)$$

$\chi^2$  was constructed for each experiment, at each polar angle bin, and summed together to get an overall  $\chi^2$  as

$$\begin{aligned} \chi^2 = & \sum_{j=1}^{N_{pnt}} \left( \frac{\sum_{2z}^j(E_\gamma, \theta) - \sum_{2z}(E_\gamma, \theta, (\{P\}))}{\sigma_{\Sigma_{2z}^j(E_\gamma, \theta)}} \right)^2 + \\ & \sum_{j=1}^{N_{pnt}} \left( \frac{\sum_{2x}^j(E_\gamma, \theta) - \sum_{2x}(E_\gamma, \theta, (\{P\}))}{\sigma_{\Sigma_{2x}^j(E_\gamma, \theta)}} \right)^2 + \\ & \sum_{j=1}^{N_{pnt}} \left( \frac{\sum_3^j(E_\gamma, \theta) - \sum_3(E_\gamma, \theta, (\{P\}))}{\sigma_{\Sigma_3^j(E_\gamma, \theta)}} \right)^2 + \text{constraints}. \end{aligned} \quad (7.6)$$

The experimental values and errors used for these constraints are the currently accepted world values for them, as discussed in Sec. 6.3.1. The minimization program ran in a loop, adjusting the values of the parameters, recomputing the theoretical values of the asymmetries and then the value of  $\chi^2$ , and finally determined where the minimum of  $\chi^2$  occurred.

The derivative of  $\chi^2$  with respect to each polarizability is

$$\begin{aligned} \frac{\partial \chi^2}{\partial P_k} &= \frac{\partial}{\partial P_k} \sum_{i=1}^{N_{obs}} \sum_{j=1}^{N_{pnt}} \left( \frac{A_{ij}^{exp}(E_\gamma, \theta) - A_i(E_\gamma, \theta, (\{P\}))}{\sigma_{A_{ij}(E_\gamma, \theta)}} \right)^2, \\ &= 2 \sum_{i=1}^{N_{obs}} \sum_{j=1}^{N_{pnt}} \left( \frac{A_{ij}^{exp}(E_\gamma, \theta) - A_i(E_\gamma, \theta, (\{P\}))}{(\sigma_{A_{ij}(E_\gamma, \theta)})^2} \right) \frac{\partial A_i(E_\gamma, \theta, (\{P\}))}{\partial P_k}. \end{aligned} \quad (7.7)$$

When the two observables are linear, the partials must be the same, i.e.,

$$\frac{\partial A_i(\{P\})}{\partial P_k} = \frac{\partial A_i(\{\bar{P}\})}{\partial P_k}. \quad (7.8)$$

We can apply this condition to our previous equation to solve for

$$\frac{\partial \chi^2}{\partial P_k} = 2 \sum_{i=1}^{N_{obs}} \sum_{j=1}^{N_{pnt}} \left( \frac{A_{ij}^{exp}(E_\gamma, \theta) - A_{ij}(E_\gamma, \theta, (\{P\}))}{(\sigma_{A_{ij}(E_\gamma, \theta)})^2} \right) \frac{\partial A_i(E_\gamma, \theta, (\{\bar{P}\}))}{\partial P_k}. \quad (7.9)$$

Since the minimum occurs at  $\frac{\partial \chi^2}{\partial P_k} = 0$ , the solution for  $\{P\}$  is at

$$\begin{aligned}
0 &= 2 \sum_{i=1}^{N_{obs}} \sum_{j=1}^{N_{pnt}} \left( \frac{A_{ij}^{exp}(E_\gamma, \theta) - \left( A_i(\{\bar{P}\}) + \frac{\partial A_i(\{\bar{P}\})}{\partial P_j} (P_j - \bar{P}_j) \right)}{(\sigma_{A_{ij}(E_\gamma, \theta)})^2} \right) \times \\
&\quad \frac{\partial A_i(E_\gamma, \theta, (\{\bar{P}\}))}{\partial P_k}, \\
&= 2 \sum_{i=1}^{N_{obs}} \sum_{j=1}^{N_{pnt}} \left( \frac{A_{ij}^{exp}(E_\gamma, \theta) - \left( A_i(\{\bar{P}\}) - \frac{\partial A_i(\{\bar{P}\})}{\partial P_j} (\bar{P}_j) \right)}{(\sigma_{A_{ij}(E_\gamma, \theta)})^2} \frac{\partial A_i(E_\gamma, \theta, (\{\bar{P}\}))}{\partial P_k} \right) - \\
&\quad 2 \sum_{i=1}^{N_{obs}} \sum_{j=1}^{N_{pnt}} \frac{1}{(\sigma_{A_{ij}(E_\gamma, \theta)})^2} \left( \frac{\partial A_i(\{\bar{P}\})}{\partial P_j} (P_j) \times \frac{\partial A_i(E_\gamma, \theta, (\{\bar{P}\}))}{\partial P_k} \right).
\end{aligned} \tag{7.10}$$

We can rearrange the second part of Equation 7.10 to isolate  $\{P\}$  and the resulting relation can be interpreted in terms of matrices as

$$0 = C_j - D_{kj}P_j \quad \rightarrow \quad P = D^{-1}C. \tag{7.11}$$

By constructing these two matrices, one can determine the values of the polarizabilities at this  $\chi^2$  minimum. The errors for these parameters (Sec. 7.1) are determined by the curvature matrix as

$$\alpha = \frac{1}{2} \begin{pmatrix} \frac{\partial^2 \chi^2}{\partial P_1^2} & \frac{\partial^2 \chi^2}{\partial P_1 P_2} & \cdot & \cdot & \cdot & \frac{\partial^2 \chi^2}{\partial P_1 P_6} \\ \frac{\partial^2 \chi^2}{\partial P_2^2 P_1} & \frac{\partial^2 \chi^2}{\partial P_2^2} & \cdot & \cdot & \cdot & \frac{\partial^2 \chi^2}{\partial P_2 P_6} \\ \cdot & \cdot & \cdot & \cdot & \cdot & \cdot \\ \cdot & \cdot & \cdot & \cdot & \cdot & \cdot \\ \frac{\partial^2 \chi^2}{\partial P_6^2 P_1} & \frac{\partial^2 \chi^2}{\partial P_6 P_2} & \cdot & \cdot & \cdot & \frac{\partial^2 \chi^2}{\partial P_6^2} \end{pmatrix}. \tag{7.12}$$

The error matrix is the inverse of the second derivative matrix of the function with respect to its free parameters. Therefore, the error matrix from Equation 7.12 is given by  $\epsilon = \alpha^{-1}$ , where

$$\epsilon = \begin{pmatrix} \sigma_{11} & \sigma_{12} & \cdot & \cdot & \cdot & \sigma_{16} \\ \sigma_{21} & \sigma_{22} & \cdot & \cdot & \cdot & \sigma_{26} \\ \cdot & \cdot & \cdot & \cdot & \cdot & \cdot \\ \cdot & \cdot & \cdot & \cdot & \cdot & \cdot \\ \cdot & \cdot & \cdot & \cdot & \cdot & \cdot \\ \sigma_{61} & \sigma_{62} & \cdot & \cdot & \cdot & \sigma_{66} \end{pmatrix}. \quad (7.13)$$

The errors associated with polarizabilities are calculated from the diagonal elements of the error matrix as  $\sigma_1 = \sqrt{\sigma_{11}}$ ,  $\sigma_2 = \sqrt{\sigma_{22}}$ , etc.

### 7.3.2 Verification of the Fitting Procedure

It often happens that the solution of a minimization problem using the  $\chi^2$  minimization technique seems very straightforward, but the calculation or interpretation of the resulting parameter uncertainties is considerably more complicated. There were several items that needed to be checked in the  $\chi^2$  minimization technique. For example, one of the main concerns that can be raised is whether the errors are being calculated properly. Furthermore, one can argue whether the linear dependence on the polarizabilities is really linear or not, and also one can argue whether there is any dependence on the starting values for the polarizabilities or not. These concerns are explained in the following section.

#### 7.3.2.1 Error Calculations

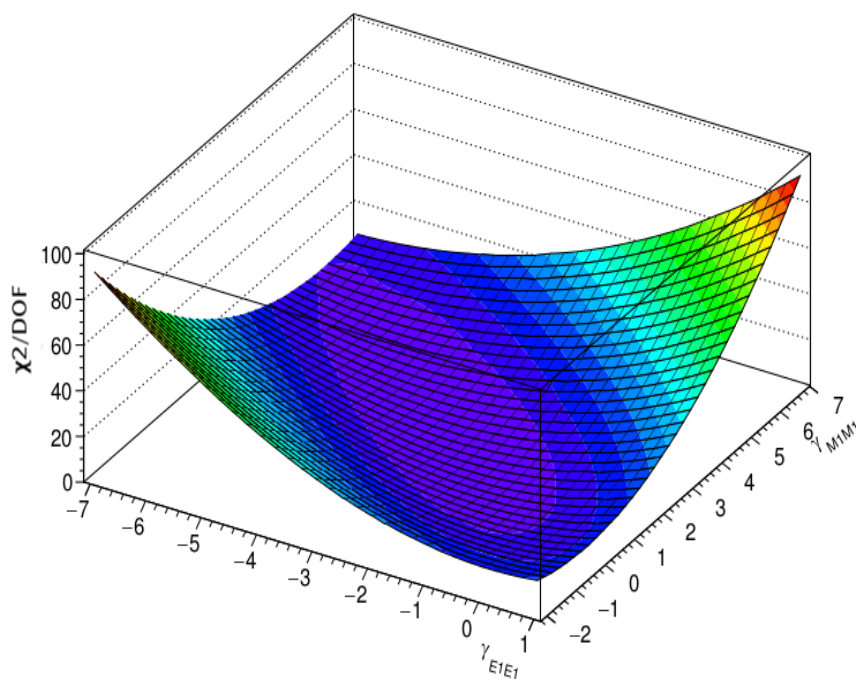
There are several ways to check if the errors are being properly calculated. It is obviously difficult to check if the errors in six dimensional phase space are being

correctly calculated or not. However, the problem can be simplified. For example, among the six input parameters, we can fix some of the parameters and scan over the remaining parameters and determine the  $\chi^2$  at each point. In this study, four out of the six parameters were fixed at their resulting values and the remaining two parameters were scanned over the  $\chi^2$  phase space for all permutations to see the  $\chi^2 + 1$  ellipsoid. This was done for all permutations but only three of them are shown in Figs. 7.1-7.3. One can see that the resulting  $\chi^2$  minima are clearly not only well defined but also well behaved.

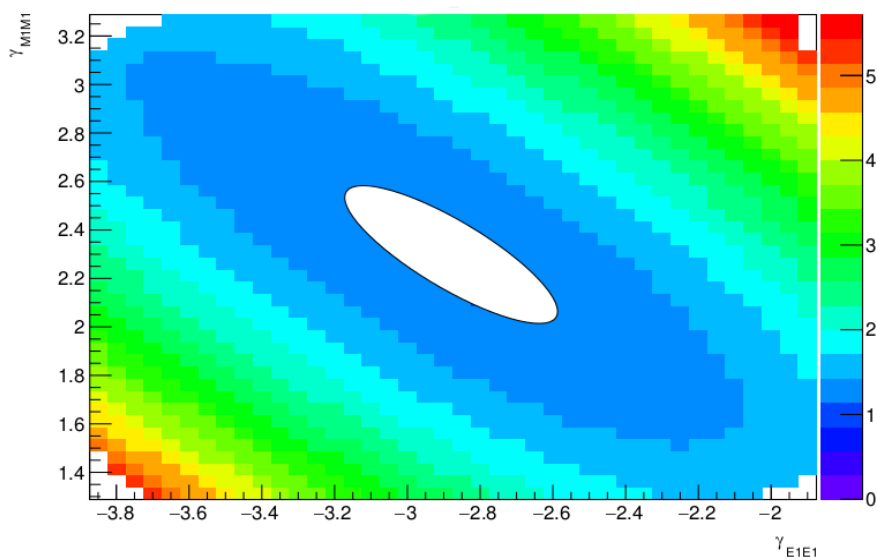
### 7.3.2.2 Linearity

In Sec. 7.3.1, while deriving the matrix equation we assumed that the polarizabilities are linearly dependent. This was an integral part of the  $\chi^2$  minimization method. Therefore, it is important to check whether they are actually linear or not. This can be tested by varying the given observable over a range of values for a single polarizability, and determining if the change is indeed linear. As can be seen from the Figs. 7.4-7.5, these are not strictly linear but the difference from linearity is quite small.

In addition, this can be handled by iterating the process multiple times. We know that the iterative process should be convergent, so the iteration can be continued until the old and new  $\chi^2$  values differ by less than some desired convergence factor. The number of iterations necessary therefore depends on this convergence factor as well as the step size chosen in calculating the partial derivatives. The linear approximation is valid for a relatively small step size compared to the errors.

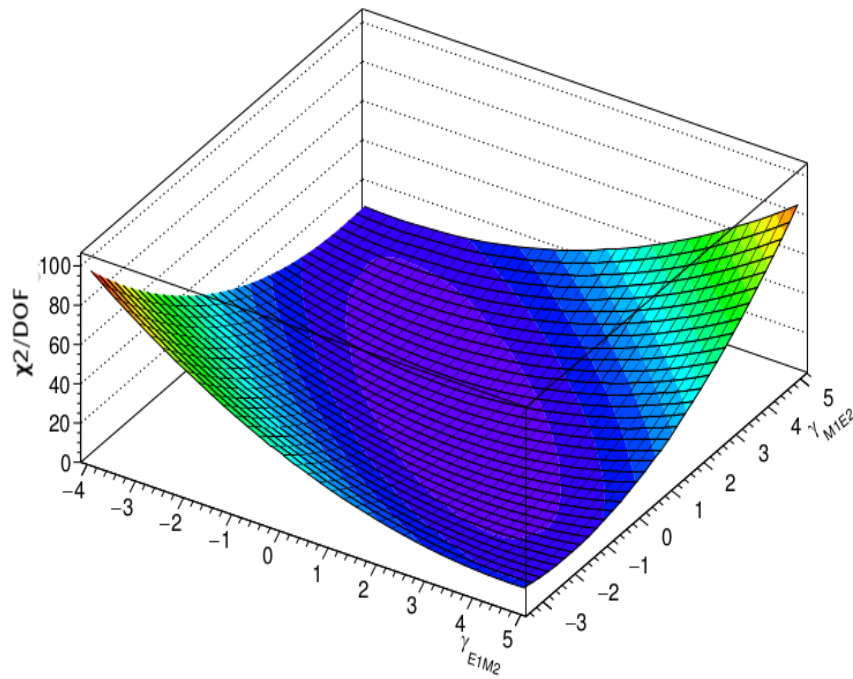


(a)

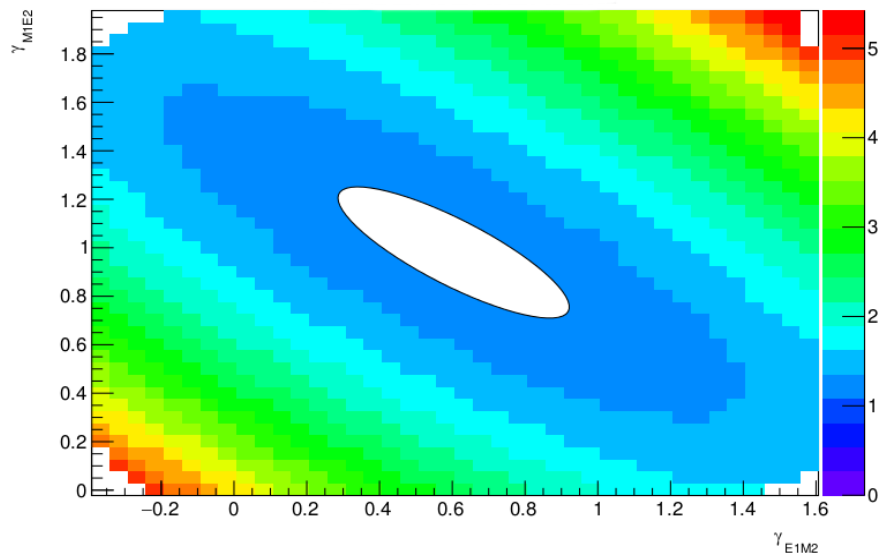


(b)

Figure 7.1: (a)  $\chi^2/\text{DOF}$  as a function of  $\gamma_{E1E1}$  and  $\gamma_{M1M1}$ , keeping the other four polarizabilities fixed at their previously fitted values. (b) Zoomed in version of the two dimensional projection, along with corresponding  $\chi^2 + 1$  ellipsoid.

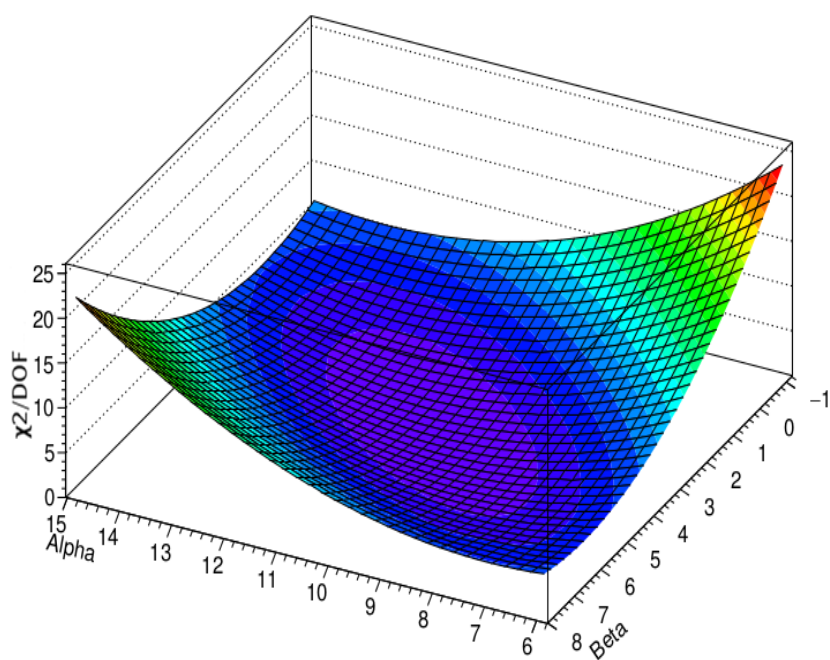


(a)

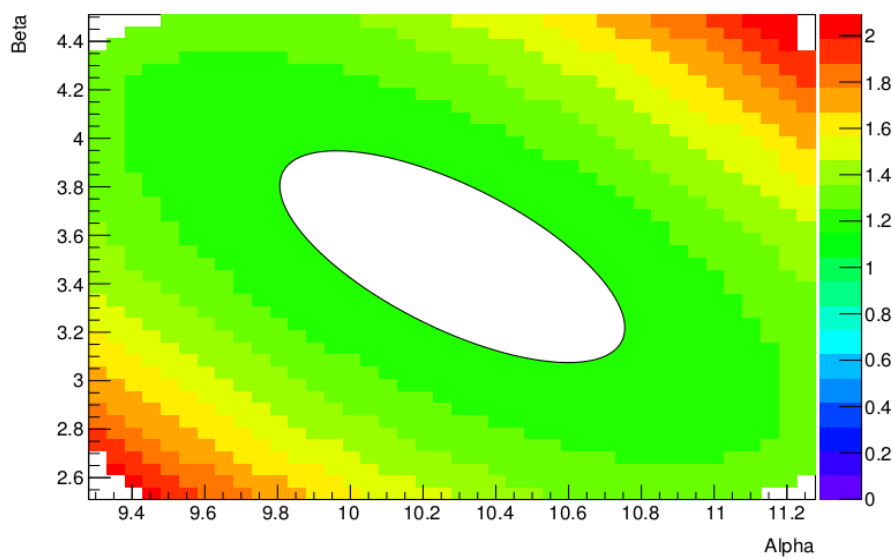


(b)

Figure 7.2: (a)  $\chi^2/\text{DOF}$  as a function of  $\gamma_{E1M2}$  and  $\gamma_{M1E2}$ , keeping the other four polarizabilities fixed at their previously fitted values. (b) Zoomed in version of the two dimensional projection, along with corresponding  $\chi^2 + 1$  ellipsoid.



(a)



(b)

Figure 7.3: (a)  $\chi^2/\text{DOF}$  as a function of  $\alpha_{E1}$  and  $\beta_{M1}$ , keeping the other four polarizabilities fixed at their previously fitted values. (b) Zoomed in version of the two dimensional projection, along with corresponding  $\chi^2 + 1$  ellipsoid.

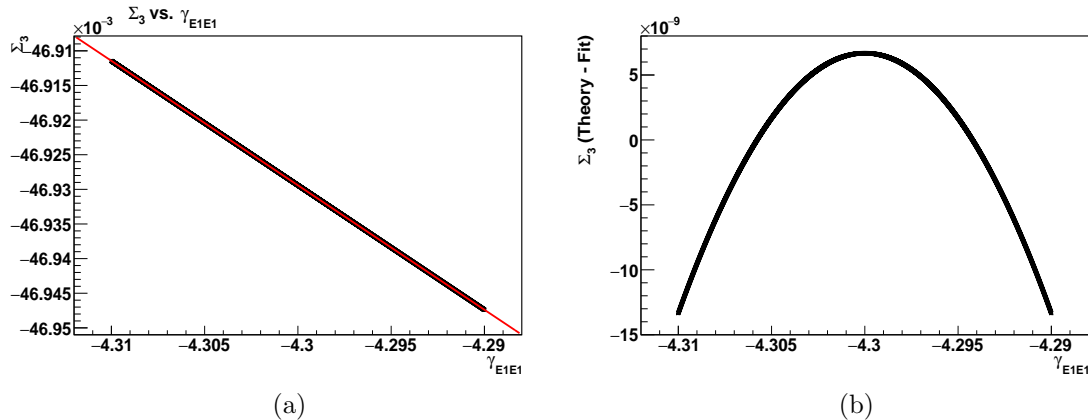


Figure 7.4:  $\Sigma_3$  for different values of  $\gamma_{E1E1}$  at  $E_\gamma = 273 \pm 10.1$  MeV. (a) shows the theory values fit with a line. (b) shows the difference between the theory points, and this fit.

### 7.3.2.3 Starting Value of Polarizabilities

The sensitivity to the starting polarizabilities is one of the challenges for fitting because, in the case of extreme non-linearity, or large correlations between the parameters, it is important to avoid so called “local minima” from the global minimum in the  $\chi^2$  phase space. This was tested by varying the input parameters randomly over a wide range of polarizabilities and in this study  $\pm 5$  in the standard units were chosen. The resulting values of the six polarizabilities from the B $\chi$ PT and HDPV model fit are shown in Fig. 7.6 and Fig. 7.7. As can be seen from these plots, the fits in all of them converge to approximately the same value. This means that the variance in each plot is much less than the actual fitted parameter errors.

## 7.4 Study of Model Dependence

Given the lack of required strength to fit the spin polarizabilities using the B $\chi$ PT code for the Paudyal data set, the Paudyal + Collicott + Martel combined data set is used to study the model dependence. Fig. 7.8 shows the comparison of the fitting

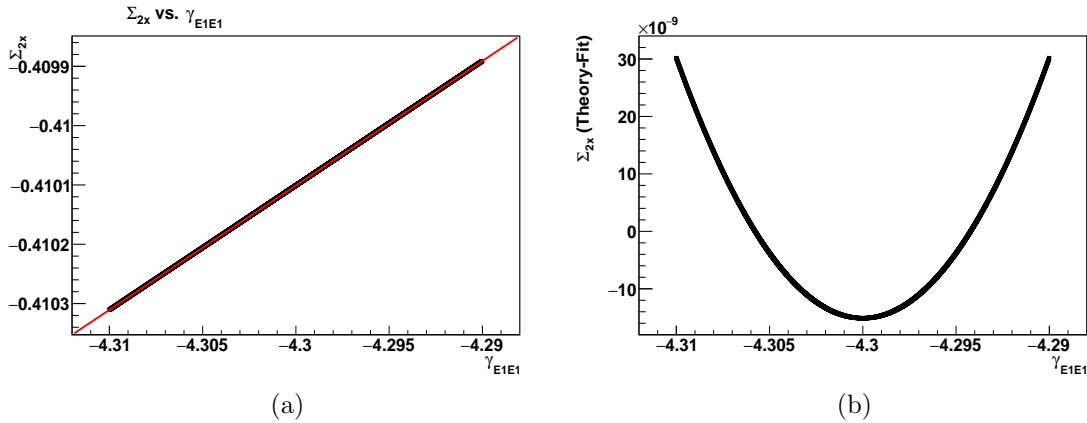


Figure 7.5:  $\Sigma_{2x}$  for different values of  $\gamma_{E1E1}$  at  $E_\gamma = 273 - 303$  MeV. (a) shows the theory values fit with a line. (b) shows the difference between the theory points, and this fit.

results obtained from the HDPV and B $\chi$ PT models. It is clear from these plots that the fit results from HDPV model for  $\gamma_{E1E1}$  differ by about  $3\sigma$  and  $\gamma_{M1M1}$  differ by about  $2\sigma$  compared to B $\chi$ PT model. B $\chi$ PT prefers smaller  $\gamma_{E1E1}$ ,  $\gamma_{M1M1}$  magnitude than HDPV. Within the uncertainties, the results for  $\gamma_{E1M2}$  and  $\gamma_{M1E2}$  from the two HDPV and B $\chi$ PT model fits are in good agreement, indicating that the model dependence of the polarizability fitting is comparable to, or smaller than, the fitting errors from data fitting.

## 7.5 Comparison With Theory Models

The extracted proton spin polarizabilities can be compared to several theoretical models. Table 7.4 lists some of the theoretical calculations. The comparison of four spin polarizability results based on the HDPV and B $\chi$ PT model fits including the best estimate based on their weighted average is shown in Fig. 7.8. The HDPV, DPV, B $\chi$ PT, HB $\chi$ PT and K-matrix calculations resulted in similar spin polarizability values, with the exception of large negative  $\gamma_{E1M2}$  by the K-matrix prediction.

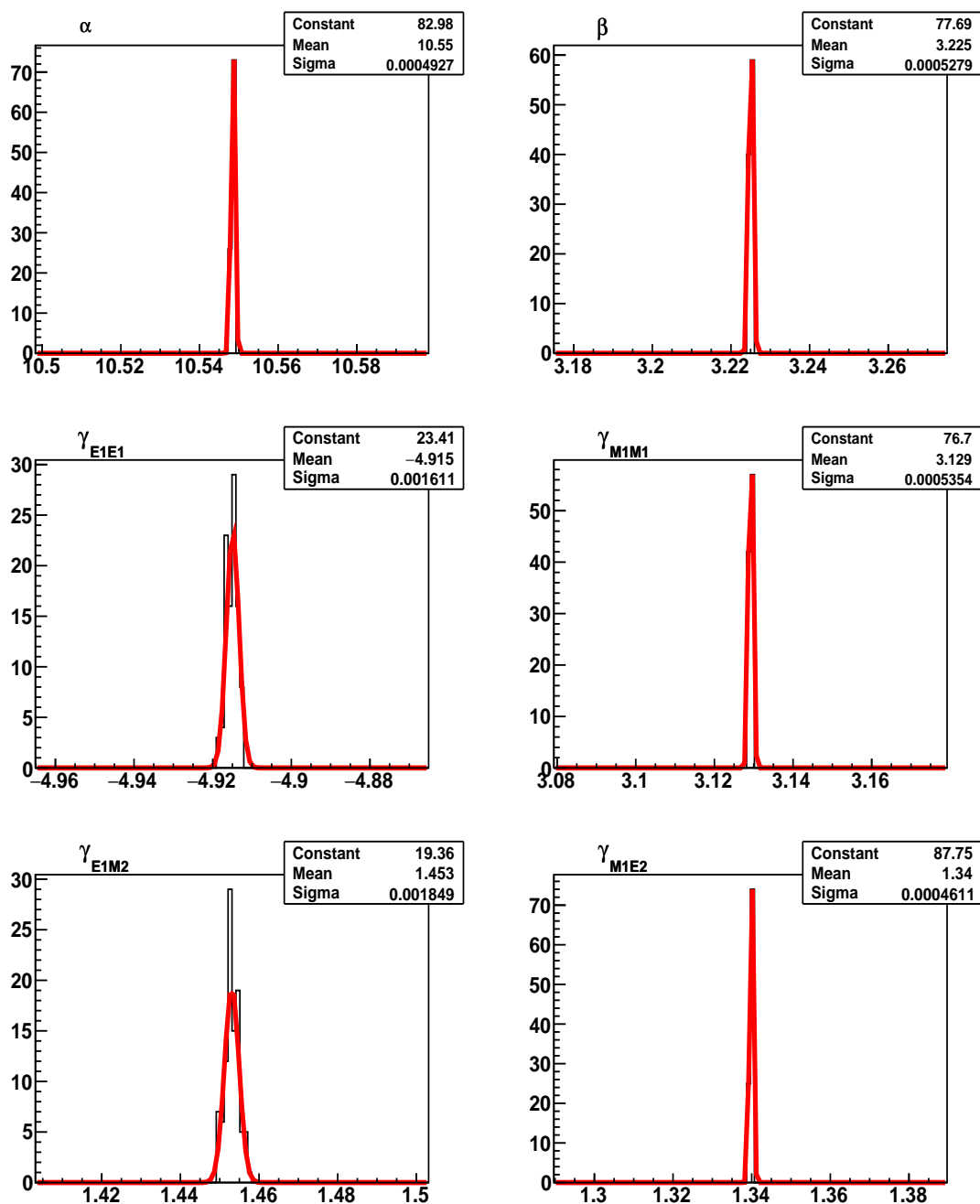


Figure 7.6: HDPV model fits with partial derivatives calculated using parameter steps of 0.001. The spread in each of these distributions represent the error in the fitting of each polarizability and y-axis represent the number of fits.

However, some of the theory calculations lack an uncertainty estimate, for example the fourth order ( $p$ -expansion) and a small scale ( $\epsilon$ -expansion) calculations seem to

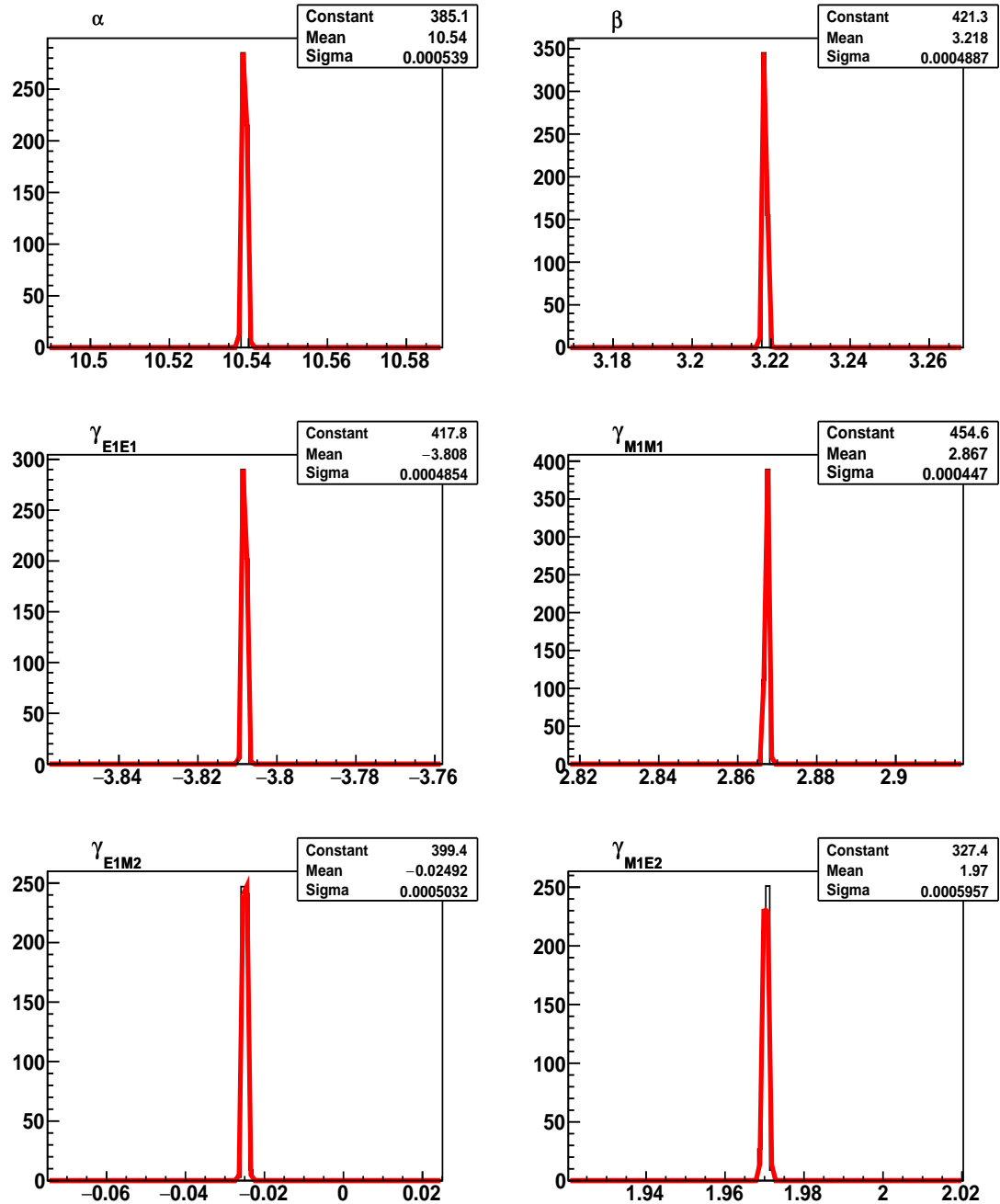


Figure 7.7:  $B\chi$ PT model fits with partial derivatives calculated using parameter steps of 0.001. The spread in each of these distributions represent the error in the fitting of each polarizability and y-axis represent the number of fits.

be quite different from the remaining model predictions and also do not agree well with the experimental spin polarizabilities.

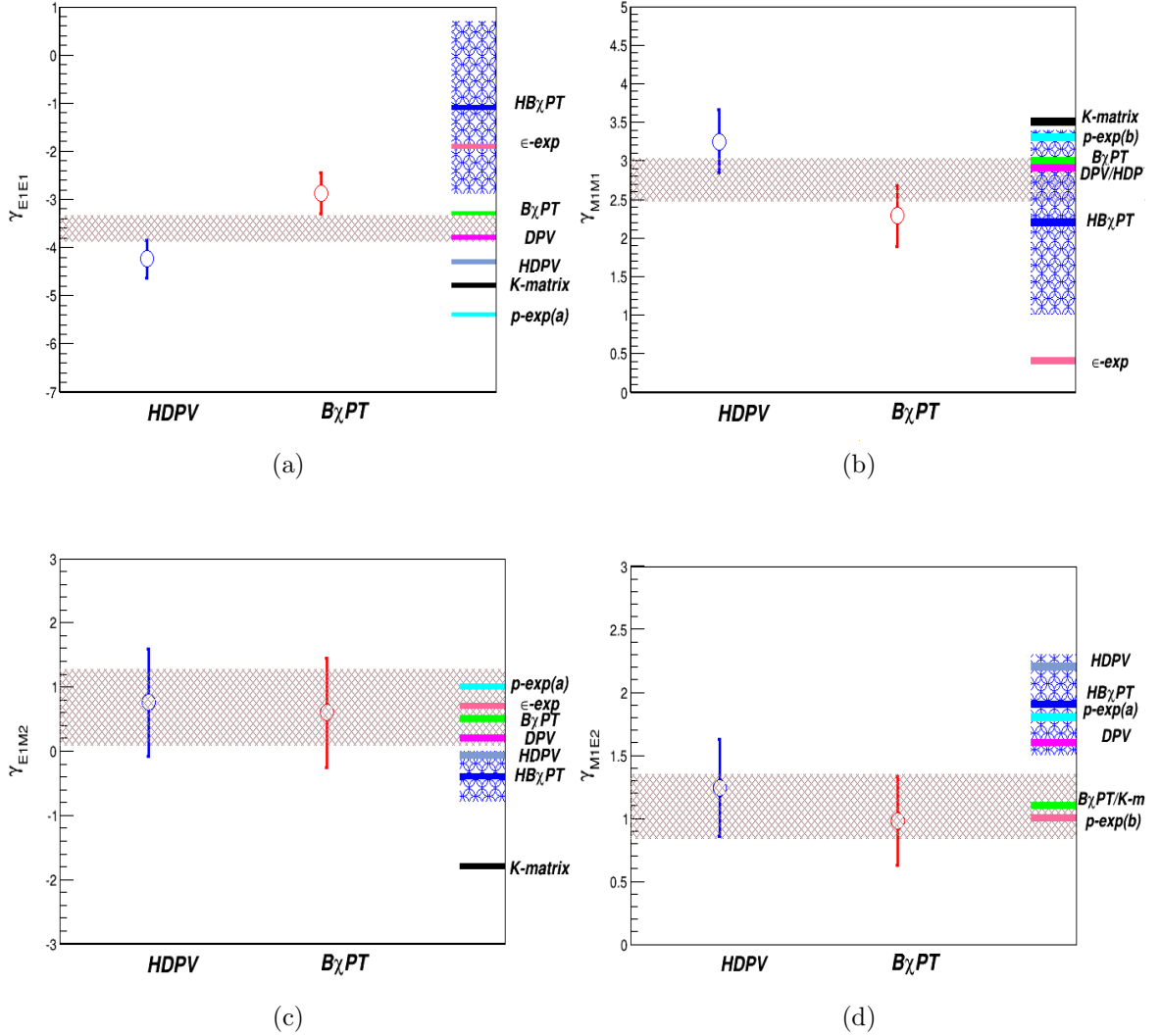


Figure 7.8: Comparison of four spin polarizabilities in  $10^{-4} \text{ fm}^4$  based on fitting results from the HDPV and  $B_{\chi PT}$  models. The colour bands on the right show different theory model predictions and the blue background shows the uncertainty in the  $HB_{\chi PT}$  model prediction. The horizontal colour band is the weighted average of the fitting results from the HDPV and  $B_{\chi PT}$  models. (a)  $\gamma_{E1E1}$ , (b)  $\gamma_{M1M1}$ , (c)  $\gamma_{E1M2}$ , (d)  $\gamma_{M1E2}$ .

Nevertheless, it is rather clear from the table and figure that the extracted polarizabilities within this work, both via  $\sum_{2z}$  asymmetry measurement and a combination of a  $\sum_{2x}$ ,  $\sum_3$  and  $\sum_{2z}$  asymmetry measurement, prefer some models over the others. For example, the extracted  $\gamma_{M1M1}$  via HDPV model fit is in good agreement with the

	HDPV	DPV	$\mathcal{O}(p^4)_a$	$\mathcal{O}(p^4)_b$	$\mathcal{O}(\epsilon^3)$	HB $\chi$ PT	B $\chi$ PT	K-matrix
$\gamma_{E1E1}$	-4.3	-3.8	-5.4	1.3	-1.9	$-1.1 \pm 1.8$	-3.3	-4.8
$\gamma_{M1M1}$	2.9	2.9	1.4	3.3	0.4	$2.2 \pm 1.2$	3.0	3.5
$\gamma_{E1M2}$	-0.02	0.5	1.0	0.2	0.7	$-0.4 \pm 0.4$	0.2	-1.8
$\gamma_{M1E2}$	2.2	1.6	1.0	1.8	1.9	$1.9 \pm 0.4$	1.1	1.1
$\gamma_0$	-0.8	-1.1	1.9	-3.9	-1.1	-2.6	-1.0	2.0
$\gamma_\pi$	9.4	7.8	6.8	6.1	3.5	5.6	7.2	11.2

Table 7.4: Theoretical model predictions of the proton spin polarizabilities in  $10^{-4} \text{ fm}^4$ . HDPV and DPV are once-subtracted fixed- $t$  and fixed-angle ( $\theta_{lab} = 180^\circ$ ) dispersion relation calculations [95],  $\mathcal{O}(p^4)_a$  and  $\mathcal{O}(p^4)_b$  are fourth order ( $p$ -expansion) calculations [45],  $\mathcal{O}(\epsilon^3)$  is a small scale ( $\epsilon$ -expansion) calculation [96], HB $\chi$ PT is a heavy baryon chiral perturbation calculation [97], B $\chi$ PT is a covariant baryon chiral perturbation calculation [98] and K-matrix is a dressed K-matrix model based on K-matrix formalism and dispersion relations [99].

HDPV, DPV, covariant B $\chi$ PT and K-matrix predictions, while the extracted  $\gamma_{M1M1}$  via B $\chi$ PT model fit is in good agreement with only the HB $\chi$ PT model prediction. Similarly, the extracted  $\gamma_{E1E1}$  via HDPV model fit is in good agreement with the HDPV, DPV, covariant and K-matrix predictions, but the extracted  $\gamma_{E1E1}$  via B $\chi$ PT model fit is off by about  $1-5\sigma$  from all the model predictions. It is to be noted here that the model predictions are based on the old data sets including results from previous experiments and when we add the new data sets to the old data set, the models give better result. This means with the addition of new data sets, the HDPV and B $\chi$ PT models are not only handling the data in a consistent manner but also giving better results compared to the old data sets.

## 7.6 Outlook

The aim of the experimental proposal submitted to the MAMI Program Advisory Committee (PAC) for the set of three Compton scattering experiments was not only to perform a measurement of the single and double polarization observables, but also to investigate the sensitivities of the proton spin polarizabilities to the  $\sum_{2x}$ ,  $\sum_3$  and  $\sum_{2z}$

asymmetries using data collected only at the MAMI tagged photon facility. These asymmetries certainly bench-marked a significant achievement in their own right, being the first double-polarized Compton scattering asymmetries ever measured. The first achievement of the Compton program at MAMI has been published by Martel, *et al.* [49], by investigating the sensitivities on the  $\sum_{2x}$  asymmetry and extracted the set of spin polarizabilities. The second achievement was the measurement of the  $\sum_3$  asymmetry by Collicott, *et al.* [51], and the extraction of the same set of spin polarizabilities. The final achievement towards this program was the measurement of the  $\sum_{2z}$  asymmetry and the extraction of the individual spin polarizabilities presented in this work. Since all three experiments have been completed, a combination of these experimental results allowed for a thorough extraction of the spin polarizabilities and the uncertainties in  $\gamma_{E1E1}$ ,  $\gamma_{M1M1}$ ,  $\gamma_{E1M2}$  are improved by a factor of two to four, but the uncertainty in  $\gamma_{M1E2}$  remained unchanged.

Given the completion of the analysis of three Compton scattering experiments at MAMI, the global analysis of the subsequent asymmetry data is a milestone in this area, leading to the extraction of all four proton spin polarizabilities:  $\gamma_{E1E1}$ ,  $\gamma_{M1M1}$ ,  $\gamma_{E1M2}$  and  $\gamma_{M1E2}$ . However, an attainable goal in this area is to further reduce the uncertainties in spin polarizabilities by approximately 50%. The A2 Collaboration at MAMI already has plans to collect more data in the near future. Since the uncertainty in the  $\sum_{2z}$  asymmetry is small compared to the uncertainty in the two other asymmetry results, the data will only be collected to measure  $\sum_{2x}$  (Sec. 2.2.2) and  $\sum_3$  (Sec. 2.2.3) by the end of 2017 and 2018, respectively.

# Appendix A

## Experimental Trigger

### Experiment Trigger

last update: 14.11.2013 Firmware (LSB): 0x75  
 Peter-Bernd Otte and John R.M. Annand

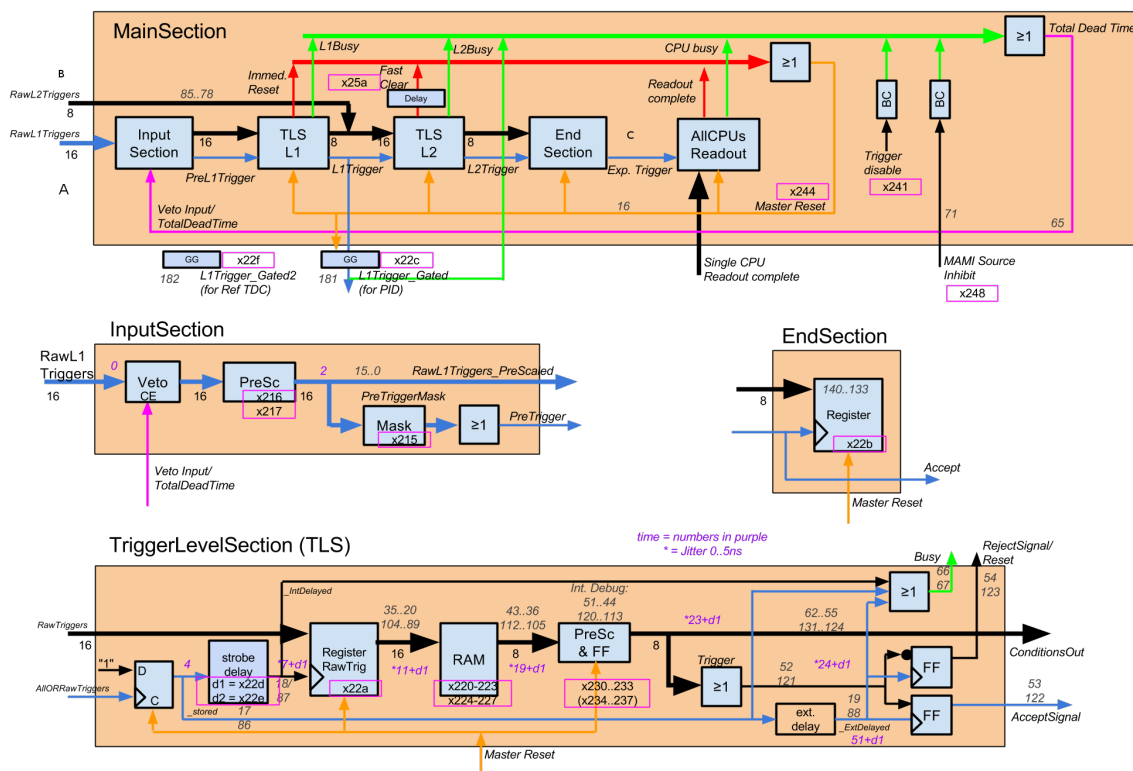


Figure A.1: A schematic diagram for the subcomponents of an experimental trigger (after October 2012) [81].

### CB Experiment Trigger - Components

last update: 7.11.2013  
Peter-Bernd Otte

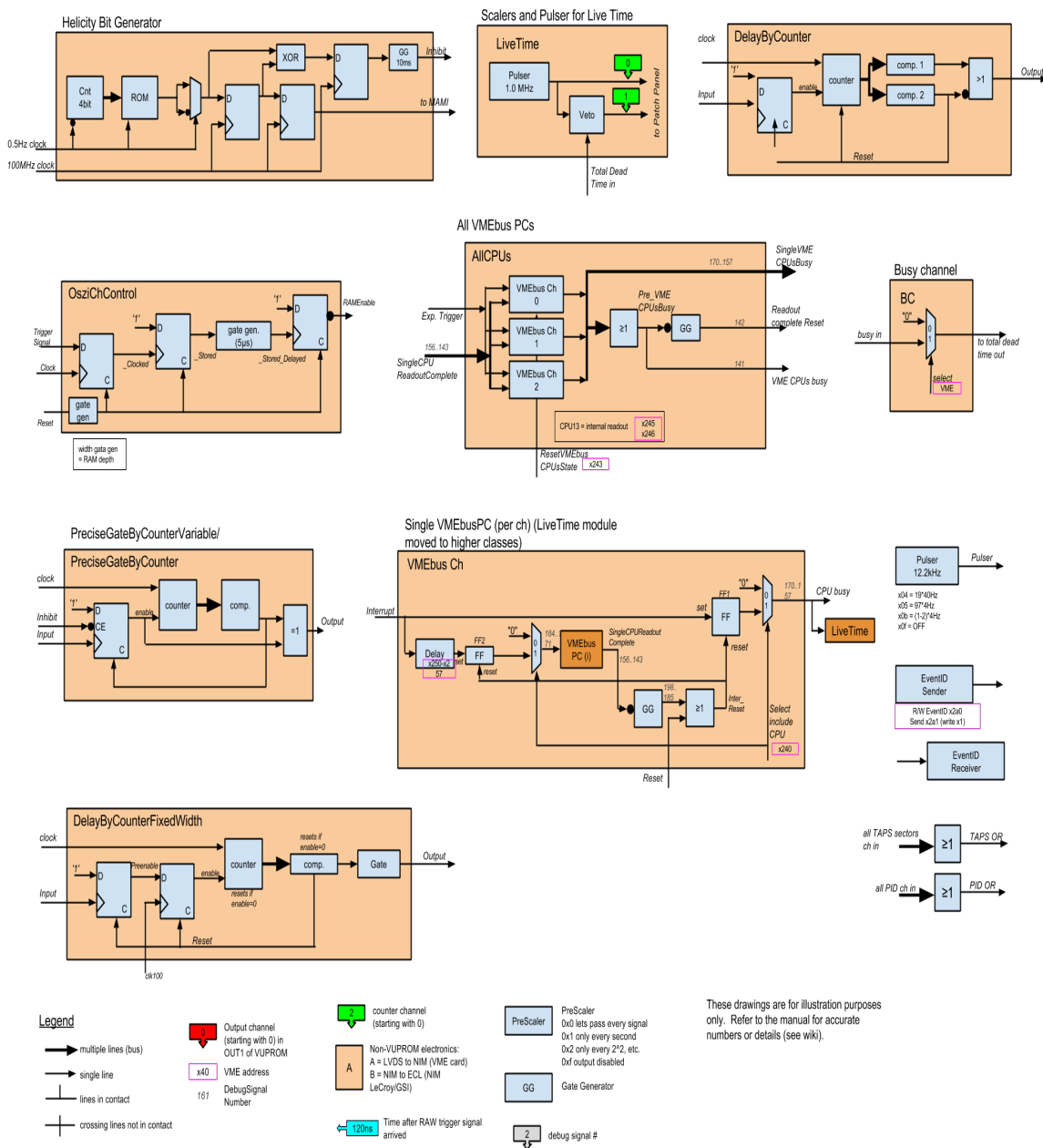


Figure A.2: A schematic diagram of the experimental trigger components (after October 2012) [81].

# Appendix B

## Carbon Scaling

### B.0.1 Extra Scaling Factor

Data Set	$\pi^0$ Angular Range	Extra scaling factor		
		$E_\gamma = 265\text{-}285$ MeV	$E_\gamma = 285\text{-}305$ MeV	$E_\gamma = 310\text{-}330$ MeV
Anti-parallel	80 – 95°	$1.216 \pm 0.044$	$1.269 \pm 0.035$	$1.335 \pm 0.040$
	95 – 110°	$1.211 \pm 0.035$	$1.260 \pm 0.037$	$1.357 \pm 0.039$
	110 – 125°	$1.204 \pm 0.037$	$1.262 \pm 0.039$	$1.364 \pm 0.040$
	125 – 140°	$1.228 \pm 0.036$	$1.272 \pm 0.038$	$1.356 \pm 0.041$
	140 – 150°	$1.221 \pm 0.035$	$1.293 \pm 0.036$	$1.409 \pm 0.037$
Parallel	80 – 95°	$1.278 \pm 0.032$	$1.287 \pm 0.034$	$1.380 \pm 0.036$
	95 – 110°	$1.216 \pm 0.034$	$1.289 \pm 0.035$	$1.373 \pm 0.035$
	110 – 125°	$1.214 \pm 0.037$	$1.261 \pm 0.038$	$1.342 \pm 0.039$
	125 – 140°	$1.211 \pm 0.036$	$1.254 \pm 0.037$	$1.341 \pm 0.038$
	140 – 150°	$1.127 \pm 0.061$	$1.212 \pm 0.087$	$1.418 \pm 0.024$

Table B.1: 2014 beamtime: The extra carbon scaling factors determined for three energy and five angular bins for anti-parallel and parallel configurations.

Data Set	$\pi^0$ Angular Range	Extra scaling factor		
		$E_\gamma = 265-285$ MeV	$E_\gamma = 285-305$ MeV	$E_\gamma = 310-330$ MeV
Anti-parallel	80 – 95°	$1.234 \pm 0.032$	$1.262 \pm 0.011$	$1.305 \pm 0.042$
	95 – 110°	$1.246 \pm 0.034$	$1.281 \pm 0.012$	$1.317 \pm 0.038$
	110 – 125°	$1.241 \pm 0.037$	$1.291 \pm 0.054$	$1.294 \pm 0.041$
	125 – 140°	$1.254 \pm 0.033$	$1.299 \pm 0.041$	$1.316 \pm 0.041$
	140 – 150°	$1.268 \pm 0.024$	$1.288 \pm 0.045$	$1.309 \pm 0.036$
Parallel	80 – 95°	$1.267 \pm 0.032$	$1.283 \pm 0.032$	$1.318 \pm 0.036$
	95 – 110°	$1.232 \pm 0.034$	$1.291 \pm 0.042$	$1.303 \pm 0.0352$
	110 – 125°	$1.228 \pm 0.036$	$1.299 \pm 0.077$	$1.312 \pm 0.039$
	125 – 140°	$1.239 \pm 0.038$	$1.286 \pm 0.069$	$1.321 \pm 0.038$
	140 – 150°	$1.167 \pm 0.024$	$1.292 \pm 0.086$	$1.301 \pm 0.034$

Table B.2: 2015 beamtime: The extra carbon scaling factors determined for three energy and five angular bins for anti-parallel and parallel configurations.

## B.0.2 Corrected Scaling Factor

Data Set	$\pi^0$ Angular Range	Corrected scaling factor		
		$E_\gamma = 265\text{-}285$ MeV	$E_\gamma = 285\text{-}305$ MeV	$E_\gamma = 310\text{-}330$ MeV
Anti-parallel	80 – 95°	2.119 ± 0.373	1.935 ± 0.354	1.810 ± 0.346
	95 – 110°	2.110 ± 0.368	1.921 ± 0.352	1.840 ± 0.351
	110 – 125°	2.100 ± 0.366	1.924 ± 0.353	1.849 ± 0.353
	125 – 140°	2.140 ± 0.373	1.939 ± 0.355	1.838 ± 0.351
	140 – 150°	2.128 ± 0.371	1.971 ± 0.361	1.910 ± 0.364
Parallel	80 – 95°	2.227 ± 0.387	1.962 ± 0.358	1.871 ± 0.356
	95 – 110°	2.119 ± 0.369	1.965 ± 0.359	1.861 ± 0.354
	110 – 125°	2.116 ± 0.369	1.923 ± 0.352	1.819 ± 0.347
	125 – 140°	2.110 ± 0.368	1.912 ± 0.350	1.818 ± 0.347
	140 – 150°	1.964 ± 0.354	1.848 ± 0.359	1.892 ± 0.364

Table B.3: 2014 beamtime: The corrected carbon scaling factors determined for three energy and five angular bins for anti-parallel and parallel configurations.

Data Set	$\pi^0$ Angular Range	Corrected scaling factor		
		$E_\gamma = 265-285$ MeV	$E_\gamma = 285-305$ MeV	$E_\gamma = 310-330$ MeV
Anti-parallel	80 – 95°	$5.649 \pm 0.620$	$5.758 \pm 0.639$	$5.888 \pm 0.663$
	95 – 110°	$5.704 \pm 0.628$	$5.845 \pm 0.649$	$5.942 \pm 0.663$
	110 – 125°	$5.681 \pm 0.630$	$5.890 \pm 0.696$	$5.838 \pm 0.656$
	125 – 140°	$5.740 \pm 0.631$	$5.927 \pm 0.683$	$5.937 \pm 0.667$
	140 – 150°	$5.804 \pm 0.629$	$5.877 \pm 0.682$	$5.906 \pm 0.657$
Parallel	80 – 95°	$5.800 \pm 0.636$	$5.895 \pm 0.664$	$5.919 \pm 0.662$
	95 – 110°	$5.640 \pm 0.622$	$5.890 \pm 0.679$	$5.879 \pm 0.650$
	110 – 125°	$5.621 \pm 0.622$	$5.927 \pm 0.744$	$5.919 \pm 0.662$
	125 – 140°	$5.672 \pm 0.630$	$5.868 \pm 0.721$	$5.960 \pm 0.665$
	140 – 150°	$5.800 \pm 0.629$	$5.895 \pm 0.761$	$5.870 \pm 0.651$

Table B.4: 2015 beamtime: The corrected carbon scaling factors determined for three energy and five angular bins for anti-parallel and parallel configurations.

### B.0.3 Detection Efficiency Fitting Parameters

Polar Range	Parameter (L)	Parameter (k)	Parameter ( $x_0$ )
20 - 25°	0.627059	0.0743982	83.6834
25 - 30°	0.602448	0.0971172	79.3318
30 - 35°	0.647931	0.0898588	78.2212
35 - 40°	0.554969	0.146317	68.6574
40 - 45°	0.517886	0.193844	64.6669
45 - 50°	0.515316	0.218918	62.2127

Table B.5: Logistic function (Equation 5.7) fitting parameters for different polar ranges (in degrees). These fitting parameters are from the parallel data set for the 2014 beamtime.

Polar Range	Parameter (L)	Parameter (k)	Parameter ( $x_0$ )
20 - 25°	0.627059	0.0743982	83.6834
25 - 30°	0.602448	0.0971172	79.3318
30 - 35°	0.647931	0.0898588	78.2212
35 - 40°	0.554969	0.146317	68.6574
40 - 45°	0.517886	0.193844	64.6669
45 - 50°	0.515316	0.218918	62.2127

Table B.6: Logistic function (Equation 5.7) fitting parameters for different polar angles in degrees. These fitting parameters are from the anti-parallel data set for the 2014 beamtime.

# Appendix C

## $\Sigma_{2z}$ Above $\gamma p \rightarrow \pi^0 \pi^0 p$ threshold

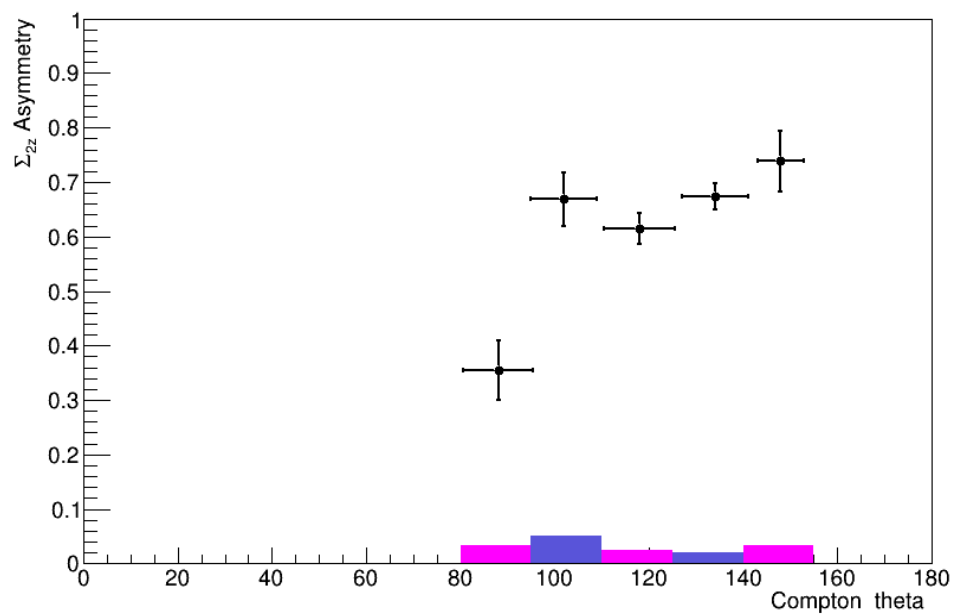


Figure C.1:  $\Sigma_{2z}$  asymmetry results at  $E_\gamma = 310 - 330$  MeV.

### C.0.4 Systematic Errors at $E_\gamma = 285 - 305$ MeV

Beamtime	Compton Angle	Types of Error ( $\pm$ )						
		stat	syst-rand	pt-to-pt	syst-target	syst-beam	syst-carbon	syst-scale
2014	88°	0.0577	0.0208	0.0613	0.0040	0.0020	0.0125	0.0133
	102°	0.0378	0.0328	0.0500	0.0066	0.0033	0.0164	0.0179
	118°	0.0316	0.0236	0.0394	0.0094	0.0047	0.0188	0.0215
	134°	0.0203	0.0330	0.0387	0.0120	0.0066	0.0263	0.0297
	148°	0.0397	0.0430	0.0585	0.0144	0.0072	0.0358	0.0393
2015	88°	0.0639	0.0117	0.0650	0.0021	0.0010	0.0088	0.0100
	102°	0.0514	0.0299	0.0594	0.0061	0.0030	0.0149	0.0163
	118°	0.0502	0.0247	0.0560	0.0099	0.0049	0.0198	0.0227
	134°	0.0273	0.0340	0.0436	0.0136	0.0068	0.0272	0.0312
	148°	0.0469	0.0473	0.0666	0.0156	0.0078	0.0395	0.0432

Table C.1: Summary of correlated as well as uncorrelated error analysis for the Compton  $\sum_{2z}$  asymmetry at  $E_\gamma = 285 - 305$  MeV.

# Bibliography

- [1] Niels H. D. Bohr. The quantum postulate and the recent development of atomic theory. *Nature Supplement.*, **121**:580–590, (1925).
- [2] E. N Andrade. *Rutherford and the Nature of the Atom*. Doubleday, New York, (1964).
- [3] J. Chadwick. Possible existence of a neutron. *Nature*, **129**:3252, (1932).
- [4] D. Griffiths. *Introduction to Elementary Particles, Second, Revised Edition*. John Wiley & Sons, Inc., New York, (2010).
- [5] M. Gell-Mann. Proc. Phys. Math. Soc. Japan. *Phys. Lett.*, **8**(3):214, (1964).
- [6] G. Zweig. Proc. Phys. Math. Soc. Japan. *CERN Report No.8182*, **401**, (1964).
- [7] de Broglie L. A tentative theory of light quanta. *Phil. Mag.*, **47**:446, (1924).
- [8] W. Heisenberg. The physical principles of the quantum theory. *Magazine of Physics*, **43**:172–198, (1927).
- [9] E. Schrodinger. To Heisenberg's uncertainty principle. *Conference reports of the Prussian Academy of Sciences, Physical-Mathematical Class*, **14**:296–303, (1930).
- [10] Wikimedia Commons. [https://upload.wikimedia.org/wikipedia/Standard\\_Model](https://upload.wikimedia.org/wikipedia/Standard_Model).

- [11] F. Halzen, A.D. Martin. *Quarks and Leptons: An introduction course in Modern Particle Physics, Second, Revised Edition*. John Wiley & Sons, Inc., New York, (1984).
- [12] R. D. Field. *Applications of Perturbative QCD*. Addison-Wesley Publishing Company, New York, (1989).
- [13] C. Patrignani et al. The review of particle physics. *Chin. Phys. C*, **40**:100001, (2016).
- [14] I. G. Aznauryan, et al. Studies of nucleon resonance structure in exclusive meson electroproduction. *arXiv:1212.4891v2*, nucl-th(3), (2013).
- [15] Huey-Wen, Meyer, Harvey B. (Eds.) Lin. *Lattice QCD for Nuclear Physics*. Springer, New York, (1998).
- [16] A. H. Compton. Proc. Phys. Math. Soc. Japan. *Phys. Rev.*, **21**(5):483, (1923).
- [17] D. Drechsel, B. Pasquini and M. Vanderhaeghen. Higher order polarizabilities of the proton. *Phys.Rev. C.*, **61**, (2000).
- [18] Olmos de Leon, et. al. Low-energy Compton scattering and the polarizabilities of the proton. *Euro.Phys.J.*, **10**:207–215, (2001).
- [19] F. J. Federspiel, et al. Proton Compton Effect: A measurement of the electric and magnetic polarizabilities of the proton. *Phys.Rev. Let.*, **67**(12):1511, (1991).
- [20] J. McGovern, D. Phillips, and H. Griesshammer. Compton scattering from the proton in an effective field theory with explicit delta degrees of freedom. *Eur.Phys. J.*, **49**, (2013).
- [21] A. Zieger, et al. 180-degrees Compton scattering by the proton below the pion threshold. *Phys.Rev. Let.*, **278**, (1992).

- [22] Baldin A. M. Polarizability of nucleons. *Nucl. Phys*, **18**:310–317, (1960).
- [23] S. Gerasimov. A sum rule for magnetic moments and the damping of the nucleon magnetic moment in nuclei. *Sov. J. Nucl. Phys.*, **2**:403, (1966).
- [24] J. D. Jackson. *Classical Electrodynamics, Third Edition*. John Wiley & Sons, Inc., New York, (1998).
- [25] S. Drell and A. Hearn. Exact sum rule for nucleon magnetic moments. *Phys. Rev. Lett.*, **16**(908), (1966).
- [26] S. Ragusa. Third-order spin polarizabilities of the nucleon. *Physical Review D*, **47**(3757), (1993).
- [27] J. A. McGovern, D. R. Phillips and G. Feldman. Using effective field theory to analyse low-energy compton scattering data from protons and light nuclei. *Prog. Part. Nucl. Phys.*, **76**:841, (2012).
- [28] B. R. Holstein. Nucleon polarizabilities. *arXiv:hep-ph/0010129*, (2000).
- [29] H. Dutz, et al. First measurement of the Gerasimov-Drell-Hearn sum rule for  $^1h$  from 0.7 to 1.8 GeV at ELSA. *Phys. Rev. Lett.*, **19**(192001), (2003).
- [30] J. Ahrens, et al. Helicity dependence of  $\gamma p \rightarrow n\pi$  below 450 MeV and contribution to the Gerasimov-Drell-Hearn sum rule. *Phys. Rev. Lett.*, **84**(5950), (2000).
- [31] K. Helbing, G. Anton, T. Michel, T. Speckner, G. Zeitler, M. Fausten, D. Menze, A. Nagel, D. Ryckbosch, R. Van de Vyver. The GDH detector. *Nucl. Instrum. Meth.*, **484**:129–139, (2002).
- [32] M. Camen, et al. Backward spin polarizability  $\gamma_\pi$  of the proton. *Phys. Rev. C*, **65**(032202), (2002).

- [33] E. L. Hallin, et al. Compton scattering from the proton. *Phys. Rev.C*, **48**(4): 1497, (1993).
- [34] G. Blanpied, et al.  $n \rightarrow \delta$  transition and proton polarizabilities from measurements of  $p(\gamma, \gamma)$ ,  $p(\gamma, \pi^0)$ , and  $p(\gamma, \pi^+)$ . *Phys.Rev. C.*, **64**, (2001).
- [35] G. Blanpied, et al.  $n \rightarrow \delta$  transition from simultaneous measurements of  $p(\gamma, \pi^0)$  and  $p(\gamma, \gamma)$ . *Phys.Rev. Lett.*, **64**, (1997).
- [36] G. Galler, et.al. Compton scattering by the proton. *Phy. Rev. C.*, **48**, (1993).
- [37] S. Wolf, et.al. Compton scattering by the proton using a large acceptance arrangement. *Eur. Phys. J.*, **12**, (2001).
- [38] Schumacher Martin. Polarizability of the nucleon and Compton scattering. *Prog. Part. Nucl. Phys.*, **55**:567–646, (2005).
- [39] D. Babusci, G. Giordano, A. I. Lvov, G. Matone, and A. M. Nathan. Low-energy Compton scattering of polarized photons on polarized nucleons. *Phys.Rev. C*, **55**(2), (1998).
- [40] A. C. Hearn and E. Leader. Fixed-angle dispersion relations for nucleon Compton scattering. *Phys. Rev.*, **126**(789), (1962).
- [41] A.I. Lvov. Compton scattering on proton at energies up to 400-MeV and finite energy sum rules. *Sov. J. Nucl. Phys.*, **34**(597), (1981).
- [42] V. Petrun'in. Scattering of low-energy photons on a system with spin 1/2. *Sov.Phys. JETP.*, **13**, (1961).
- [43] V. Petrun'in. Scattering of low-energy photons on a zero-spin particle. *Nucl.Phys.*, **55**, (1964).

- [44] B. Pasquini, D. Drechsel and M. Vanderhaeghen. Proton spin polarizabilities from polarized Compton scattering. *Phys.Rev. C.*, **76**, (2007).
- [45] D. Drechsel, B. Pasquini and M. Vanderhaeghen. Dispersion relations in real and virtual Compton scattering. *Phys. Rept.*, **378**, (2003).
- [46] V. Lensky and V. Pascalutsa. Predictive powers of chiral perturbation theory in Compton scattering off protons. *Eur. Phys. J.C.*, **65**, (2010).
- [47] Veronique Bernard. Chiral perturbation theory and baryon properties. *Prog. Part. Nucl. Phys.*, **76**:82–160, (2008).
- [48] D. Hornidge, E.J.Downie, J.R.M. Annand and R. Miskimen. Measurement of the proton spin polarizabilities: An A2 collaboration proposal for an experiment at MAMI, (2012).
- [49] P. Martel, et al. Measurements of the proton spin polarizabilities with double-polarized Compton scattering. *Phys. Rev. Lett.*, **114**(112501), (2015).
- [50] P. Martel. *Measuring Proton Spin Polarizabilities with Polarized Compton Scattering*. PhD thesis, University of Massachusetts, Amherst, MA, USA, (2012).
- [51] C. Collicot. *Probing Proton Structures Through Single Polarization Observables of Compton Scattering and  $\pi^0$  Photoproduction Within the  $\Delta(1232)$  Region*. PhD thesis, Dalhousie University, Halifax, Nova Scotia, Canada, (2015).
- [52] A. Jankowiak. The Mainz Microtron MAMI-past and future. *Eur. Phys. J.*, **28**: 149–160, (2006).
- [53] Mott, N.F. The scattering of fast electrons by atomic nuclei. *Proc. R. Soc.Long.*, **123**:435–442, (1929).

- [54] H. Olsen and L. C. Maximon. Photon and electron polarization in high energy bremsstrahlung and pair production with screening. *Phys. Rev.*, **114**(3), (1959).
- [55] K. Aulenbacher, et al. The MAMI source of polarized electrons,. *Nucl.Instr. and Meth.*, **391**:498–506, (1997).
- [56] Tioukine V., Aulenbacher K. Operation of the MAMI accelerator with a wien filter based spin rotation system. *Nucl. Instrum. Methods*, **82**:568, (2006).
- [57] Tioukine V., Aulenbacher K. and Riehn. A Mott polarimeter operating at MeV electron beam energies. *Rev. Sci. Instrum.*, **82**:033303, (2011).
- [58] H. Herminghaus, K. H. Kaiser and U. Ludwig-Mertin. The design of a cascaded 800 MeV normal conducting c.w. Race Track Microtron. *Nucl. Instr. Meth.*, **138**:1, (1976).
- [59] M. Dehn, et al. The MAMI C: The beauty of normal conducting multiturn recirculators. *Eur. Phys. J. Special Topics*, **198**:385–403, (2011).
- [60] S. J. Hall, et al. A focal plane system for the 855 MeV tagged photon spectrometer at MAMI-B. *Nucl. Instr. and Meth. Phys. Res.*, **368**:698–708, (1995).
- [61] David A. Howdle. *Measurement of Polarization Observables using Linearly Polarized Photons with the Crystal Ball at MAMI*. PhD thesis, University of Glasgow, Scotland, UK, (2012).
- [62] P. Martel, M. Biroth, C. Collicott, D. Paudyal and A. Rajabi. Compton scattering program studying nucleon polarizabilities. *EPJ Web of Conferences*, **142**:01021, (2017).
- [63] R. Partridge, et al. Decay of  $j/\psi \rightarrow 3\gamma$  and a search for a  $\eta_c$ . *Phys.Rev. Let.*, **44**(11), (1980).

- [64] M. Qreglia, et al. Study of the reaction  $\psi \rightarrow \gamma\gamma j/\psi$ . *Phys.Rev. D*, **25**:2260–2277, (1982).
- [65] S. Prakhov, et al. Measurement of the slope parameter  $\alpha$  for the  $\eta \rightarrow 3\pi^0$  decay with the Crystal Ball detector at the Mainz Microtron MAMI-C. *Phys.Rev. C*, **79**(035204), (1982).
- [66] D. Werthmueller. *Experimental Study of Nucleon Resonance Contributions to  $\eta$  Photoproduction on the Neutron*. PhD thesis, University of Basel, Basel, Switzerland, (2014).
- [67] E. D. Bloom and C. W. Peck. Physics with Crystal Ball detector. *Ann.Rev. Nucl. Part. Sci.*, **33**:97–143, (1983).
- [68] Linturi James Mugambi. *Study of the Helicity Dependence of  $\pi^0$  Photoproduction on Proton at MAMI*. PhD thesis, Johannes Gutenberg University Mainz, Mainz, Germany, (2015).
- [69] D. Vernekohl. Measurements with a Multi-Wire Proportional Chamber for small animal positron emission tomography. Master’s thesis, University Munster, Munster, Germany, (2010).
- [70] P. A. Bartolome. *First Doubly Polarized Photoproduction on  $^3\text{He}$  at the Photon Beam of MAMI*. PhD thesis, Johannes Gutenberg University Mainz, Mainz, Germany, (2010).
- [71] F Sauli. Principles and operation of multi wire proportional and drift chambers. *Nucl. Instr. and Meth. Phys. Res.*, (1977).
- [72] A.R. Gabler, et al. Response of TAPS to monochromatic photons with energies between 45 and 790 MeV. *Nucl. Instr. and Meth. Phys. Res.*, **346**:168–176, (1994).

- [73] R. Novotny. Performance of the BaF<sub>2</sub> calorimeter TAPS. *Nucl. Phys. B. Proc. Suppl.*, **6**:137–142, (1998).
- [74] M. Thiel. *In-medium Properties of the  $\omega$ -Meson Studied in Photo-nuclear Reactions near the Production Threshold*. PhD thesis, University Giessen, Gießen, Germany, (2010).
- [75] A. W. Overhauser. Polarization of nuclei in metals. *Phys. Rev.*, **92**:411, (1953).
- [76] T. R. Carver and C. P. Slichter. Polarization of nuclear spins in metals. *Phys. Rev.*, **92**:212, (1953).
- [77] D. G. Crabb and W. Mayer. Solid polarized target for nuclear and particle physics. *Annu. Rev. Nucl. Part. Sci.*, **47**:67–109, (1997).
- [78] T.D. Averett, et al. A solid polarized target for high-luminosity experiments. *Nucl. Instr. Meth.*, **427**:440–454, (1999).
- [79] W. Meyer, et al. Polarization measurements of TEMPO-doped butanol targets. *Nucl. Instrum. Methods, A* **400**:133–136, (1997).
- [80] Farrar, et al. High-frequency dynamic nuclear polarization in the nuclear rotating frame. *J. Mag. Reson.*, **144**:134–141, (2000).
- [81] A2 Wiki. <http://www.a2.kph.uni-mainz.de/intern/daqwiki/trigger/experiment>, (2017).
- [82] A2 Wiki. <http://www.a2.kph.uni-mainz.de/intern/daqwiki/media/experiment>, (2017).
- [83] J.R.M. Annand. Data analysis within an AcQuRoot framework. *Root Version 4v4*, University of Glasgow, (2008).

- [84] E.J. Downie. *Radiative  $\pi^0$  Photoproduction in the Region of the  $\Delta(1232)$  Resonance*. PhD thesis, University of Glasgow, Scotland, UK, (2006).
- [85] D. Krambrich. *ufbau des Crystal Ball-Detektorsystems und Untersuchung der Helizitatsasymmetrie in  $\gamma p \rightarrow \pi^0 \pi^0$* . PhD thesis, Johannes Gutenberg University Mainz, Mainz, Germany, (2007).
- [86] Peter-Bernd Otte. *Erste Messung der  $\pi^0$ -photoproduktion an transversal polarisierten protonen nahe der schwelle*. PhD thesis, Johannes Gutenberg University Mainz, Mainz, Germany, (2015).
- [87] D. Glazier. A Geant4 simulation for the Crystal Ball MAMI setup. *Technical report*, University of Edingurgh, (2007).
- [88] S. Agostinelli. A Geant4 simulation toolkit. *Nucl. Instrum. Methods*, **506**:250, (2003).
- [89] University of Basel group. Calibration procedure of A2 data using the CaLib software.
- [90] M. Oberle. *Photoproduction of pion pairs off nucleons*. PhD thesis, University of Basel, Basel, Switzerland, (2014).
- [91] Particle Data Group. <http://pdg.lbl.gov/2015/atomicnuclearproperties>, (2015).
- [92] R. Workman, W. Briscoe, M. Paris, and I. Strakovsky. Updated SAID analysis of pion photoproduction data. *Phys. Rev.C*, **85**(025201), (2012).
- [93] R. Workman, W. Briscoe, and I. Strakovsky. Partial-wave analysis of nucleon-nucleon elastic scattering data. *Phys. Rev.C*, **94**(065203), (2016).
- [94] John R. Taylor. *An Introduction to Error Analysis, Second Edition*. University Science Books, California, (1997).

- [95] B. R. Holstein, D. Drechsel, B. Pasquini and M. Vanderhaeghen. Studies of nucleon resonance structure in exclusive meson electroproduction. *Phys. Rev.C*, **61**, (2000).
- [96] K. Vijaya Kumar, J. McGovern, and M. Birse. Spin polarisabilities of the nucleon at NLO in the chiral expansion. *Phys. Lett. B*, **479**, (2000).
- [97] J. A. McGovern, D. R. Phillips and H. Griesshammer. Compton scattering from the proton in an effective field theory with explicit delta degrees of freedom. *Eur.Phys. J. A*, **49**, (2013).
- [98] V. Lensky and J. McGovern. Proton polarizabilities from Compton data using covariant chiral effective field theory,. *Phys. Review C*, **89**, (2014).
- [99] S. Kondratyuk and O. Scholten. Compton scattering on the nucleon at intermediate energies and polarizabilities in a microscopic model,. *Phys. Review C*, **64**, (2001).

**List of Abbreviations**

QCD	Quantum Chromodynamics
QED	Quantum Electrodynamics
DR	Dispersion Relation
$\chi$ EFT	Chiral Effective Field Theory
$\chi$ PT	Chiral Perturbation Theory
MAMI	MAInz MIcrotron
PDG	Particle Data Group
GDH	Gerasimov-Drell-Hearn
SPs	Spin Polarizabilities
LARA	LARge Acceptance
RCS	Real Compton Scattering
LEX	Low Energy Expansion
HDPV	Holstein, Drechsel, Pasquini and Vanderhaeghen
$B\chi$ PT	Baryon Chiral Perturbation Theory
NNLO	Next-to-Next-to-Leading Order
CB	Crystal Ball
MWPCs	Multi-Wire Proportional Chambers
PID	Particle Identification Detector
TAPS	Two Arms Photon Spectrometer
RTM	Race Track Microtron
HDSM	Harmonic Double Sided Microtron

RF	Radio Frequency
FPD	Focal Plane Detector
PMT	PhotoMultiplier Tube
DESY	Deutsches Elecktronen Synchrotron
WLS	WaveLength Shifting
DNP	Dynamic Nuclear Polarization
BFP	Brute Force Polarization
FST	Frozen Spin Target
NMR	Nuclear Magnetic Resonance
JINR	Joint Institute for Nuclear Research
TDC	Time to Digital Converter
ADC	Analog to Digital Converter
DAQ	Data AcQuisition
TLS	Trigger Level Sections
VME	Versa Module Europe single board computer
CAMAC	Computer Aided Measurement And Control
FPGA	Field Programmable Gate Array
CATCH	Compass, Accumulation, Transfer Control Hardware
TCS	Trigger Control System
LED	Leading-Edge Discriminator
CFD	Constant Fraction Discriminator
FWHM	Full Width at Half Maximum

LINAC	LINEar ACcelerator
GUI	Graphical User Interface
VPN	Virtual Private Network
GoAT	Generation of Analysis Trees
PSA	Pulse Shape Analysis
SAID	Scattering Analysis Interactive Database
TOF	Time Of Flight
EventGen	Event Generator